



HAL
open science

Propriétés thermo-mécaniques des matériaux pour les piles à combustible

Desirée Ciria Matamoros

► **To cite this version:**

Desirée Ciria Matamoros. Propriétés thermo-mécaniques des matériaux pour les piles à combustible. Autre. Université Paris Saclay (COMUE); Universidad de Sevilla (Espagne), 2017. Français. NNT : 2017SACLC064 . tel-02426004

HAL Id: tel-02426004

<https://theses.hal.science/tel-02426004v1>

Submitted on 1 Jan 2020

HAL is a multi-disciplinary open access archive for the deposit and dissemination of scientific research documents, whether they are published or not. The documents may come from teaching and research institutions in France or abroad, or from public or private research centers.

L'archive ouverte pluridisciplinaire **HAL**, est destinée au dépôt et à la diffusion de documents scientifiques de niveau recherche, publiés ou non, émanant des établissements d'enseignement et de recherche français ou étrangers, des laboratoires publics ou privés.



CentraleSupélec



THERMO-MECHANICAL PROPERTIES OF MATERIALS FOR FUEL CELLS

Thèse de doctorat de l'Université Paris-Saclay
préparée à CentraleSupélec

École doctorale n°573: Approches interdisciplinaires, fondements,
applications et innovation (Interfaces)

Spécialité de doctorat: Physique

Thèse présentée et soutenue à Gif sur Yvette, 06 November 2017 par

Desirée Ciria Matamoros

Composition du Jury :

M. Alfonso Bravo León Professor, Universidad de Sevilla, Espagne	Président
M. Tor Grande Professor, Norwegian University of Science and Technology, Norvège	Rapporteur
M. Pierre-Marie Geffroy Chargé de Recherche - CRNS, France	Rapporteur
Mme. Veronique Aubin Professor, Université Paris-Saclay, France	Examineur
M. Guilhem Dezanneau Head of SPMS Laboratory, Université Paris-Saclay, France	Directeur de thèse
M. Manuel Jiménez Melendo Professor, Universidad de Sevilla, Espagne	Directeur de thèse

ACKNOWLEDGEMENTS

On the one hand, I would like to express my gratitude to the following people from **CentraleSupélec** who have kindly helped me in my research and in the preparation of this thesis.

To begin with, my deepest thanks and sincere appreciation to my supervisors. I would like to say a big thank you to Dr. Guilhem Dezanneau, my thesis director in France, for giving me the opportunity to continue working in research, for guiding me during this work, for his kind attention, patience, comprehension and invaluable help with my personal and professional issues. Thank you Guilhem for everything, I was so fortunate to work with you.

A very special thanks to Dr. Veronique Aubin, for her encouragement, helpful advice, great help and for the time devoted to carrying out the simulations and discussing the results.

I would like to thank all members of SPMS and MSSMAT laboratory, for their technical help and support. Moreover, I would particularly like to thank Nicolas Roubier for his total availability, his endless help and kind attention; Eva Heripre for her ideas, cooperation and time; Christine Vinée-Jacquing for her thoughtful attention and help. And my heartfelt gratitude goes to Xavier Brill for his kindness, constant help and for his friendship.

I am also thankful to all PhD students from both laboratories, especially to Anastasia, Charles, Charlotte, Fabien, Gilles, Halyna and Michael for their kind assistance and suggestions.

A special thanks to Chen Yi for our talks, walks and dinners, for his trust, his support and for the time we spent together. Vamos Chen Yi!

And naturally, thank you to Cintia, my companion from the start, with whom I have shared every minute of this PhD. I must thank you for always trusting me, for your company, your constant help, support and understanding, for the moments we spent together and for making this hard journey more pleasant. It wasn't easy my friend, but we managed it in the end. Without you, this adventure would never have been the same. Thanks for everything.

I also wish to express my sincere gratitude to Florencia Mariscal for opening up her home to me when I arrived in Paris, for offering me her selfless assistance at all times, for her amiable, friendly treatment and for her incredible human qualities. I have no words to thank you for so much generosity, I was so fortunate to have you with me.

On the other hand, I would also like to extend my heartfelt gratitude to the following people from the **University of Sevilla** who have helped and contributed to making this work possible.

En primer lugar, mi más sincero agradecimiento al Dr. Manuel Jiménez-Melendo, mi director de tesis en España, por haber confiado en mí, por su infinita paciencia y ayuda, por el constante apoyo y ánimo que me ha brindado desde el principio, y por su total disponibilidad. Asimismo, he de agradecerle por sus enseñanzas, por los largos días de trabajo en el laboratorio, por el tiempo dedicado a discutir los resultados y preparar esta memoria, y por el enorme compromiso que tiene con su trabajo. Con su entusiasmo, generosidad, profesionalidad y cercanía ha sido un auténtico placer poder trabajar a su lado.

Al Dr. Alfonso Bravo León por su amabilidad, por sus sugerencias e ideas siempre acertadas y por el tiempo dedicado a aclarar algunas dudas de este trabajo.

Agradecer también a todos los miembros del grupo de investigación de Materiales Biomiméticos y Multifuncionales y del CITIUS por su tiempo, paciencia y colaboración, en especial al Dr. Joaquín Ramírez por su trato amable y su ayuda.

Al Dr. Javier Quispe por su gran ayuda, por mostrarse siempre solícito y por su amistad.

A Carmen, Antonio, Pilar, Fredy y Saúl por su atención, ayuda y por el tiempo que hemos compartido. Además quiero expresar especialmente mi gratitud a Aurora por sus consejos, su paciencia, su ayuda y su generosidad. Y como no a Rafa, mi compañero de laboratorio, estancias, congresos y piso, hemos vivido un poco de todo juntos y quiero darte las gracias por haber estado siempre ahí, nada hubiera sido lo mismo sin ti. Además agradeceremos a todos por el extraordinario ambiente de amistad, ya que es muy estimulante trabajar en unas condiciones tan agradables.

A Nuria, Marta, Carmen Y Rosana, con las que coincidí por casualidad en algún congreso o estancia y enseguida nos hicimos inseparables. Gracias chicas por esas horas y horas de conversaciones y de paseos turísticos, por vuestra compañía y por vuestra amistad.

A mis amigos Juan, Fati, Almudena, Miguelón, Bea, Alex y Marina, por estar siempre a mi lado, por vuestras reconfortantes visitas, por vuestra comprensión y por vuestra valiosa amistad. Agradecer también a Nikki por su tiempo y su ayuda. Y a Pilar por su amabilidad, por su compañía, y por los momentos que hemos vivido juntas.

Y muy especialmente a mi amigo Víctor por su constante apoyo, por su paciencia, por sus comentarios y sugerencias, y por ofrecerme siempre su ayuda humilde y desinteresada. Gracias amigo.

Quiero agradecer también a Kiko, Gumi, Mónica, Fran, Cristina, Jaime y a mis pequeñines, especialmente a Sergio, por haber estado siempre ahí, por contar siempre conmigo, por su compañía y apoyo, por recibirme siempre con una sonrisa y los brazos abiertos, y por mantener y cuidar ese vínculo tan especial que tenemos. Gracias por tanto.

Finalmente, un agradecimiento muy especial merecen mis padres, mi hermana y mis abuelos por creer tanto en mí, por el cariño que siempre me han dado haciendo que les sienta a centímetros incluso estando a miles de kilómetros, por su infinita generosidad y por el ánimo y el apoyo firme e incondicional prestado en todo momento, no sólo a la hora de realizar este trabajo sino a lo largo de mi vida. También he de agradecer a mis tíos, Puri, José y Julián, por su constante preocupación, apoyo y ayuda. Y como no a Sofía, que a tu corta edad has sido capaz de entender mis ausencias, sacar lo mejor de mí y mostrarme siempre el lado más dulce de la vida. Sois el pilar fundamental de mi vida, yo no sería nada sin vosotros, os quiero.

CONTENTS

Abstract	13
Résumé	15
Resumen	17
CHAPTER 1. INTRODUCTION	19
1.1 Fuel cells	19
1.1.1 Solid Oxide Fuel Cells (SOFCs).....	20
1.1.2 Electrolyte materials for SOFCs	22
1.1.2.1 Lanthanum Silicate	23
1.1.2.2 Yttrium-doped Barium Zirconate	24
1.2 Importance of mechanical properties in SOFCs	25
1.2.1 Thermo-elastic properties	27
1.2.2 Creep behaviour	28
1.2.2.1 Diffusional creep	29
1.2.2.2 Grain boundary sliding	31
1.2.2.2.1 Diffusion-accommodated process: Ashby-Verrall model.....	31
1.2.2.2.2 Dislocation-accommodated process	32
1.2.2.3 Interface-reaction creep	33
1.2.2.3.1 Diffusion creep controlled by interface-reaction	33
1.2.2.3.2 GBS creep controlled by interface-reaction	33
1.2.2.4 Phenomenological relationships for superplasticity	34
1.2.3 Previous results in SOFC electrolytes	35
1.2.3.1 Ytria-Stabilised Zirconia	35
1.2.3.2 Apatites-compounds.....	35
1.2.3.3 Proton-conducting compounds.....	36
1.3 References	36

CHAPTER 2. PREPARATION OF MATERIALS	47
2.1 Introduction	47
2.2 Lanthanum Silicate	48
2.2.1 Commercial starting precursors for LSO nanopowders preparation	49
2.2.2 Freeze-drying synthesis	49
2.2.3 Compaction of LSO nanopowders	51
2.2.4 High temperature sintering	51
2.2.4.1 Conventional sintering	51
2.2.4.2 Spark plasma sintering	51
2.3 Yttrium-doped Barium Zirconate	52
2.3.1 Commercial starting precursors for BZY nanopowders preparation	53
2.3.2 Modified EDTA-citrate complexing synthesis	53
2.3.3 Compaction of BZY nanopowders	55
2.3.4 High temperature sintering	55
2.3.5 Commercial Yttrium-doped Barium Zirconate	56
NiO-extraction	56
2.4 References	56
CHAPTER 3. STRUCTURAL AND MICROSTRUCTURAL CHARACTERIZATION	61
3.1 Introduction	62
3.2 Characterization techniques	62
3.2.1 X-Ray Diffraction	62
3.2.2 Particle size	64
3.2.3 Density	64
3.2.4 Electron microscopy analysis	64
3.2.4.1 Preparation of samples	65
3.2.4.2 Morphological parameters	65
3.2.4.2.1 Grain size	65
3.2.4.2.2 Form factor	67
3.2.4.2.3 Orientation angle	67
3.3 Experimental results	68
3.3.1 Lanthanum Silicates	68
3.3.1.1 Density	68
3.3.1.2 X-Ray Diffraction analysis	68

3.3.1.3 Particle size.....	70
3.3.1.4 Microstructural analysis.....	72
3.3.2 Yttrium-doped Barium Zirconate.....	75
3.3.2.1 Density	75
3.3.2.2 X-ray diffraction analysis.....	75
3.3.2.3 Particle size.....	78
3.3.2.4 Microstructural analysis.....	79
3.3.3 Yttrium-doped Barium Zirconate after NiO-extraction	82
3.3.3.1 Density	82
3.3.3.2 X-ray diffraction analysis.....	82
3.3.3.3 Microstructural analysis.....	85
3.4 References	87
CHAPTER 4. ROOM-TEMPERATURE MECHANICAL CHARACTERIZATION	91
4.1 Introduction	91
4.2 Experimental characterization of room-temperature mechanical properties.....	92
4.2.1 Experimental procedure	92
4.2.1.1 Nanoindentation	93
4.2.1.2 Mechanical compression tests with optical imaging	95
4.2.1.3 Resonant Ultrasound Spectroscopy.....	97
4.2.1.4 Microindentation	100
4.2.2 Experimental results	101
4.2.2.1 Room-temperature mechanical properties of Lanthanum Silicate	101
4.2.2.1.1 Nanoindentation.....	101
4.2.2.1.2 Mechanical compression tests with optical imaging.....	103
4.2.2.1.3 Resonant Ultrasound Spectroscopy.....	103
4.2.2.1.4 Microindentation	104
4.2.2.1.5 Comparison of the different techniques	105
4.2.2.2 Room-temperature mechanical properties of Y-doped Barium Zirconate....	105
4.2.2.2.1 Nanoindentation.....	105
4.2.2.2.2 Mechanical compression tests with optical imaging.....	107
4.2.2.2.3 Resonant Ultrasound Spectroscopy.....	108
4.2.2.2.4 Microindentation	108
4.2.2.2.5 Comparison of the different techniques	110
4.3 Density Functional Theory calculations.....	110

4.3.1 DFT calculation procedure: Elastic coefficients determination.....	111
4.3.1.1 DFT Calculations details for Lanthanum Silicate oxy-apatites	112
4.3.1.2 DFT calculations for Yttrium-doped Barium Zirconates.....	113
4.3.2 DFT calculation results.....	113
4.3.2.1 Elastic properties of Lanthanum Silicate.....	113
4.3.2.2 Elastic properties of Y-doped Barium Zirconate	114
4.4 References	115

CHAPTER 5. THERMO-MECHANICAL CHARACTERIZATION 119

5.1 Introduction	120
5.2 Experimental characterization of thermo-mechanical properties	120
5.2.1 Experimental procedure.....	120
5.2.1.1 High-temperature X-Ray diffraction	120
5.2.1.2 Thermo-mechanical analysis.....	121
5.2.1.3 High-temperature Resonant Ultrasound Spectroscopy.....	122
5.2.2 Experimental results.....	123
5.2.2.1 Thermo-mechanical properties of Lanthanum Silicate.....	123
5.2.2.1.1 Coefficient of thermal expansion	123
5.2.2.1.2 Elastic constants	124
5.2.2.2 Thermo-mechanical properties of Yttrium-doped Barium Zirconate.....	126
5.2.2.2.1 Coefficient of thermal expansion	126
5.2.2.2.2 Elastic constants	127
5.3 Numerical simulation of residual stresses state in lanthanum silicate	128
5.3.1 Computation procedure.....	129
5.3.1.1 Description of microstructure.....	129
5.3.1.2 Numerical simulations	131
5.3.1.2.1 Material properties	131
5.3.1.2.2 Loading and boundary conditions.....	132
5.3.1.3 Analysis of Stress fields: Localization and prediction of fracture	135
5.3.1.3.1 Maximum principal stress theory.....	135
5.3.1.3.2 Stress intensity approach	136
5.3.1.4 Strategy of Simulations	137
5.3.1.4.1 Determination of the Mesh Size.....	137
5.3.1.4.2 Multiple realizations.....	138
5.3.2 Computation results.....	139

5.3.2.1 Distribution of stresses	139
5.3.2.2 Prediction of failure	141
5.4 References	144
CHAPTER 6. HIGH-TEMPERATURE MECHANICAL CHARACTERIZATION	149
6.1 Introduction	150
6.2 Working conditions experiments (T = 700 °C)	150
6.2.1 Experimental procedure	150
6.2.2 Experimental results	151
6.2.2.1 Mechanical response of Lanthanum Silicates in SOFC WCs	151
6.2.2.2 Mechanical response of Yttrium-doped Barium Zirconate in SOFC WCs	151
6.3 Creep experiments (T > 1000 °C)	156
6.3.1 Experimental procedure	156
6.3.1.1 Mechanical magnitudes	157
6.3.1.2 High-temperature mechanical tests	159
6.3.1.2.1 Constant cross-head speed tests	159
6.3.1.2.2 Constant load tests	160
6.3.1.3 Steady-state deformation	160
6.3.1.4 Determination of creeps parameters.....	161
6.3.1.4.1 Conventional method	162
6.3.1.4.2 Differential method	162
6.3.2 Experimental results	163
6.3.2.1 High-temperature mechanical behavior of LSO-CS	163
6.3.2.1.1 Fragile-ductile transition	163
6.3.2.1.2 Microstructure after deformation	165
6.3.2.1.3 Creep parameters	170
6.3.2.1.4 High-temperature deformation mechanism.....	176
6.3.2.2 High-temperature mechanical behavior of LSO-SPS	178
6.3.2.2.1 Fragile-ductile transition	178
6.3.2.2.2 Microstructure after deformation	180
6.3.2.2.3 Creep parameters	182
6.3.2.2.4 High-temperature deformation mechanism.....	187
6.3.2.3 High-temperature mechanical behavior of BZY	189
6.3.2.3.1 Fragile-ductile transition	189
6.3.2.3.2 Microstructure after deformation	191

6.3.2.3.3 Creep parameters	193
6.3.2.3.4 High-temperature deformation mechanism	199
6.3.2.3.5 Creep behaviour of other perovskite-structured oxides	200
6.4 References	202
CHAPTER 7. GENERAL CONCLUSIONS	205
CHAPTER 7. CONCLUSIONS GÉNÉRALES	211
CHAPTER 7. CONCLUSIONES GENERALES	217

ABSTRACT

Solid oxide fuel cells (SOFCs) offer a real alternative to classical technologies for the generation of electricity by clean, efficient and environmental-friendly means. Nevertheless, the main limitation of SOFCs lies in their unsatisfactory durability and reliability due to the high operating temperatures and thermal cycling characteristic of these devices. An intense search is currently underway for materials for SOFCs with the objective of lowering the working temperature and then overcoming these limitations. Among the different candidates which have emerged, Lanthanum Silicate (LSO) and Yttrium-doped Barium Zirconate (BZY) were considered as potential alternatives to be used as electrolyte materials for intermediate-temperature solid oxide fuel cells. While numerous studies have been devoted to characterizing and optimizing the microstructural and electro-chemical properties of SOFC components, as yet there is little research available on mechanical properties and the influence they have on SOFC lifespan. The reliability and durability of these devices depends not only on their electro-chemical stability, but also on the ability of their structure to withstand residual stresses arising from the cell manufacturing process and mechanical stresses from operation. Owing to the fact that SOFCs are composed by stacking of several single cells which in turn are made up of individual brittle layers in close contact, these stresses mainly originate from the difference between the coefficient of thermal expansion and elastic properties of adjacent layers and creep deformation. Mismatched stresses can result in the mechanical failure of a single cell and have dramatic consequences on the whole stack. Therefore, knowledge of mechanical properties of the cell components becomes an important issue for the mechanical integrity and development of SOFCs (**Chapter 1**).

The aim of this PhD thesis is the fabrication and structural, microstructural and mechanical characterization of Lanthanum Silicate and Yttrium-doped Barium Zirconate. To this end, high density ($d > 97\%$) ceramics made through conventional or spark plasma sintering were prepared from nanopowders synthesized by chemical routes. The details of the synthesis routes and the sintering conditions are described in **Chapter 2**. The resulting nanopowders and pellets were structurally and microstructurally characterized by X-Ray diffraction, particle size analysis by laser diffraction and electron microscopy in **Chapter 3**.

The dense ceramics were then characterized mechanically at different temperatures. First, the mechanical properties of LSO and BZY compounds were examined by different techniques at room temperature in **Chapter 4**. Nanoindentation, microindentation, resonant ultrasound

spectroscopy, compression tests and density functional theory were used to determine their elastic constants, hardness and fracture toughness. Then, the influence of temperature on the thermo-elastic properties of both materials was investigated in **Chapter 5**. In this chapter finite elements numerical simulations were also carried out to characterize the state of stress and predict fracture in Lanthanum Silicate. Later on, the mechanical response of both electrolyte materials was evaluated by means of compressive mechanical tests at solid oxide fuel cell operating temperatures (700 °C) under different atmospheres (**Chapter 6**). Moreover, this chapter is also devoted to studying the fracture and plastic deformation mechanisms of these compounds at high temperature by means of creep experiments.

Finally, **Chapter 7** summarizes the most relevant conclusions derived in this work.

Keywords: Solid oxide fuel cells, electrolyte materials, mechanical properties, creep.

RÉSUMÉ

Les piles à combustible à oxyde solide (SOFC) offrent une alternative réelle aux technologies classiques de génération d'électricité en étant à la fois propre, efficace et respectueuse de l'environnement. Toutefois, leur principale limitation réside en leur durée de vie et fiabilité limitées dues à leur haute température de fonctionnement. Des recherches intenses de matériaux pour SOFC sont actuellement poursuivies pour essayer d'abaisser la température de fonctionnement de ces dispositifs afin de dépasser ces limitations. Parmi les différents candidats qui ont émergé, le Silicate de Lanthane (LSO) et le Zirconate de Baryum dopé à l'Yttrium (BZY) ont été identifiés comme des alternatives potentielles à utiliser comme matériaux d'électrolyte pour les piles à combustible à oxyde solide à température intermédiaire. De manière surprenante, alors que de nombreuses études concernent l'optimisation microstructurale et électrochimiques des composants de la pile, très peu d'études concernant l'évaluation de leurs propriétés mécaniques et de leur influence sur la durée de vie du dispositif. La fiabilité et durée de ces dispositifs dépend non seulement de leur stabilité électrochimique, mais aussi de la capacité de leur structure à supporter les contraintes résiduels issus du procédé de fabrication et de contraintes mécaniques de fonctionnement. En raison du fait que les SOFC sont composés d'empilement de plusieurs cellules individuelles qui, à leur tour, sont constituées de couches fragiles individuelles en contact étroit, ces contraintes proviennent principalement de la différence entre le coefficient de dilatation thermique et les propriétés élastiques des couches adjacentes et la déformation du fluage. Des contraintes non coordonnées peuvent entraîner une défaillance mécanique d'une seule cellule et avoir des conséquences dramatiques sur l'ensemble de la pile. De ce fait, la connaissance des propriétés mécaniques des composants de la cellule est une étape importante pour préserver l'intégrité et le développement des SOFC (**Chapitre 1**).

Le but de cette thèse est la fabrication et l'étude des propriétés structurale, microstructurales et mécaniques de matériaux de type Silicate de Lanthane et de Zirconate de Baryum dopé à l'Yttrium. A cette fin, des céramiques denses ($d > 97\%$) ont été préparées par voie chimique pour l'obtention de poudres suivie de frittage conventionnel ou spark plasma. Les détails de l'élaboration de ces matériaux sont donnés dans le **Chapitre 2**. Les nanopoudres et céramiques obtenues ont été caractérisées sur le plan structural et microstructural par diffraction des rayons X, diffusion laser et microscopie électronique (**Chapitre 3**).

Ces céramiques denses ont ensuite été caractérisées sur le plan des propriétés mécaniques à différentes températures. Tout d'abord, les propriétés mécaniques des céramiques LSO et BZY ont été évaluées par différentes techniques à température ambiante dans le **Chapitre 4**. Les méthodes de nanoindentation, de microindentation, de résonance ultrasonore, de tests en compression et la méthode théorique de la théorie de la fonctionnelle densité ont été utilisées afin de déterminer les propriétés élastiques, de dureté et de résistance à la fracture des matériaux obtenus. L'influence de la température sur les propriétés thermo-élastiques a été explorée dans le **Chapitre 5**. Dans ce chapitre, des calculs par éléments finis ont également permis de caractériser l'état de stress résiduel présent au sein de l'oxyapatite après la procédure de frittage ou lors des essais mécaniques. Nous avons ensuite évalué la réponse mécanique des deux matériaux dans des conditions proches de celles de fonctionnement d'une pile i.e. à 700 °C sous atmosphère contrôlée, successivement oxydante et réductrice (**Chapitre 6**). Ce chapitre est également consacré à l'étude des mécanismes de déformation plastique à haute température et à l'extraction des paramètres de fluage.

Finalement, le **Chapitre 7** dresse une conclusion regroupant les principaux résultats.

Mots clés: Piles à combustible à oxide solide, matériaux d'électrolyte, propriétés mécaniques, fluage

RESUMEN

Las pilas de combustible de óxido sólido (SOFCs) ofrecen una alternativa real a las tecnologías de producción de electricidad convencionales ya que son más limpias, eficientes y respetuosas con el medio ambiente. Sin embargo, la principal limitación de las SOFC radica en su insatisfactoria durabilidad y fiabilidad debido a las altas temperaturas de funcionamiento y a los ciclos térmicos característicos de estos dispositivos. Actualmente se está realizando una intensa búsqueda de materiales para SOFC con el objetivo de reducir la temperatura de trabajo y superar estas limitaciones. Entre los diferentes candidatos que han surgido, el Silicato de Lantano (LSO) y el Zirconato de Bario dopado con Itrio (BZY) han sido considerados como potenciales alternativas para ser utilizados como electrolitos en pilas de combustible de óxido sólido a temperaturas intermedias. Mientras numerosos estudios se han centrado en la caracterización y optimización de las propiedades microestructurales y electroquímicas de los componentes que forman una SOFC, todavía hay muy pocos trabajos de investigación sobre las propiedades mecánicas y su influencia en la vida útil de una SOFC. La fiabilidad y durabilidad de estos dispositivos no sólo depende de su estabilidad electroquímica, sino también de su capacidad estructural para soportar las tensiones residuales que aparecen en el proceso de fabricación de la pila y tensiones mecánicas que surgen durante la operación. Debido al hecho de que las SOFCs están compuestas por apilamiento de varias celdas individuales y que a su vez estas están constituidas por capas frágiles individuales en íntimo contacto, estas tensiones se originan principalmente por la diferencia entre el coeficiente de dilatación térmica y las propiedades elásticas de capas adyacentes y por la deformación plástica causada por fluencia. La incompatibilidad de tensiones puede provocar el fallo mecánico de una sola celda y tener consecuencias dramáticas en toda la pila. Por lo tanto, el conocimiento de las propiedades mecánicas de cada componente es una cuestión esencial para la integridad mecánica y el desarrollo de las SOFCs (**Capítulo 1**).

El objetivo de esta tesis doctoral es la fabricación y caracterización estructural, microestructural y mecánica del Silicato de Lantano y Zirconato de Bario dopado con Itrio. Con este fin, se prepararon cerámicas de alta densidad ($d > 97\%$) mediante sinterización convencional o asistida por descarga eléctrica pulsada a partir de nanopulvos sintetizados mediante rutas químicas. Los detalles de las rutas de síntesis y las condiciones de sinterización se describen en el **Capítulo 2**. Los nanopulvos y masivos obtenidos fueron caracterizados estructural y microestructuralmente por difracción de rayos X, análisis de tamaño de partícula por difracción láser y microscopía electrónica de barrido y transmisión en el **Capítulo 3**.

Los cerámicos densos se caracterizaron mecánicamente a diferentes temperaturas. En primer lugar, se examinaron las propiedades mecánicas de los compuestos LSO y BZY mediante diferentes técnicas a temperatura ambiente en el **Capítulo 4**. Nanoindentación, microindentación, espectroscopía de resonancia ultrasónica, ensayos de compresión y cálculos DFT fueron usados para determinar sus constantes elásticas, su dureza y su tenacidad de fractura. A continuación, se estudió la evolución de las propiedades termoelásticas de ambos materiales con la temperatura en el **Capítulo 5**. En este capítulo también se realizaron simulaciones numéricas de elementos finitos para caracterizar el estado de tensión y predecir la fractura en el Silicato de Lantano. Posteriormente, se evaluó la respuesta mecánica de ambos materiales electrolíticos mediante ensayos mecánicos de compresión a temperaturas de funcionamiento de las pilas de combustible de óxido sólido (700 °C) y en diferentes atmósferas (**Capítulo 6**). Además, este capítulo también se dedica al estudio de los mecanismos de fractura y deformación plástica de estos compuestos a alta temperatura por medio de experimentos de fluencia.

Finalmente, el **Capítulo 7** resume las conclusiones más relevantes derivadas de este trabajo.

Palabras clave: Pilas de combustible de óxido sólido, materiales electrolíticos, propiedades mecánicas, fluencia.

Chapter 1

INTRODUCTION

Contents

1.1 Fuel cells	19
1.1.1 Solid Oxide Fuel Cells (SOFCs)	20
1.1.2 Electrolyte materials for SOFCs	22
1.1.2.1 Lanthanum Silicate	23
1.1.2.2 Yttrium-doped Barium Zirconate	24
1.2 Importance of mechanical properties in SOFCs	25
1.2.1 Thermo-elastic properties	27
1.2.2 Creep behaviour	28
1.2.2.1 Diffusional creep	29
1.2.2.2 Grain boundary sliding	31
1.2.2.2.1 Diffusion-accommodated process: Ashby-Verrall model	31
1.2.2.2.2 Dislocation-accommodated process	32
1.2.2.3 Interface-reaction creep	33
1.2.2.3.1 Diffusion creep controlled by interface-reaction	33
1.2.2.3.2 GBS creep controlled by interface-reaction	33
1.2.2.4 Phenomenological relationships for superplasticity	34
1.2.3 Previous results in SOFC electrolytes	35
1.2.3.1 Ytria-Stabilised Zirconia	35
1.2.3.2 Apatites-compounds	35
1.2.3.3 Proton-conducting compounds	36
1.3 References	36

1.1 FUEL CELLS

In order to cope with the climate change environmental threat and the exhaustion of fossil fuel reserves, the development of sustainable, more effective and cleaner energy sources becomes a major global challenge. Among the different solutions, fuel cells have stood out in the last years

as one of the most promising alternatives for sustainable energy production and one that is compatible with preservation of the environment [1-3]. They are electro-chemical devices that convert chemical energy present in fuels into electricity and heat. Moreover, fuel cells are the only technology of energy-production potentially fed by renewable fuels which can be used for stationary and mobile applications [4].

The operating principle of a fuel cell is similar to that of a battery in the sense that both generate electrical energy through electrochemical processes, however, in a fuel cell the chemical energy is provided by an oxidant and a fuel supplied from external sources. Therefore fuel cell electricity generation cannot run out while fuel is continuously supplied, in contrast to the characteristic charge - discharge cycles of the batteries [4].

A single fuel cell presents a sandwich type geometry and consists of three main components: cathode, electrolyte and anode. An oxidant and a fuel are fed to the cathode and anode, respectively, where the oxidant is reduced and the fuel oxidized (**Figure 1.1**). These half-reactions generate a chemical potential gradient of ions from one side of the electrolyte to the other and therefore, direct-current electricity is produced in the external circuit.

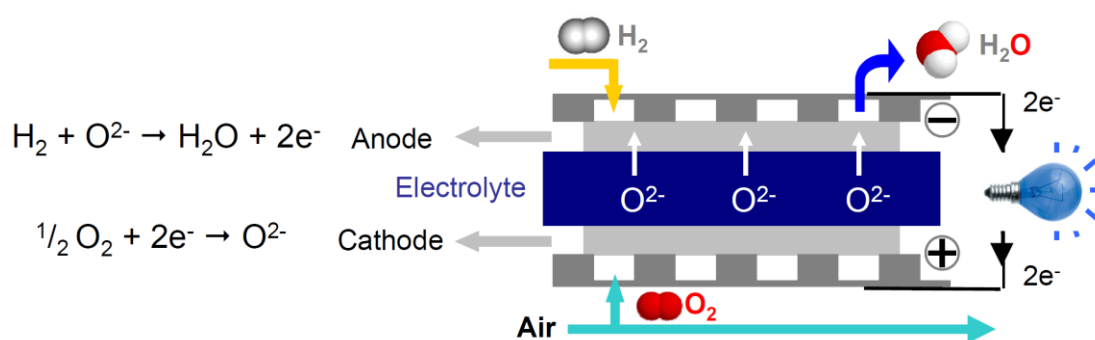


Figure 1.1. A schematic representation of a working fuel cell.

1.1.1 Solid Oxide Fuel Cells (SOFCs)

Among all types of fuel cells, those based on solid oxides have been considered as a leading technology for future power generation. SOFCs have received special interest because of their low levels of pollutant emissions, fuel flexibility and high efficiency [3-5]. Solid Oxide Fuel Cells require oxidant reactants such as air or oxygen, and fuel such as hydrogen to electrochemically react and generate electricity. Schematics representations of SOFCs based on oxide-ion conducting and proton conducting electrolytes are shown in **Figure 1.2**. In a conventional SOFC utilizing oxide-ion conducting electrolyte, the oxygen is partially reduced at the cathode giving rise to O^{2-} anions which migrate across the electrolyte to the anode side, where they react with H_2 to form water and

generate an electrical voltage. In Proton Conducting Fuel Cells (PCFCs), hydrogen is oxidized at the anode giving rise to H^+ ions that are transported to the cathode side across the proton conducting electrolyte. H^+ ions then react with O_2 to form water. The main advantage of PCFCs compared to the classical SOFCs lies in the fact that H_2O is produced at the cathode instead of at the anode. This allows the hydrogen to be completely utilized without compromising the system overall efficiency [4].

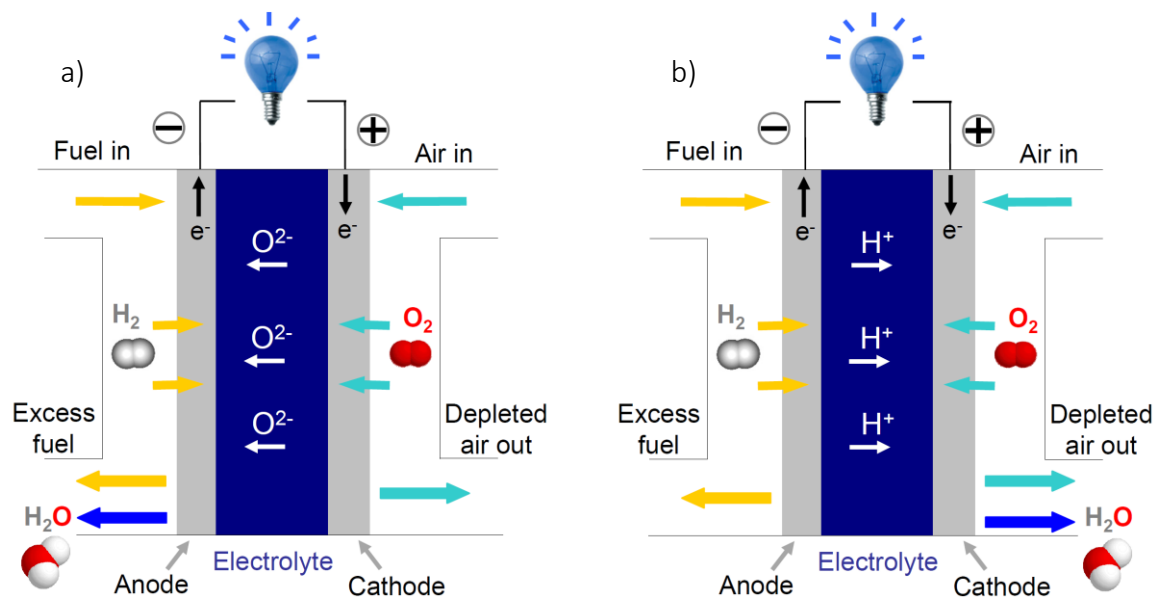


Figure 1.2. Schematic representations of the reactions taking place in a SOFC during operation for (a) oxide-ion conducting electrolyte, and (b) proton conducting electrolyte.

In contrast to other fuel-cell types, SOFCs are composed of solid-state ceramics and require operating temperatures ranging between 500 and 1000 °C. The best established SOFC systems are those based on an Ytria-Stabilized Zirconia (YSZ) electrolyte, which requires operating temperatures between 800 - 1000 °C [5-7] to achieve sufficient ionic conductivity in order to assure the efficient transport of O^{2-} . These high operating temperatures are directly linked to the main limitations of SOFCs, which lie mainly in their unsatisfactory durability and reduced lifetime. These problems are caused by the difficulty of maintaining the sealing of the cells, by the too short-term stability of the materials and by the mechanical incompatibility between electrodes and electrolyte due to the thermal cycling to which the SOFCs components are subjected during operation [8]. To overcome such disadvantages, lowering the working temperature to 500 - 700 °C becomes an important challenge in improving SOFC technology. For this purpose, there has been huge interest in the development of new electrolyte materials which exhibit high ion conductivities at intermediate temperatures combined with low electronic conductivity, high density and good chemical stability [3].

1.1.2 Electrolyte materials for SOFCs

In the attempt to search for an alternative to replace YSZ electrolytes, different candidates have emerged. On the one hand, materials science research has been mainly focused on developing new oxygen ion conducting electrolytes for intermediate-temperature solid oxide fuel cells (IT-SOFC) [9-11]. In particular, several families of oxide-ion conductors have attracted considerable interest and are being widely investigated; some of them are: fluorite oxides such as Ceria-Gadolinia [12], perovskite oxides such as Strontium and Magnesium doped Lanthanum Gallate [13, 14], LAMOX oxides [15, 16] and apatites such as Lanthanum Silicate [17-20]. On the other hand, proton-conducting perovskite materials have recently received increasing attention for SOFC electrolyte applications because of the higher mobility of protons with respect to the oxygen ions, which allows for safe reduction of the operating temperature of SOFCs (450 - 700 °C) without degrading performance [3, 21-24]. The most interesting proton conducting materials for electrolytes are doped Barium Cerate [25-31] and doped Barium Zirconate [21, 22, 24, 32-37].

Figure 1.3 shows a plot of the conductivity of Yttria-Stabilized Zirconia together with the new families of oxide-ion and proton conductors electrolytes discussed above. It can be observed that all the ceramics exhibit higher conductivities than YSZ at temperatures ranging from 500 to 700 °C, what explains the growing interest that these materials have received since they could be successfully used to reduce the SOFC operating temperatures.

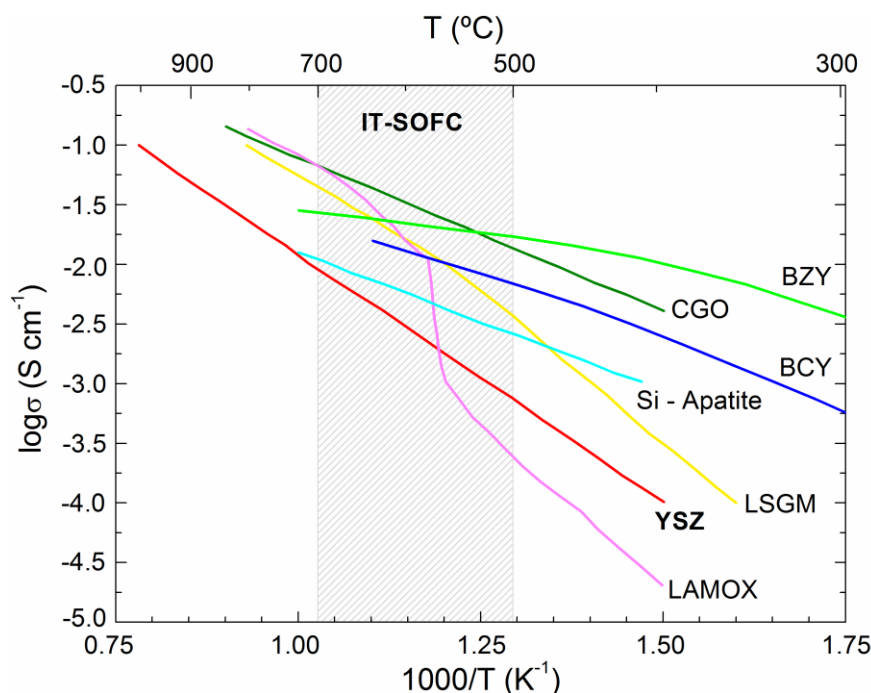


Figure 1.3. Comparison of $(\text{ZrO}_2)_{0.92}(\text{Y}_2\text{O}_3)_{0.08}$ (YSZ) total conductivity with others oxide ion and proton conductors electrolytes as a function of temperature [3]: $\text{La}_2\text{Mo}_2\text{O}_9$ (LAMOX), $\text{Ce}_{0.8}\text{Gd}_{0.2}\text{O}_{1.9}$ (CGO), $\text{La}_{0.9}\text{Sr}_{0.1}\text{Ga}_{0.8}\text{Mg}_{0.2}\text{O}_{2.85}$ (LSGM), $\text{La}_{10}(\text{SiO}_4)_6\text{O}_3$ (Si-Apatite), $\text{BaCe}_{0.9}\text{Y}_{0.1}\text{O}_3$ (BCY), and $\text{BaZr}_{0.8}\text{Y}_{0.2}\text{O}_3$ (BZY).

This thesis was focused on the mechanical characterization of two of these materials: Lanthanum Silicate and Yttrium-doped Barium Zirconate, since their ion conductivities at intermediate temperatures together with the lack of electronic conductivity and chemical stability, required for electrolyte application in SOFC, contributed to the consideration of these compounds as two of the most promising materials to be used as SOFC electrolytes. Their characteristics, crystal structure and ion-conductivity are briefly described below.

1.1.2.1 Lanthanum Silicate

Rare-earth-based oxy-apatites $\text{La}_{9.33+x}\text{Si}_6\text{O}_{26+3x/2}$ have been considered as a potential alternative to Yttria-Stabilized Zirconia (YSZ) to be used as electrolyte material for intermediate and low temperature Solid Oxide Fuel Cells due to their high oxide-ion conductivity, chemical stability, thermal properties and low conductivity activation energy [18, 38-40].

The oxy-apatite structure usually shows hexagonal symmetry and can be described in the $P6_3/m$ space group. It involves two non-equivalent positions for La ions, one for Si, and four positions for O ions (**Figure 1.4**) [41], where O1 - O3 ions form SiO_4 tetrahedra with La2 located in two cavity sites, one 7-coordinated and another 9-coordinated, and O4 ion arranged along the c axis, forming the O4 column along which oxide ions can migrate. These channels are presumed to be responsible for the high oxide ion conduction of this material [42-44].

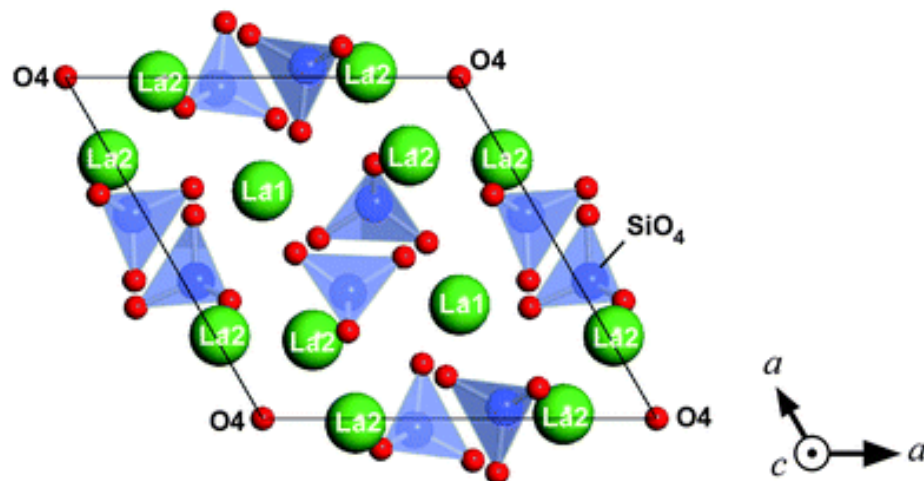


Figure 1.4. Crystal structure of $\text{La}_{9.33}\text{Si}_6\text{O}_{26}$ oxy-apatite [41].

Lanthanum Silicates with this apatite-type structure are of great interest, exhibiting conductivities even higher than those of the well-known oxide ionic conductor YSZ at intermediate temperatures [17, 20, 42, 45, 46]. For example, Nakayama et al. [18] have reported that the

conductivity of Lanthanum Silicates is $4.3 \times 10^{-3} \text{ Scm}^{-1}$ at 500 °C, whereas for YSZ it is $1.1 \times 10^{-3} \text{ Scm}^{-1}$ at 500 °C [5].

1.1.2.2 Yttrium-doped Barium Zirconate

Yttrium-doped Barium Zirconate is another attractive material to be used as electrolyte material for intermediate temperature SOFCs because it combines a high proton conductivity with high chemical stability in CO₂ containing atmospheres [21, 26, 47, 48].

Y-substituted Barium Zirconate structure shows a cubic perovskite symmetry, similar to BaZrO₃ (**Figure 1.5**), which can be described in the $Pm\bar{3}m$ space group. Yttrium is considered as one of the most suitable dopants for Barium Zirconate to achieve the highest proton conductivity [21, 22, 37] (for doping content up to 20% of Y), presumably as a result of the good matching between Zr⁴⁺ and Y³⁺ ionic radii (0.72 Å and 0.90 Å [49], respectively). The fast proton mobility and the entropic stabilization of protonic defects through water incorporation lead to the high proton conductivity of this material [21, 22, 50].

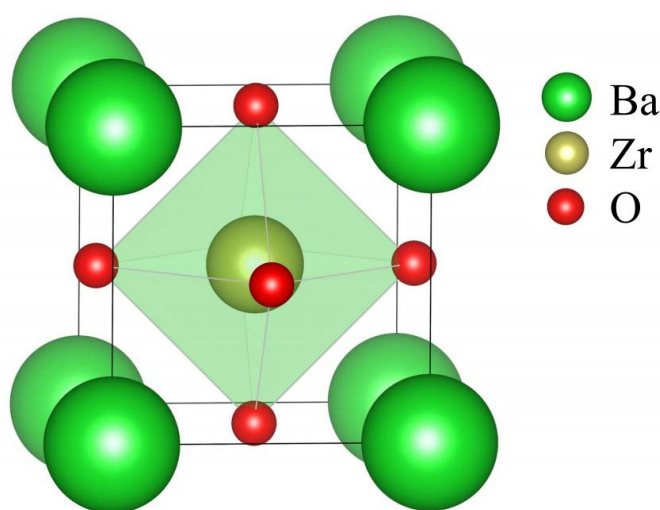


Figure 1.5. Crystal structure of Barium Zirconate [51].

Electrical measurements of BZY demonstrated very high bulk proton conductivity, in particular, Pergolesi *et al.* [35] have found that the conductivity of grain boundary-free Yttrium-doped Barium Zirconate thin films is 0.11 S cm^{-1} at 500 °C. However, the proton conductivities reported in the literature by other authors vary by more than one order of magnitude [52-54]. This poor reproducibility of the conductivity properties is due to the difficulty of fabricating dense compounds [21]. Moreover proton conductivity seems to be strongly affected by grain size, Ba evaporation and secondary phases.

1.2 IMPORTANCE OF MECHANICAL PROPERTIES IN SOFCs

Aside from the characterization of the chemical and electro-chemical behaviour of ceramic SOFC materials, which has been addressed in numerous studies since this property gives the functionality to these materials, it also is essential to characterize their mechanical behaviour because SOFCs are subjected to long-term operation and thermal cycles that may cause mechanical degradation. Therefore, different mechanical phenomena, such as micro-cracks, creep, electrode-electrolyte delamination, microstructural evolution, etc., can compete with other chemical or electro-chemical effects that limit the overall performance of the device and potentially lead to its ultimate failure.

In order to understand the origin of these mechanical phenomena it is necessary to know the arrangement of the different materials in a functional SOFC system. As mentioned above, a single cell is composed of an electrolyte in intimate contact with an anode and a cathode. Moreover, stacking of several single cells is required to generate an applicable amount of electricity for real applications. In this configuration, an interconnect plate is always installed between neighbouring fuel cells to provide the electronic contact [55], while a sealant is required to obtain gas tightness [56]. In order to maximize the electrode-interconnect contact, these stacks are subjected to a minimum compression pressure of 64 - 74 kPa [57]. A schematic representation of SOFC stack is shown in **Figure 1.6**.

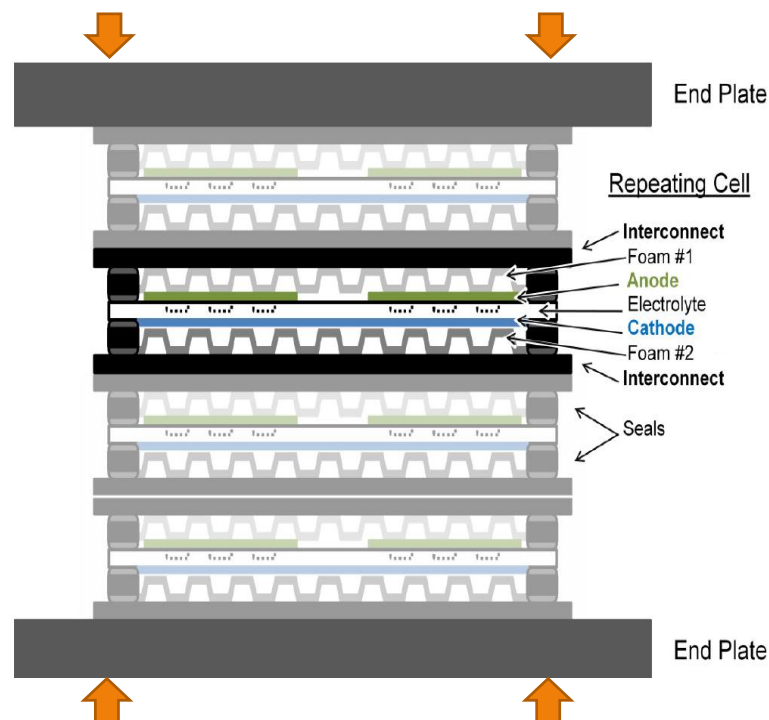


Figure 1.6. A schematic representation of planar SOFC stack [58] under compression.

The problems associated with durability and reliability are the major hurdle to overcome for improving SOFC technology. Due to this, there is a growing research effort which aims at understanding the different degradation mechanisms affecting SOFCs [59]. The manufacturing process of these devices (material sintering, components assembly and stacking, sealing procedure and reduction of the anode [60]) together with repeated thermal cycles and prolonged exposure to aggressive environments during their operation are responsible for physical-chemical alterations at the interfaces, creep deformations, thermo-elastic mismatch between the different materials and uneven temperature distribution.

1. Physical-chemical alterations: The high temperature and the aggressive environment characteristic of SOFC operation entails detrimental alterations at the interfaces between the different ceramics [60-62], such as grain growth [63, 64], modifications of the composition [65, 66] and development of new phases [67, 68], which can alter the mechanical response of SOFC materials and cause their weakening [69, 70].
2. Creep deformations: The elevated temperature operation together with the mechanical compression load to which SOFCs are subjected due to the stacking and sealing procedure by means of compressive gaskets or glass sealant induce active and permanent deformations at the stack components [71].
3. Thermo-elastic mismatch: The incompatibility between the thermo-elastic properties of the different layers is responsible for much of the degrading forces originated in the system [57, 72, 73].
4. Uneven temperature distribution: During operation, gradients of temperature between gas-inlet and -outlet of about 100 °C occur in the SOFC system [74]. These gradients may result in an uneven distribution of the thermo-mechanical strains [75], the electro-chemical potentials and current density in the cell [74-76].

All these undesirable phenomena induce stresses in the system, which could reach critical values and cause the mechanical failure of a single cell because of an improper choice of its components, since mismatched stresses between the different layers can result in problems of delamination or micro-cracking in the layers or interfaces during fabrication and operation [55, 72, 77-79].

Delamination consists of the separation of one of the electrodes from the electrolyte and has dramatic consequences on cell performance, since it impedes the transport of ions between

the electrode-electrolyte in the delaminated area inducing a harmful current density redistribution [80, 81]. Another important problem is cracking, micro-cracks in the electrode layers also break the electronic/ionic conduction pathways with the corresponding local performance loss [71], while cracking of electrolyte does not only impede the transport of ions between the electrodes but also allows leakage of the fuel to take place from the anode side to the cathode side that lead to the end of life of the cell [77].

These problems could cause the mechanical failure of a single cell and have dramatic consequences on the whole stack, since the mechanical degradation of a single repeating unit lead to a series of detrimental effects that end the life of the stack [71]. Thus, knowledge of the mechanical properties of all the cell components is required (i) for a comprehensive residual stress analysis of the multi-layered system, (ii) for an effective mitigation of the foregoing issues, (iii) to ensure the mechanical integrity of the stack and (iv) to success in the development of SOFCs. In particular, the elastic properties, the coefficient of thermal expansion and the creep behaviour of the different components are necessary to characterize the state of stresses in a SOFC during operation. These properties are discussed in depth in the following sections.

Moreover, for the purpose of analysing the risk of failure of SOFC compounds it is also necessary the knowledge of their strength and fracture toughness. Strength strongly depends on the manufacturing defects and acts as a concentrator of stresses, while fracture toughness is used to determine the amount of stress which is critical to give rise to opening and propagation of cracks.

1.2.1 Thermo-elastic properties

Owing to the fact that a single cell is composed of individual brittle layers, which differ widely in their mechanical properties, and presents a sandwich type geometry, the mismatch in the elastic properties and coefficient of thermal expansion of the successive layers during fabrication and operation may act as a detrimental source of stress and cause the fast mechanical failure of the cell [72, 73]. Therefore, knowledge of the thermo-elastic properties of the different components and their evolution with temperature are needed to estimate the stress fields in the SOFC stack.

During manufacturing process, the multi-layered system cools down from the sintering temperature to room temperature, that inducing residual stresses which arise from the disparity in the thermal expansion coefficient of the adjacent layers and depends on their elastic properties [71, 82]. Moreover, the reduction reaction that takes place in the anode during the first cycle of

operation introduces mismatch stresses in the other cell components [78, 83] which could impair the SOFC structural integrity and reliability.

During stack operation, the high-temperature, thermal cycles and temperature gradients characteristic of SOFC devices give rise to internal stresses and their redistribution due to a disparity in the thermo-elastic response of the different components [75, 78, 84].

Due to this, SOFC components must have similar thermal expansion coefficients and elastic properties in order to avoid the development of these stresses between the different layers that could affect adversely to the mechanical integrity of a single cell during fabrication and operation [55, 77]. In this context, the compatibility of the thermo-elastic behaviour of SOFC components becomes one of the most important design criteria in order to ensure durability and reliability of SOFC technology [72].

1.2.2 Creep behaviour

In order to complete the stress characterization in SOFC materials, it is essential to include their creep behaviour. The active, local and permanent deformation generated by creep can act as source of stress relaxation under constant operating conditions, as well as induce additional stresses and changes in the stress distribution. These modifications of the state of stress in the SOFC components can cause local loss of contact pressure with the ensuing cell failure [76].

Creep can be described as the set of microscopic mechanisms responsible for continuing plastic deformation under a constant stress [85]. Therefore, the interest in studying the creep deformation of SOFC materials lies not only in their technological applications, but also in the understanding of the atomistic mechanisms responsible for this phenomenon. In addition, it is sometimes possible to extract very valuable information on the transport processes of the slowest moving ionic species in the compound, which is currently unknown: diffusion coefficients, activation energy for creep, etc. Such information is essential for other mass transport-related processes, such as sintering and grain growth.

The most relevant theoretical models used to explain plastic deformation are briefly described below. They were employed to discuss the atomistic mechanisms that govern the high-temperature deformation of the studied compounds. The intra-granular mechanisms, by creation and movement of dislocations, are not included, because they are not relevant in fine-grained polycrystalline ceramic materials.

1.2.2.1 Diffusional creep

In this case, the plastic deformation is controlled by mass transport through atomic diffusion processes between grain boundaries, without participation of dislocations. There are two possible diffusion paths in ceramics: through the bulk (Nabarro-Herring creep) and along the grain boundaries (Coble creep).

At very high temperatures ($T \approx 0.9 T_f$, where T_f is the melting point) and low stress, creep occurs by mass transport through bulk diffusion as shown in **Figure 1.7a**. Considering a single crystal under an uniaxial tensile stress, Nabarro [86] suggested that vacancies would move from tensile to compressive regions. This flow of vacancies is equivalent to a counter-flow of atoms in the opposite direction resulting in a macroscopic deformation of the crystal.

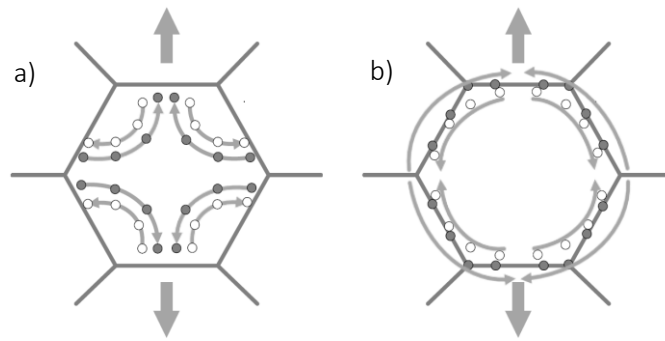


Figure 1.7. Schematic representation of vacancies (open dots) and atoms flow (solid dots) in a single crystal under a uniaxial stress for: (a) Nabarro-Herring creep by lattice diffusion, and (b) Coble creep by grain boundary diffusion [87].

C. Herring [88] refined the suggestion of Nabarro taking into account the grain geometry and the grain boundary compatibility. For the Nabarro-Herring model, the steady-state strain rate is given by:

$$\dot{\epsilon} = \frac{B\Omega\sigma}{k_B T d^2} \cdot D^{\text{lat}} \quad (1.1)$$

where B is a constant which depends on the grain geometry and stress distribution, Ω is the atomic volume, σ is the applied stress, D^{lat} is the self-diffusion coefficient for mass transport through the crystal lattice, k_B is the Boltzmann constant, T is the absolute temperature and d is the grain size.

At lower temperature and for fine grained ceramics, the dominant diffusion paths for mass transport may be along the grain boundaries as shown in **Figure 1.7b**. In this case, the process is termed Coble creep [89], and the creep rate is:

$$\dot{\epsilon} = \frac{150}{\pi} \cdot \frac{\Omega\sigma}{k_b T d^3} \cdot \delta D^{gb} \quad (1.2)$$

where D^{gb} is the self-diffusion coefficient for mass transport along the grain boundaries and δ is the grain boundary thickness.

The activation energy for grain boundary diffusion is generally lower than for the lattice ($Q^{gb} \approx 0.6 - 0.7Q^{lat}$), thus Coble creep is favoured over the Nabarro- Herring creep at lower temperatures. Moreover, it is noted from Equation 1.2 that creep rate varies inversely with d^3 , so that Coble creep is also favoured over Nabarro- Herring creep at very fine grain size.

Diffusional creep occurs both through the bulk of the grains and along the grain boundaries, since Nabarro-Herring and Coble creep are independent processes and can take place in parallel. Combining Equations 1.1 and 1.2, the total diffusional creep rate is given by:

$$\dot{\epsilon} = \frac{B\Omega\sigma}{k_b T d^2} \cdot \left(D^{lat} + \frac{\pi\delta}{d} D^{gb} \right) \quad (1.3)$$

The models of Nabarro-Herring and Coble consider the creep deformation of a single grain. When applied to a polycrystalline material, the macroscopic deformation comes from the shape change of the grains generated by mass transport. In order prevent the formation of voids between the grains, a relative movement of the neighbouring grains is necessary. Otherwise, cracks along the boundaries aligned with the tension axis would be opened and the polycrystal would fracture. This movement is carried out by a local grain boundary sliding (GBS) of the neighbouring grains, called Lifshitz sliding [90]. This process is illustrated in **Figure 1.8**.

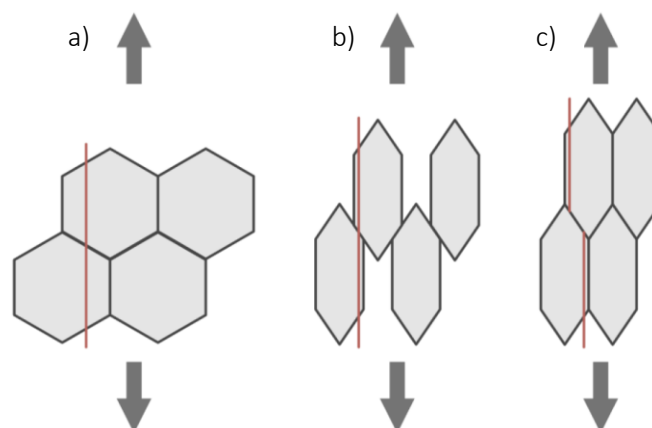


Figure 1.8. Relative movement of the grains by diffusion processes to maintain the cohesion of the crystal [87]. (a) Un-deformed grains with marker line. (b) Diffusion creep without GBS resulting in the formation of voids. (c) Diffusion creep with GBS preventing the formation of voids.

1.2.2.2 Grain boundary sliding

In the aforementioned conditions of diffusional creep, a polycrystal of equiaxed grains would exhibit a morphological evolution of the grains equivalent to the macroscopic deformation of the material. However, this grain elongation has not been generally observed in ceramics, which preserve an equiaxed shape even after undergoing large strains [91-94]. There is a deformation mechanism by grain boundary sliding that takes into account this fact: the Ratchinger sliding [95]. This mechanism is based on a grain rearrangement process in which the grains change their relative position to one another, thus obtaining large and permanent macroscopic deformations of the aggregate without requiring any substantial grain elongation.

Grain boundary sliding generates stresses at grain boundary triple-points and irregularities. The stress relaxation or accommodation process is generally believed to control the strain rate of GBS [96, 97]. The most relevant mechanisms of accommodation are either diffusional flow or dislocation climb in the vicinity of grain boundaries or through the grain.

1.2.2.2.1 Diffusion-accommodated process: Ashby-Verrall model

Ashby and Verrall [98] proposed a grain-switching mechanism which requires a combination of grain boundary sliding and diffusional creep. This model is similar to Nabarro-Herring and Coble creep from a mechanical point of view but differs in a topological sense. In particular, Ashby and Verrall model accounts for: the absence of changes in the form factor of the grains which retain their equiaxed shape even after very large strains; the absence of significant creep transients before the establishment of the steady-state regime; and a proper prediction of the magnitude of the strain rates (or flow stresses). Assuming that the mass transport takes place simultaneously through the bulk and along the grain boundaries, the steady-state strain rate in the Ashby-Verrall model is given by [98]:

$$\dot{\epsilon} = \frac{98\Omega}{k_B T d^2} \cdot \left(\sigma - \frac{0.72\Gamma}{d} \right) \cdot \left(D^{\text{lat}} + \frac{\pi\delta}{d} D^{\text{gb}} \right) \quad (1.4)$$

where Γ is the grain boundary free energy. This equation is similar to the classical diffusional creep (Equation 1.3) with the exception of the term involving $0.72\Gamma/d$, which corresponds to a threshold stress that comes from the fluctuations of boundary area when the grains pass through the necking position (**Figure 1.9b**). This term can be usually neglected because it is very small (< 1 MPa) compared to the applied stress σ .

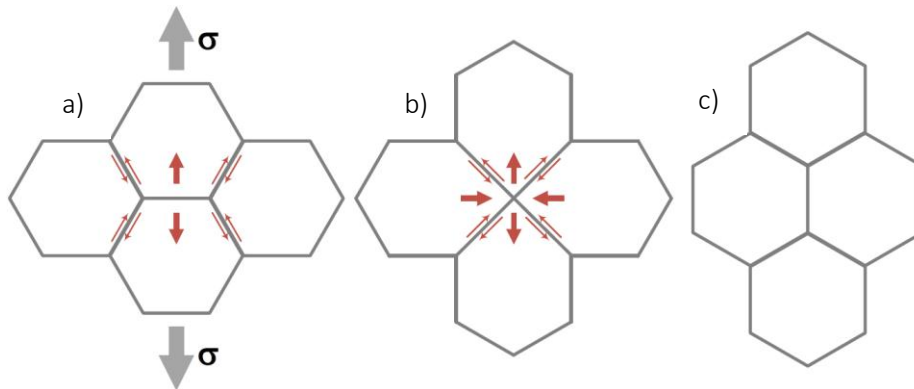


Figure 1.9. Grain deformation according to Ashby and Verrall model [98]. (a) Initial state, (b) intermediate state: necking, and (c) final state.

Equation 1.4 predicts a steady-state strain rate about an order of magnitude faster than Equation 1.3, since less matter diffusion is needed for a given strain than in the Nabarro-Herring and Coble models, and the diffusive paths length are shorter [98]. This model explains successfully the mechanical and microstructural features observed in different ceramic materials with grain sizes between 1 and 10 μm , such as UO_2 [99], NiO [100], YSZ [101], YBCO [102], and YAG [103]. Yet despite the success of the Ashby-Verrall model, it has been criticized because of its 2D nature, which leads to unrealistic diffusion paths. Spingarn and Nix [104] modified the topology of the grain-switching process to produce a more realistic transient configuration during the change of the grain shape, but leading to the same final grain configuration.

1.2.2.2 Dislocation-accommodated process

Another mechanism that can account for the accommodation of grain boundary sliding is the movement and multiplication of dislocations. Numerous models have been proposed for this accommodation mechanism [97, 105-109], although none of them is able to completely explain the deformation process in polycrystalline materials. In general, all these models lead to a steady-state strain rate equation as follows:

$$\dot{\epsilon} = A \frac{Gb}{k_b T} \cdot \left(\frac{b}{d}\right)^p \cdot \left(\frac{\sigma}{G}\right)^n \cdot D \quad (1.5)$$

where A is a constant, G is the shear modulus, b is the Burgers vector, D a diffusion coefficient and p and n the exponents of grain size and stress, respectively. Some models introduce a threshold stress σ_0 necessary to initiate the sliding, modifying the Equation 1.5 with the effective stress $\sigma - \sigma_0$. Dislocation-accommodated grain boundary sliding mechanisms can be based on stacking of dislocations or movement of individual dislocations.

1.2.2.3 Interface-reaction creep

The aforementioned models are based on the assumption that grain boundaries act as perfect sources and sinks for vacancies. If this assumption is not satisfied, the creep rate will be controlled by interface reaction [110], i.e. by the processes of absorption/emission of vacancies by grains boundaries. Burton [111] for the case of diffusional creep, and Ashby and Verrall [98] and Burton [112] for the case of GBS, developed models to account for this process.

1.2.2.3.1 Diffusion creep controlled by interface-reaction

The operation of sources and sinks for vacancies at grain boundaries is required by diffusional creep as shown in **Figure 1.7**. Considering that dislocations having a component of their Burger's vector perpendicular to the grain boundary can act as sinks and sources by climbing along the boundary, Burton [111] model led the process of diffusion creep controlled by interface-reaction in the case of bulk diffusion, defining the creep rate as:

$$\dot{\epsilon} = \frac{P_j (Z - 1) b \sigma^2 \Omega D^{\text{lat}}}{8\pi E d k_B T} \quad (1.6)$$

where P_j is the probability of finding a jog on a dislocation, Z the coordination number and E the energy per unit length of a dislocation line.

1.2.2.3.2 GBS creep controlled by interface-reaction

Burton [112] introduced the characteristic-area concept as the product of the grain diameter and the spacing between linear defects at the interfaces. Taking into account the same considerations than in the case of diffusional creep, the strain rate equations for the grain boundary sliding accommodated by interface-reaction are given by:

$$\dot{\epsilon} = A \frac{Gb}{k_B T} \cdot \left(\frac{b}{d}\right) \cdot \left(\frac{\sigma}{G}\right)^2 \cdot D^{\text{lat}} \quad (1.7)$$

$$\dot{\epsilon} = A \frac{Gb}{k_B T} \cdot \left(\frac{b}{d}\right)^2 \cdot \left(\frac{\sigma}{G}\right)^2 \cdot D^{\text{gb}} \quad (1.8)$$

In both equations $A \sim P_j/\beta$, where P_j has a meaning analogous to the previous case and β is a constant ≤ 1 .

In a similar way to Burton's development, and assuming that there is a viscous force opposing the movement of dislocations along the grain boundaries, Ashby and Verral propose the following equation:

$$\dot{\epsilon} = \frac{\beta b M}{0.84 \Omega G} \cdot \frac{\sigma^2}{d} \quad (1.9)$$

where M is the mobility of the boundary dislocation and β a constant of the order of unity. Consideration of the IRC process leads to an increase of one unit in the stress exponent n and a decrease also in one unit of the exponent of grain size p with respect to the original expressions

1.2.2.4 Phenomenological relationships for superplasticity

Many different models have been developed to explain superplasticity based in different relaxation processes of the stresses generated by the sliding of the grains on each other: dislocation motion inside the volume of the grains or along the grain boundaries, diffusional flow, interface-reaction-controlled diffusion (i.e. boundaries are not perfect sources and sinks for point defects), grain boundary migration or cavitation. None of them, however, is able to explain successfully the body of experimental data in superplastic materials. Sherby *et al.* [113] carried out a phenomenological study of fine-grained superplastic metals taking into account the following considerations: (i) most fine-grained metal materials under superplastic conditions exhibit an stress exponent $n=2$ ($\dot{\epsilon} \propto \sigma^2$); (ii) the temperature-dependence of strain rate corresponds to the atoms diffusion by either along the grain boundaries ($\dot{\epsilon} \propto D^{gb}$) or through the volume of the grains ($\dot{\epsilon} \propto D^{lat}$); (iii) for grain boundary diffusion, the strain rate is $\dot{\epsilon} \propto d^{-3}$ while for lattice diffusion is $\dot{\epsilon} \propto d^{-2}$. With these considerations, the authors proposed the following phenomenological relationships:

$$\dot{\epsilon} = 8 \times 10^6 \frac{Gb}{k_B T} \cdot \left(\frac{b}{d}\right)^2 \cdot \left(\frac{\sigma}{G}\right)^2 D^{lat} \quad (1.10)$$

$$\dot{\epsilon} = 2 \times 10^5 \frac{Gb}{k_B T} \cdot \left(\frac{b}{d}\right)^3 \cdot \left(\frac{\sigma}{G}\right)^2 D^{gb} \quad (1.11)$$

The strain rate values predicted by these expressions reproduce the experimental results of all the studied materials within an order of magnitude. Equation 1.10 has been shown to account for the superplastic deformation of fine-grained Yttria-Stabilized tetragonal Zirconia with a grain size smaller than $1 \mu\text{m}$ [91] and Equation 1.11 for fine-grained $\text{YBa}_2\text{Cu}_3\text{O}_{7-x}$ superconductor [114].

1.2.3 Previous results in SOFC electrolytes

Although the knowledge of the mechanical properties of SOFC components have received a growing interest in recent years, the available data still remain scarce. In the present section a brief literature review is performed in which previous results concerning the mechanical characterization of electrolyte materials are presented.

1.2.3.1 Yttria-Stabilised Zirconia

8 mol% Yttria-Stabilised Zirconia (8YSZ) is the SOFC electrolyte material more used and studied due to its excellent electrical and thermal properties. The evolution of the coefficient of thermal expansion of 8YSZ has been evaluated in different works by dilatometry from room temperature to 1273 K [115-118]. The results obtained were very closed and in the range of $10.0 - 11.0 \times 10^{-6} \text{ K}^{-1}$. On the other hand, various studies have been devoted to investigate the elastic properties of 8YSZ using different techniques at room temperature and all of them reported comparable values between 190 and 223 GPa [119-123]. For example, Selçuk *et al.* [124] determined the elastic constant of 8YSZ by the impulse excitation technique (IET) and found values of Young's modulus (E) and Poisson ratio (ν) in the ranges of 219 - 223 GPa and 0.319 - 0.321, respectively. Similarly, Radovic *et al.* [125] reported values of 216 GPa and 0.315 measured by Resonant Ultrasound Spectroscopy for the same composition at room temperature. The temperature dependence of Young's modulus for 8YSZ has been also addressed in several studies, and all of them showed similar results [121, 123, 126]. Selçuk *et al.* [126] found an average value of E of 216 ± 5 GPa at 298 K and 155 ± 8 GPa at 1173 K. They also determined the fracture toughness by double-torsion loading at the same temperatures obtaining values of $1.61 \pm 0.12 \text{ MPa}\cdot\text{m}^{1/2}$ at room temperature and $1.02 \pm 0.05 \text{ MPa}\cdot\text{m}^{1/2}$ at 1173 K.

Concerning the creep behaviour, data on bending tests in the temperature range of 1223 - 1563 K for 8YSZ with a grain size between 2.4 - 6.9 μm led to a stress exponent close to the unity and an energy activation $\simeq 400$ kJ/mol, indicating that grain boundary sliding accommodated by diffusion is the main deformation mechanism [122, 127].

1.2.3.2 Lanthanum Silicate

To our knowledge, very few studies have reported mechanical properties of apatites compounds. Santos *et al.* [128] obtained $\text{La}_{9.33}\text{Si}_2\text{Ge}_4\text{O}_{26}$ compounds through different sintering temperatures and evaluated their mechanical properties by means of nano and microindentation

tests. They reported values of Young's Modulus, nanohardness and microhardness in the ranges of 106 - 135 GPa, 7.3 - 9.6 GPa and 2.9 - 5.8 GPa, respectively. These results showed a strong dependence of the mechanical properties on the microstructure and the experimental condition used. On the opposite, the values of fracture toughness remained practically constant (3.5 to 3.9 MPa·m^{1/2}) with the sintering temperature. In the same line, Suarez *et al.* [129] measured the microhardness of different La_{9.33}Si₆O₂₆ ceramics obtaining values between 6.99 and 7.57 GPa. They concluded that higher densifications lead to higher values of microhardness while an increase in the grain size tend to decrease this property. Concerning the temperature dependence of the coefficient of thermal expansion in LSO compounds, Iwata *et al.* [130] reported a value of $9.4 \times 10^{-6} \text{ K}^{-1}$ for La_{9.33}Si₆O₂₆ measured by high-temperature X-ray diffraction (HT-XRD) in the range of temperature from 295 to 1073 K, and Jiang *et al.* [131] found values between 9.7×10^{-6} and $10.3 \times 10^{-6} \text{ K}^{-1}$ for La₁₀Si₆O₂₇ compounds by thermo-mechanical analysis at temperatures between 298 and 1173 K. Unlike the case of the elastic properties and hardness, the coefficient of thermal expansion was found to be independent of the processing method and material microstructure.

1.2.3.3 Yttrium-doped Barium Zirconate

The data available in the literature about mechanical properties of BZY is even scarcer than for Lanthanum Silicate compounds. To our knowledge, there is no information about the elastic properties and creep behaviour of these material. Only one previous work by Sazinas *et al.* [132] studied the hardness and fracture toughness of BaZr_{1-x}Y_xO_{3-x/2} (x = 0.1 and 0.2) by microindentation. They found values of microhardness and fracture toughness ranging from 675 to 1005 Hv and 1.49 to 2.43 MPa·m^{1/2}, respectively, for different hydration/dehydration conditions. On the other hand, Han *et al.* [133] measured the thermal expansion coefficient by HT-XRD on 2 to 30 at% yttrium-doped Barium Zirconate from room temperature to 1273 K. They found values from $8.47 \times 10^{-6} \text{ K}^{-1}$ to $10.2 \times 10^{-6} \text{ K}^{-1}$ increasing the doping level. Whereas, Lyagaeva *et al.* [134] reported a mean thermal expansion coefficient of BZY compounds of $8.2 \times 10^{-6} \text{ K}^{-1}$ in the temperature range of 323 - 1173 K.

1.3 REFERENCES

1. Boudghene Stambouli, A. and E. Traversa, *Fuel cells, an alternative to standard sources of energy*. Renewable and Sustainable Energy Reviews, 2002. 6(3): p. 295-304.
2. Traversa, E., *Toward the miniaturization of solid oxide fuel cells*. The Electrochemical Society Interface, 2009. 18(3): p. 49.

3. Malavasi, L., C.A.J. Fisher, and M.S. Islam, *Oxide-ion and proton conducting electrolyte materials for clean energy applications: structural and mechanistic features*. Chemical Society Reviews, 2010. 39(11): p. 4370-4387.
4. Fabbri, E., D. Pergolesi, and E. Traversa, *Materials challenges toward proton-conducting oxide fuel cells: a critical review*. Chemical Society Reviews, 2010. 39(11): p. 4355-4369.
5. Steele, B.C.H. and A. Heinzl, *Materials for fuel-cell technologies*. Nature, 2001. 414(6861): p. 345-352.
6. Singhal, S.C., *Solid oxide fuel cells for stationary, mobile, and military applications*. Solid State Ionics, 2002. 152: p. 405-410.
7. de Souza, S., S.J. Visco, and L.C. De Jonghe, *Reduced-temperature solid oxide fuel cell based on YSZ thin-film electrolyte*. Journal of the Electrochemical Society, 1997. 144(3): p. L35-L37.
8. Lefebvre-Joud, F., G. Gauthier, and J. Mougín, *Current status of proton-conducting solid oxide fuel cells development*. Journal of Applied Electrochemistry, 2009. 39(4): p. 535-543.
9. Brett, D.J.L., et al., *Intermediate temperature solid oxide fuel cells*. Chemical Society Reviews, 2008. 37(8): p. 1568-1578.
10. Hibino, T., et al., *A low-operating-temperature solid oxide fuel cell in hydrocarbon-air mixtures*. Science, 2000. 288(5473): p. 2031-2033.
11. Steele, B., *Appraisal of $Ce_{1-y}Gd_yO_{2-y/2}$ electrolytes for IT-SOFC operation at 500 C*. Solid state ionics, 2000. 129(1): p. 95-110.
12. Torrens, R.S., N.M. Sammes, and G.A. Tompsett, *Characterisation of $(CeO_2)_{0.8}(GdO_{1.5})_{0.2}$ synthesised using various techniques*. Solid State Ionics, 1998. 111(1): p. 9-15.
13. Ishihara, T., H. Matsuda, and Y. Takita, *Doped LaGaO₃ Perovskite Type Oxide as a New Oxide Ionic Conductor*. Journal of the American Chemical Society, 1994. 116(9): p. 3801-3803.
14. Ma, X.Q., et al., *Intermediate temperature solid oxide fuel cell based on fully integrated plasma-sprayed components*. Journal of Thermal Spray Technology, 2005. 14(1): p. 61-66.
15. Lacorre, P., et al., *Designing fast oxide-ion conductors based on La₂Mo₂O₉*. Nature, 2000. 404(6780): p. 856.
16. Goutenoire, F., et al., *Crystal Structure of La₂Mo₂O₉, a New Fast Oxide– Ion Conductor*. Chemistry of materials, 2000. 12(9): p. 2575-2580.
17. Nakayama, S., et al., *Ionic conductivity of lanthanoid silicates, Ln₁₀(SiO₄)₆O₃ (Ln = La, Nd, Sm, Gd, Dy, Y, Ho, Er and Yb)*. Journal of Materials Chemistry, 1995. 5(11): p. 1801-1805.
18. Nakayama, S. and M. Sakamoto, *Electrical properties of new type high oxide ionic conductor RE₁₀Si₆O₂₇ (RE = La, Pr, Nd, Sm, Gd, Dy)*. Journal of the European Ceramic Society, 1998. 18(10): p. 1413-1418.

19. Tao, S. and J.T.S. Irvine, *Preparation and characterisation of apatite-type lanthanum silicates by a sol-gel process*. Materials Research Bulletin, 2001. 36(7–8): p. 1245-1258.
20. Abram, E.J., D.C. Sinclair, and A.R. West, *A novel enhancement of ionic conductivity in the cation-deficient apatite $\text{La}_{9.33}(\text{SiO}_4)_6\text{O}_2$* . Journal of Materials Chemistry, 2001. 11(8): p. 1978-1979.
21. *Proton-Conducting Oxides*. Annual Review of Materials Research, 2003. 33(1): p. 333-359.
22. Kreuer, K.D., *Aspects of the formation and mobility of protonic charge carriers and the stability of perovskite-type oxides*. Solid State Ionics, 1999. 125(1–4): p. 285-302.
23. Duan, C., et al., *Readily processed protonic ceramic fuel cells with high performance at low temperatures*. Science, 2015.
24. Zhu, B., X. Liu, and T. Schober, *Novel hybrid conductors based on doped ceria and BCY20 for ITSOFC applications*. Electrochemistry Communications, 2004. 6(4): p. 378-383.
25. Shima, D. and S.M. Haile, *The influence of cation non-stoichiometry on the properties of undoped and gadolinia-doped barium cerate*. Solid State Ionics, 1997. 97(1–4): p. 443-455.
26. Katahira, K., et al., *Protonic conduction in Zr-substituted BaCeO_3* . Solid State Ionics, 2000. 138(1–2): p. 91-98.
27. Medvedev, D.A., et al., *Advanced materials for SOFC application: Strategies for the development of highly conductive and stable solid oxide proton electrolytes*. Progress in Materials Science, 2016. 75: p. 38-79.
28. Medvedev, D., et al., *Sulfur and carbon tolerance of BaCeO_3 – BaZrO_3 proton-conducting materials*. Journal of Power Sources, 2015. 273: p. 716-723.
29. Shishkin, M. and T. Ziegler, *Structural, electronic, stability and reduction properties of perovskite surfaces: The case of rhombohedral BaCeO_3* . Surface Science, 2012. 606(13): p. 1078-1087.
30. Dauter, J., et al., *Studies on Chemical Stability and Electrical Properties of Proton Conducting Perovskite-Like Doped BaCeO_3* . Journal of The Electrochemical Society, 2010. 157(10): p. B1413-B1418.
31. LÜ, J., et al., *Chemical stability of doped BaCeO_3 – BaZrO_3 solid solutions in different atmospheres*. Journal of Rare Earths, 2008. 26(4): p. 505-510.
32. Babilo, P., T. Uda, and S.M. Haile, *Processing of yttrium-doped barium zirconate for high proton conductivity*. Journal of Materials Research, 2007. 22(5): p. 1322-1330.
33. Yamazaki, Y., R. Hernandez-Sanchez, and S.M. Haile, *High Total Proton Conductivity in Large-Grained Yttrium-Doped Barium Zirconate*. Chemistry of Materials, 2009. 21(13): p. 2755-2762.
34. Tong, J., et al., *Solid-state reactive sintering mechanism for large-grained yttrium-doped barium zirconate proton conducting ceramics*. Journal of Materials Chemistry, 2010. 20(30): p. 6333-6341.

35. Pergolesi, D., et al., *High proton conduction in grain-boundary-free yttrium-doped barium zirconate films grown by pulsed laser deposition*. *Nat Mater*, 2010. 9(10): p. 846-852.
36. Iwahara, H., et al., *Protonic conduction in calcium, strontium and barium zirconates*. *Solid State Ionics*, 1993. 61(1): p. 65-69.
37. Schober, T. and H.G. Bohn, *Water vapor solubility and electrochemical characterization of the high temperature proton conductor BaZr_{0.9}Y_{0.1}O_{2.95}*. *Solid State Ionics*, 2000. 127(3-4): p. 351-360.
38. Okudera, H., et al., *Structure of oxide ion-conducting lanthanum oxyapatite, La_{9.33}(SiO₄)₆O₂*. *Solid State Ionics*, 2005. 176(15-16): p. 1473-1478.
39. Tian, C., et al., *Direct synthesis of La_{9.33}Si₆O₂₆ ultrafine powder via sol-gel self-combustion method*. *Journal of Alloys and Compounds*, 2008. 458(1-2): p. 378-382.
40. Nakao, T., et al., *Chemical stability of La₁₀Si₆O₂₇ and its application to electrolytes for solid oxide fuel cells*. *Solid State Ionics*, 2008. 179(27-32): p. 1567-1569.
41. Matsunaga, K. and K. Toyoura, *First-principles analysis of oxide-ion conduction mechanism in lanthanum silicate*. *Journal of Materials Chemistry*, 2012. 22(15): p. 7265-7273.
42. Leon-Reina, L., et al., *Interstitial oxygen conduction in lanthanum oxy-apatite electrolytes*. *Journal of Materials Chemistry*, 2004. 14(7): p. 1142-1149.
43. Masubuchi, Y., et al., *Oxide ion conduction mechanism in RE_{9.33}(SiO₄)₆O₂ and Sr₂RE₈(SiO₄)₆O₂ (RE = La, Nd) from neutron powder diffraction*. *Solid State Ionics*, 2006. 177(3-4): p. 263-268.
44. León-Reina, L., et al., *Crystalchemistry and Oxide Ion Conductivity in the Lanthanum Oxygermanate Apatite Series*. *Chemistry of Materials*, 2003. 15(10): p. 2099-2108.
45. Nakayama, S. and M. Sakamoto, *Ionic conductivities of apatite-type La_X(GeO₄)₆O_{1.5X-12} (X=8-9.33) polycrystals*. *Journal of Materials Science Letters*, 2001. 20(17): p. 1627-1629.
46. Susumu, N., A. Hiromichi, and S. Yoshihiko, *Ionic Conductivity of Ln₁₀(SiO₄)₆O₃ (Ln = La, Nd, Sm, Gd and Dy)*. *Chemistry Letters*, 1995. 24(6): p. 431-432.
47. Ryu, K.H. and S.M. Haile, *Chemical stability and proton conductivity of doped BaCeO₃-BaZrO₃ solid solutions*. *Solid State Ionics*, 1999. 125(1-4): p. 355-367.
48. Akbarzadeh, A.R., et al., *Combined theoretical and experimental study of the low-temperature properties of $\{\mathrm{BaZrO}\}_3$* . *Physical Review B*, 2005. 72(20): p. 205104.
49. Shannon, R., *Revised effective ionic radii and systematic studies of interatomic distances in halides and chalcogenides*. *Acta Crystallographica Section A*, 1976. 32(5): p. 751-767.
50. Nomura, K. and H. Kageyama, *Transport properties of Ba(Zr_{0.8}Y_{0.2})O₃ - δ perovskite*. *Solid State Ionics*, 2007. 178(7-10): p. 661-665.
51. Kedvik, E., *Chemical Expansion in Barium Zirconate*. 2014, Chalmers University of Technology, Göteborg, Sweden.

52. Slade, R.C.T., S.D. Flint, and N. Singh, *Investigation of protonic conduction in Yb- and Y-doped barium zirconates*. Solid State Ionics, 1995. 82(3): p. 135-141.
53. Bohn, H.G. and T. Schober, *Electrical Conductivity of the High-Temperature Proton Conductor BaZr_{0.9}Y_{0.1}O_{2.95}*. Journal of the American Ceramic Society, 2000. 83(4): p. 768-772.
54. Snijkers, F.M.M., et al., *Proton conductivity and phase composition in BaZr_{0.9}Y_{0.1}O_{3-δ}*. Scripta Materialia, 2004. 50(5): p. 655-659.
55. Minh, N.Q., *Ceramic Fuel Cells*. Journal of the American Ceramic Society, 1993. 76(3): p. 563-588.
56. Dicks, J.L.a.A., *Fuel Cell Systems Explained*. 2003.
57. Dey, T., et al., *Study of contact resistance at the electrode–interconnect interfaces in planar type Solid Oxide Fuel Cells*. Journal of Power Sources, 2013. 233: p. 290-298.
58. Berke, R. and M.E. Walter, *Mechanical Characterization and Modeling of Solid Oxide Fuel Cells and Stacks*, in *Experimental and Applied Mechanics, Volume 6: Proceedings of the 2011 Annual Conference on Experimental and Applied Mechanics*, T. Proulx, Editor. 2011, Springer New York: New York, NY. p. 37-44.
59. Gazzarri, J.I. and O. Kesler, *Short-stack modeling of degradation in solid oxide fuel cells*. Journal of Power Sources, 2008. 176(1): p. 138-154.
60. Nakajo, A., et al., *Mechanical reliability and durability of SOFC stacks. Part I : Modelling of the effect of operating conditions and design alternatives on the reliability*. International Journal of Hydrogen Energy, 2012. 37(11): p. 9249-9268.
61. Liu, Y.L., et al., *Microstructural studies on degradation of interface between LSM–YSZ cathode and YSZ electrolyte in SOFCs*. Solid State Ionics, 2009. 180(23): p. 1298-1304.
62. Hagen, A., et al., *Degradation of anode supported SOFCs as a function of temperature and current load*. Journal of the Electrochemical Society, 2006. 153(6): p. A1165-A1171.
63. Simwonis, D., F. Tietz, and D. Stöver, *Nickel coarsening in annealed Ni/8YSZ anode substrates for solid oxide fuel cells*. Solid State Ionics, 2000. 132(3): p. 241-251.
64. Tanasini, P., et al., *Experimental and theoretical investigation of degradation mechanisms by particle coarsening in SOFC electrodes*. Fuel Cells, 2009. 9(5): p. 740-752.
65. Vels Jensen, K., et al., *Microstructural and chemical changes at the Ni/YSZ interface*. Solid State Ionics, 2001. 144(3): p. 197-209.
66. Liu, Y.L. and C. Jiao, *Microstructure degradation of an anode/electrolyte interface in SOFC studied by transmission electron microscopy*. Solid State Ionics, 2005. 176(5): p. 435-442.
67. Mitterdorfer, A. and L.J. Gauckler, *La₂Zr₂O₇ formation and oxygen reduction kinetics of the La_{0.85}Sr_{0.15}MnO₃, O₂(g)/YSZ system*. Solid State Ionics, 1998. 111(3): p. 185-218.
68. Chen, M., et al., *LSM–YSZ reactions in different atmospheres*. Fuel Cells, 2009. 9(6): p. 833-840.

69. Lara-Curzio, E., et al., *Effect of thermal cycling and thermal aging on the mechanical properties of, and residual stresses in, Ni-YSZ/YSZ bi-layers*. IV. A, 2009. 11: p. 383-391.
70. Kübler, J., R. Primas, and B. Gut, *Mechanical strength of thermally aged and cycled thin zirconia sheets*, *Advances in Science and Technology, Ceramics: Charting the Future*, ed. P. Vincenzini, Techna, Florence, Italy. 1995, ISBN 88-86538-02-2.
71. Nakajo, A., et al., *Compilation of mechanical properties for the structural analysis of solid oxide fuel cell stacks. Constitutive materials of anode-supported cells*. Ceramics International, 2012. 38(5): p. 3907-3927.
72. Selçuk, A. and A. Atkinson, *Elastic properties of ceramic oxides used in solid oxide fuel cells (SOFC)*. Journal of the European Ceramic Society, 1997. 17(12): p. 1523-1532.
73. Atkinson, A. and A. Selçuk, *Mechanical behaviour of ceramic oxygen ion-conducting membranes*. Solid State Ionics, 2000. 134(1): p. 59-66.
74. Ivers-Tiffée, E., A. Weber, and D. Herbristrit, *Materials and technologies for SOFC-components*. Journal of the European Ceramic Society, 2001. 21(10): p. 1805-1811.
75. Chiang, L.-K., et al., *Thermo-electrochemical and thermal stress analysis for an anode-supported SOFC cell*. Renewable Energy, 2008. 33(12): p. 2580-2588.
76. Nakajo, A., et al., *Mechanical reliability and durability of SOFC stacks. Part II: Modelling of mechanical failures during ageing and cycling*. International Journal of Hydrogen Energy, 2012. 37(11): p. 9269-9286.
77. Bouhala, L., et al., *Study of interface influence on crack growth: Application to Solid Oxide Fuel Cell like materials design*. Materials & Design, 2010. 31(3): p. 1033-1041.
78. Biswas, S., et al., *High-temperature mechanical properties of reduced NiO–8YSZ anode-supported bi-layer SOFC structures in ambient air and reducing environments*. Ceramics International, 2013. 39(3): p. 3103-3111.
79. Young, J.L. and V.I. Birss, *Crack severity in relation to non-homogeneous Ni oxidation in anode-supported solid oxide fuel cells*. Journal of Power Sources, 2011. 196(17): p. 7126-7135.
80. Nakajo, A., et al., *The effects of dynamic dispatch on the degradation and lifetime of solid oxide fuel cell systems*. Journal of The Electrochemical Society, 2011. 158(11): p. B1329-B1340.
81. Gazzarri, J.I. and O. Kesler, *Non-destructive delamination detection in solid oxide fuel cells*. Journal of Power Sources, 2007. 167(2): p. 430-441.
82. Pandey, A., et al., *In-situ Young's moduli of the constitutive layers in a solid oxide fuel cell*. Journal of Power Sources, 2015. 273: p. 522-529.
83. Radovic, M. and E. Lara-Curzio, *Elastic Properties of Nickel-Based Anodes for Solid Oxide Fuel Cells as a Function of the Fraction of Reduced NiO*. Journal of the American Ceramic Society, 2004. 87(12): p. 2242-2246.

84. Lin, C.-K., et al., *Thermal stress analysis of a planar SOFC stack*. Journal of Power Sources, 2007. 164(1): p. 238-251.
85. Wachtman, J.B., W.R. Cannon, and M.J. Matthewson, *Mechanical properties of ceramics*. 2009, Hoboken, N.J.: Wiley.
86. Nabarro, F.R.N., *Report of a Conference on the Strength of Solids*. The Physical Society of London, London., 1948: p. 75-79.
87. Mamani, F.A.H., *Estudio de compuestos de composición eutéctica del sistema ternario Al₂O₃-M₂O₃-ZrO₂ (M=Y,Er)*. 2014, University of Seville.
88. Herring, C., *Diffusional Viscosity of a Polycrystalline Solid*. Journal of Applied Physics, 1950. 21(5): p. 437-445.
89. Coble, R.L., *A Model for Boundary Diffusion Controlled Creep in Polycrystalline Materials*. Journal of Applied Physics, 1963. 34(6): p. 1679-1682.
90. Cannon, W.R., *The contribution of grain boundary sliding to axial strain during diffusion creep*. Philosophical Magazine, 1972. 25(6): p. 1489-1497.
91. Jiménez-Melendo, M., A. Domínguez-Rodríguez, and A. Bravo-León, *Superplastic Flow of Fine-Grained Yttria-Stabilized Zirconia Polycrystals: Constitutive Equation and Deformation Mechanisms*. Journal of the American Ceramic Society, 1998. 81(11): p. 2761-2776.
92. Nieh, T.-G., J. Wadsworth, and O.D. Sherby, *Superplasticity in metals and ceramics*. 1997: Cambridge university press.
93. Vaquero-Aguilar, C. and M. Jiménez-Melendo, *Characterization and creep properties of proton-conducting Yb-doped barium cerate*. Journal of the European Ceramic Society, 2011. 31(14): p. 2671-2676.
94. Wakai, F., S. Sakaguchi, And Y. Matsuno, *Superplasticity of yttria-stabilized tetragonal ZrO₂ polycrystals*. Advanced Ceramic Materials, 1986. 1(3): p. 259-263.
95. Cannon, W. and W. Nix, *Models for grain rearrangement resulting from grain boundary sliding*. Philosophical Magazine, 1973. 27(1): p. 9-16.
96. Edington, J.W., K.N. Melton, and C.P. Cutler, *Superplasticity*. Progress in Materials Science, 1976. 21(1): p. 61-170.
97. Gifkins, R.C., *Grain-boundary sliding and its accommodation during creep and superplasticity*. Metallurgical Transactions A, 1976. 7(8): p. 1225-1232.
98. Ashby, M.F. and R.A. Verrall, *Diffusion-accommodated flow and superplasticity*. Acta Metallurgica, 1973. 21(2): p. 149-163.
99. Chung, T.E. and T.J. Davies, *The low-stress creep of fine-grain uranium dioxide*. Acta Metallurgica, 1979. 27(4): p. 627-635.
100. Jiménez-Melendo, M., et al., *Diffusional and dislocation creep of NiO polycrystals*. Philosophical Magazine A, 1987. 56(6): p. 767-781.

101. Bravo-León, A., M. Jiménez-Melendo, and A. Domínguez-Rodríguez, *Mechanical and microstructural aspects of the high temperature plastic deformation of yttria-stabilized zirconia polycrystals*. Acta Metallurgica et Materialia, 1992. 40(10): p. 2717-2726.
102. Jiménez-Melendo, M., et al., *Diffusion-controlled plastic deformation of YBa₂Cu₃O_x*. Acta Metallurgica et Materialia, 1995. 43(6): p. 2429-2434.
103. Jiménez-Melendo, M., H. Haneda, and H. Nozawa, *Ytterbium Cation Diffusion in Yttrium Aluminum Garnet (YAG)—Implications for Creep Mechanisms*. Journal of the American Ceramic Society, 2001. 84(10): p. 2356-2360.
104. Nieh, T.-G. and J. Wadsworth, *Dynamic Grain Growth During Superplastic Deformation of Yttria-Stabilized Tetragonal Zirconia Polycrystals*. Journal of the American Ceramic Society, 1989. 72(8): p. 1469-1472.
105. Ball, A. and M.M. Hutchison, *Superplasticity in the Aluminium–Zinc Eutectoid*. Metal Science Journal, 1969. 3(1): p. 1-7.
106. Ball, A., *Superplasticity in the aluminium-zinc eutectoid—an early model revisited*. Materials Science and Engineering: A, 1997. 234: p. 365-369.
107. Mukherjee, A.K., *The rate controlling mechanism in superplasticity*. Materials Science and Engineering, 1971. 8(2): p. 83-89.
108. Hayden, H.W., S. Floreen, and P.D. Goodell, *The deformation mechanisms of superplasticity*. Metallurgical Transactions, 1972. 3(4): p. 833-842.
109. Crossman, F.W. and M.F. Ashby, *The non-uniform flow of polycrystals by grain-boundary sliding accommodated by power-law creep*. Acta Metallurgica, 1975. 23(4): p. 425-440.
110. Ashby, M.F., *On interface-reaction control of Nabarro-Herring creep and sintering*. Scripta Metallurgica, 1969. 3(11): p. 837-842.
111. Burton, B., *Interface reaction controlled diffusional creep: A consideration of grain boundary dislocation climb sources*. Materials Science and Engineering, 1972. 10: p. 9-14.
112. Burton, B., *The characteristic equation for superplastic flow*. Philosophical Magazine A, 1983. 48(3): p. L9-L13.
113. Nieh, T.G., et al. *Superplasticity in Metals and Ceramics*. 1997.
114. Jiménez-Melendo, M., A. Domínguez-Rodríguez, and J.L. Routbort, *Deformation maps of YBa₂Cu₃O_{7-x} superconductors*. Scripta Metallurgica et Materialia, 1995. 32(4): p. 621-626.
115. Gauckler, L.J., et al., *Solid oxide fuel cells: systems and materials*. CHIMIA International Journal for Chemistry, 2004. 58(12): p. 837-850.
116. Skarmoutsos, D., et al., *5 mol% TiO₂-doped Ni–YSZ anode cermets for solid oxide fuel cells*. Solid State Ionics, 2000. 135(1): p. 439-444.

117. Pratihari, S.K., A. Dassharma, and H.S. Maiti, *Properties of Ni/YSZ porous cermets prepared by electroless coating technique for SOFC anode application*. Journal of materials science, 2007. 42(17): p. 7220-7226.
118. Tietz, F., *Thermal expansion of SOFC materials*. Ionics, 1999. 5(1): p. 129-139.
119. Giraud, S. and J. Canel, *Young's modulus of some SOFCs materials as a function of temperature*. Journal of the European Ceramic Society, 2008. 28(1): p. 77-83.
120. Buckley, J.D. and D.N. Braski, *Elastic Modulus of Stabilized Zirconia*. Journal of the American Ceramic Society, 1967. 50(4): p. 220-221.
121. Atkinson, A. and A. Selçuk, *Mechanical behaviour of ceramic oxygen ion-conducting membranes*. Solid State Ionics, 2000. 134(1): p. 59-66.
122. Lakki, A., et al., *Mechanical loss, creep, diffusion and ionic conductivity of ZrO₂-8 mol%Y₂O₃ polycrystals*. Journal of the European Ceramic Society, 2000. 20(3): p. 285-296.
123. Atkinson, A. and A. Selçuk, *Residual stress and fracture of laminated ceramic membranes*. Acta materialia, 1999. 47(3): p. 867-874.
124. Selçuk, A. and A. Atkinson, *Elastic properties of ceramic oxides used in solid oxide fuel cells (SOFC)*. Journal of the European Ceramic Society, 1997. 17(12): p. 1523-1532.
125. Radovic, M., et al., *Thermophysical properties of YSZ and Ni-YSZ as a function of temperature and porosity*. Advances in Solid Oxide Fuel Cells II: Ceramic Engineering and Science Proceedings, Cocoa Beach, Volume 27, 2009(4): p. 79.
126. Selçuk, A. and A. Atkinson, *Strength and Toughness of Tape-Cast Yttria-Stabilized Zirconia*. Journal of the American Ceramic Society, 2000. 83(8): p. 2029-2035.
127. Lowrie, F. and R. Rawlings, *Room and high temperature failure mechanisms in solid oxide fuel cell electrolytes*. Journal of the European Ceramic Society, 2000. 20(6): p. 751-760.
128. Santos, M., et al., *Mechanical properties of sintered La_{0.933}Si₂Ge₄O₂₆ oxyapatite materials for SOFC electrolytes*. Ceramics International, 2012. 38(8): p. 6151-6156.
129. Suarez, G., et al., *Electrophoretic deposition for obtaining dense lanthanum silicate oxyapatite (LSO)*. Ceramics International, 2016. 42(16): p. 19283-19288.
130. Iwata, T., et al., *Structural change of oxide-ion-conducting lanthanum silicate on heating from 295 to 1073 K*. Solid State Ionics, 2007. 178(27): p. 1523-1529.
131. Jiang, S.P., et al., *Synthesis and characterization of lanthanum silicate apatite by gel-casting route as electrolytes for solid oxide fuel cells*. Journal of Power Sources, 2009. 189(2): p. 972-981.
132. Sazinas, R., M.-A. Einarsrud, and T. Grande, *Toughening of Y-doped BaZrO₃ proton conducting electrolytes by hydration*. Journal of Materials Chemistry A, 2017. 5(12): p. 5846-5857.

133. Han, D., N. Hatada, and T. Uda, *Chemical Expansion of Yttrium-Doped Barium Zirconate and Correlation with Proton Concentration and Conductivity*. Journal of the American Ceramic Society, 2016. 99(11): p. 3745-3753.
134. Lyagaeva, J., et al., *A detailed analysis of thermal and chemical compatibility of cathode materials suitable for BaCe_{0.8}Y_{0.2}O_{3-δ} and BaZr_{0.8}Y_{0.2}O_{3-δ} proton electrolytes for solid oxide fuel cell application*. International Journal of Hydrogen Energy, 2017. 42(3): p. 1715-1723.

Chapter 2

PREPARATION OF MATERIALS

Contents

2.1 Introduction	47
2.2 Lanthanum Silicate	48
2.2.1 Commercial starting precursors for LSO nanopowders preparation.....	49
2.2.2 Freeze-drying synthesis	49
2.2.3 Compaction of LSO nanopowders.....	51
2.2.4 High temperature sintering.....	51
2.2.4.1 Conventional sintering	51
2.2.4.2 Spark plasma sintering	51
2.3 Yttrium-doped Barium Zirconate	52
2.3.1 Commercial starting precursors for BZY nanopowders preparation.....	53
2.3.2 Modified EDTA-citrate complexing synthesis	53
2.3.3 Compaction of BZY nanopowders	55
2.3.4 High temperature sintering.....	55
2.3.5 Commercial Yttrium-doped Barium Zirconate.....	56
NiO-extraction	56
2.4 References	56

2.1 INTRODUCTION

This chapter outlines the experimental procedures followed for the preparation of the different materials studied during this thesis and the results obtained. The initial parameters of the different stages (synthesis, calcination and sintering) have been taken from previous studies carried out in our research group [1-3].

In this work, two different materials for SOFC electrolytes have been studied: Lanthanum Silicate and Yttrium-doped Barium Zirconate.

2.2 LANTHANUM SILICATE

Densification is a serious challenge in the fabrication of $\text{La}_{9.33+x}\text{Si}_6\text{O}_{26+3x/2}$ compounds. Many efforts have thus been made to prepare fully dense ceramics for SOFC electrolyte applications, where flow gas impermeability and thus low porosity (which greatly limits the electrical performance [17]) are required. The most widely technique used for the preparation of these compounds is via conventional solid-state reaction methods, where very high temperatures (> 1600 °C) are necessary to obtain relative densities higher than 90% (**Table 2.1**). The sol-gel route has been also proposed to decrease the formation temperature of the oxy-apatite phase; this technique however, leads to densities lower than 95% after conventional sintering (**Table 2.1**).

Table 2.1. Preparation techniques, sintering temperatures and relative densities for $\text{La}_{9.33}\text{Si}_6\text{O}_{26}$ oxy-apatite.

Technique	Sintering temperature (°C)	Relative density (%)	Reference
Solid-state reaction	1500 - 1500	70 - 80	[18]
Solid-state reaction	1600-1700	> 90	[19]
Solid-state reaction	1600	97	[20]
Solid-state reaction	1700	95	[15]
Sol-gel	1400	69	[21]
Sol-gel	1400	66	[22]
Sol-gel	1450	92	[23]
Sol-gel	1500	90	[6]
Freeze drying + Conventional sintering	1500	> 95	[1, 2]
Freeze drying + Spark plasma sintering	1250	100	[1, 2]

In this context, previous works of our research group have shown two strategies to achieve excellent results in the densification of Lanthanum Silicate by combining highly dispersed nanopowders obtained by freeze drying with conventional or spark plasma sintering, which resulted in densities between 95 % and 100 % [1, 2]. Therefore, in this work, these two routes have been followed to prepare fully dense materials.

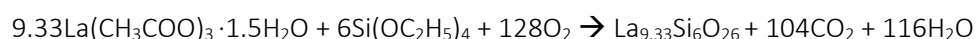
2.2.1 Commercial starting precursors for LSO nanopowders preparation

Two high purity commercial precursors were used as starting materials: lanthanum acetate sesquioxide $\text{La}(\text{CH}_3\text{COO})_3 \cdot 1.5\text{H}_2\text{O}$ and tetraethoxysilane (TEOS, $\text{Si}(\text{OC}_2\text{H}_5)_4$), their characteristics are summarized in **Table 2.2**.

Table 2.2. Commercial precursors used for the preparation of $\text{La}_{9.33}\text{Si}_6\text{O}_{26}$.

Precursor	Vendor	Purity (%)	Molecular weight (g/mol)
$\text{La}(\text{CH}_3\text{COO})_3 \cdot 1.5\text{H}_2\text{O}$	Alfa-Aesar	99.9	343.05
$\text{Si}(\text{OC}_2\text{H}_5)_4$	Alfa-Aesar	99.9	208.33

Stoichiometric amounts of precursors were used to form the $\text{La}_{9.33}\text{Si}_6\text{O}_{26}$ compound according to the following equation:



2.2.2 Freeze-drying synthesis

Freeze-drying allows the preparation of a large variety of high purity powders with an accurate control of the composition [24, 25]. It consists in the instant freezing of a solution and the further ice sublimation under vacuum conditions [26], resulting in highly dispersed precursor nanoparticles. A subsequent conventional thermal treatment is necessary to remove the organic ligands and form the desired phase.

$\text{La}_{9.33}\text{Si}_6\text{O}_{26}$ (LSO) was synthesized by the freeze drying method following the experimental process presented in **Figure 2.1**. Firstly, lanthanum acetate was dissolved in 200 ml of ultra-pure water with magnetic stirring until a transparent solution was obtained. Then, TEOS was put in another beaker, and acetic acid and a small amount of deionized water were added. The mixture was stirred, resulting in a clear transparent solution. Acetic acid acts as a double agent since it catalyzes and controls the TEOS hydrolysis reaction. The volumetric ratio, $r = V_{\text{acetic acid}} / V_{\text{TEOS}}$, was set to 4 [1, 2]. The two aforementioned solutions were then mixed, and ultra-pure water was added up to a total volume of 600 mL, with a pH value close to 4. The resulting solution was sprayed in a liquid nitrogen bath to form a “snow” containing water and the precursors. Due to the instantaneous freezing, the homogeneity of the original solution was retained in the solid phase. These frozen droplets were transferred into the freeze-dryer chamber, where the dehydration process was carried out in a Christ Alpha 2-4 LSC apparatus under vacuum (≤ 1 Pa). By maintaining

the temperature of the condenser at $-47\text{ }^{\circ}\text{C}$ for 48 hours, water was continuously removed by sublimation and the temperature of the powder increased up to $+4\text{ }^{\circ}\text{C}$. Finally the precursor was progressively warmed up to $+50\text{ }^{\circ}\text{C}$ to get rid of the adsorbed water. The resulting powder was a whitish amorphous precursor.

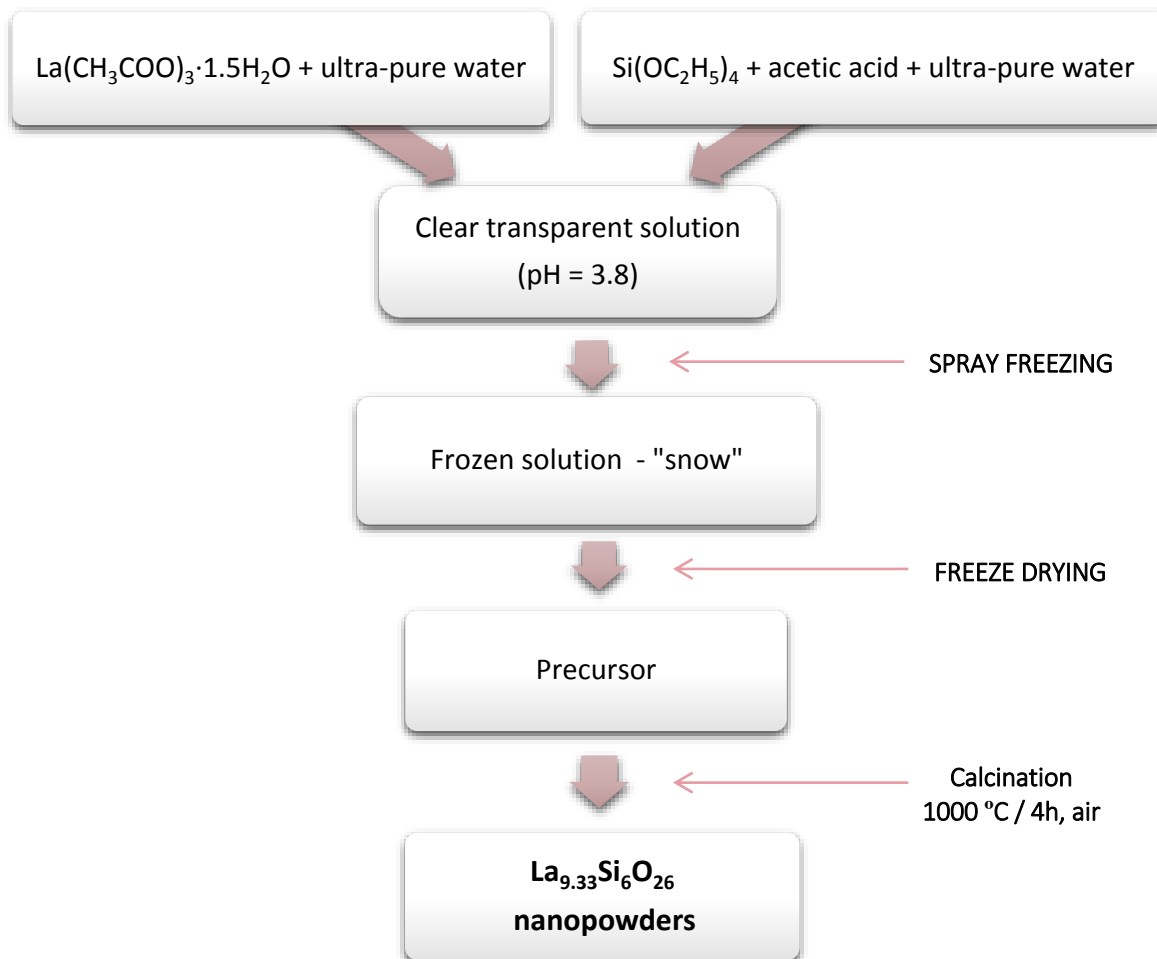


Figure 2.1. Freeze-drying synthesis process for $\text{La}_{9.33}\text{Si}_6\text{O}_{26}$ nanopowders.

Calcination is a thermal treatment by which a set of chemical reactions of decomposition produce a new compound. It is commonly used in the production of simple oxide powders from carbonates, hydroxides, nitrates, sulfates, etc. This step of the fabrication process is essential to remove any residual carbon species and form pure oxy-apatite nanopowders. After freeze-drying, the precursors contain a high amount of organic residues and ligands, which decompose between room temperature and $900\text{ }^{\circ}\text{C}$, this decomposition being associated with an important weight loss ($\sim 45\%$). The thermal treatments at $T > 900\text{ }^{\circ}\text{C}$ lead to well crystallised powder without any parasitic phase [2]. In this work, freeze-dried powder calcination was carried out at $1000\text{ }^{\circ}\text{C}$ for 4 hours, with heating/cooling rates of $5\text{ }^{\circ}\text{C}/\text{min}$, in air.

2.2.3 Compaction of LSO nanopowders

Cold mechanical compaction increases the cohesion between particles in the powder and allows to obtain easy-to-handle compact pellets, which are later on subjected to sintering at high temperature. In this work, a double pressing system was used, consisting of:

- Uniaxial pressing: A pre-compaction of the nanopowders was performed on a uniaxial press under 100 MPa for 3 min in a 20 mm diameter cylindrical steel die filled with about 6 g of powder. After pressing, pellets of 20 mm in diameter and 7 mm in height were obtained.

- Isostatic pressing: These pellets were vacuum-packed in plastic bags using a domestic vacuum sealer and then isostatically pressed at 750 MPa for 10 min. Pellets of 19 mm in diameter and 6 mm in height were finally obtained.

2.2.4 High-temperature sintering

In order to prepare fully dense materials from the freeze-dried nanopowders, two different sintering routes have been used: conventional and spark plasma sintering.

2.2.4.1 Conventional sintering

Conventional sintering is the pressureless sintering of a previously pressed powder. Powder compacts were placed on an alumina crucible covered previously with a layer of Lanthanum Silicate powder and then sintered at 1500 °C for 12 h in air. Very slow heating/cooling rates were used, 2 °C/min, in order to avoid possible internal residual stresses which could cause the formation and propagation of cracks. After sintering, the pellets dimensions decreased to approximately 15 and 5 mm in diameter and height, respectively.

2.2.4.2 Spark Plasma Sintering

Spark plasma sintering (SPS) is a powerful technique to sinter powders applying an external pressure and an electric field simultaneously. It allows a faster densification at lower temperatures than conventional sintering methods [27], giving rise to materials with higher densities, smaller grain sizes, cleaner grain boundaries, in addition to other interesting properties [28]. SPS has been carried out in a Dr. Sinter SPS furnace (Plateforme frittage flash, Thiais, France) (**Figure 2.2**) which allows the recording of the shrinkage, shrinkage rate, temperature, current, voltage and pressure in real time.

Before SPS treatment, a 20 mm-diameter high-strength graphite mold/dies ensemble was filled with about 6 g of calcined LSO powder. To minimize heat losses, the mold was lined with a foil of graphite and surrounded by a blanket of graphite (**Figure 2.7**). The mold/die/powder assembly was then put into the sintering chamber and a thermocouple was inserted into the graphite die to measure the temperature. The assembly was progressively heated up to 1250 °C under a constant pressure of 100 MPa. Firstly, the temperature was increased up to 600 °C at a rate of 200 °C/min. After this first step, the target temperature of 1250 °C was reached at a heating rate of 50 °C/min and maintained for 5 min. After that, both the heating and pressure were rapidly released. The system took around 10 min cooling-down naturally. The whole sintering process, from sample preparation until final cooling, lasted less than 1 h. The pellets were finally submitted to a conventional thermal treatment at 800 °C in air for 24 h to burn all residual carbon species.

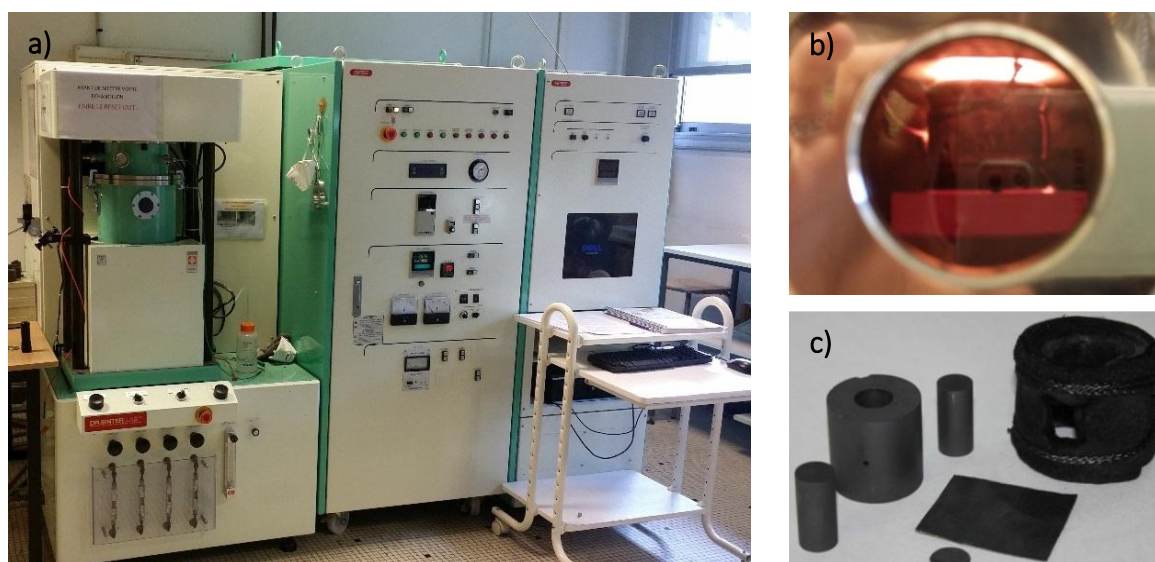


Figure 2.2. Spark-plasma sintering system: (a) Hot press furnace (left), unit control (center) and power unit (right). (b) Detail of the chamber interior during sintering. (c) Die, blanket and graphite foil used in the process.

2.3 YTTRIUM-DOPED BARIUM ZIRCONATE

In order to prepare fully dense and pure $\text{BaZr}_{1-x}\text{Y}_x\text{O}_{3-\delta}$ compounds, several approaches have been developed. High sintering temperature (> 1700 °C) and long sintering time enable density values higher than 90%. For example, Iguchi *et al.* [41] obtained ~97% dense $\text{BaZr}_{0.95}\text{Y}_{0.05}\text{O}_3$ at 1700 to 1800 °C, while Duval *et al.* [42] reported densities of about 91% at 1720 °C for $\text{BaZr}_{0.9}\text{Y}_{0.1}\text{O}_3$, which unfortunately also lead to variation in chemical composition due to Barium evaporation and the emergence of parasite phases, which have a detrimental effect on the proton conductivity [39,

41, 43]. To overcome the disadvantages, wet chemical methods were adopted to obtain high quality nanopowders and the desired perovskite compound [44, 45].

In the present work, Y-substituted Barium Zirconate has been synthesized by the modified EDTA-citrate complexing method, and sintered at high temperature by conventional sintering following the suggestion of Babilo *et al.* [46]. It has been also used a commercial NiO-added BZY sintered pellet, as explained below.

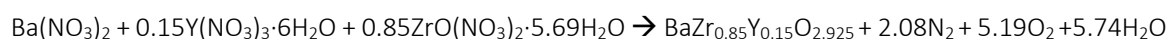
2.3.1 Commercial starting precursors for BZY nanopowders preparation

High purity commercial precursor powders of Barium Nitrate $\text{Ba}(\text{NO}_3)_2$, Yttrium Nitrate ($\text{Y}(\text{NO}_3)_3 \cdot 6\text{H}_2\text{O}$) and Zirconium Nitrate ($\text{ZrO}(\text{NO}_3)_2 \cdot 5.69\text{H}_2\text{O}$) were used as starting materials. Their characteristics are summarized in **Table 2.3**.

Table 2.3. Commercial precursors used for the preparation of $\text{BaZr}_{0.85}\text{Y}_{0.15}\text{O}_{2.925}$.

Precursor	Vendor	Purity (%)	Molecular weight (g/mol)
$\text{Ba}(\text{NO}_3)_2$	Alfa-Aesar	99.95	261.35
$\text{Y}(\text{NO}_3)_3 \cdot 6\text{H}_2\text{O}$	Alfa-Aesar	99.9	383.01
$\text{ZrO}(\text{NO}_3)_2 \cdot 5.69\text{H}_2\text{O}$	Strem chemicals	99.9	231.23

Stoichiometric amounts of precursors were used to form the $\text{BaZr}_{0.85}\text{Y}_{0.15}\text{O}_{2.925}$ compound according to the following equation:



2.3.2 Modified EDTA-citrate complexing synthesis

The modified EDTA–citrate complexing method is a successful wet chemical route used to synthesize a large variety of oxide materials [47]. Due to the EDTA-citrate combination, several metal ions present in a solution are chelated to make up metal complexes which undergo polyesterification, when heated, to form a polymer with the metal ions uniformly distributed throughout [48]. As a result, ultrafine powders of high purity and homogeneity are obtained [49, 50]. Taking into account the advantages of this method, $\text{BaZr}_{0.85}\text{Y}_{0.15}\text{O}_{2.925}$ (BZY) was prepared by the modified EDTA-citrate complexing synthesis following the experimental process presented on **Figure 2.3**.

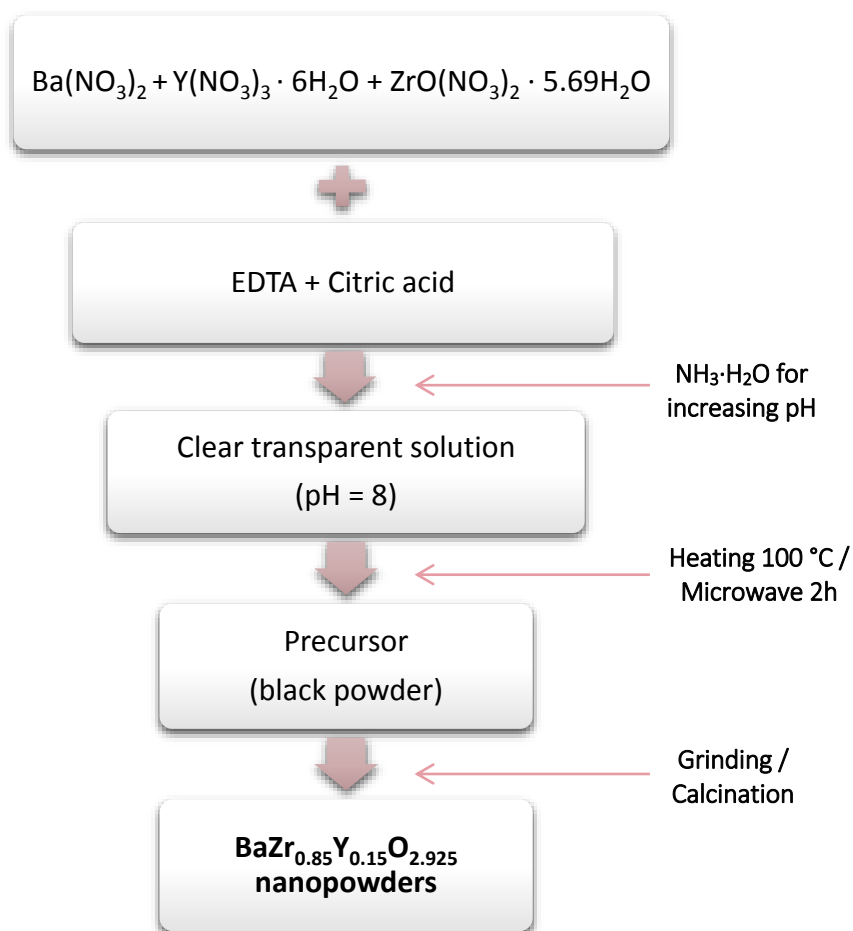


Figure 2.3. Microwave-assisted citric acid-EDTA synthesis process of $\text{BaZr}_{0.85}\text{Y}_{0.15}\text{O}_{2.925}$ nanopowders.

First of all, the necessary amounts of nitrates were dissolved in 150 ml of ultra-pure water with magnetic stirring until a transparent solution was obtained. Afterwards, citric acid and EDTA were added as chelating agents. The cooperation of citrate and EDTA allows obtaining more stable chelate complexes [50]. The mole ratio of (EDTA acid): (citric acid): (total metal ions) was fixed at 1.5:1.5:1. Then, aqueous ammonia was added to the solution to facilitate the EDTA dissolution, forming a water-soluble ammonium salt [3] with a pH value adjusted to about 8. Solution was heated up under continuous stirring to obtain a viscous gel. Then, dry gel combustion was carried out into a domestic microwave for 2 h, obtaining a black porous precursor.

After this synthesis step, the precursor was calcined to obtain a pure crystalline phase. It was first ground into an agate mortar and placed in an alumina crucible. Then, calcination was carried out at $1000\text{ }^\circ\text{C}$ for 5 h in air, with heating/cooling rates of $3\text{ }^\circ\text{C}/\text{min}$. Once finished the thermal treatment, the black precursor became a whitish powder (**Figure 2.4**).



Figure 2.4. (a) Black porous sponge-puffy stuff; (b) Black milled precursor; (c) Whitish powder after calcination.

2.3.3 Compaction of BZY nanopowders

Cold mechanical compaction was used to obtain compact pellets of BZY15, which were later on sintered at high temperature. Firstly, a pre-compaction of nanopowders was performed by means of a uniaxial press. For this propose, a powder amount of 6 g was loaded into a 20 mm-diameter cylindrical steel mold and pressed at 100 MPa for 3 min, obtaining pellets of 20 mm in diameter and 8 mm in thickness. These pellets were vacuum packed in plastic bags using a domestic vacuum sealer and subsequently isostatically pressed at 750 MPa for 10 min. 17 mm-diameter and 7 mm-height pellets were obtained.

2.3.4 High temperature sintering

High temperature pressureless sintering was carried out after powder compaction to obtain a fully dense material. The pellets were placed in an alumina crucible and fully covered by BZY powder with a 10 wt%-excess Barium carbonate, as suggested by Babilo *et al.* [46] (**Figure 2.5**), to avoid Barium evaporation found at temperatures above 1550 °C [43, 51]. Conventional sintering was performed at 1600 °C during 24 h in air, with very slow heating/cooling rates of 3 °C/min.

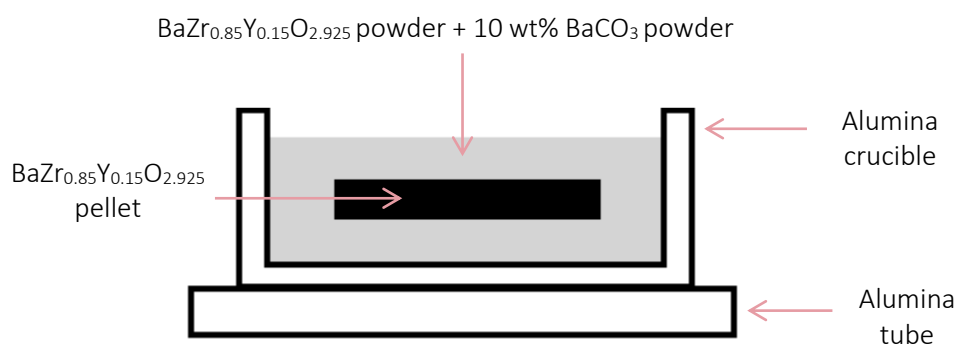


Figure 2.5. Sintering configuration: BaZr_{0.85}Y_{0.15}O_{2.925} green pellet covered with a powder mixture of BYZ and BaCO₃ (10 wt%) [46].

2.3.5 Commercial Yttrium-doped Barium Zirconate

In order to overcome the low sinterability of Barium Zirconate, a new approach based on the use of additives (mostly transition metal oxides: NiO, ZnO, CuO, ...) during the fabrication process has been recently proposed [52-54]. It results in dense materials with grain sizes of typically 2 - 4 μm , and therefore limited grain-boundary resistance. Yttrium-doped Barium Zirconate was prepared through this strategy starting from stoichiometric amounts of simple precursors (ZrO_2 , Y_2O_3 and BaCO_3 or BaSO_4) with 1-2 wt% transition metal oxide addition. The overall mixture was ball-milled during 24 h, pressed into a pellet and sintered at 1400 - 1550 $^\circ\text{C}$ for 24 h. The resulting compounds have densities higher than 90 %. In this sense, Nikodemski *et al.* [54] have reported densities higher than 98% in 20% Yttrium-doped Barium Zirconate with 1 wt% NiO sintered at 1500 $^\circ\text{C}$ for 24 h; the grain size was in the 3 - 5 μm range. Different explanations have been proposed to explain the efficiency of such a process [54]. With NiO addition, it has been suggested that low melting point intermediate phases, such as BaY_2NiO_5 or BaNiO_4 , are formed, enhancing the sintering rate through the presence of a liquid phase [53]. This material also shows a high total proton conductivity, similar to that of bulk material [53].

In this study, $\text{BaZr}_{0.85}\text{Y}_{0.15}\text{O}_{2.925}$ with 1 wt% NiO-content provided by NorecsTM in the form of large pellets of 20 mm in diameter and 5 mm in thickness has been studied.

NiO-extraction

In order to study the influence of Nickel on the mechanical properties, the mechanical characterization was also carried out on the BZY commercial samples after NiO-extraction.

For NiO-extraction, commercial ceramics were placed in an alumina crucible and surrounded with a powder mixture of BZY15 with 10 wt% excess of barium carbonate, as shown in **Figure 2.5**. Then, a firing cycle was carried out at 1600 $^\circ\text{C}$ for 120 h in air, with very slow heating/cooling rates of 3 $^\circ\text{C}/\text{min}$. NiO extraction is based on the NiO diffusion along grain boundaries towards the sample surface, where it sublimates and is captured by the surrounding BZY powder [55].

2.4 REFERENCES

1. Chesnaud, A., et al., *Preparation of transparent oxyapatite ceramics by combined use of freeze-drying and spark-plasma sintering*. Chemical Communications, 2007(15): p. 1550-1552.

2. Chesnaud, A., et al., *Influence of synthesis route and composition on electrical properties of $La_{9.33} + xSi_6O_{26} + 3x/2$ oxy-apatite compounds*. Solid State Ionics, 2008. 179(33–34): p. 1929-1939.
3. Iakovleva, A., *Study of novel proton conductors for high temperature Solid Oxide Cells*. 2016, CentraleSupélec, Université Paris-Saclay, France.
4. Nakayama, S. and M. Sakamoto, *Electrical properties of new type high oxide ionic conductor $RE_{10}Si_6O_{27}$ ($RE = La, Pr, Nd, Sm, Gd, Dy$)*. Journal of the European Ceramic Society, 1998. 18(10): p. 1413-1418.
5. Okudera, H., et al., *Structure of oxide ion-conducting lanthanum oxyapatite, $La_{9.33}(SiO_4)_6O_2$* . Solid State Ionics, 2005. 176(15–16): p. 1473-1478.
6. Tian, C., et al., *Direct synthesis of $La_{9.33}Si_6O_{26}$ ultrafine powder via sol–gel self-combustion method*. Journal of Alloys and Compounds, 2008. 458(1–2): p. 378-382.
7. Nakao, T., et al., *Chemical stability of $La_{10}Si_6O_{27}$ and its application to electrolytes for solid oxide fuel cells*. Solid State Ionics, 2008. 179(27–32): p. 1567-1569.
8. Matsunaga, K. and K. Toyoura, *First-principles analysis of oxide-ion conduction mechanism in lanthanum silicate*. Journal of Materials Chemistry, 2012. 22(15): p. 7265-7273.
9. Leon-Reina, L., et al., *Interstitial oxygen conduction in lanthanum oxy-apatite electrolytes*. Journal of Materials Chemistry, 2004. 14(7): p. 1142-1149.
10. Masubuchi, Y., et al., *Oxide ion conduction mechanism in $RE_{9.33}(SiO_4)_6O_2$ and $Sr_2RE_8(SiO_4)_6O_2$ ($RE = La, Nd$) from neutron powder diffraction*. Solid State Ionics, 2006. 177(3–4): p. 263-268.
11. León-Reina, L., et al., *Crystalchemistry and Oxide Ion Conductivity in the Lanthanum Oxygermanate Apatite Series*. Chemistry of Materials, 2003. 15(10): p. 2099-2108.
12. Nakayama, S. and M. Sakamoto, *Ionic conductivities of apatite-type $LaX(GeO_4)_6O_{1.5X-12}$ ($X=8-9.33$) polycrystals*. Journal of Materials Science Letters, 2001. 20(17): p. 1627-1629.
13. Nakayama, S., et al., *Ionic conductivity of lanthanoid silicates, $Ln_{10}(SiO_4)_6O_3$ ($Ln = La, Nd, Sm, Gd, Dy, Y, Ho, Er$ and Yb)*. Journal of Materials Chemistry, 1995. 5(11): p. 1801-1805.
14. Susumu, N., A. Hiromichi, and S. Yoshihiko, *Ionic Conductivity of $Ln_{10}(SiO_4)_6O_3$ ($Ln = La, Nd, Sm, Gd$ and Dy)*. Chemistry Letters, 1995. 24(6): p. 431-432.
15. Abram, E.J., D.C. Sinclair, and A.R. West, *A novel enhancement of ionic conductivity in the cation-deficient apatite $La_{9.33}(SiO_4)_6O_2$* . Journal of Materials Chemistry, 2001. 11(8): p. 1978-1979.
16. Steele, B.C.H. and A. Heinzel, *Materials for fuel-cell technologies*. Nature, 2001. 414(6861): p. 345-352.
17. Panteix, P.J., et al., *Influence of porosity on the electrical properties of $La_{9.33}(SiO_4)_6O_2$ oxyapatite*. Ceramics International, 2008. 34(7): p. 1579-1586.

18. Panteix, P.J., et al., *Synthesis and characterization of oxide ions conductors with the apatite structure for intermediate temperature SOFC*. Materials Chemistry and Physics, 2006. 95(2–3): p. 313-320.
19. Najib, A., et al., *Doping strategies to optimise the oxide ion conductivity in apatite-type ionic conductors*. Dalton Transactions, 2004(19): p. 3106-3109.
20. Vincent, A., S.B. Savignat, and F. Gervais, *Elaboration and ionic conduction of apatite-type lanthanum silicates doped with Ba, $La_{10-x}Ba_x(SiO_4)_6O_{3-x/2}$ with $x = 0.25-2$* . Journal of the European Ceramic Society, 2007. 27(2–3): p. 1187-1192.
21. Celerier, S., et al., *Synthesis by sol–gel route of oxyapatite powders for dense ceramics: Applications as electrolytes for solid oxide fuel cells*. Journal of the European Ceramic Society, 2005. 25(12): p. 2665-2668.
22. Tao, S. and J.T.S. Irvine, *Preparation and characterisation of apatite-type lanthanum silicates by a sol-gel process*. Materials Research Bulletin, 2001. 36(7–8): p. 1245-1258.
23. Célérier, S., et al., *New chemical route based on sol–gel process for the synthesis of oxyapatite $La_{9.33}Si_6O_{26}$* . Ceramics International, 2006. 32(3): p. 271-276.
24. Paulus, M., *Effect Of Homogeneity On Sintering And The Processes To Improve It*. Science of Sintering, 1980. 12(1): p. 25-37.
25. Lacour, C. and M. Paulus, *Lyophilisation Parameters Of Ceramic Compounds*. Science Of Sintering, 1979. 11(3): p. 193-202.
26. Abdelwahed, W., et al., *Freeze-drying of nanoparticles: Formulation, process and storage considerations*. Advanced Drug Delivery Reviews, 2006. 58(15): p. 1688-1713.
27. Pérez-Estébanez, M., et al., *Spark plasma versus conventional sintering in the electrical properties of Nasicon-type materials*. Journal of Alloys and Compounds, 2015. 651: p. 636-642.
28. Munir, Z.A., U. Anselmi-Tamburini, and M. Ohyanagi, *The effect of electric field and pressure on the synthesis and consolidation of materials: A review of the spark plasma sintering method*. Journal of Materials Science, 2006. 41(3): p. 763-777.
29. Katahira, K., et al., *Protonic conduction in Zr-substituted $BaCeO_3$* . Solid State Ionics, 2000. 138(1–2): p. 91-98.
30. *Proton-Conducting Oxides*. Annual Review of Materials Research, 2003. 33(1): p. 333-359.
31. Ryu, K.H. and S.M. Haile, *Chemical stability and proton conductivity of doped $BaCeO_3$ – $BaZrO_3$ solid solutions*. Solid State Ionics, 1999. 125(1–4): p. 355-367.
32. Akbarzadeh, A.R., et al., *Combined theoretical and experimental study of the low-temperature properties of $BaZrO_3$* . Physical Review B, 2005. 72(20): p. 205104.
33. Kreuer, K.D., *Aspects of the formation and mobility of protonic charge carriers and the stability of perovskite-type oxides*. Solid State Ionics, 1999. 125(1–4): p. 285-302.

34. Schober, T. and H.G. Bohn, *Water vapor solubility and electrochemical characterization of the high temperature proton conductor BaZr_{0.9}Y_{0.1}O_{2.95}*. Solid State Ionics, 2000. 127(3–4): p. 351-360.
35. Shannon, R., *Revised effective ionic radii and systematic studies of interatomic distances in halides and chalcogenides*. Acta Crystallographica Section A, 1976. 32(5): p. 751-767.
36. Nomura, K. and H. Kageyama, *Transport properties of Ba(Zr_{0.8}Y_{0.2})O_{3-δ} perovskite*. Solid State Ionics, 2007. 178(7–10): p. 661-665.
37. Kedvik, E., *Chemical Expansion in Barium Zirconate*. 2014, Chalmers University of Technology, Göteborg, Sweden.
38. Slade, R.C.T., S.D. Flint, and N. Singh, *Investigation of protonic conduction in Yb- and Y-doped barium zirconates*. Solid State Ionics, 1995. 82(3): p. 135-141.
39. Bohn, H.G. and T. Schober, *Electrical Conductivity of the High-Temperature Proton Conductor BaZr_{0.9}Y_{0.1}O_{2.95}*. Journal of the American Ceramic Society, 2000. 83(4): p. 768-772.
40. Snijkers, F.M.M., et al., *Proton conductivity and phase composition in BaZr_{0.9}Y_{0.1}O_{3-δ}*. Scripta Materialia, 2004. 50(5): p. 655-659.
41. Iguchi, F., et al., *The influence of grain structures on the electrical conductivity of a BaZr_{0.95}Y_{0.05}O₃ proton conductor*. Solid State Ionics, 2006. 177(26–32): p. 2381-2384.
42. Duval, S.B.C., et al., *Electrical conductivity of the proton conductor BaZr_{0.9}Y_{0.1}O_{3-δ} obtained by high temperature annealing*. Solid State Ionics, 2007. 178(25–26): p. 1437-1441.
43. Shima, D. and S.M. Haile, *The influence of cation non-stoichiometry on the properties of undoped and gadolinia-doped barium cerate*. Solid State Ionics, 1997. 97(1–4): p. 443-455.
44. Sin, A., et al., *Synthesis and Sintering of Large Batches of Barium Zirconate Nanopowders*. Journal of the American Ceramic Society, 2002. 85(8): p. 1928-1932.
45. Yamazaki, Y., R. Hernandez-Sanchez, and S.M. Haile, *High Total Proton Conductivity in Large-Grained Yttrium-Doped Barium Zirconate*. Chemistry of Materials, 2009. 21(13): p. 2755-2762.
46. Babilo, P., T. Uda, and S.M. Haile, *Processing of yttrium-doped barium zirconate for high proton conductivity*. Journal of Materials Research, 2007. 22(5): p. 1322-1330.
47. Shao, Z., et al., *Investigation of the permeation behavior and stability of a Ba_{0.5}Sr_{0.5}Co_{0.8}Fe_{0.2}O_{3-δ} oxygen membrane*. Journal of Membrane Science, 2000. 172(1–2): p. 177-188.
48. Ding, X., et al., *Synthesis and characterization of doped LaCrO₃ perovskite prepared by EDTA–citrate complexing method*. Journal of Alloys and Compounds, 2008. 458(1–2): p. 346-350.
49. Tao, Y., et al., *Synthesis and properties of La_{0.6}Sr_{0.4}CoO_{3-δ} nanopowder*. Journal of Power Sources, 2008. 185(2): p. 609-614.

50. Abdullah, N.A., S. Hasan, and N. Osman, *Role of CA-EDTA on the Synthesizing Process of Cerate-Zirconate Ceramics Electrolyte*. Journal of Chemistry, 2013. 2013: p. 7.
51. Wu, J., et al., *Defect chemistry and transport properties of $Ba_{x}Ce_{0.85}MO_{1.5}O_{3-\delta}$* . Journal of Materials Research, 2004. 19(8): p. 2366-2376.
52. Ricote, S., et al., *Conductivity study of dense $BaCe_{x}Zr_{(0.9-x)}Y_{0.1}O_{3-\delta}$ prepared by solid state reactive sintering at 1500 °C*. International Journal of Hydrogen Energy, 2012. 37(9): p. 7954-7961.
53. Tong, J., et al., *Solid-state reactive sintering mechanism for large-grained yttrium-doped barium zirconate proton conducting ceramics*. Journal of Materials Chemistry, 2010. 20(30): p. 6333-6341.
54. Nikodemski, S., J. Tong, and R. O'Hayre, *Solid-state reactive sintering mechanism for proton conducting ceramics*. Solid State Ionics, 2013. 253: p. 201-210.
55. Coors, W.G., et al., *Fabrication of Yttrium-Doped Barium Zirconate for High Performance Protonic Ceramic Membranes*. Perovskite Materials - Synthesis, Characterisation, Properties, and Applications. 2016.

Chapter 3

**STRUCTURAL AND MICROSTRUCTURAL
CHARACTERIZATION**

Contents

3.1 Introduction	62
3.2 Characterization techniques	62
3.2.1 X-Ray Diffraction	62
3.2.2 Particle size	64
3.2.3 Density	64
3.2.4 Electron microscopy analysis	64
3.2.4.1 Preparation of samples	65
3.2.4.2 Morphological parameters	65
3.3 Experimental results	68
3.3.1 Lanthanum Silicates	68
3.3.1.1 Density	68
3.3.1.2 X-Ray Diffraction analysis	68
3.3.1.3 Particle size	70
3.3.1.4 Microstructural analysis	72
3.3.2 Yttrium-doped Barium Zirconate	75
3.3.2.1 Density	75
3.3.2.2 X-ray diffraction analysis	75
3.3.2.3 Particle size	78
3.3.2.4 Microstructural analysis	79
3.3.3 Yttrium-doped Barium Zirconate after NiO-extraction	82
3.3.3.1 Density	82
3.3.3.2 X-ray diffraction analysis	82
3.3.3.3 Microstructural analysis	85
3.4 References	87

3.1 INTRODUCTION

This chapter presents the different techniques used for the characterization of the nanopowders and sintered materials: particle size analysis by laser diffraction, structural analysis by X-Ray diffraction (XRD), scanning electron microscopy (SEM) and transmission electron microscopy (TEM). The experimental results are also presented and compared to literature data.

3.2 CHARACTERIZATION TECHNIQUES

3.2.1 X-Ray Diffraction

X-ray diffraction is a highly accurate, versatile and non-destructive structural characterization technique, which has been used to identify the crystalline phases present in both the prepared powders and the fabricated materials. XRD analysis was performed in air at room temperature using a Bruker Advance D2 diffractometer (X-ray Laboratory, SPMS, CentraleSupélec, France) in a Bragg-Brentano configuration and equipped with x-flash detector for X-ray fluorescence (XRF) measurements. The wavelength used was Cu-K α ($\lambda = 1.54060 \text{ \AA}$) filtered with nickel. Data were collected in the 2θ region between 20° and 130° with a step size of 0.02° and 10 s/step of acquisition.

The crystalline phases were identified with the aid of EVA 2 (Bruker AXS) and the database PDF-2002 (International Centre for Diffraction Data, ICDD). **Table 3.1** shows the XRD patterns used in this work. Then, XRD spectra were analyzed by the Le Bail refinement method [1] using the TOPAS 4.2 Bruker AXS software package.

Table 3.1. X-ray diffraction patterns used in the identification of the crystalline phases (PDF-2002).

ID pattern	Space group	Cell parameters			Volume (\AA^3)	
		a (\AA)	b (\AA)	c (\AA)		
49-0443	La _{9.33} Si ₆ O ₂₆	Hexagonal <i>P6₃/m</i>	9.71	-	7.19	587.08
04-015-2511	BaZr _{0.8} Y _{0.2} O _{3-δ}	Cubic <i>Pm$\bar{3}$m</i>	4.22	-	-	75.18
41-0463	BaY ₂ NiO ₅	Orthorhombic <i>Immm</i>	3.76	5.76	11.33	245.47
04-0835	NiO	Cubic <i>Fm-3m</i>	4.18	-	-	72.87

In the Le Bail method, the lattice parameters and the space group of the material must be predetermined since they are required for the fitting. The parameters to be fitted are the unit cell

dimensions, the instrumental zero error and the peak shape/width; the reflection intensities are however not calculated from the cell content but adjusted automatically at each refinement step. Once these magnitudes have been refined, the intensities at each point are determined, and used in turn as input intensities for the next fitting cycle. The number of free variables for the Le Bail fitting procedure is, therefore, independent of the number of reflections in the diffraction pattern, significantly shortening the calculation time.

The refinement quality is assessed by different R-factors, which measure how well the calculated model fits the observed intensities and how well the background, diffraction positions and shape of peaks have been fitted. The commonly used R-factors in the refinement are [2, 3]:

· R - weighted pattern, R_{wp} : reflects the progress of the refinement (the numerator of this expression is precisely the residue function to be minimized). It is defined by:

$$R_{wp} = \left[\frac{\sum_i w_i \cdot (Y_i^{obs} - Y_i^{calc})^2}{\sum_i w_i \cdot (Y_i^{obs})^2} \right]^{\frac{1}{2}} \quad (3.1)$$

where w_i , Y_i^{obs} and Y_i^{calc} are the statistical weight, observed intensity at the i^{th} step and calculated intensity at the i^{th} step, respectively.

· R - expected, R_{exp} : reflects the quality of the experimental data. It is defined by:

$$R_{exp} = \left[\frac{(N-P)}{\sum_i w_i \cdot (Y_i^{obs})^2} \right]^{\frac{1}{2}} \quad (3.2)$$

where N and P are the number of points and number of parameters, respectively.

· Goodness of Fit, GOF or χ^2 : reflects the overall goodness of the fit, and it is given by:

$$GOF = \chi^2 = \frac{R_{wp}}{R_{exp}} = \left[\frac{\sum_i w_i \cdot (Y_i^{obs} - Y_i^{calc})^2}{N-P} \right]^{\frac{1}{2}} \quad (3.3)$$

This factor is unity for an ideal model.

· R-Bragg factor, R_{Bragg} : reflects the quality of the agreement between the observed and computed reflections and it is defined by:

$$R_{Bragg} = \frac{\sum_k |Y_k^{obs} - Y_k^{calc}|}{\sum_k Y_k^{obs}} \quad (3.4)$$

where Y_k^{obs} and Y_k^{calc} are the observed and calculated intensities of the k^{th} reflection at the completion of refinement procedure, respectively. Good agreement between observed and computed reflections results in a small value of the R_{Bragg} index.

3.2.2 Particle size

The particle size distribution of the calcined powders was measured using a Malvern Zetasizer Nano ZS particle size analyzer (Functional Characterization Service, CITIUS, University of Sevilla, Spain), which allows the determination of particle diameters in the range 0.6 nm - 6 μ m. This equipment uses the low angle laser light scattering technique to measure particle sizes through the intensity and angle of the dispersed beams by the suspended particles in a given medium. For the measurements, a suspension of 0.5 g of calcined powder in 25 ml of ethanol was prepared under 30 min-ultrasonication.

3.2.3 Density

The density of the sintered compounds was determined by two different ways. On the one hand, by direct measurement of mass and dimensions, using a balance and a caliper, respectively. On the other hand, using the Archimedes' method, by means of an analytical balance equipped with a hydrostatic weighing accessory. The measurements were performed at ambient conditions using distilled water as immersion medium. The density was then calculated by the following equation:

$$\rho = \frac{W_d \cdot \rho_{H_2O}}{W_w - W_i} \quad (3.5)$$

where W_d , W_w and W_i are the weight in dry, wet, and immersion conditions, respectively, and ρ_{H_2O} is the water density at room-temperature.

Finally, the relative density was obtained from the theoretical density.

3.2.4 Electron microscopy analysis

The microstructural characterization of the materials was performed using a high-resolution FEI Teneo scanning electron microscope, equipped with an X-ray dispersive energy microanalysis system (EDS, Energy Dispersive X-ray Spectroscopy), and also with a FEI Talos transmission electron microscope operating at 200 kV voltage (Microscopy Service, CITIUS, University of Seville).

3.2.4.1 Preparation of samples

For SEM observations, sintered samples were carefully polished using SiC papers (1500 grit and 2500 grit, Buehler), and then ultrasonically cleaned in acetone for 15 min. After polishing, and in order to reveal grain boundaries, the samples were thermally etched at a temperature 20% below the sintering temperature for 3 hours and then mounted on aluminum holders using carbon paper. It was not necessary to deposit any conductive coating on the surface of the sample due to the low voltage used (1 - 5 kV).

For TEM observations, the samples were cut into thin slices of less than 100 μm -thickness using a high precision diamond saw. Afterwards, the slices were polished down to 50 μm and then dimpled using a dimple grinder to less than 20 μm -thickness in the center of the disc. Finally, the slices were ion-milled using argon at low incidence angles until a hole was formed.

3.2.4.2 Morphological parameters

The most relevant morphological parameters taken into account for the microstructural characterization of the different materials were the grain size d , the form factor F and the orientation angle θ of the grains. These parameters were measured from SEM micrographs using the Image J semiautomatic image analyzer software averaging over more than 500 grains on each material.

3.2.4.2.1 Grain size

The grain size has been taken as the equivalent planar diameter d , defined by:

$$d = \left(\frac{4 \cdot \text{Area}}{\pi} \right)^{\frac{1}{2}} \quad (3.6)$$

where *Area* is the measured grain surface.

It has been found (see later in this Chapter) that the grain size distributions are consistent with a lognormal law, as found in many other ceramics [4]. The lognormal distribution law is given by [5, 6]:

$$f(d|\mu, \sigma) = \frac{1}{\sqrt{2\pi\sigma^2}} \frac{1}{d} \exp \left[-\frac{\ln^2(d/\mu)}{2\sigma^2} \right] \quad (3.7)$$

with the normalization condition:

$$\int_0^{\infty} f(d|\mu, \sigma) d(d) = 1 \quad (3.8)$$

The parameters μ and σ are related to the mean grain size \bar{d} and its standard deviation σ_d by:

$$\bar{d} = \mu \cdot \exp\left(\frac{\sigma^2}{2}\right) ; \quad \sigma_d = \mu \cdot \exp\left(\frac{\sigma^2}{2}\right) \left[\exp(\sigma^2) - 1\right]^{\frac{1}{2}} \quad (3.9)$$

The parameters μ and σ of the lognormal distribution that best fit a set of experimental results are easily obtained from the representation of the accumulated fraction of grains n versus grain size d . This fraction is given by:

$$n = \int_0^d f(x) dx \quad (3.10)$$

which, for a lognormal distribution, results:

$$n = \frac{1}{\sqrt{2\pi\sigma^2}} \int_0^d \frac{1}{x} \exp\left[-\frac{\ln^2(x/\mu)}{2\sigma^2}\right] dx \quad (3.11)$$

By making the substitution:

$$u(x) = \frac{1}{\sigma} \ln\left(\frac{x}{\mu}\right) ; \quad du = \frac{1}{\sigma_x} dx \quad (3.12)$$

Equation 3.11 is rewritten as:

$$n = \frac{1}{\sqrt{2\pi}} \int_{-\infty}^{u(d)} \exp\left(-\frac{u'^2}{2}\right) du' \quad (3.13)$$

Equivalently:

$$n = Z\left[\frac{1}{\sigma} \ln\left(\frac{d}{\mu}\right)\right] \quad (3.14)$$

where $Z(y)$ is the error function given by:

$$Z(y) = \frac{1}{\sqrt{2\pi}} \int_{-\infty}^y \exp\left(-\frac{u^2}{2}\right) du \quad (3.15)$$

Inverting this equation, finally results in:

$$Z^{-1}(n) = \frac{1}{\sigma} \ln\left(\frac{d}{\mu}\right) = \frac{1}{\sigma} \ln d - \frac{1}{\sigma} \ln \mu \quad (3.16)$$

The plot of $Z^{-1}(n)$ versus $\ln(d)$ is therefore a straight line, called Henry's line, which can be written as:

$$Z^{-1}(n) = A \ln(d) + B \rightarrow \sigma = \frac{1}{A} ; \mu = \exp\left(-\frac{B}{A}\right) \quad (3.17)$$

where $\ln(\mu)$ is the average value of $\ln(d)$, $\ln(\mu) = \overline{\ln(d)}$, and σ is the standard deviation of $\ln(d)$.

The mean value of \bar{d} and its standard deviation σ_d (Equation 3.9) can also be easily expressed as a function of the parameters A and B of the Henry's line:

$$\bar{d} = \exp\left(-\frac{B}{A} + \frac{1}{2A^2}\right) ; \sigma_d = \exp\left(-\frac{B}{A} + \frac{1}{2A^2}\right) \left[\exp\left(\frac{1}{A^2}\right) - 1 \right]^{\frac{1}{2}} \quad (3.18)$$

3.2.4.2.2 Form factor

The form factor is a dimensionless parameter which gives quantitative information of the grain shape. It is defined as:

$$F = \frac{4 \pi \text{ Area}}{(\text{Grain perimeter})^2} \quad (3.19)$$

It has a maximum value of 1 for a circle and 0 for a segment. For polygonal grains with N sides, it is easily found that:

$$F = \frac{\pi/N}{\text{tg}(\pi/N)} \quad (3.20)$$

3.2.4.2.3 Orientation angle

The orientation angle of a grain, θ , is defined as the orientation of the largest diameter of the grain relative to a direction of reference. For non-circular grains, the distribution of this parameter gives information about the preferential alignment of the grains.

3.3 EXPERIMENTAL RESULTS

3.3.1 Lanthanum Silicates

3.3.1.1 Density

By using the theoretical density of $\text{La}_{9.33}\text{Si}_6\text{O}_{26}$, 5300 kg/m^3 , relative density values higher than 95% (required for the desired application) were achieved by the two different routes chosen for the material preparation.

Table 3.2. Relative densities of $\text{La}_{9.33}\text{Si}_6\text{O}_{26}$ compounds.

Material	Synthesis	Sintering	Relative density (%)	
			Mass / volume	Archimedes
LSO-CS	Freeze-drying	CS at $1500 \text{ }^\circ\text{C}$	97.1 ± 0.8	96.7 ± 0.2
LSO-SPS	Freeze-drying	SPS at $1250 \text{ }^\circ\text{C}$	99.6 ± 0.4	100.0 ± 0.2

Table 3.2 shows that the combination of freeze-drying and spark plasma sintering yields higher densities than conventional sintering and allows to obtain fully dense compounds (almost 100% of the theoretical density). These results are in accordance with what was reported by Chesnaud *et al.* [7] in a previous work following the same fabrication routes.

3.3.1.2 X-Ray Diffraction analysis

Calcined nanopowders

Identification of the crystalline phases was performed at room temperature using X-ray diffraction (XRD) and the diffraction patterns of the PDF-2002 database collected in **Table 3.1**.

Figure 3.1 displays the XRD pattern of the powder obtained after calcination. Comparison with PDF-2002 reference patterns confirms the presence of $\text{La}_{9.33}\text{Si}_6\text{O}_{26}$ single phase ($P6_3/m$). The crystallites size was estimated to be about 80 - 90 nm from the diffraction peaks width by using the Scherrer equation.

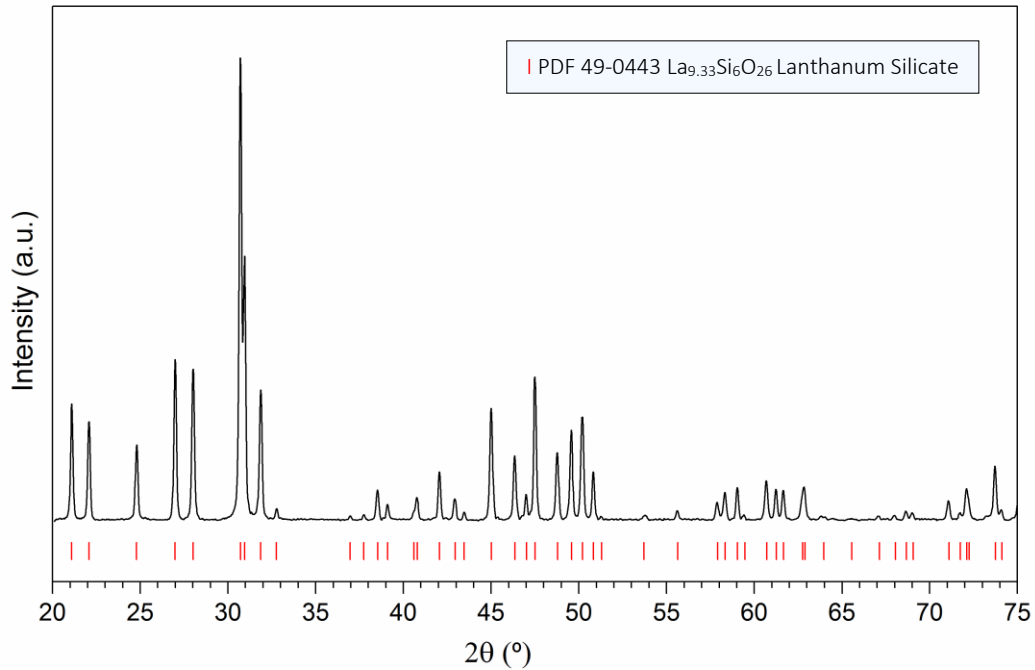


Figure 3.1. XRD pattern of calcined LSO powder (black). PDF-2002 XRD pattern of $\text{La}_{9.33}\text{Si}_6\text{O}_{26}$ (red).

Le Bail fitting of diffraction patterns was carried out using the space group $P6_3/m$ and the initial unit cell parameters $a = 9.728(6)$ Å and $c = 7.190(4)$ Å reported by León-Reina *et al.* [8].

Table 3.3. Refined cell parameters of $\text{La}_{9.33}\text{Si}_6\text{O}_{26}$ calcined powders.

Material	a (Å)	b (Å)	c (Å)	V (Å ³)	R _{wp}	GOF	R _{Bragg}
$\text{La}_{9.33}\text{Si}_6\text{O}_{26}$	9.729(3)	-	7.183(2)	588.76(4)	11.12	1.10	0.415

Refined cells parameters, gathered in **Table 3.3**, are similar to those found in the literature for the calcined powder. For example, Célérier *et al.* [9] reported unit cell parameters for $\text{La}_{9.33}\text{Si}_6\text{O}_{26}$ of $a = 9.726(3)$ Å and $c = 7.184(5)$ Å, while Kolisch *et al.* [10] have presented values of $a = 9.713(5)$ Å and $c = 7.186(5)$ Å.

Sintered ceramics

After sintering, both LSO-CS and LSO-SPS materials present a single lanthanum silicate crystalline phase. In order to obtain a more detailed structural information, Le Bail fitting of the diffraction patterns was carried out in the $P6_3/m$ space group taking into account once again the structural description given by León-Reina *et al.* [8]. **Figure 3.2** shows XRD patterns of LSO-CS and LSO-SPS sintered ceramics. Bragg angle positions corresponding to the structure are indicated by red vertical bars.

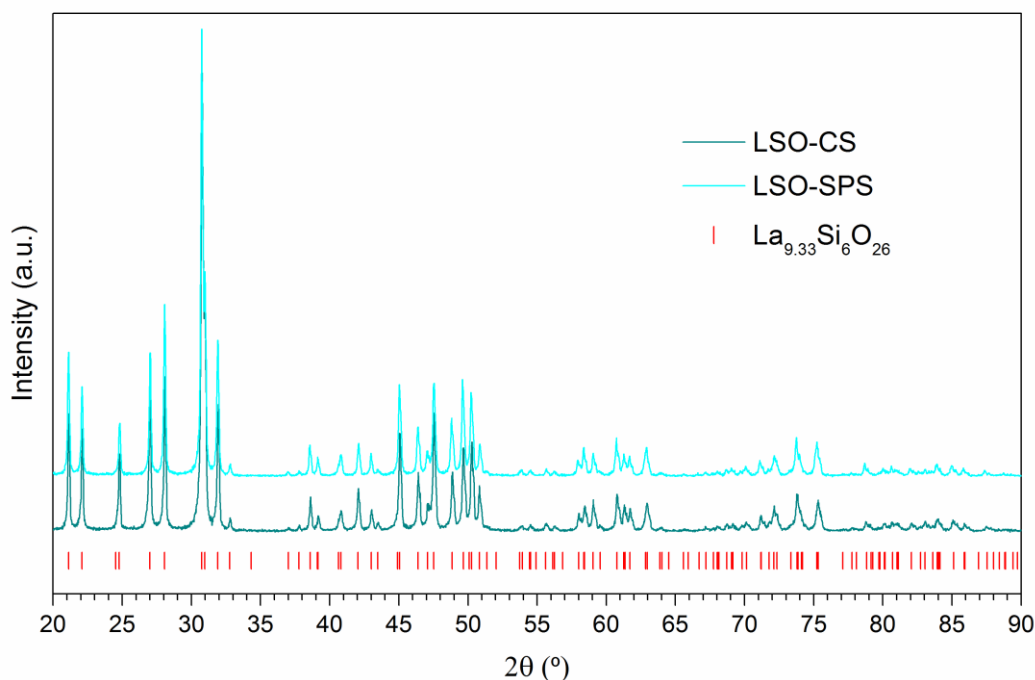


Figure 3.2. X-ray diffraction diagram for $\text{La}_{9.33}\text{Si}_6\text{O}_{26}$ sintered ceramics.

The refined parameters deduced from the Le Bail method are summarized in **Table 3.4**, which are in good agreement with literature data for $\text{La}_{9.33}\text{Si}_6\text{O}_{26}$ ceramics [7, 10-13]. For instance, Sansom *et al.* [14] found $a = 9.721(3)$ and $c = 7.187(3)$, similar to the present results.

Table 3.4. Refined cell parameters of $\text{La}_{9.33}\text{Si}_6\text{O}_{26}$ sintered compounds.

Material	a (Å)	b (Å)	c (Å)	V (Å ³)	R _{wp}	GOF	R _{Bragg}
LSO-CS	9.724(5)	-	7.186(4)	588.49(3)	12.22	1.38	0.627
LSO-SPS	9.723(6)	-	7.183(4)	588.01(8)	11.32	1.30	0.542

It can be thus conclude that the two sintered materials, LSO-CS and LSO-SPS, exhibit identical lattice parameters, which are indeed the same as in the original calcined powder (**Table 3.3**).

3.3.1.3 Particle size

Figure 3.3 shows the particle size distribution of the $\text{La}_{9.33}\text{Si}_6\text{O}_{26}$ as-obtained nanopowders after calcination, of five measurements, which yields an average particle size of 550 ± 60 nm, much larger than the mean value of 85 nm obtained by XRD. This difference, along with the microstructural results of the sintered material (presented later in section 3.3.1.4), which shows an average grain of about 200 nm, suggest that the sizes measured by the laser diffraction technique correspond to powder agglomerates and not to individual single-crystallite particles. To confirm

this result, an additional analysis of the powders was performed by transmission electron microscopy (TEM). To this end, several drops of the same suspension were placed on carbon-coated copper TEM grids (200 mesh). Observations were then performed on a Philips CM200 microscope (Microscopy Service, CITIUS, University of Sevilla, Spain) operating at 200 kV.

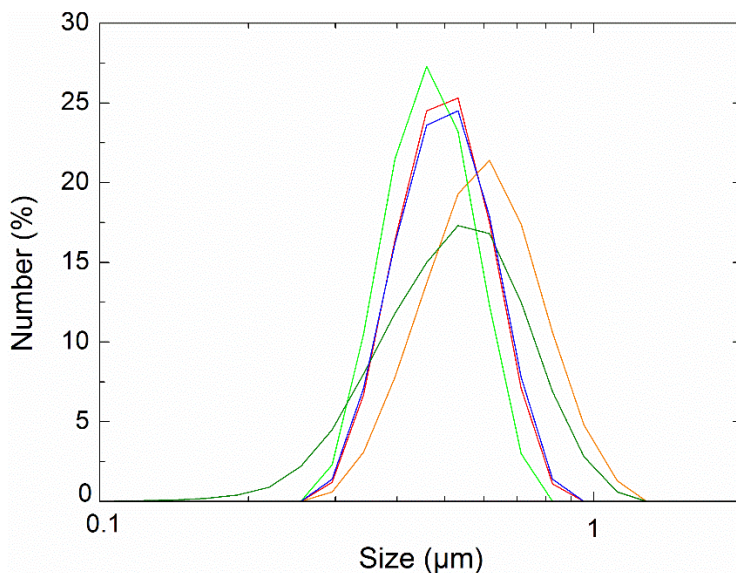


Figure 3.3. Particle size distribution of $\text{La}_{9.33}\text{Si}_6\text{O}_{26}$ as-obtained nanopowders after calcination.

The morphology of the $\text{La}_{9.33}\text{Si}_6\text{O}_{26}$ nanopowder is shown in **Figure 3.4**. It can be seen agglomerates of 300 - 800 nm, which consist of irregular particles of average size of about 100 nm. This value correlates well with the crystallite sizes calculated from XRD analysis, confirming the nanometric nature of the LSO powder. On the other hand, the size of the agglomerates observed by TEM agrees with the value measured by laser diffraction.

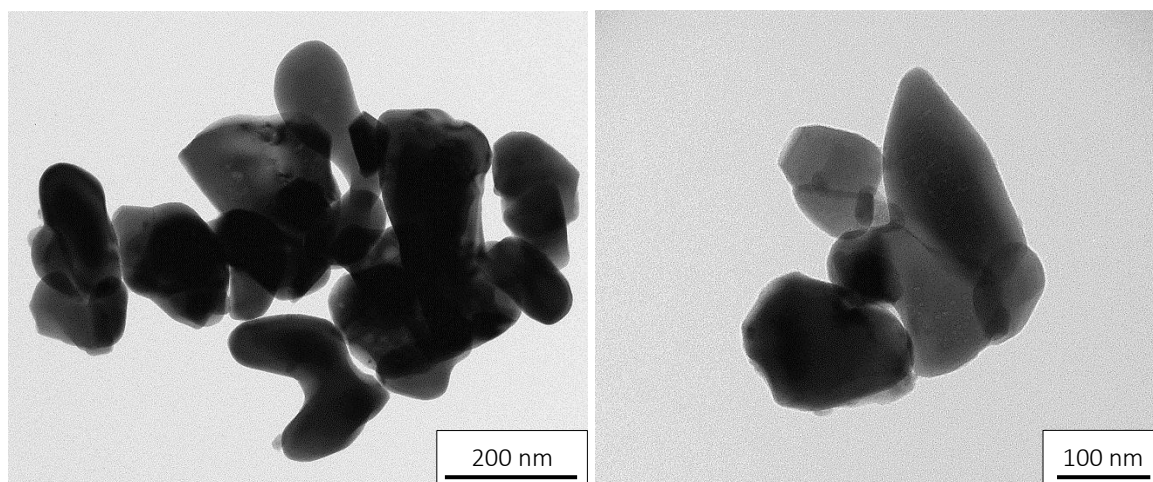


Figure 3.4. TEM micrographs of $\text{La}_{9.33}\text{Si}_6\text{O}_{26}$ as-obtained nanopowders after calcination.

3.3.1.4 Microstructural analysis

Figure 3.5 shows SEM micrographs of $\text{La}_{9.33}\text{Si}_6\text{O}_{26}$ sintered in air through conventional sintering at 1500 °C for 12 h. These images clearly reflect a homogenous and dense microstructure consisting of equiaxed grains with average sizes of about 1 μm and delimited by well-defined grain boundaries. Porosity is small in agreement with density measurements.

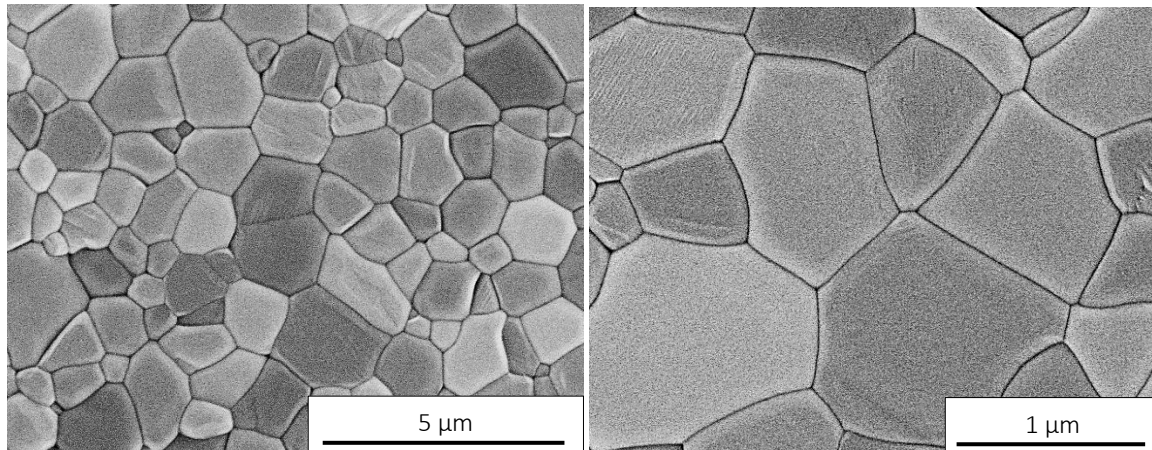


Figure 3.5. SEM micrographs of sintered LSO-CS compounds.

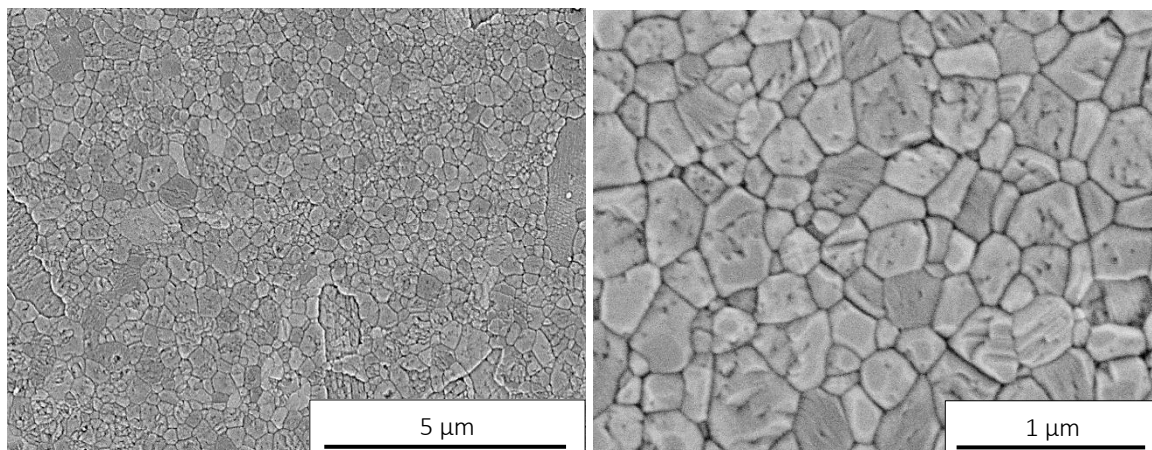


Figure 3.6. SEM micrographs of sintered LSO-SPS compounds.

Figure 3.6 shows SEM micrographs of $\text{La}_{9.33}\text{Si}_6\text{O}_{26}$ sintered in vacuum through spark plasma sintering at 1250° C for 5 min. These materials present a fine-grained microstructure consisting of equiaxed grains with grain sizes in the range 100 - 500 nm, with practically no porosity.

These results show a large difference in grain size between both materials, indicating the influence of the sintering method on the microstructure. The lower temperature and shorter sintering time used during SPS restrict strongly the grain growth.

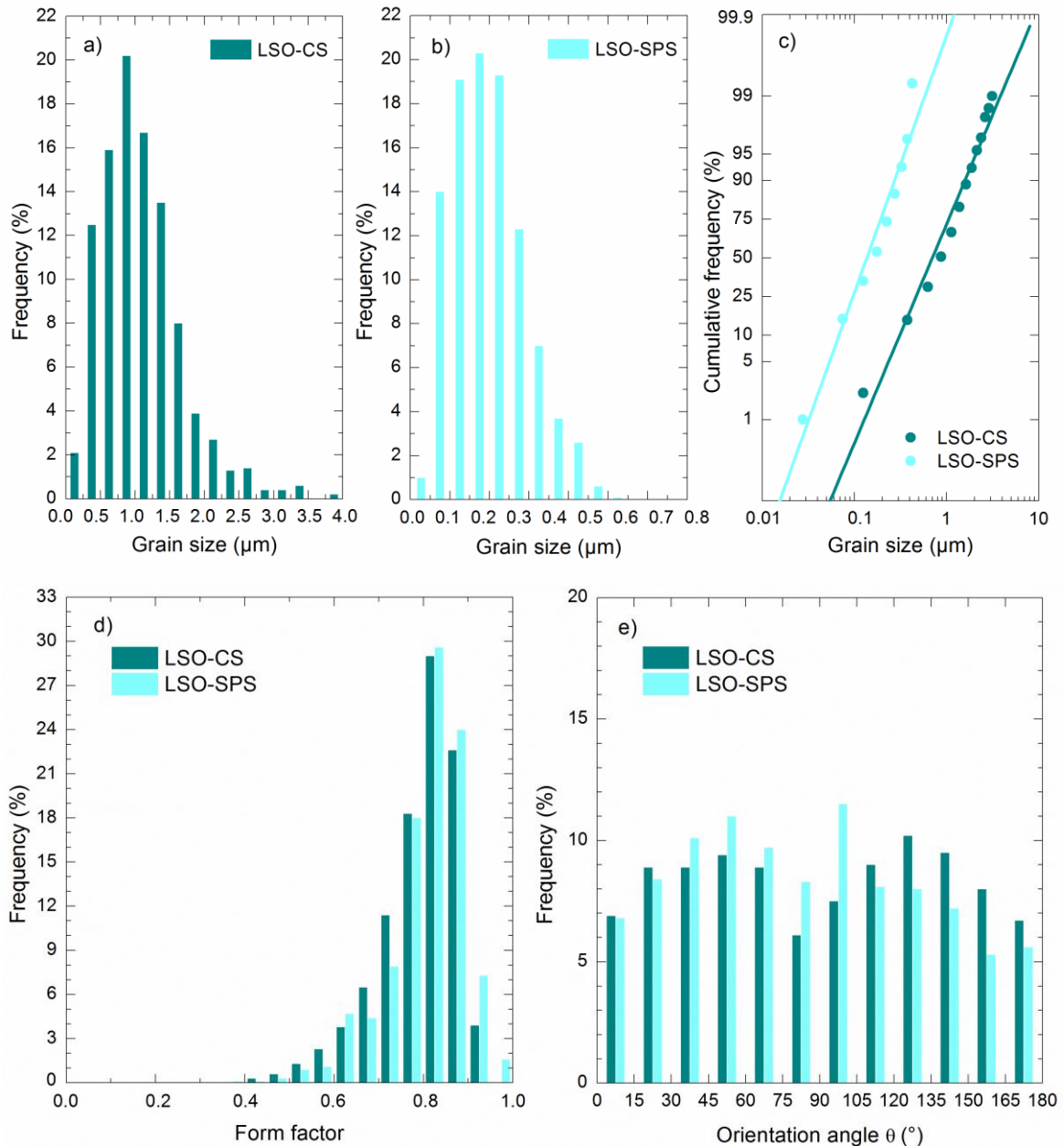


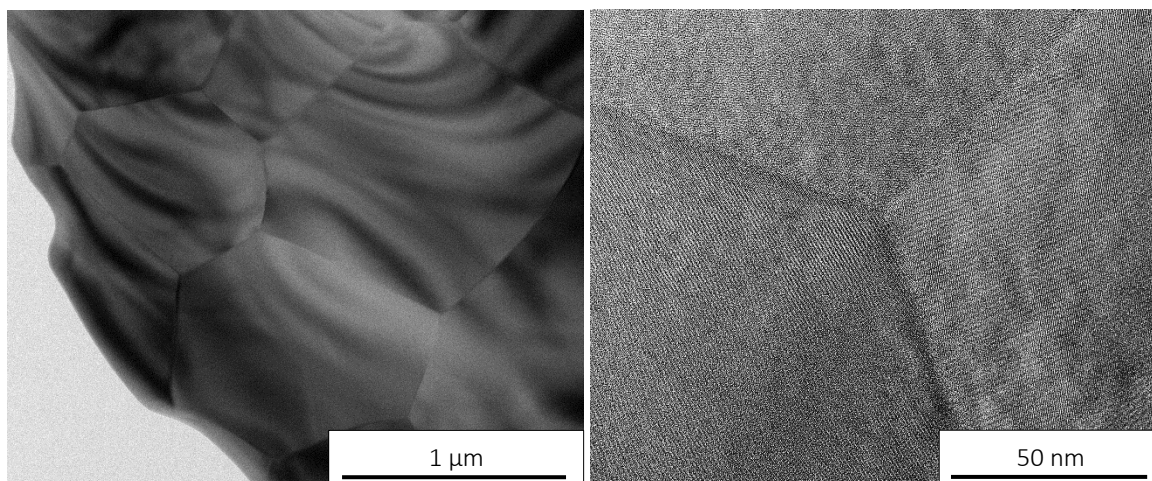
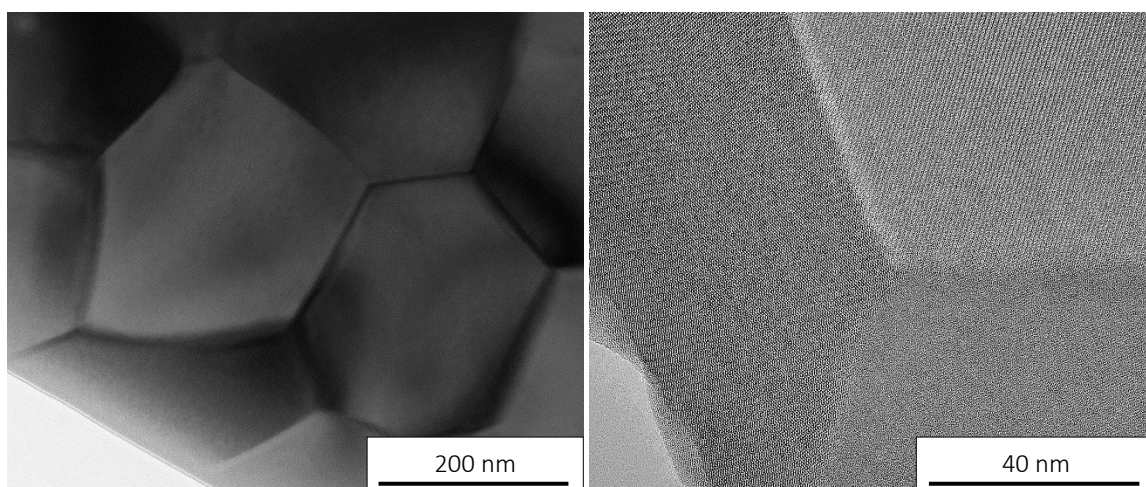
Figure 3.7. Morphological distributions of $\text{La}_{9.33}\text{Si}_6\text{O}_{26}$ compounds made from conventional sintering (LSO-CS) and Spark plasma sintering (LSO-SPS): (a) Grain size; (b) Henry's lines for the grain size distribution; (c) Form factor; (d) Orientation angles.

The morphological parameters d , F and θ of the different materials were measured from SEM micrographs and are summarized in **Table 3.5** and displayed in **Figure 3.7**. Though the grain size of LSO-CS is larger than LSO-SPS materials, they exhibit similar grain size-scaled distributions, corresponding to a lognormal law. Regarding the form factor F , both materials have equiaxed grains with average values of 0.8, which means a stable grain distribution. The absence of preferential directions in the polycrystal is also reflected in the orientation angle formed by the maximum diameter of the grain with an arbitrary direction. Average values, close to 90 $^\circ$ and standard deviation near 45 $^\circ$, indicate the absence of preferred directions in grain populations.

Table 3.5. Morphological parameters of $\text{La}_{9.33}\text{Si}_6\text{O}_{26}$ compounds: grain size d , grain size lognormal distribution parameters μ , σ , form factor F and orientation angle θ .

Material	\bar{d} (μm)	μ (μm)	σ (μm)	\bar{F}	θ ($^\circ$)
LSO-CS	1.1 ± 0.6	0.86	0.37	0.8 ± 0.1	90 ± 51
LSO-SPS	0.2 ± 0.1	0.18	0.32	0.8 ± 0.1	84 ± 47

TEM observations were carried out on both materials to complete the microstructural characterization. **Figure 3.8** and **Figure 3.9** show typical images of the internal structure of the grains in LSO-CS and LSO-SPS compounds, respectively. In both cases, the grains are generally free of defects, with clean and straight grain boundaries and well-defined triple points. No dislocations and secondary phase pockets were observed.

**Figure 3.8.** TEM images of sintered LSO-CS compounds.**Figure 3.9.** TEM images of sintered LSO-SPS compounds.

3.3.2 Yttrium-doped Barium Zirconate

3.3.2.1 Density

By using the theoretical density of 15% Yttrium-doped Barium Zirconate (6166 kg/m^3), the relative density of the BZY compound fabricated in this work is 97% (**Table 3.6**). The commercial material prepared with NiO as sintering aid shows a higher density, practically 100%, revealing the influence of sintering aids in densification, as it was already tested by Tong *et al.* [15] and Nikodemski *et al.* [16].

Table 3.6. Relative densities of $\text{BaZr}_{0.85}\text{Y}_{0.15}\text{O}_{2.925}$ compounds.

Material	Relative density (%)	
	Mass / volume	Archimedes
Home-made BZY	97.0 ± 0.5	97.2 ± 0.2
Commercial BZY-NiO	99 (Norecs TM)	

3.3.2.2 X-ray diffraction analysis

Calcined nanopowders

Crystalline phase identification was performed using X-ray diffraction and the diffraction patterns of the PDF-2002 database collected in **Table 3.1**. XRD diagrams of the nanopowders obtained after calcination show the presence of the single Y-doped BaZrO_3 perovskite phase (**Figure 3.10**) with the $Pm\bar{3}m$ space group. From peaks width, the crystallites size, estimated once again from the Scherrer law, is about 15 - 20 nm.

Le Bail fitting of these diffraction patterns was carried out using the $Pm\bar{3}m$ space group and the initial unit cell parameters $a = 4.221(3)$ reported by Nomura *et al.* [17]. Refined lattice parameters, gathered in **Table 3.7**, are comparable to the values found in the literature for substituted Barium Zirconate with a 15 % Y content calcined powders. For example, Iguchi *et al.* [18] found a cubic cell parameter $a = 4.216(1) \text{ \AA}$ slightly higher than the results of this work, while Duval *et al.* [19] have reported values slightly lower, $a = 4.19(3) \text{ \AA}$.

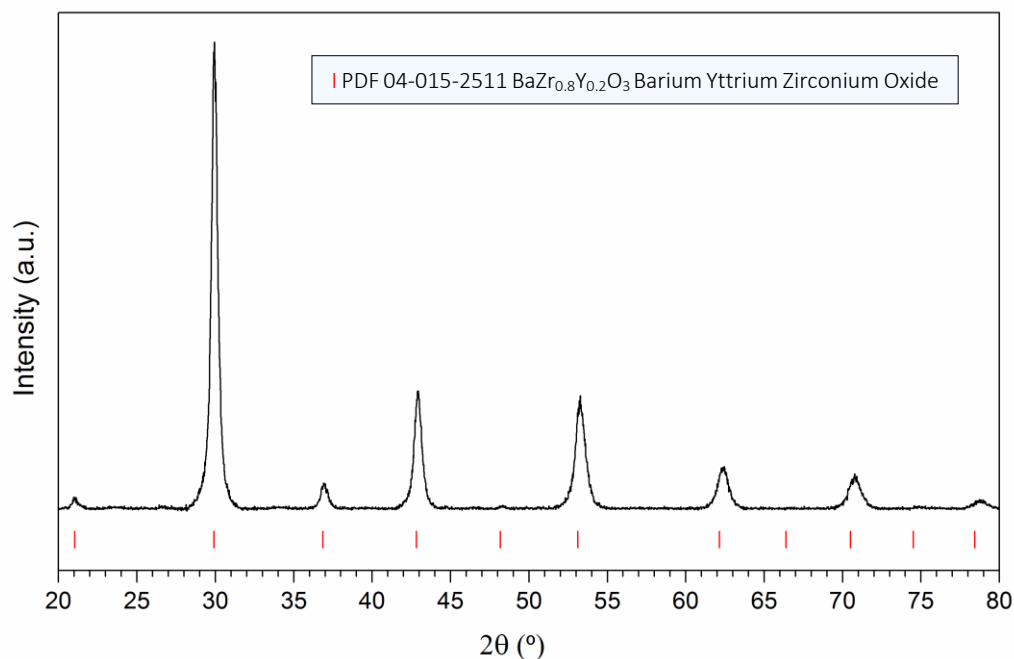


Figure 3.10. XRD diagram of BaZr_{0.85}Y_{0.15}O_{2.925} calcined powder (black). Bragg peaks positions of BaZr_{0.8}Y_{0.2}O₃ (red).

Table 3.7. Refined cell parameters of BaZr_{0.85}Y_{0.15}O_{2.925} calcined powder.

Material	a (Å)	V (Å ³)	R _{wp}	GOF	R _{Bragg}
BaZr _{0.85} Y _{0.15} O _{2.925}	4.203(1)	74.26(8)	12.74	1.36	0.854

Sintered ceramic

For the structural study of BaZr_{0.85}Y_{0.15}O_{2.925} sintered ceramics, first of all, the crystalline phases were identified by using the reference diffraction patterns gathered in **Table 3.1** and then, Le Bail fitting was applied to analyze the XRD data. **Figure 3.11** shows the diffraction data of the different materials. Bragg angle positions corresponding to the different structures are indicated by vertical bars. Whereas lab-made BZY exhibits only the single crystalline phase of yttrium-doped barium zirconate ($Pm\bar{3}m$), BZY-NiO also contains BaY₂NiO₅ ($Immm$) as shown in **Figure 3.11**. The overlap of BZY peaks with those of NiO makes difficult the identification of this last phase, however its presence should not be excluded.

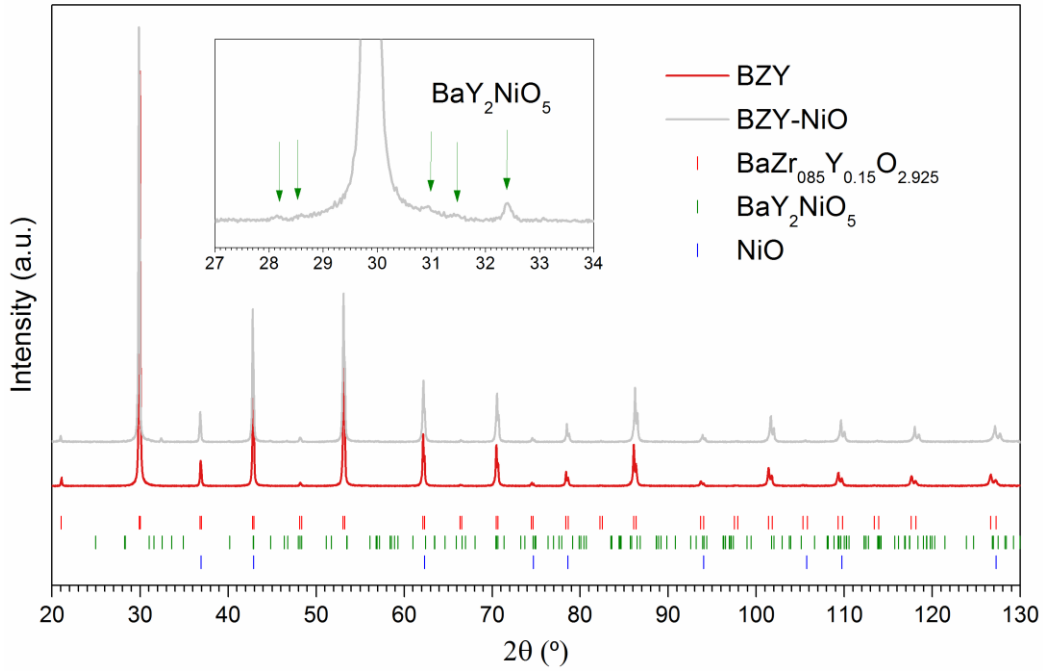


Figure 3.11. X-ray diffraction diagram for $\text{BaZr}_{0.85}\text{Y}_{0.15}\text{O}_{2.925}$ sintered ceramics.

The lattice parameters deduced from LeBail method are summarized in **Table 3.8**, which are in good agreement with the $\text{BaZr}_{0.85}\text{Y}_{0.15}\text{O}_{2.925}$ cell parameters reported in the literature (from 4.210 Å [20] to 4.2317(1) Å [21]). This seems to indicate that the NiO content slightly reduces the lattice structure of BZY. In this regard, Shafi et al. [22] also found a decrease in the cubic unit cell parameter with increasing in NiO content.

Table 3.8. Refined cell parameters of $\text{BaZr}_{0.85}\text{Y}_{0.15}\text{O}_{2.925}$ sintered compounds.

Material	a (Å)	V (Å ³)	R_{wp}	GOF	R_{Bragg}
BZY	4.223(2)	75.317(2)	10.09	1.20	0.656
BZY-NiO	4.212(6)	74.737(3)	13.11	1.32	1.027

Furthermore, it has been found an increase in the lattice parameters from $a = 4.203(1)$ Å in the calcined powder (**Table 3.7**) to $a = 4.223(2)$ Å after sintering (**Table 3.8**). A similar evolution of the lattice parameter was reported by Duval *et al.* [19] which was associated to the fact that, below 1250 °C, the formation reactions may not be completed leading to a BZY precursor with a smaller cell parameter after calcination at 1000 °C [23].

3.3.2.3 Particle size

The particle size of the calcined nanopowder was measured by laser diffraction and TEM. **Figure 3.12** shows the particle size distribution of the BZY powder obtained by laser diffraction from five measurements, yielding an average particle size of 530 ± 60 nm.

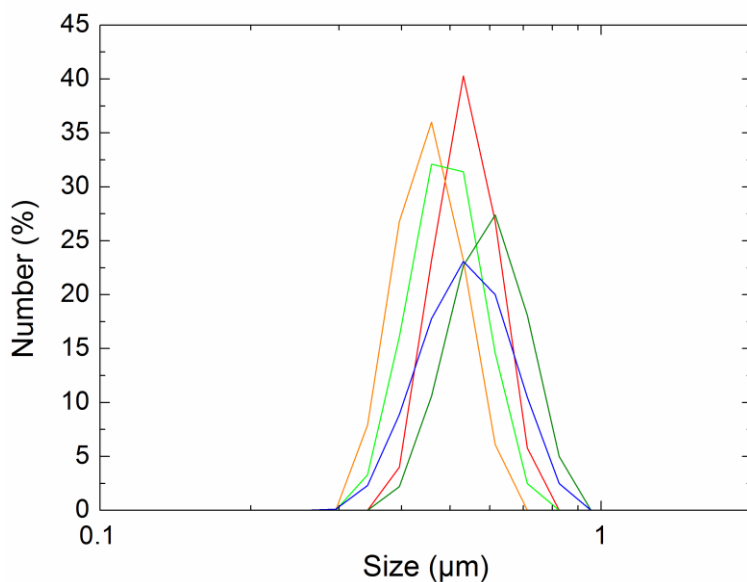


Figure 3.12. Particle size distribution of $\text{BaZr}_{0.85}\text{Y}_{0.15}\text{O}_{2.925}$ nanopowders as-obtained after calcination.

On the other hand, TEM analysis (**Figure 3.13**) shows that the nanopowders were strongly agglomerated. These agglomerates, of about 500 nm in size, consist of very small spherical particles between 10 and 40 nm. This particle size agrees with the value of the crystallite sizes calculated from XRD, confirming the nanometric nature of this powder.

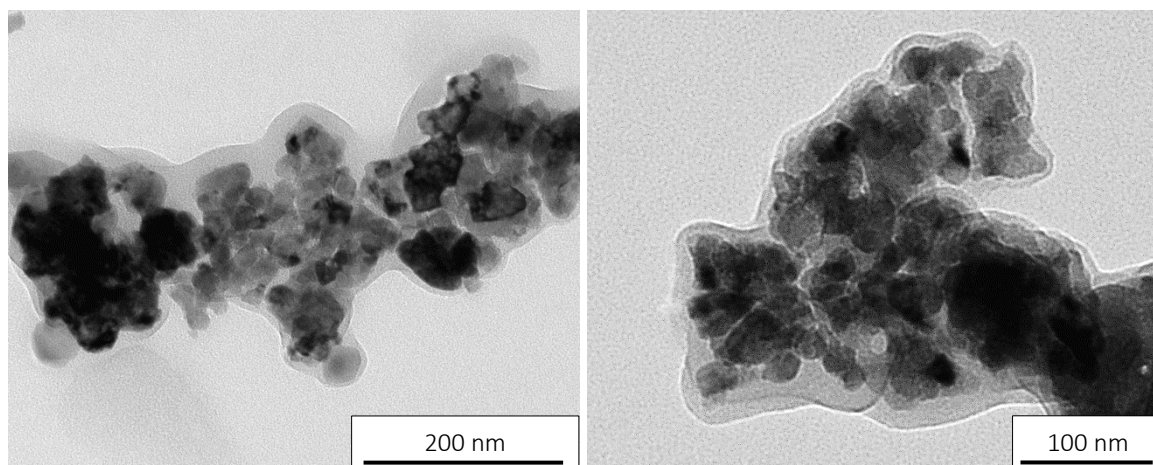


Figure 3.13. TEM micrographs of $\text{BaZr}_{0.85}\text{Y}_{0.15}\text{O}_{2.925}$ as-obtained nanopowders after calcination.

3.3.2.4 Microstructural analysis

Figure 3.14 shows SEM micrographs of BZY sintered in air by conventional sintering at 1600 °C for 24 h. The material presents a fine-grained microstructure consisting of equiaxed grains with grain sizes of about 200 nm. Porosity is small, according to density measurements, and consisted in small pores below 100 nm in size, preferably located at multiple grain junctions.

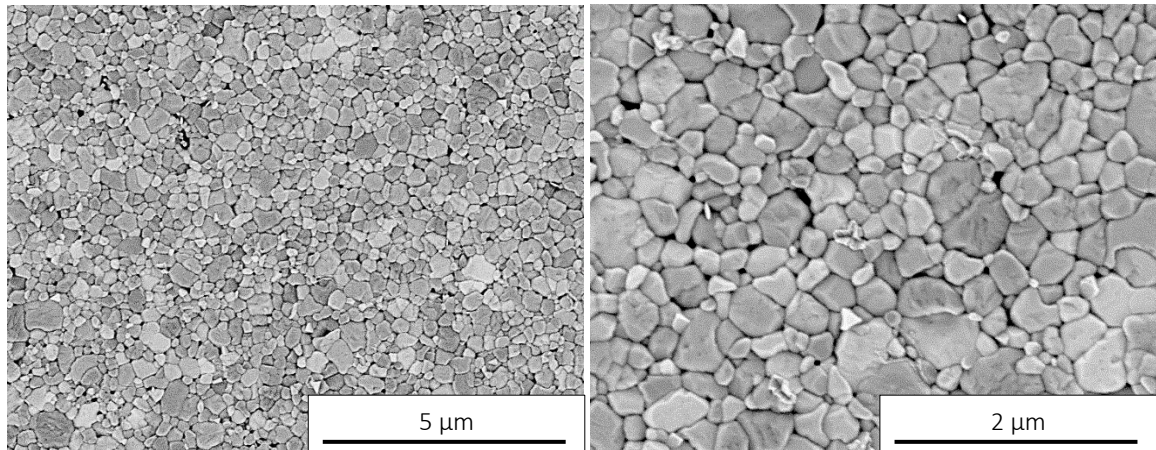


Figure 3.14. SEM micrographs of sintered lab-made BZY compounds.

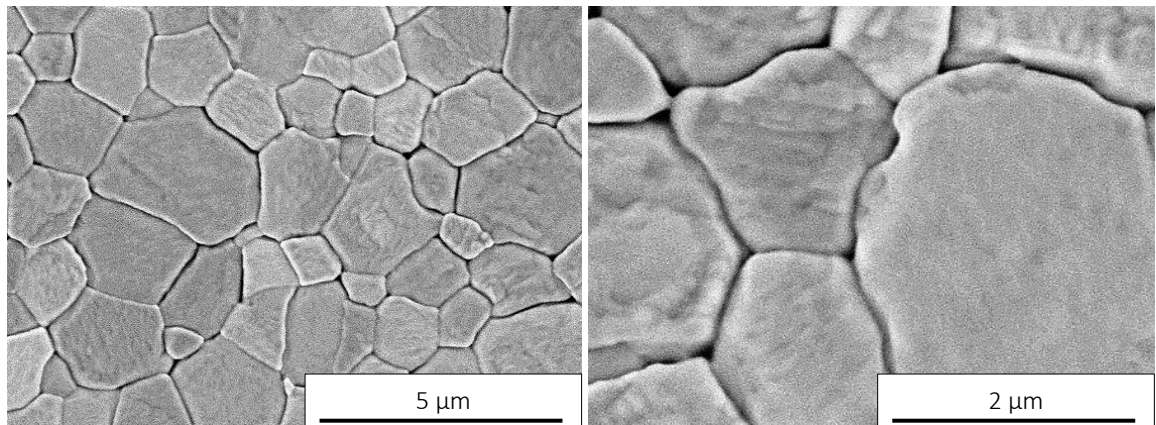


Figure 3.15. SEM micrographs of sintered commercial BZY-NiO compounds.

Figure 3.15 shows SEM micrographs of BZY-NiO commercial material. These images clearly reflect a homogenous and dense microstructure consisting of equiaxed grains with average sizes in the range 1 - 2 µm and delimited by well-defined grain boundaries, with practically no porosity.

These results show a large difference in grain size between both materials, indicating the influence of the additive in the diffusion process. Tong *et al.* [24] suggested that the enhancement of densification could be ascribed to the formation of BaY₂NiO₅ second-phase and its role as a sintering aid (see Section 2.3.5), while the significant grain growth is as a result of the melting of the BaY₂NiO₅ phase [24].

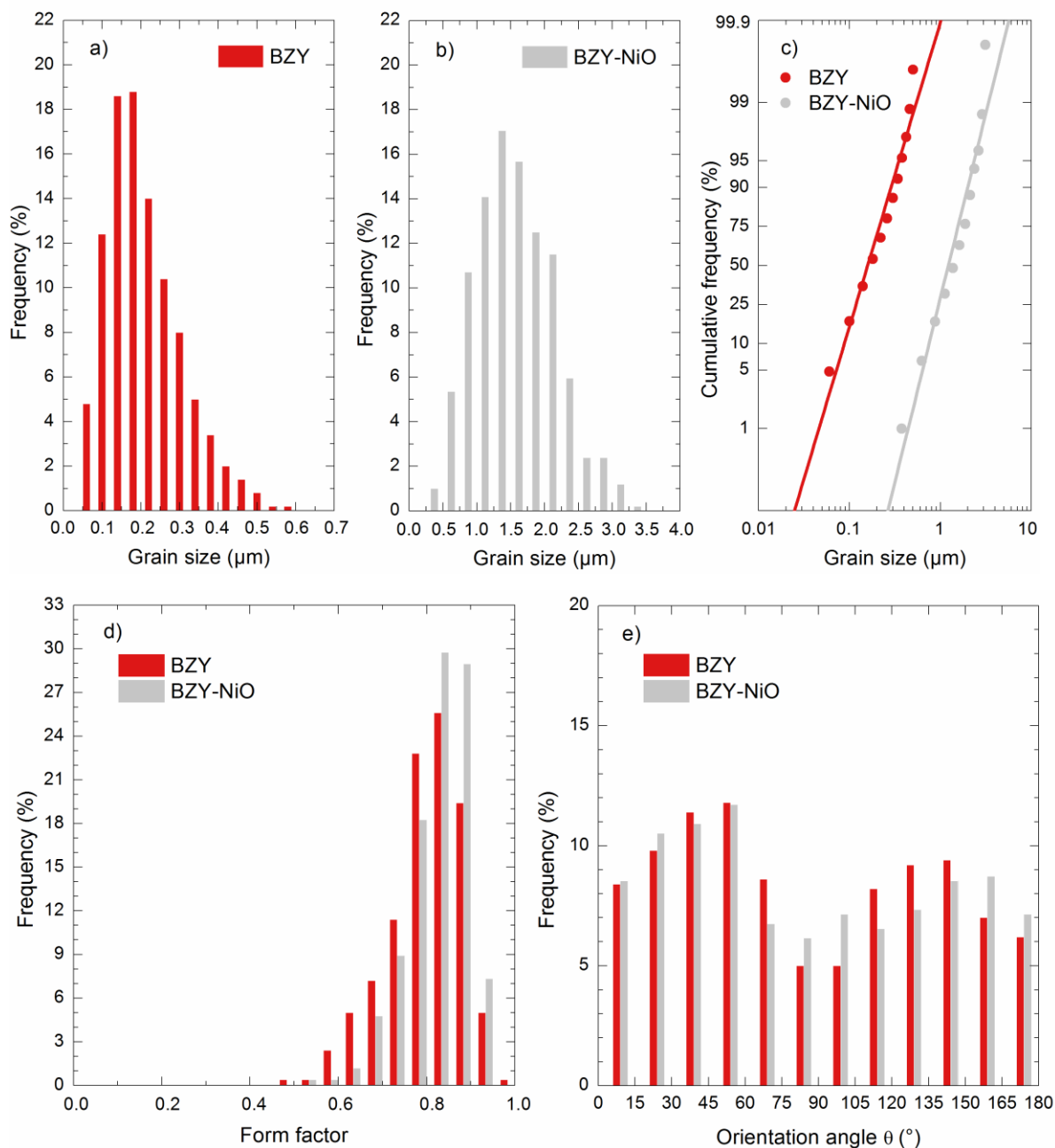


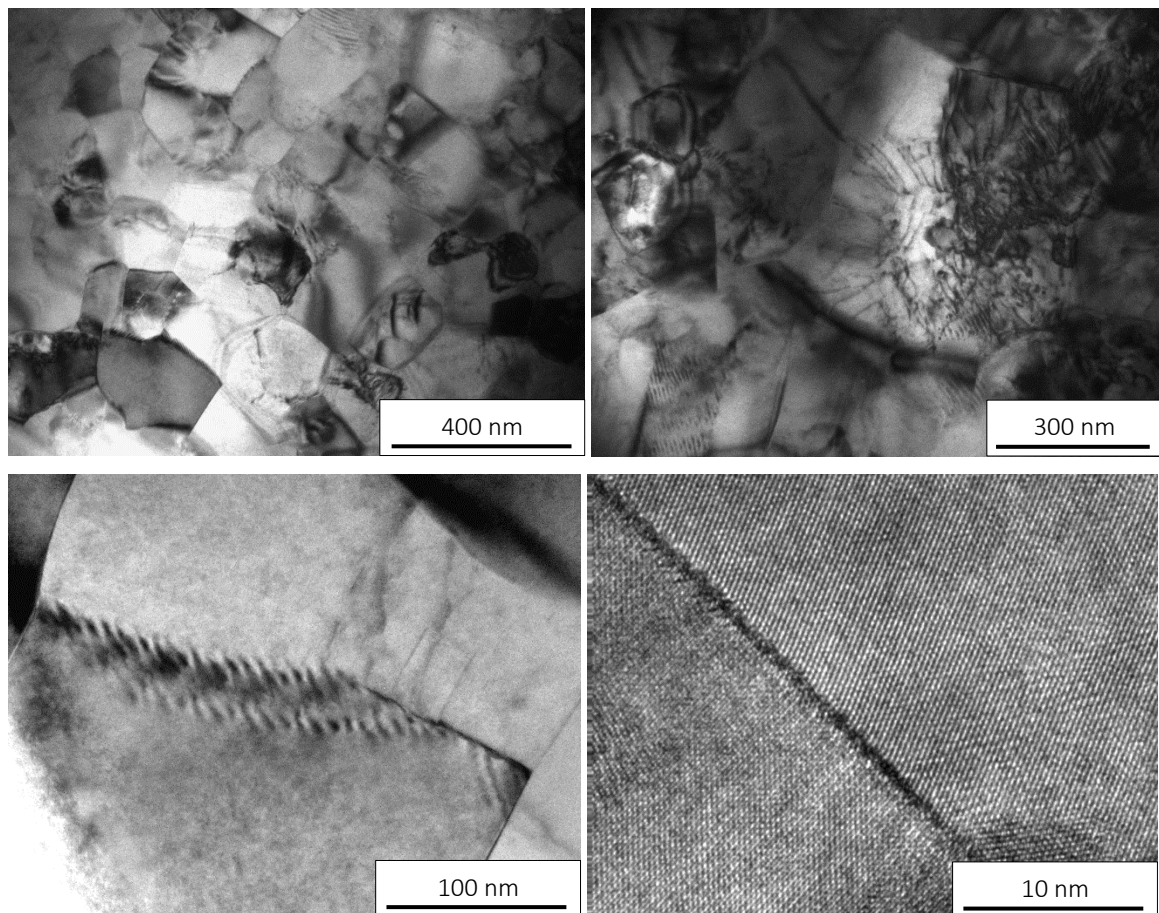
Figure 3.16. Morphological distributions of $\text{BaZr}_{0.85}\text{Y}_{0.15}\text{O}_{2.925}$ compounds: (a) Grain size; (b) Form factor; (c) Orientation angles; (d) Henry's lines for the grain size distribution.

The morphological parameters d , F and θ of the different materials were measured from SEM micrographs and are summarized in **Table 3.9** and displayed in **Figure 3.16**. All the compounds exhibit similar distributions, corresponding to a lognormal law. Regarding the form factor F , they have equiaxed grains with average values of 0.8, which means a stable grain size distribution. The absence of preferential directions in the polycrystal is also reflected in the orientation angle formed by the maximum diameter of the grain with an arbitrary direction. Average values close to 90° and standard deviation near 45° , indicate the absence of preferred directions in grain populations.

Table 3.9. Morphological parameters of $\text{BaZr}_{0.85}\text{Y}_{0.15}\text{O}_{2.925}$ compounds: grain size d , grain size lognormal distribution parameters μ , σ , form factor F and orientation angle θ .

Material	\bar{d} (μm)	μ (μm)	σ (μm)	\bar{F}	θ ($^\circ$)
BZY (lab-made)	0.2 ± 0.1	0.18	0.22	0.8 ± 0.1	84 ± 52
BZY-NiO (commercial)	1.6 ± 0.6	1.37	0.27	0.8 ± 0.1	85 ± 52

Finally, in order to complete the microstructural characterization, TEM observations were carried out on all the materials. **Figure 3.17** and **Figure 3.18** show typical images of the internal structure of the grains in the different compounds. Lab-made BZY grains are often very stressed, with dislocations arranged in dense tangles and also forming pile-ups and low-angles sub-boundaries. On the opposite, BZY-NiO grains are generally free of defects, with clean and straight grain boundaries and well-defined triple points.

**Figure 3.17.** TEM images of sintered lab-made BZY compounds.

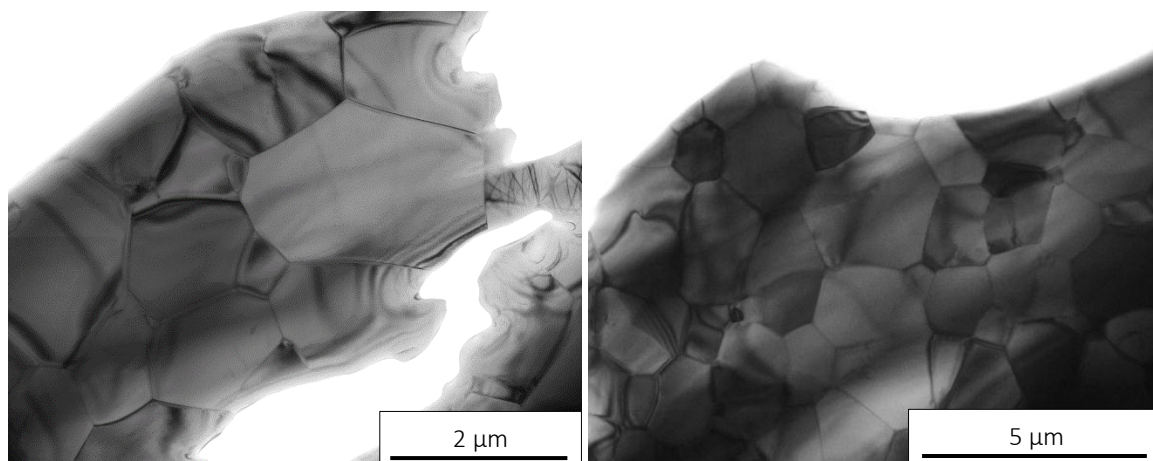


Figure 3.18. TEM images of sintered commercial BZY-NiO compounds.

3.3.3 Yttrium-doped Barium Zirconate after NiO-extraction

3.3.3.1 Density

By using the theoretical density of 15% Yttrium-doped Barium Zirconate (6166 kg/m^3), the relative density of BZY after NiO-extraction was $95.4 \pm 0.9 \%$ which contrast with the value of 99% of the material before the extraction process. This decrease in density reveals the influence of sintering aids in densification as it was already tested by Tong *et al.* [15] and Nikodemski *et al.* [16].

3.3.3.2 X-ray diffraction analysis

In order to ensure that the extraction process did not modify the Yttrium-doped Barium Zirconate crystalline phase, X-ray diffraction was performed and the data obtained were compared with that of BZY-NiO. **Figure 3.19** shows the XRD patterns of the different commercial BZY-NiO compounds where it can be observed that, in /BZY after NiO-extraction, all the peaks of the $\text{BaZr}_{0.85}\text{Y}_{0.15}\text{O}_{2.925}$ cubic phase are present. Moreover, in comparison with BZY-NiO, the extra peaks of BaY_2NiO_5 which come from the NiO used as additive in the sintering step have disappeared, as can be more easily observed in the magnified pattern of the **Figure 3.19**. The lattice parameter deduced from the Le Bail method for the material after NiO-extraction was $4.223 (3) \text{ \AA}$, the same value found for BZY and slightly higher than for BZY-NiO (**Table 3.8**).

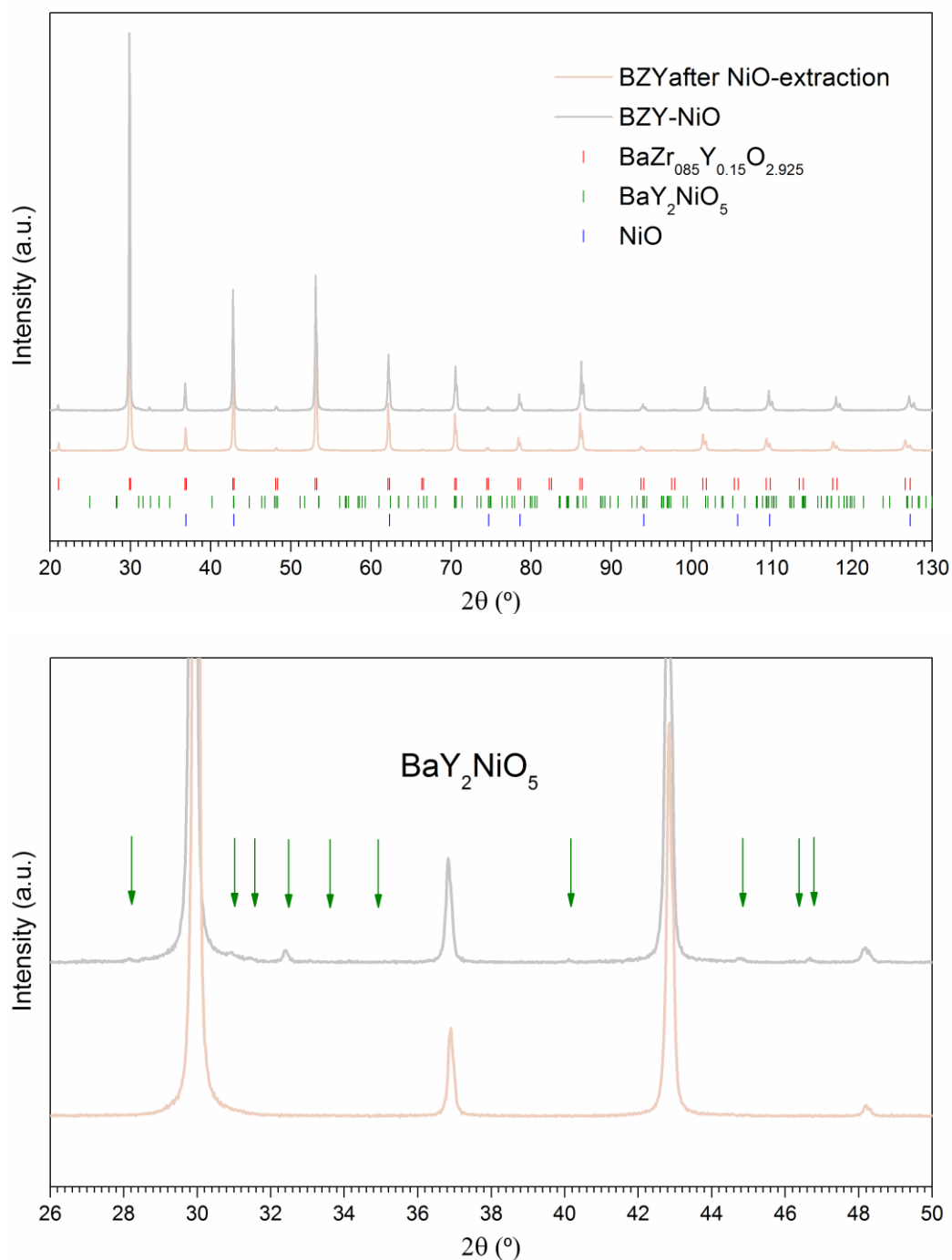


Figure 3.19. X-ray diffraction diagram of commercial BZY sintered ceramic. Full (upper) and magnified (lower) patterns.

Simultaneously with XDR, X-Ray Fluorescence (XRF) measurements were collected for BZY-NiO and BZY after NiO-extraction to identify the elemental composition of the samples. **Figure 3.20** shows the XRF spectra of both materials. No evidence of Ni after the NiO-extraction process was found, in agreement with the XRD measurements.

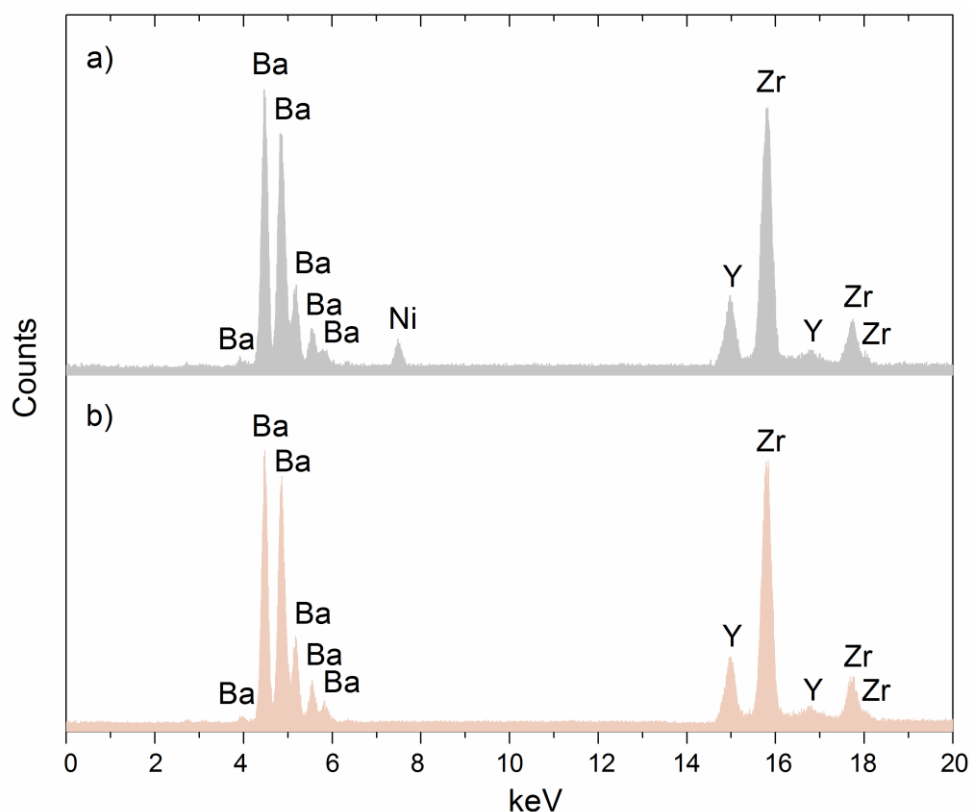


Figure 3.20. X-ray fluorescence analysis of BZY-NiO (a) before and (b) after NiO-extraction.

A magnetometry technique has been used in order to quantify any possible residual nickel content after NiO-extraction, not detected by XRD or XRF. This technique allows the measurement of ferromagnetic elements down to the parts per million level. To this end, the samples were annealed in a reducing atmosphere of 5% H₂/Ar at 800 °C for 24 hours, and then analyzed in a MPMS 5 Quantum Design magnetometer (Plateforme Technique de l'ICMMO, Magnetic measurements service, France) at 300 K under an uniform field of -60000 Oe to 60000 Oe.

Figure 3.21 shows the magnetization curves for the commercial material before and after the NiO-extraction. NIST standard of 54.888 emu/g-Ni was used to determine the amount of metallic Ni in the samples. In this way, the BZY-NiO after annealing had a magnetic moment of 0.155 emu/g-Ni, corresponding to an amount of metallic Ni of about 0.3 wt%, which is in roughly agreement with the NiO content of 1 wt% introduced in the process. On the contrary, the specimens after NiO-extraction exhibited a null magnetic moment, indicating the absence of Ni and therefore the success of the extraction process.

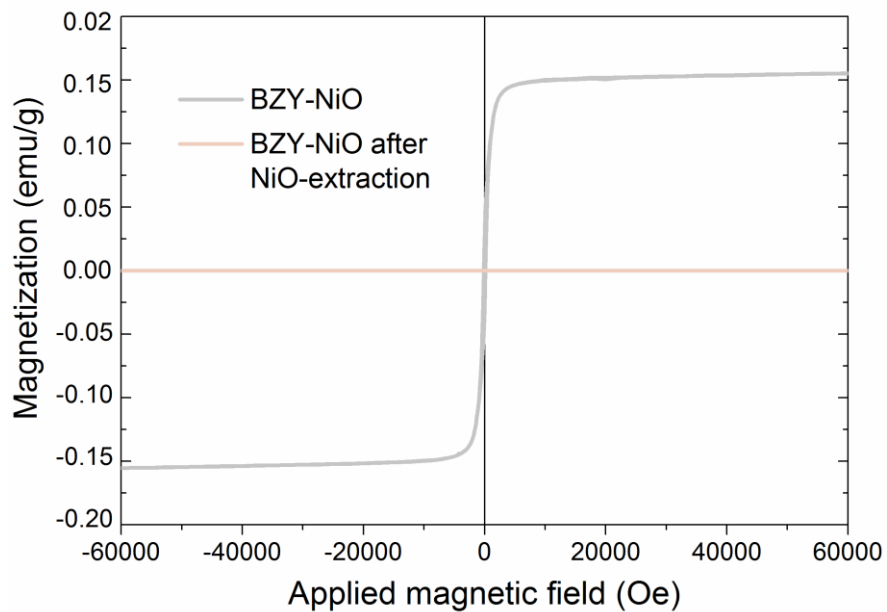


Figure 3.21. Magnetization curve for BZY-NiO before and after NiO-extraction.

3.3.3.3 Microstructural analysis

Figure 3.22 shows back-scattered electron images of BZY ceramic after NiO-extraction. This material presents a microstructure with equiaxed and large grains (from 2 to 20 μm).

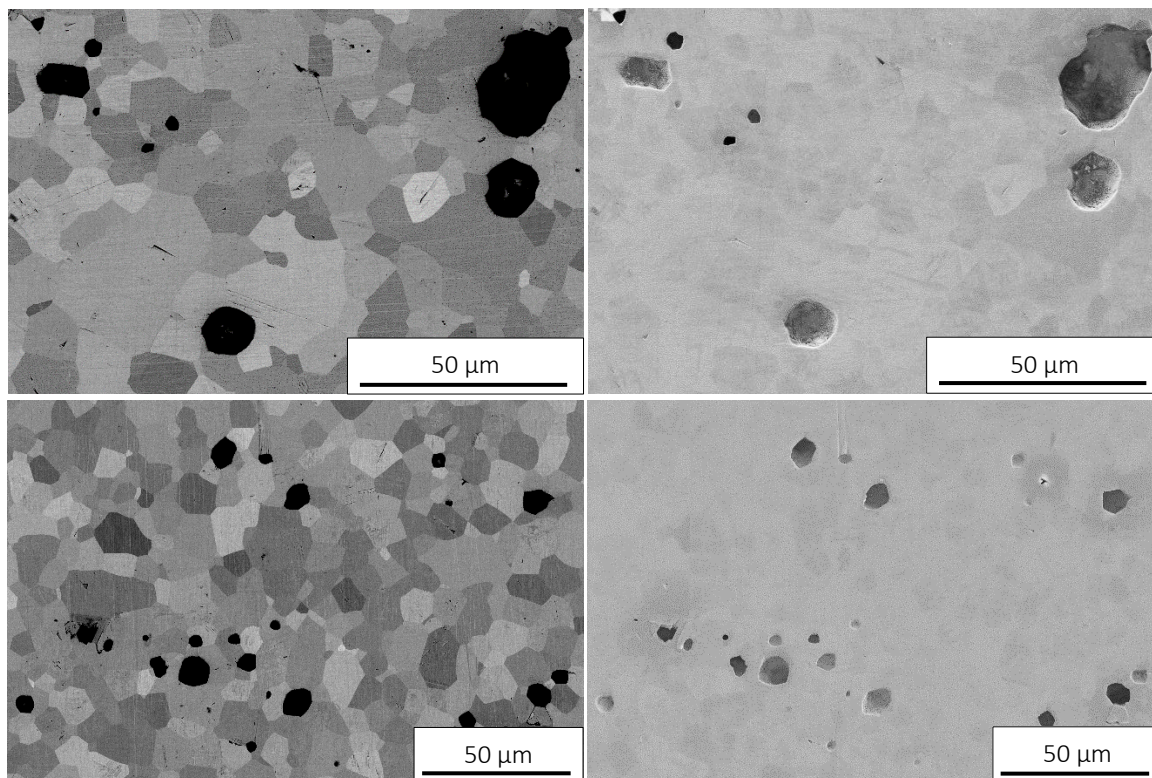


Figure 3.22. Back-scattered electron micrographs of BZY after NiO-extraction (left) and their equivalent images with secondary electrons detector (right).

A comparison with the original material with NiO, which exhibited a grain size of 1.6 μm with no pores (**Figure 3.15**), these images reflect a significant grain growth as well as an increase in porosity during the NiO-extraction. Coarsening of the BZY microstructure has been also reported by Coors *et al.* [25] after subjecting BZY-NiO compounds to a similar NiO-extraction process; in this case, they used a heat treatment at 1600 °C for 16 hours and observed an increase in the average grain size from 5 to 6.5 μm . Due to the fact that the amount of time required for a total extraction depends on the dimensions of the samples, it has been tested that 120 hours were necessary for a successful NiO-extraction in the case of specimens of 3 x 3 x 5 mm³. This long high-temperature heat treatment favoured a significant grain growth as well as an increase in porosity. As evidenced by **Figure 3.22**, the black regions are porosity, which consisted in cavities of about 10 μm preferably located at multiple grain junctions.

The morphological parameters d , F and θ of BZY after NiO-extraction were measured from Back-scattered electron micrographs and are summarized in **Table 3.10**. This material exhibits similar distribution, form factor and angle orientation than the others BZY compounds (**Table 3.9**) which means a stable grain size distribution with absence of preferential directions in the polycrystal. However, these results show a large difference in grain size with respect to the other ceramics, confirming the influence of the long firing cycle in the microstructure as just commented above.

Table 3.10. Morphological parameters of BZY after NiO-extraction: grain size d , grain size lognormal distribution parameters μ , σ , form factor F and angle orientation θ .

Material	\bar{d} (μm)	μ (μm)	σ (μm)	\bar{F}	θ (°)
BZY after NiO-extraction	9 ± 3	8.32	0.23	0.8 ± 0.1	87 ± 53

Finally TEM observations were carried out on the materials. **Figure 3.23** shows typical images of the internal structure of the grains, where most of them display large densities of dislocation and other defects, not seen in the original material (**Figure 3.18**).

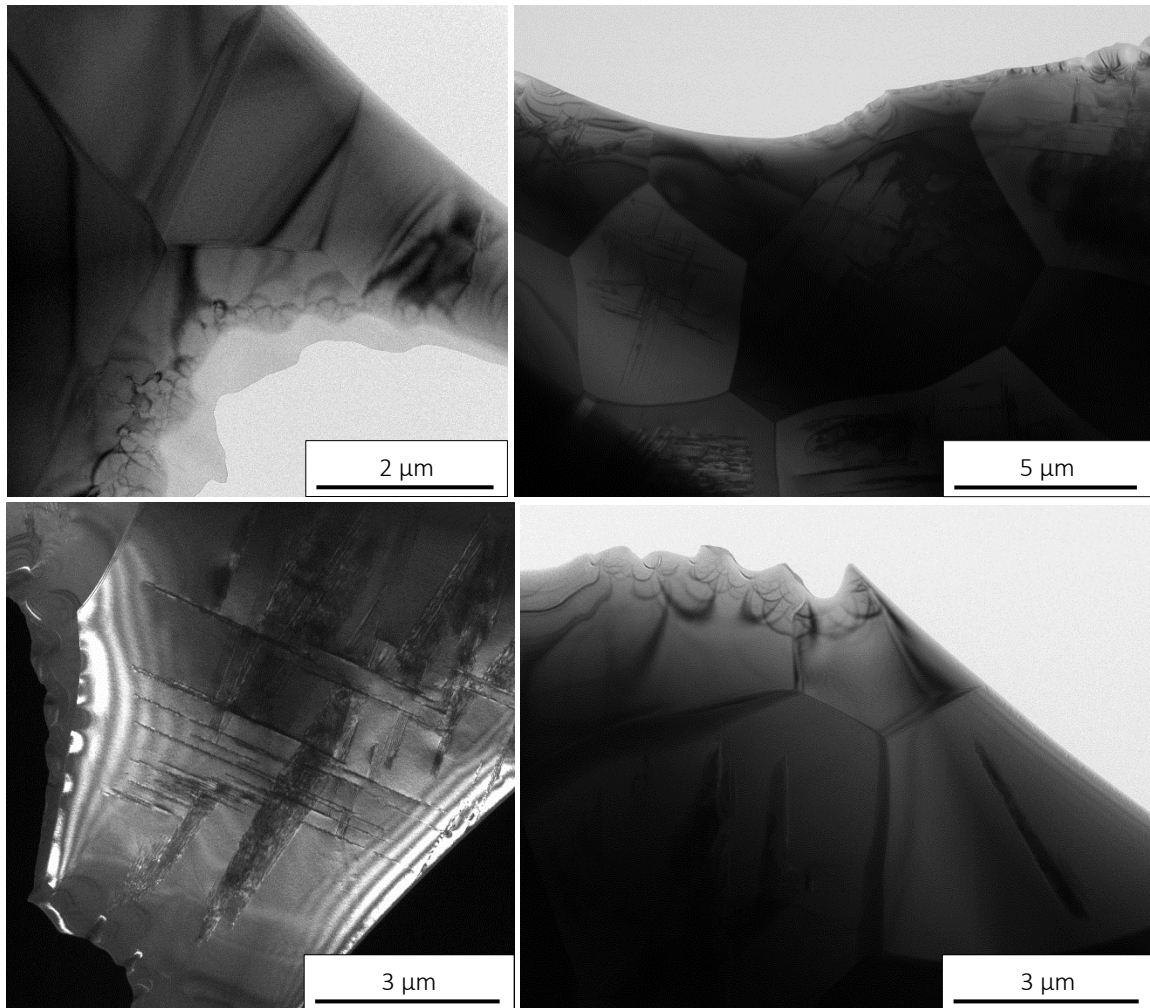


Figure 3.23. TEM images of sintered BZY compounds after NiO-extraction.

3.4 REFERENCES

1. Le Bail, A., *Whole powder pattern decomposition methods and applications: A retrospection*. Powder Diffraction, 2012. 20(4): p. 316-326.
2. Paufler, P., R. A. Young (ed.). *The Rietveld Method*. International Union of Crystallography. Oxford University Press 1993. 298 p. Price £ 45.00. ISBN 0-19-855577-6. Crystal Research and Technology, 1995. 30(4): p. 494-494.
3. Toby, B.H., *R factors in Rietveld analysis: How good is good enough?* Powder Diffraction, 2006. 21(1): p. 67-70.
4. Bravo-León, A., M. Jiménez-Melendo, and A. Domínguez-Rodríguez, *Mechanical and microstructural aspects of the high temperature plastic deformation of yttria-stabilized zirconia polycrystals*. Acta Metallurgica et Materialia, 1992. 40(10): p. 2717-2726.
5. Kurtz, S.K. and F.M.A. Carpay, *Microstructure and normal grain growth in metals and ceramics. Part I. Theory*. Journal of Applied Physics, 1980. 51(11): p. 5725-5744.

6. Kurtz, S.K. and F.M.A. Carpay, *Microstructure and normal grain growth in metals and ceramics. Part II. Experiment*. Journal of Applied Physics, 1980. 51(11): p. 5745-5754.
7. Chesnaud, A., et al., *Influence of synthesis route and composition on electrical properties of $La_{9.33} + xSi_6O_{26} + 3x/2$ oxy-apatite compounds*. Solid State Ionics, 2008. 179(33–34): p. 1929-1939.
8. Leon-Reina, L., et al., *Interstitial oxygen in oxygen-stoichiometric apatites*. Journal of Materials Chemistry, 2005. 15(25): p. 2489-2498.
9. Célérier, S., et al., *New chemical route based on sol–gel process for the synthesis of oxyapatite $La_{9.33}Si_6O_{26}$* . Ceramics International, 2006. 32(3): p. 271-276.
10. Kolitsch, U., H.J. Seifert, and F. Aldinger, *The Identity of Monoclinic La_2O_3 and Monoclinic Pr_2O_3 with $La_{9.33}(SiO_4)_6O_2$ and $Pr_{9.33}(SiO_4)_6O_2$, Respectively*. Journal of Solid State Chemistry, 1995. 120(1): p. 38-42.
11. Lambert, S., et al., *Structural investigation of $La_{9.33}Si_6O_{26}$ - and $La_9AESi_6O_{26+\delta}$ -doped apatites-type lanthanum silicate ($AE=Ba, Sr$ and Ca) by neutron powder diffraction*. Journal of Solid State Chemistry, 2006. 179(8): p. 2602-2608.
12. Masubuchi, Y., et al., *Oxide ion conduction mechanism in $RE_{9.33}(SiO_4)_6O_2$ and $Sr_2RE_8(SiO_4)_6O_2$ ($RE = La, Nd$) from neutron powder diffraction*. Solid State Ionics, 2006. 177(3–4): p. 263-268.
13. Okudera, H., et al., *Structure of oxide ion-conducting lanthanum oxyapatite, $La_{9.33}(SiO_4)_6O_2$* . Solid State Ionics, 2005. 176(15–16): p. 1473-1478.
14. Sansom, J.E.H., et al., *A comparison of the effect of rare earth vs Si site doping on the conductivities of apatite-type rare earth silicates*. Journal of Solid State Electrochemistry, 2006. 10(8): p. 562-568.
15. Tong, J., et al., *Proton-conducting yttrium-doped barium cerate ceramics synthesized by a cost-effective solid-state reactive sintering method*. Solid State Ionics, 2010. 181(33–34): p. 1486-1498.
16. Nikodemski, S., J. Tong, and R. O'Hayre, *Solid-state reactive sintering mechanism for proton conducting ceramics*. Solid State Ionics, 2013. 253: p. 201-210.
17. Nomura, K. and H. Kageyama, *Transport properties of $Ba(Zr_{0.8}Y_{0.2})O_3 - \delta$ perovskite*. Solid State Ionics, 2007. 178(7–10): p. 661-665.
18. Iguchi, F., et al., *The relationship between chemical composition distributions and specific grain boundary conductivity in Y-doped $BaZrO_3$ proton conductors*. Solid State Ionics, 2009. 180(6–8): p. 563-568.
19. Duval, S., *Y-Substituted Barium Zirconate, a Proton Conducting Electrolyte for Applications at Intermediate Temperatures* 2008, University of Munich.
20. Park, K.-Y., et al., *Electrical and physical properties of composite $BaZr_{0.85}Y_{0.15}O_{3-d}Nd_{0.1}Ce_{0.9}O_{2-\delta}$ electrolytes for intermediate temperature-solid oxide fuel cells*. Journal of Power Sources, 2016. 336: p. 437-446.

21. Kreuer, K.D., et al., *Proton conducting alkaline earth zirconates and titanates for high drain electrochemical applications*. Solid State Ionics, 2001. 145(1–4): p. 295-306.
22. S. P. Shafi, L.B., S. Boulfrad and E. Traversa, *Yttrium and Nickel Co-Doped BaZrO₃ as a Proton-Conducting Electrolyte for Intermediate Temperature Solid Oxide Fuel Cells*. The Electrochemical Society, 2014.
23. Magrez, A. and T. Schober, *Preparation, sintering, and water incorporation of proton conducting Ba_{0.99}Zr_{0.8}Y_{0.2}O_{3-δ}: comparison between three different synthesis techniques*. Solid State Ionics, 2004. 175(1): p. 585-588.
24. Tong, J., et al., *Solid-state reactive sintering mechanism for large-grained yttrium-doped barium zirconate proton conducting ceramics*. Journal of Materials Chemistry, 2010. 20(30): p. 6333-6341.
25. Coors, W.G., et al., *Fabrication of Yttrium-Doped Barium Zirconate for High Performance Protonic Ceramic Membranes*. Perovskite Materials - Synthesis, Characterisation, Properties, and Applications. 2016.

Chapter 4

ROOM-TEMPERATURE MECHANICAL CHARACTERIZATION

Contents

4.1 Introduction	91
4.2 Experimental characterization of room-temperature mechanical properties	92
4.2.1 Experimental procedure.....	92
4.2.1.1 Nanoindentation	93
4.2.1.2 Mechanical compression test with optical imaging	95
4.2.1.3 Resonant Ultrasound Spectroscopy.....	97
4.2.1.4 Microindentation	100
4.2.2 Experimental results.....	101
4.2.2.1 Room-temperature mechanical properties of Lanthanum Silicate.....	101
4.2.2.2 Room-temperature mechanical properties of Y-doped Barium Zirconate	105
4.3 Density Functional Theory calculations	110
4.3.1 DFT calculation procedure: Elastic coefficient determination.....	111
4.3.1.1 DFT Calculations details for lanthanum silicate oxy-apatites	112
4.3.1.2 DFT calculations for Yttrium-doped barium zirconates.....	113
4.3.2 DFT calculation results.....	113
4.3.2.1 Elastic properties of Lanthanum Silicate.....	113
4.3.2.2 Elastic properties of Y-doped Barium Zirconate	114
4.4 References	115

4.1 INTRODUCTION

The main purpose of this chapter is to investigate and compare the mechanical properties, including Young's modulus (E), hardness (H), Poisson ratio (ν) and fracture toughness (K_{IC}), of Lanthanum Silicate and Yttrium-doped Barium Zirconate by means of different experimental techniques at room temperature. Another objective is to explore the precision and reliability of

these techniques to see whether they could be developed for high temperature measurements. Finally, for the sake of completeness, theoretical calculations by Density Functional Theory (DFT) was carried out to determine the full elastic tensor of materials, evaluate the potential differences in the elastic properties between polycrystalline and single crystal compounds in order to identify possible sources of internal stress and compare with the experimental results.

4.2 EXPERIMENTAL CHARACTERIZATION OF ROOM-TEMPERATURE MECHANICAL PROPERTIES

4.2.1 Experimental procedure

The experimental mechanical parameters were determined considering the polycrystals to be elastic isotropic materials. The relationship between stress σ and strain ε can be described by the Hooke's law for an isotropic material and is given by:

$$\begin{bmatrix} \varepsilon_{xx} \\ \varepsilon_{yy} \\ \varepsilon_{zz} \\ \varepsilon_{yz} \\ \varepsilon_{xz} \\ \varepsilon_{xy} \end{bmatrix} = \frac{1}{E} \begin{bmatrix} 1 & -\nu & -\nu & 0 & 0 & 0 \\ -\nu & 1 & -\nu & 0 & 0 & 0 \\ -\nu & -\nu & 1 & 0 & 0 & 0 \\ 0 & 0 & 0 & 1+\nu & 0 & 0 \\ 0 & 0 & 0 & 0 & 1+\nu & 0 \\ 0 & 0 & 0 & 0 & 0 & 1+\nu \end{bmatrix} \begin{bmatrix} \sigma_{xx} \\ \sigma_{yy} \\ \sigma_{zz} \\ \sigma_{yz} \\ \sigma_{xz} \\ \sigma_{xy} \end{bmatrix}$$

where E and ν are the Young's modulus and the Poisson ratio, respectively. This matrix relating $\bar{\sigma}$ to $\bar{\varepsilon}$ is called the compliance matrix (the inverse relation involves the use of the stiffness tensor). It will be seen in section 4.3 dedicated to Density Functional Theory calculations, that, for single crystals, the compliance matrix has to be modified to take into account the inherent symmetries of the structure and the fact that crystals are by definition not isotropic.

In this study, the Young's modulus and hardness were first analyzed by nanoindentation and the results were interpreted by the Oliver and Pharr method. Besides, fracture toughness was calculated from the cracks information on the residual indents using the method of Palmqvist. Then, E and ν were also measured by mechanical compression tests together with an optical marker tracking method and by Resonant Ultrasound Spectroscopy (RUS). Finally, the fracture toughness and hardness were also determined from classical microindentation tests. The different experiments were carried out in air at room temperature in specimens of approximately $5 \times 3 \times 3 \text{ mm}^3$ in size which were cut from the sintered pellets with a low-speed diamond saw. After cutting, the samples were rectified to eliminate imperfections and to ensure completely flat-parallel surfaces which is essential to avoid a wrong estimation of the mechanical properties. The different techniques used in this work are briefly described below.

4.2.1.1 Nanoindentation

Nanoindentation tests were performed on polished surfaces using a Nano Indenter XP system (Mechanical testing laboratory, MSSMAT, CentraleSupélec, France) with a Berkovich diamond indenter to evaluate the mechanical properties at the nanometer scale [1]. The nanoindentations were carried out under the control load mode at room temperature. Mechanical properties depend on surface defects such as roughness, porosity, dislocations or cracks, which create an Indentation Size Effect (ISE). Because such an effect increases when the nanoindentation size decreases [2], different loads were applied: 10, 30, 60, 100 and 500 mN. ISE is stronger when the applied load is very small because the influence of surface defects at low penetration could introduce errors at the contact point and therefore in the estimation of E and H . For this reason, higher loads are required to determine the global mechanical properties. The loading/unloading and hold times at the maximum load were 30 s, which were kept constant for all indentations. In order to have significative average values for the evaluated properties, 100 indentation tests were performed on each material. The experimental results were interpreted by the Oliver and Pharr [2] and Doerner and Nix [3] methods which were developed to measure E and H from the experimental load-displacement curve obtained during the loading and unloading of isotropic materials.

Figure 4.1 shows a schematic illustration of a typical curve obtained with a Berkovich indenter. During loading it is assumed that the deformation is not only elastic but also plastic due to the residual impression that remains in the surface after the indentation. During unloading, only the elastic deformations are recovered and, so this section of the curve is used to extract the Young's modulus and hardness [4].

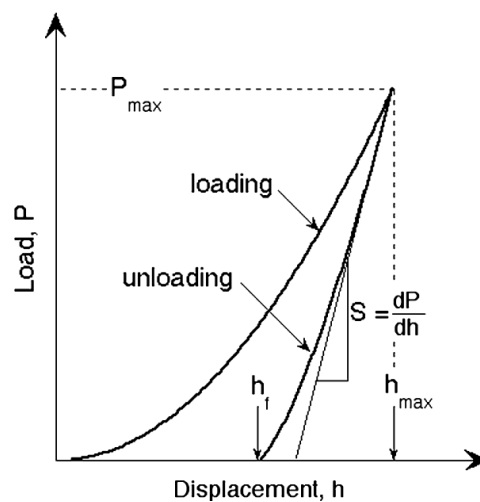


Figure 4.1. Schematic representation of a load-displacement curve [4].

From this curve (**Figure 4.1**), three important parameters can be extracted: the maximum load, P_{max} , the maximum displacement, h_{max} , and the contact stiffness, S , which is defined as the slope of the initial stage of the unloading part [2]:

$$S = \frac{dP}{dh} = 2\beta E_r \sqrt{\frac{A}{\pi}} \quad (4.1)$$

where β is the indenter geometric coefficient (with a constant value for pyramidal Berkovich diamond indenter of 1.034 [4]), A is the contact area of the indentation under the maximum load and E_r is the reduced modulus defined as:

$$\frac{1}{E_r} = \frac{1-\nu^2}{E} + \frac{1-\nu_i^2}{E_i} \quad (4.2)$$

The reduced elastic modulus is a combination of the indenter elastic constants (E_i, ν_i) and those of the specimen (E, ν). The diamond indenter tip Young's modulus is 1141 GPa and the Poisson's ratio is 0.07 [2]. E_r can be thus rewritten as:

$$E_r = \frac{\sqrt{\pi}}{2\beta} \frac{S}{\sqrt{A}} \quad (4.3)$$

Another important parameter is the final depth, h_f , which is the permanent depth of the impression after the indenter is withdrawn (**Figure 4.1** and **Figure 4.2**). **Figure 4.2** displays a schematic illustration of a cross section of an indentation, where a is the radius of the contact circle, h_c is the contact penetration and h_s is the surface displacement at the perimeter of the residual impression.

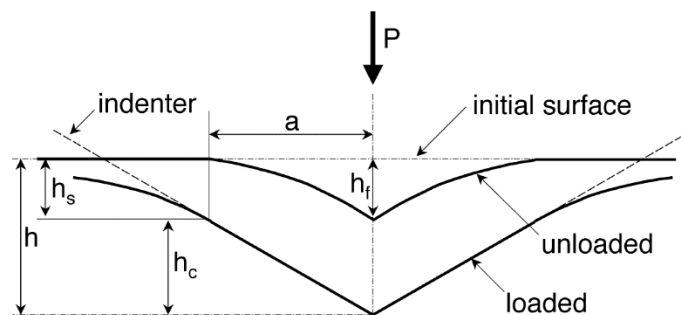


Figure 4.2. A schematic representation of loading-unloading process [4].

Hardness can be estimated from the relationship between the contact area and load according to the following equations [2]:

$$h_c = h_{\max} - h_s ; h_s = \epsilon \frac{P_{\max}}{S} \quad (4.4)$$

$$A = 24.5h_c^2 \quad (4.5)$$

$$H = \frac{P_{\max}}{A} \quad (4.6)$$

where ϵ is a correction factor which depends on the geometry of the indenter (for the Berkovich indenter, $\epsilon = 0.75$ [2]).

4.2.1.2 Mechanical compression tests with optical imaging

Uniaxial mechanical compression tests were performed on parallelepipedic specimens using an Instron 4482 machine (Mechanical testing laboratory, MSSMAT, CentraleSupélec, France) with a 10 kN load cell. The cross-head displaced down at a constant speed of 5 $\mu\text{m}/\text{min}$ (corresponding to a strain rate of $1.8 \times 10^{-5} \text{ s}^{-1}$). The experiments were carried out at room temperature, using loading/unloading cycles of 2.5/1 kN for Lanthanum Silicate compounds and 6/1 kN for Y-doped Barium Zirconate ceramics, to remain within the range of elastic behavior. The load level was chosen after a first test to rupture for each material.

Together with the mechanical compression machine, an optical marker tracking method (**Figure 4.3**) was used to measure in a precise way the strain in the specimen during the test. The image acquisition system consists of a Canon 60D DSLR camera with a long distance optical microscope, Questar QM100, which was used to record images of the specimen during the compression test with an acquisition frequency of one image per 2 s. The maximum resolution of the camera is 2500 x 1700 pixels. The optical system was located at 0.3 m from the sample, therefore one pixel corresponds to about of 2-2.5 μm depending of the adjustment.

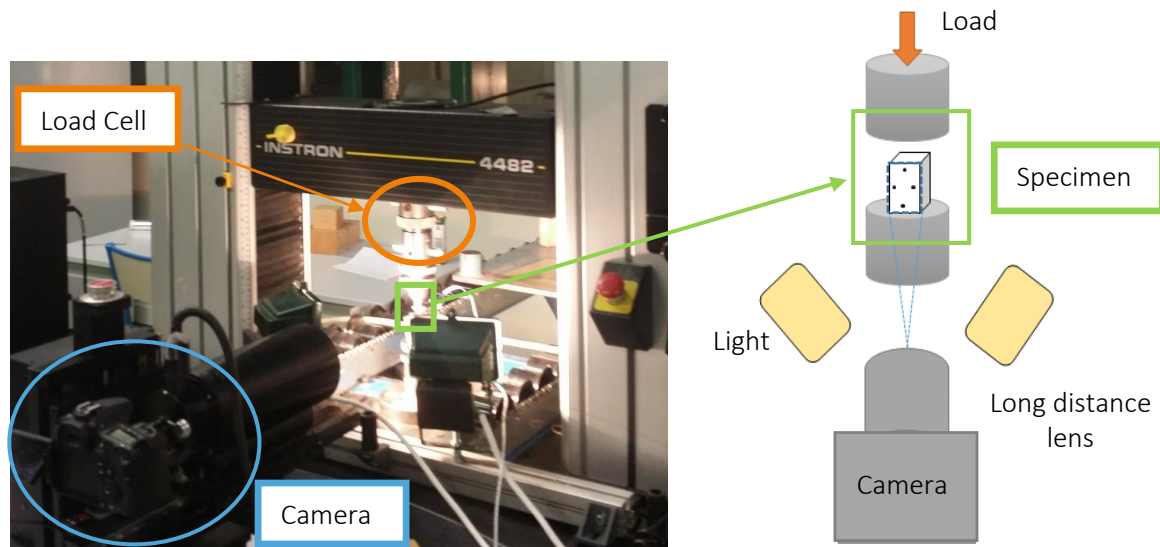


Figure 4.3. Compression test setup and optical acquisition system.

In order to measure accurately the displacements between successive images, the specimen was marked along its longitudinal and transversal axes, which allowed to obtain the evolution in the position of each marker between the first image and the deformed ones, and determine the strain along both axes.

As indicated at the beginning of this chapter, the Young's modulus and Poisson ratio were determined by considering the materials to be elastic isotropic. In 2D, the isotropic elastic strain-stress relationship (y-axis being axis of symmetry) can be written as:

$$\begin{bmatrix} \varepsilon_{yy} \\ \varepsilon_{xx} \\ \varepsilon_{yx} \end{bmatrix} = \begin{bmatrix} \frac{1}{E} & -\frac{\nu}{E} & 0 \\ -\frac{\nu}{E} & \frac{1}{E} & 0 \\ 0 & 0 & \frac{1}{2G} \end{bmatrix} \begin{bmatrix} \sigma_{yy} \\ \sigma_{xx} \\ \sigma_{yx} \end{bmatrix} \quad (4.7)$$

where ε_{ij} and σ_{ij} are the strain and the stress tensor respectively, and the parameters E , ν and G are the corresponding elastic properties that can be determined from 2D experiments.

In a mechanical compression test, a uniaxial stress σ is applied, then the stress vector can be written as:

$$\begin{bmatrix} \sigma_{yy} \\ \sigma_{xx} \\ \sigma_{yx} \end{bmatrix} = \begin{bmatrix} \sigma \\ 0 \\ 0 \end{bmatrix} \quad (4.8)$$

Considering a prismatic specimen of section S under a load F , the applied stress σ is defined by the following equation:

$$\sigma = \frac{F}{S} \quad (4.9)$$

Therefore, from Equation 4.7 only two elastic constants can be determined, the Young's modulus E and Poisson ratio ν , which are defined as follows:

$$E = \frac{\sigma}{\varepsilon_{yy}} \quad (4.10)$$

$$\nu = -\frac{\varepsilon_{xx}}{\varepsilon_{yy}} \quad (4.11)$$

During the image acquisition, the longitudinal ε_{yy} and transversal ε_{xx} strains were calculated in real time both during the loading and unloading steps.

4.2.1.3 Resonant Ultrasound Spectroscopy

These experiments were carried out using a typical RUS setup (SPMS Laboratory, CentraleSupélec, France) which was used to determine the elastic properties with a very high accuracy. The RUS method is based on the measurement of the resonant frequencies of vibration of a specimen with well-defined geometry. A parallelepipedic sample was placed between two piezoelectric transducers, one of them being used to excite the mechanical resonances of the specimen, whereas the opposite transducer is used to detect them (**Figure 4.4**). The frequency was swept between 0.2 and 2 MHz allowing to activate the sample's resonant modes. When the frequency corresponds to one of the own resonance frequencies of the specimen, a large response is detected at the receptor transducer and appears as a peak in the resonance spectrum [5].

The mechanical resonance of a given solid depends on its elastic constants, density and geometry [6]. Therefore by measuring a large quantity of resonant modes on one sample, the elastic constants can be then determined by solving two processes: the direct and inverse problems. The direct problem implies the calculation of the mechanical resonance from known material properties while the inverse problem is based on finding the best fit between the measured and the calculated (direct process) frequencies to determine the elastic components.

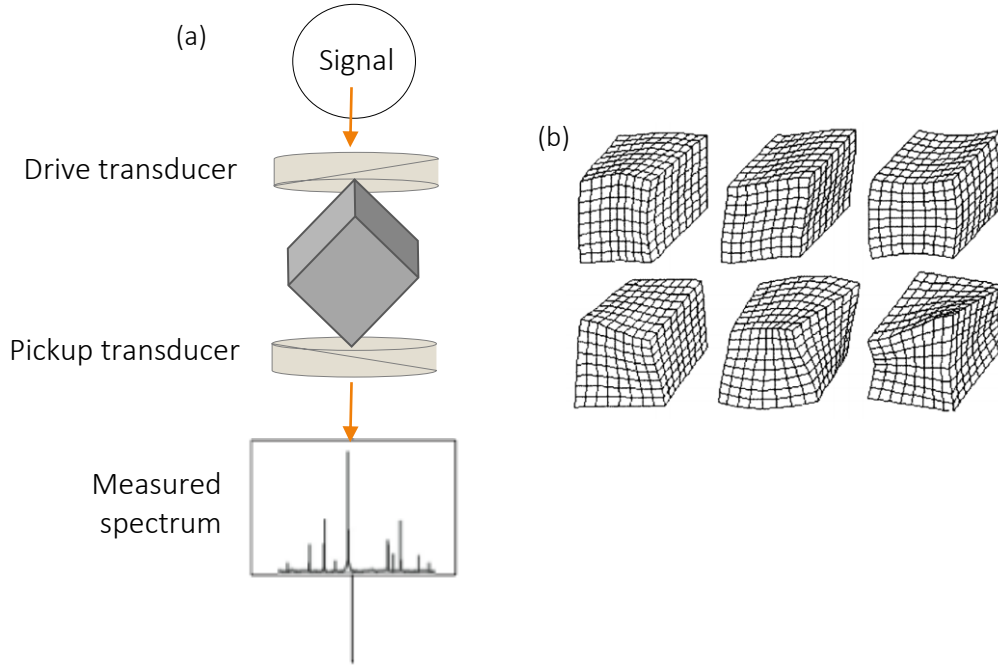


Figure 4.4. (a) A schematic representation of a typical RUS setup and (b) several resonant frequencies of vibration for a prismatic specimen [5].

Direct process

In the direct problem, the natural resonant frequencies ω of an elastic solid can be calculated if the elastic tensor C_{ijkl} , volume V , and density ρ are given. This procedure seeks stationary points of the Lagrangian L for a freely vibrating elastic body [6].

$$L = \frac{1}{2} \int_V (\rho \omega^2 u_i^2 - C_{ijkl} u_{i,j} u_{k,l}) dV \quad (4.12)$$

where u_i is the i th component of the displacement field and the indices following a comma denote differentiation with respect to that coordinate. u_i is expanded in a complete set of basis functions Φ_α , following the Rayleigh-Ritz method:

$$u_i = a_{i\alpha} \Phi_\alpha \quad (4.13)$$

where $a_{i\alpha}$ is the expansion coefficient. The Φ_α are chosen depending on the geometry of the specimen and, for parallelepipeds, the Legendre polynomials are selected [5]. Substituting in Equation 4.12, this can be rewritten in a matrix form as:

$$L = \frac{1}{2} ((\rho \omega^2) a^T M a - a^T \Gamma a) \quad (4.14)$$

where a is the vector containing the expansion coefficients, and M and Γ are the mass and stiffness matrices, respectively, of the vibration problem. Equation 4.12 is stationary if the displacements u_i are solutions of freely vibrating elastic body, therefore by setting $\delta L=0$, the equation turns to:

$$\Gamma a = (\rho \omega^2) M a \quad (4.15)$$

Thus, the natural resonant frequencies of an elastic solid can be determined straightforward if the geometry, density and elastic tensor of the specimen are well known.

Inverse process

In the inverse problem, the elastic components are generally estimated through an optimization process in which the stiffness components are adjusted until the best fitting between the measured and computed frequencies is found [7]. The cost function is defined and minimized as:

$$F = \sum_n \left(\frac{f_n^{\text{meas}} - f_n^{\text{pred}}(C_{ij})}{f_n^{\text{meas}}} \right)^2 \quad (4.16)$$

where f_n^{meas} are the frequencies measured, f_n^{pred} are the frequencies predicted and C_{ij} are the stiffness constants. The main difficulty in this procedure is to obtain a good pairing between calculated and measured modes.

Determination of the elastic constants

Assuming that the material behavior is isotropic, only two elastic constants are required to define the elastic tensor:

$$C_{ij} = \begin{vmatrix} C_{11} & C_{12} & C_{12} & 0 & 0 & 0 \\ C_{12} & C_{11} & C_{12} & 0 & 0 & 0 \\ C_{12} & C_{12} & C_{11} & 0 & 0 & 0 \\ 0 & 0 & 0 & \frac{C_{11}-C_{12}}{2} & 0 & 0 \\ 0 & 0 & 0 & 0 & \frac{C_{11}-C_{12}}{2} & 0 \\ 0 & 0 & 0 & 0 & 0 & \frac{C_{11}-C_{12}}{2} \end{vmatrix}$$

where C_{11} is also defined as the longitudinal modulus L , and $\frac{C_{11}-C_{12}}{2}$ as the shear modulus G . These

two constants are related to the Young's modulus and the Poisson ratio by the following equations:

$$E = \frac{G(3L - 4G)}{L - G} \quad (4.17)$$

$$\nu = \frac{L - 2G}{2(L - G)} \quad (4.18)$$

Therefore, E and ν determination can be performed once the elastic tensor is extracted by the inverse problem.

4.2.1.4 Microindentation

Mechanical properties were also investigated by microindentation using a Wolpert Teswell indenter (Mechanical Testing Laboratory, MSMAT, CentraleSupélec, France) equipped with a Vickers diamond tip. The experiments were performed on polished surfaces at room temperature. A load of 2 N and a hold time at the maximum load of 10 s were selected and kept constant for all indentations. At least 10 indentation tests were performed on each material. The Vickers hardness, H_v , was calculated using the following equation:

$$H_v = 1.8544 \frac{P}{d^2} \quad (4.19)$$

where P is the applied load (kg) and d is the mean length of the diagonals (mm) (Figure 4.5). The hardness values were converted in GPa for comparison with the nanoindentation measurements.

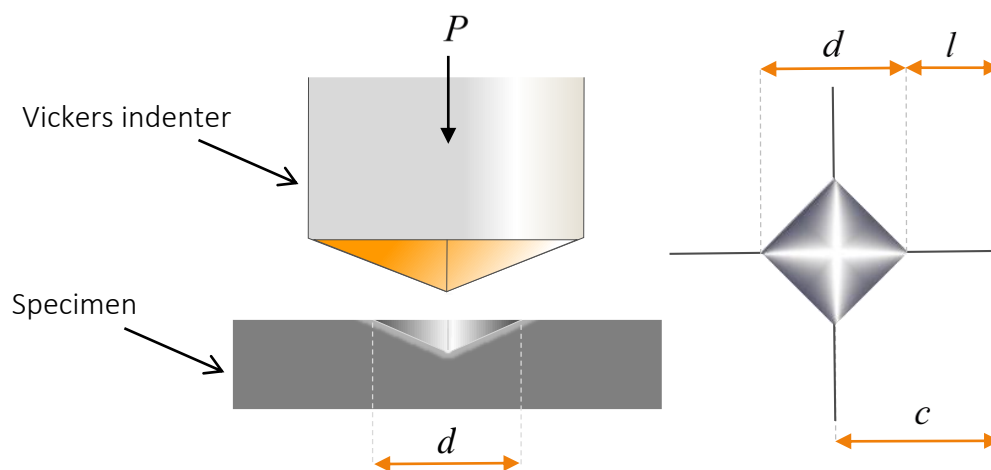


Figure 4.5. A schematic representation of Vickers microindentation.

The fracture toughness K_{IC} was estimated by applying the normalized Niihara's expression [8]:

$$K_{IC} = 9.518 \left(\frac{c}{a} \right)^{-1.5} (H_V^{0.6}) (a^{0.5}) \quad (4.20)$$

where a and c are half of the indentation diagonal (d) and radial crack length, respectively (Figure 4.5). Due to the criterion $c/a > 2.5$, the Niihara's equation was used to determine the fracture toughness.

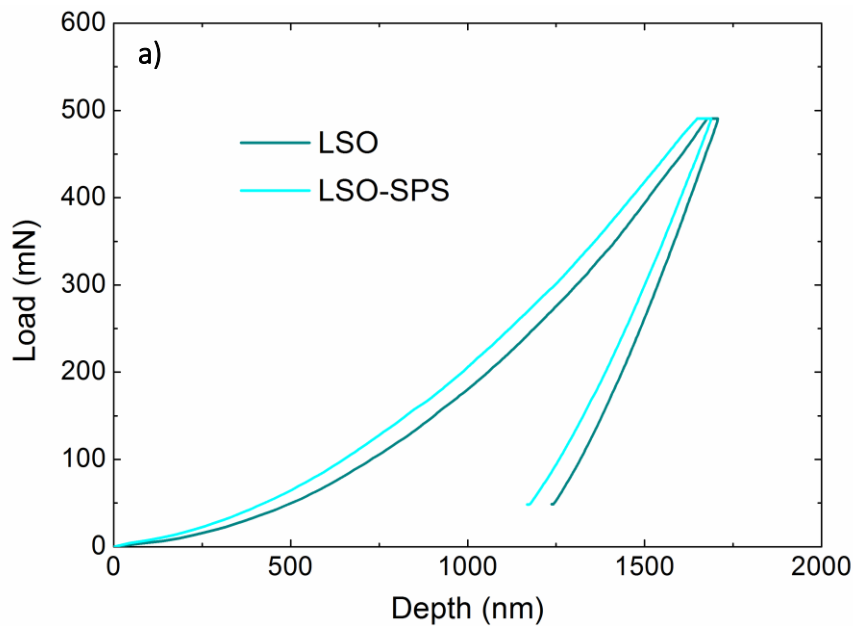
The measurement of the diagonals of the residual indents and of the radial-crack diameters were done with an optical microscope Alicona InfiniteFocus (Microscopy Resource Centre, MSSMAT, CentraleSupélec, France).

4.2.2 Experimental results

4.2.2.1 Room-temperature mechanical properties of Lanthanum Silicate

4.2.2.1.1 Nanoindentation

Typical load-displacement curves for the different oxy-apatite compounds are shown in Figure 4.6 along with SEM micrographs of their respective indentations performed at 500 mN. Based on the upper one-third sections of these curves, the Young's modulus and nanohardness were determined as a function of the applied load (Table 4.1). The results for each material represent the mean value of all the indents and the associated error is the standard deviation of the values.



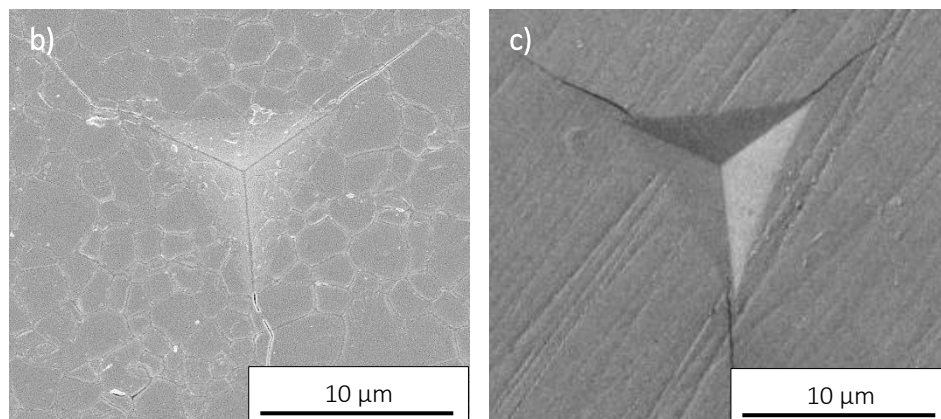


Figure 4.6. (a) Load-depth indentation curves from $\text{La}_{9.33}\text{Si}_6\text{O}_{26}$ materials at 500mN. SEM micrographs of indents performed at 500 mN for (b) LSO-CS and (c) LSO-SPS.

Table 4.1. Young's modulus E , hardness H and fracture toughness K_{IC} of $\text{La}_{9.33}\text{Si}_6\text{O}_{26}$ compounds as a function of the applied load.

Applied load (mN)	LSO-CS		LSO-SPS	
	E (GPa)	H (GPa)	E (GPa)	H (GPa)
10	147 ± 10	11 ± 2	132 ± 5	10.3 ± 0.7
30	142 ± 8	10.2 ± 0.6	133 ± 5	10.1 ± 0.7
60	143 ± 6	10.5 ± 0.7	131 ± 4	9.9 ± 0.6
100	138 ± 6	9.8 ± 0.8	131 ± 3	9.8 ± 0.5
500	138 ± 3	9.5 ± 0.4	129 ± 3	9.8 ± 0.4

The results gathered in **Table 4.1** for the LSO-CS compounds show a slight decrease with increasing load. This tendency is due to the ISE [2] and has been also reported in other studies on mechanical properties by nanoindentation [9-11]. For applied loads higher than 100 mN, the values show a stabilization because the penetration depth is larger (100 and 500 mN correspond to penetration depths of 750 and 1750 nm, respectively) and the influence of the surface defects is therefore lower. In order to study the overall mechanical properties of a polycrystalline material, it is essential to control the indent size according to the grain size of the sample [12]. For this, the contact diameter of the indenter must be one order of magnitude larger than the average grain size. In LSO-CS samples, the grain size is $1.1 \pm 0.6 \mu\text{m}$, therefore an indentation depth of 1750 nm, which would result in an equivalent contact diameter of about $12 \mu\text{m}$, appears to agree with the requirements for determining the macroscopic mechanical properties. **Figure 4.6b** shows the contact area of an indentation performed at 500 mN in which it is possible to compare the grain size of the ceramic with the residual imprint of the indenter.

In contrast with the LSO-CS results, the Young's modulus and the hardness of the LSO-SPS material remain practically constant with the different loads. This could be explained by the high relative sample density (99.6 ± 0.4 %) with practically no porosity and very small grain size (0.2 ± 0.1 μm). For an applied load of 10 mN, the penetration depth is 230 nm, which corresponds to an equivalent contact diameter of about 1.6 μm , i.e., one order of magnitude larger than the grain size, indicating that, even at the minimum load, reliable values of the macroscopic mechanical properties can be obtained.

Similar values of H were determined for both materials, however the Young's modulus of LSO-SPS is slightly lower than that of the LSO-CS. To the author's knowledge, only one previous work deals with the mechanical properties by nanoindentation of similar Lanthanum silicates compounds [13]. In this case, it was reported a Young's Modulus of 135 GPa and a nanohardness of 9.6 GPa for the samples with the highest density, which are in good agreement with the results obtained in this work.

4.2.2.1.2 Mechanical compression tests with optical imaging

The mechanical parameters such as the Young's modulus and Poisson ratio were determined by the stress and strain measurement within the elastic range of specimens. The experimental results, summarized in **Table 4.2**, show similar values of ν for both materials while E is slightly higher for LSO-CS. The uncertainty is given by the standard deviations of the values from the different loading/unloading cycles.

Table 4.2. Young's modulus E and Poisson ratio ν of $\text{La}_{9.33}\text{Si}_6\text{O}_{26}$ compounds determined by mechanical compression tests.

Material	E (GPa)	ν
LSO-CS	141 ± 22	0.31 ± 0.07
LSO-SPS	136 ± 16	0.32 ± 0.08

4.2.2.1.3 Resonant Ultrasound Spectroscopy

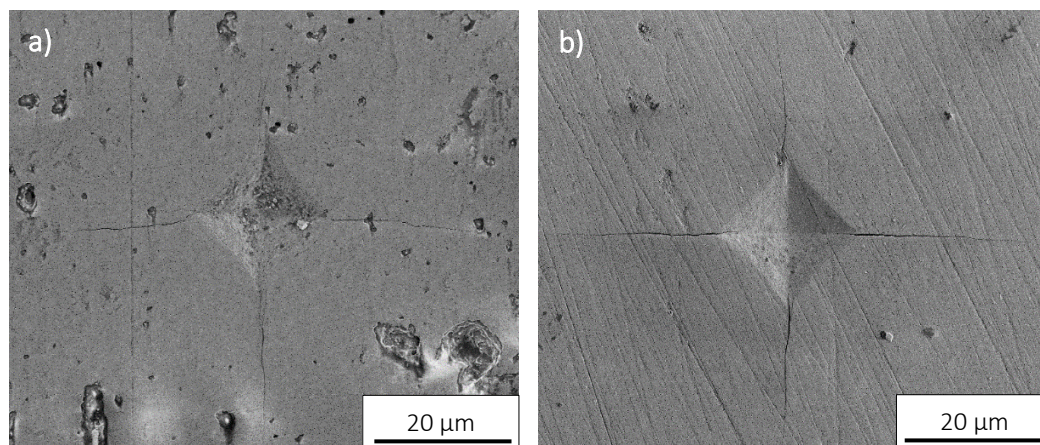
Table 4.3 shows the experimental results obtained by RUS with an extremely low uncertainty, which comes from the error between the experimental and computed frequencies. With this technique both Young's modulus and Poisson ratio for LSO-CS were slightly higher than those for LSO-SPS.

Table 4.3. Young's modulus E and Poisson ratio ν of $\text{La}_{9.33}\text{Si}_6\text{O}_{26}$ compounds determined by RUS.

Material	E (GPa)	ν
LSO-CS	135 ± 1	0.31 ± 0.01
LSO-SPS	129 ± 1	0.28 ± 0.01

4.2.2.1.4 Microindentation

Typical Vickers indents of the $\text{La}_{9.33}\text{Si}_6\text{O}_{26}$ compounds are shown in **Figure 4.7**. In both cases symmetrical pyramid indents were observed in which a single crack propagates from each corner. Based on these indentations, Vickers hardness and fracture toughness were determined for each ceramic (**Table 4.4**).

**Figure 4.7.** SEM images of Vickers microindentations on the surface of (a) LSO-CS and (b) LSO-SPS.**Table 4.4.** Vickers hardness HV and fracture toughness K_{IC} of $\text{La}_{9.33}\text{Si}_6\text{O}_{26}$ compounds.

Material	HV	HV (GPa)	K_{IC} ($\text{MPa m}^{1/2}$)
LSO-CS	744 ± 24	7.3 ± 0.2	1.2 ± 0.1
LSO-SPS	787 ± 12	7.7 ± 0.1	1.3 ± 0.1

Table 4.4 summarizes the experimental results obtained by microindentation where HV is also given in GPa for comparison with the values measured by nanoindentation (**Table 4.1**). Similar values of fracture toughness were obtained for both materials, however LSO-SPS presents a slightly higher hardness than LSO-CS. Several parameters can affect the hardness of a ceramic material such as chemical bond strength, grain size, porosity and applied load among others [12]. The Hall-Petch law describes the relationship between the yield strength σ_y and the grain size and predicts

that σ_y is inversely proportional to grain growth. On the other hand, Vickers hardness can be directly related to the yield strength through the following equation [14]:

$$HV = 3\sigma_y \quad (4.21)$$

Therefore a decrease in grain size implies an increase in hardness because the grain boundaries block the dislocations generated by the indenter [12]. Then, hardening of LSO-SPS could be attributed to the higher grain boundary density due to its smaller grain size in comparison with LSO-CS (0.2 and 1.1 μm , respectively).

Concerning these oxy-apatites, only one previous work deals with the mechanical properties of similar compounds by microindentation [15]. In this case, it was reported a Vickers hardness of 7.57 ± 0.24 GPa for $\text{La}_{9.33}\text{Si}_6\text{O}_{26}$, which agrees with the results obtained in this work.

4.2.2.1.5 Comparison of the different techniques

From the comparison of the mechanical parameters determined using the different techniques, the values of Young's modulus obtained were in the range of 135 - 141 GPa for LSO-CS and 129 - 136 GPa for LSO-SPS, while the values of Poisson ratio obtained were in the range of 0.29 - 0.32 for both materials. Although all the techniques showed similar results of the elastic parameters for the two compounds, it worth mentioning that, compression tests showed the values with the highest uncertainty while RUS was the most precise technique.

Concerning hardness, the values obtained by nanoindentation were 9.6 and 9.8 GPa for an applied load of 500 mN, whereas by microindentation they were 7.3 and 7.7 GPa at 2 N for LSO-CS and LSO-SPS, respectively. As expected, microhardness is significantly lower than nanohardness because of the differences in load. These values are in concordance with the well-known hardness dependence on the applied load, as found in other ceramics [10, 11, 16].

4.2.2.2 Room-temperature mechanical properties of Yttrium-doped Barium Zirconate

4.2.2.2.1 Nanoindentation

Figure 4.8 shows typical load-displacement curves obtained from sintered Yttrium-doped Barium Zirconate compounds at the maximum applied load of 500 mN together with SEM

micrographs of their respective indentations. Based on the first part of the unloading curves, Young's modulus and nanohardness were extracted as a function of the applied load (**Table 4.5**).

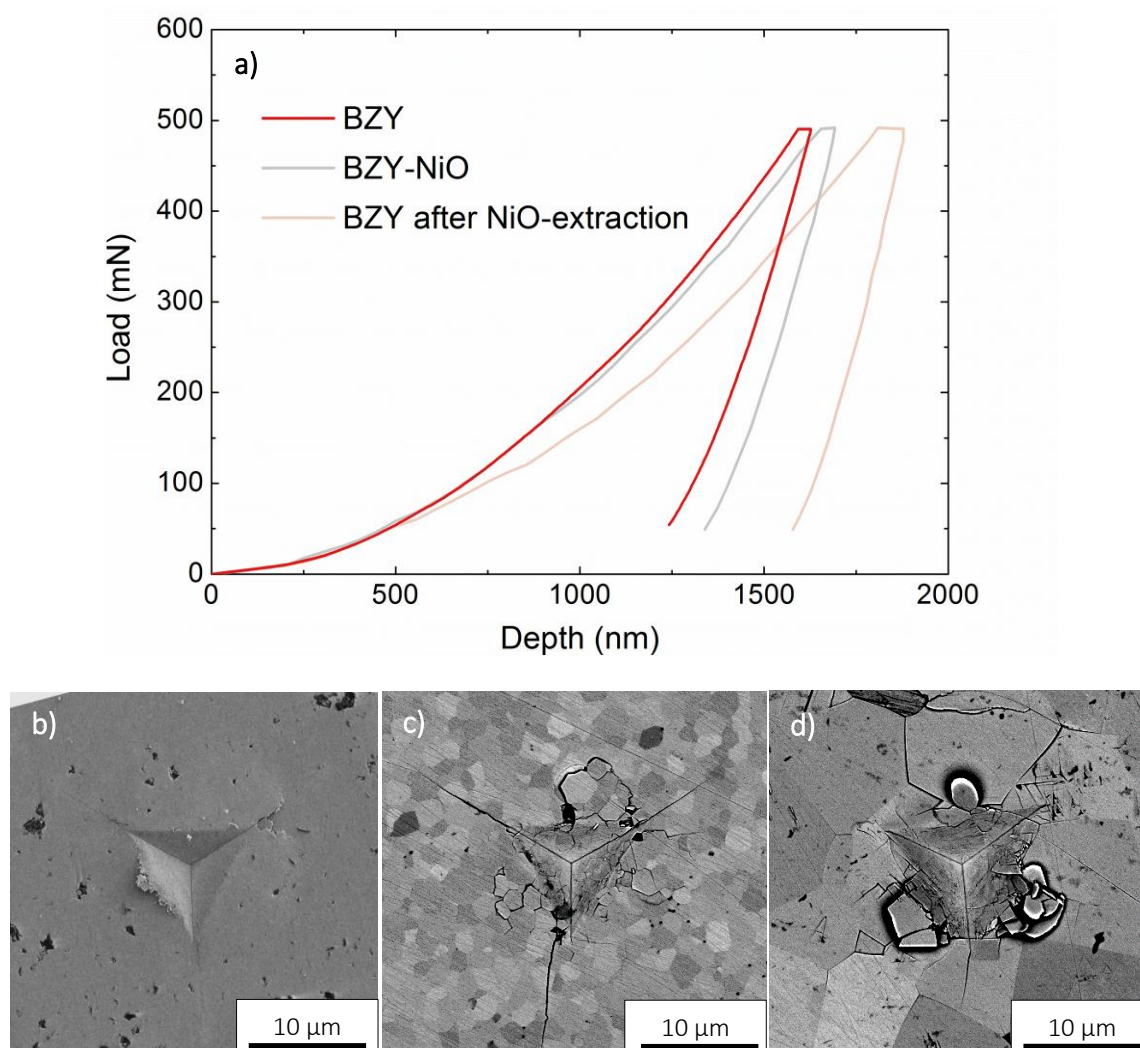


Figure 4.8. (a) Load-depth indentation curves for $\text{BaZr}_{0.85}\text{Y}_{0.15}\text{O}_{2.925}$ compounds at 500mN. SEM micrographs of indents performed at an applied load of 500 mN for (b) BZY; (c) BZY-NiO and (d) BZY after NiO-extraction.

The experimental results of E obtained for the different compounds did not show significant differences as a function of the applied load, although the values for BZY after NiO-extraction present a higher uncertainty. At the maximum load of 500 mN, the penetration depth in BZY was about 1600 nm, 1700 nm in the case of BZY-NiO and 1900 nm for BZY after NiO-extraction (**Figure 4.8a**), which results in equivalent contact diameters of about 10, 11 and 12.5 μm , respectively (**Figure 4.8**). The requirements for determining the macroscopic mechanical properties are then fulfilled except for the commercial material after NiO-extraction because of its large grain size $d = 9 \pm 3 \mu\text{m}$. This feature might explain the higher uncertainty in the experimental results.

Table 4.5. Young's modulus E and hardness H of $\text{BaZr}_{0.85}\text{Y}_{0.15}\text{O}_{2.925}$ compounds as a function of the applied load.

Applied load (mN)	BZY		BZY-NiO		BZY after NiO-extraction	
	E (GPa)	H (GPa)	E (GPa)	H (GPa)	E (GPa)	H (GPa)
10	201 ± 6	10.6 ± 0.8	214 ± 10	10.2 ± 0.6	201 ± 12	10 ± 1
30	204 ± 6	10.7 ± 0.5	206 ± 6	10.3 ± 0.5	194 ± 11	9 ± 1
60	203 ± 6	10.5 ± 0.8	208 ± 6	9.9 ± 0.3	201 ± 9	8 ± 1
100	200 ± 5	10.2 ± 0.5	208 ± 4	9.3 ± 0.3	205 ± 12	8 ± 1
500	200 ± 3	10.1 ± 0.3	207 ± 4	9.0 ± 0.3	206 ± 6	6.7 ± 0.3

Concerning the hardness, the values obtained show a decrease with increasing load. This trend is more noticeable in BZY after NiO-extraction probably because of the influence of its larger porosity (a documented ISE, Section 4.2.1.1) in the measurements.

Table 4.5 shows similar values of E for all the materials, those for commercial materials being slightly higher than for home-made BZY. However, concerning nanohardness, the results reflect larger differences which are directly related with the differences found in the load-depth curves. As the Equation (4.6) indicates, hardness is inversely proportional to the contact area, thus the deeper the penetration, the bigger the contact area and the lower the hardness. This difference in hardness was also found by microindentation tests (see Section 4.2.2.2.4 below) and may be explained by the relationship between hardness and grain size.

4.2.2.2.2 Mechanical compression tests with optical imaging

Young's modulus and Poisson ratio were determined by the stress and strain measurement within the elastic range of specimens. The experimental results obtained for the different ceramics are gathered in **Table 4.6** and show similar values of E for the commercial materials while that of BZY is slightly lower. The Poisson ratio was found to be in the range of 0.27 - 0.31.

Table 4.6. Young's modulus E and Poisson ratio ν of $\text{BaZr}_{0.85}\text{Y}_{0.15}\text{O}_{2.925}$ compounds determined by mechanical compression tests.

Material	E (GPa)	ν
BZY	186 ± 14	0.27 ± 0.13
BZY-NiO	198 ± 24	0.29 ± 0.06
BZY after NiO-extraction	191 ± 10	0.31 ± 0.05

4.2.2.2.3 Resonant Ultrasound Spectroscopy

Table 4.7 shows the experimental results obtained by RUS. With this technique both the Young's modulus and the Poisson ratio of home-made BZY were lower than those for commercial materials, being the elastic constants of BZY after NiO-extraction slightly higher than those of BZY-NiO.

Table 4.7. Young's modulus E and Poisson ratio ν of $\text{BaZr}_{0.85}\text{Y}_{0.15}\text{O}_{2.925}$ compounds determined by RUS.

Material	E (GPa)	ν
BZY	195 ± 1	0.24 ± 0.01
BZY-NiO	207 ± 1	0.26 ± 0.01
BZY after NiO-extraction	211 ± 3	0.32 ± 0.02

4.2.2.2.4 Microindentation

Figure 4.9 and **Figure 4.10** show back-scattered electron micrographs of a typical Vickers indentation on the surface of the different compounds. For BZY, symmetrical pyramid indentations were observed in which a single crack propagated from each corner along the grain boundaries. For BZY-NiO and BZY after NiO-extraction, no well-defined indentations were observed with many cracks around them which propagated both along grain boundaries and through the grains.

Based on these indentations, Vickers hardness was determined for all the compounds. However fracture toughness could not be calculated for the commercial materials due to the presence of circumferential cracks surrounding the residual imprints which prevent a reliable determination of K_{IC} . [17]. **Table 4.8** summarizes the values obtained where HV is also given in GPa for comparison with the nanohardness measured by nanoindentation (**Table 4.5**).

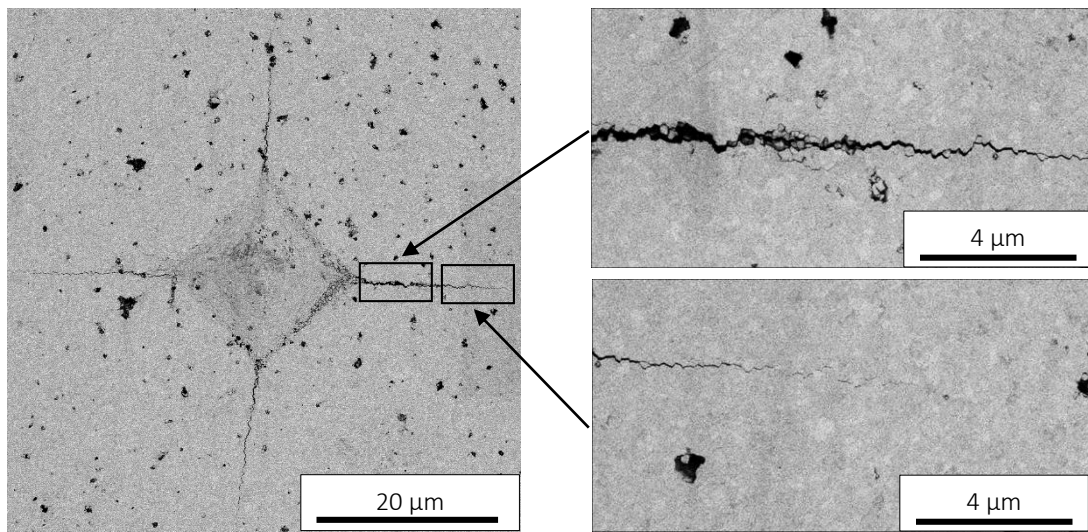


Figure 4.9. Back-scattered electron micrographs of a Vickers microindentation and cracks on the surface of BZY.

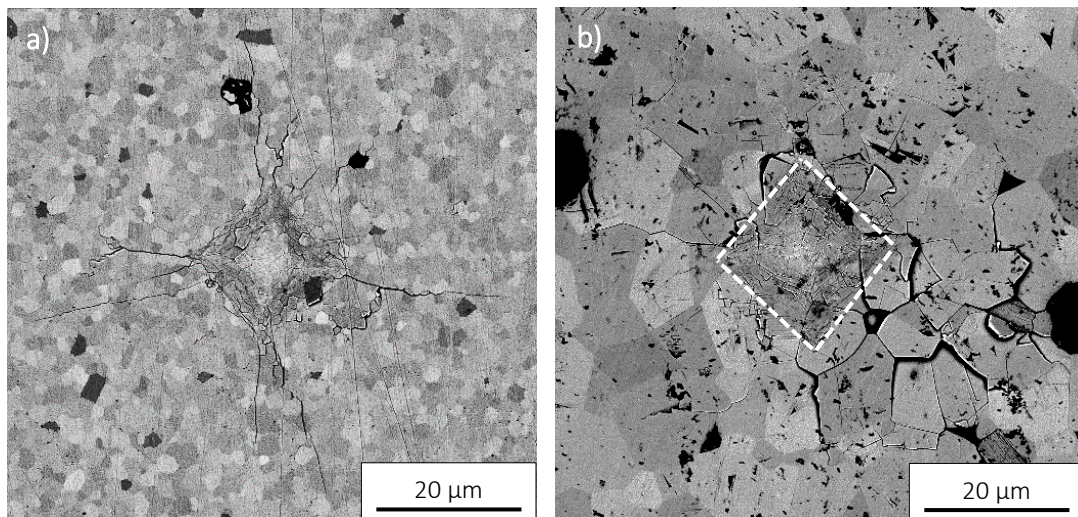


Figure 4.10. Back-scattered electron micrographs of a Vickers microindentation and cracks on the surface of (a) BZY-NiO and (b) BZY after NiO-extraction. White lines indicate the outline of the imprint.

Table 4.8. Vickers hardness HV and fracture toughness K_{IC} of $BaZr_{0.85}Y_{0.15}O_{2.925}$ compounds.

Material	HV	HV (GPa)	K_{IC} (MPa m ^{1/2})
BZY	781 ± 22	7.7 ± 0.2	1.59 ± 0.06
BZY-NiO	713 ± 30	7.0 ± 0.3	-
BZY after NiO-extraction	483 ± 17	4.7 ± 0.2	-

These results show a large difference in hardness for the different materials. Considering the Hall-Petch law which predicts that yield strength is inversely proportional to grain size and the relationship between Vickers hardness and yield strength (Equation 4.21 [14]), the hardening of the

home-made BZY could be ascribed to its smaller grain size in comparison with the commercial BZY-NiO ($0.2 \pm$ and $1.6 \mu\text{m}$, respectively). It also would allow explaining the softening of the BZY after NiO-extraction since the grain size increased from 1.6 to $9 \mu\text{m}$ after extraction, resulting in a significant reduction of hardness. However, others factors as the increase in porosity also contributes to decrease this magnitude [12].

Concerning Y-doped Barium Zirconates, only one previous work deals with the mechanical properties of similar compounds by microindentation [18]. In this case, it was reported a Vickers hardness of 742 ± 7 and a fracture toughness of $1.58 \pm 0.13 \text{ MPa m}^{1/2}$ for BZY10, in agreement with the present results.

4.2.2.2.5 Comparison of the different techniques

The values of the Young's modulus obtained by the different techniques were in the range of $179 - 211 \text{ GPa}$. E values from RUS were always larger than those obtained by compression tests and very similar to nanoindentation tests although with a lower uncertainty. On the contrary, the values of the Poisson ratio obtained by compression tests were slightly higher than those obtained by RUS, displaying also a higher dispersion. The elastic properties of Y-doped Barium Zirconate have not been studied previously. At least for the mechanical properties, this material may be compared with undoped- Barium Zirconate. For example, Vassen *et al.* [19] reported values of E of 181 GPa for BaZrO_3 which is comparable with the results obtained in this work. Regarding hardness, the values obtained by nanoindentation were significantly lower than those obtained by microindentation, as expected due to the hardness dependence with applied load. For Yttrium-doped Barium Zirconate, Sazinas *et al.* [18] found a value of $HV = 7.3 \text{ GPa}$, which agree with the results reported in this study.

4.3 DENSITY FUNCTIONAL THEORY CALCULATIONS

Density Functional Theory (DFT) is an approach to compute the electronic structure of atoms, molecules and materials. DFT allows to determine the ground-state properties of a system by means of functionals, i.e. functions of another function that depends on electron density. Thus, the name of this theory derives from the use of electron density functionals. DFT is currently one of the most popular and versatile techniques in Physics of Condensed Matter. In particular, this theory has been widely used in Solid State Physics since the 1970s. In Chemistry, however, it was considered not to be a theory precise enough for calculations until the 1990s, when the

approximations were refined in order to better model the exchange and correlation interactions. One of the main advantages of DFT is its computational cost, which is relatively low in comparison to conventional methods. Details on the method are not given here but can be found in the specific literature [20-22]. The obtained results have been used in a forthcoming part (Chapter 5).

4.3.1 DFT calculation procedure: Elastic coefficients determination

DFT was carried out to calculate the elastic properties of Lanthanum Silicates and Yttrium-doped Barium Zirconate, in particular to determine possible elastic anisotropies in oxy-apatites and to understand the effect of hydration in Barium Zirconate. Calculations were performed by G. Dezanneau (SPMS / CNRS - CentraleSupélec) and G. Geneste (CEA/DAM) for oxy-apatites and Barium Zirconates compounds, respectively.

The process starts by performing a precise structural relaxation of the original structure to a zero-stress state which corresponds to the most stable state at 0 K. Then, the lattice vectors are subjected to perturbations, and DFT allows to calculate the resulting stress tensor and the associated energy. Subsequently, the relationship between stress and strain from linear elasticity is used to fit the full elastic tensor. Finally, aggregate properties can also be derived and compared to measurements of elastic properties in ceramics.

More concretely, two kinds of formula can be used to determine the elastic tensor from DFT calculations. The first approach follows:

$$\begin{bmatrix} \sigma_1 \\ \sigma_2 \\ \sigma_3 \\ \sigma_4 \\ \sigma_5 \\ \sigma_6 \end{bmatrix} = \begin{bmatrix} C_{11} & C_{12} & C_{13} & C_{14} & C_{15} & C_{16} \\ & C_{22} & C_{23} & C_{24} & C_{25} & C_{26} \\ & & C_{33} & C_{34} & C_{35} & C_{36} \\ & & & C_{44} & C_{45} & C_{46} \\ & & & & C_{55} & C_{56} \\ & & & & & C_{66} \end{bmatrix} \begin{bmatrix} \epsilon_1 \\ \epsilon_2 \\ \epsilon_3 \\ \epsilon_4 \\ \epsilon_5 \\ \epsilon_6 \end{bmatrix}$$

Where the elastic coefficients C_{ij} are determined from the knowledge of the applied strain chosen by the operator and the associated stress, calculated through DFT calculations. The strength of this approach is that strain can be chosen arbitrarily so it is possible to study specific components of the elastic matrix.

The second formulation uses the Taylor expansion till the second order of the unit cell energy with strain:

$$E(\boldsymbol{\varepsilon}) = E(0) + \sum_i^6 \frac{\delta E}{\delta \varepsilon_i} \cdot \varepsilon_i + \frac{1}{2} \sum_{i,j}^6 \frac{\delta^2 E}{\delta \varepsilon_i \delta \varepsilon_j} \cdot \varepsilon_i \varepsilon_j \quad (4.22)$$

where $E(0)$ refers to the equilibrium configuration, the first derivatives being zero. According to this equation, the elastic constants can then be obtained by evaluating the energy as a function of strain.

In both approaches, several perturbations are used in order to fit the linear behaviour of the stress with applied strain with a significant amount of points (typically 10 points are used thus 10 DFT calculations are made to determine one elastic coefficient C_{ij}). In all cases, the maximum applied strain was limited to 1% in order to respect the laws presented before.

4.3.1.1 DFT Calculations details for Lanthanum Silicate oxy-apatites

For the determination of the elastic tensor in oxy-apatite, calculations were performed using the commercial program VASP. The interactions between electrons and ions were described by the potential Projector Augmented Wave (PAW) method [23] within the generalized gradient approximation (GGA). The wavefunctions are then expanded in terms of a discrete plane wave basis set, which is truncated at a predefined maximum cut-off energy, the rest of the coefficients in the expansion are set to zero. A careful analysis of the convergence of the calculated total energy, within a given tolerance, with the cut-off energy was firstly conducted, showing that a value of 800 eV was adequate enough to ensure stress and energy values convergence. The k-point mesh for the Brillouin zone integration was selected according to the Monkhorst–Pack scheme with 6*6*6 Brillouin zone sampling.

The nominal composition $\text{La}_{9.33}\text{Si}_6\text{O}_{26}$ supposes that it exists one lanthanum vacancy in the structure per 3 unit cells. The presence of this lanthanum vacancy complicates the analysis since it breaks the overall symmetry. Thus, in order to keep the hexagonal symmetry to calculate the elastic properties, the lanthanum sites were thus kept fully occupied which leads to a nominal composition of $\text{La}_{10}\text{Si}_6\text{O}_{26}$ per unit cell. From a solid state chemistry point of view, this corresponds to a situation where the original compound $\text{La}_{10}\text{Si}_6\text{O}_{27}$ would have lost 1 oxygen atom (ideally the interstitial one), for instance in reducing conditions. The main advantage of such an approach is that, all along the analysis, we can perform the calculations in the original hexagonal cell with unit cell parameters $a \simeq 9.8 \text{ \AA}$ and $c \simeq 7.2 \text{ \AA}$ and thus keep a simplified elastic tensor. The elasticity tensor for a hexagonal

phase only presents 5 independent elastic coefficients, while null and coupled coefficients exist due to symmetry as represented in **Figure 4.11**:

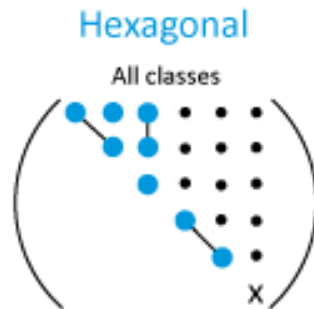


Figure 4.11. Simplified scheme of the elastic tensor in hexagonal phase, where $X=(C_{11}-C_{12})/2$ [24].

4.3.1.2 DFT calculations for Yttrium-doped Barium Zirconates

Calculations were performed using the code ABINIT. The interaction of electron-ion was taken into account here in the same form than for oxy-apatite. The wave functions were expanded in a set of plane waves up to a kinetic energy cut-off of 680 eV, which ensured a good convergence of energy and stress values. The k-point meshes were selected according to the Monkhorst-Pack scheme. Depending on the size of the system, containing respectively 5, 40 and 135 atoms, the Brillouin zone sampling was adapted to be 6*6*6, 4*4*4 and 2*2*2, respectively. Several calculations were performed to take into account the presence of defects like dopant ions, oxygen vacancies and protons. The main difficulty here lies in the choice of a system of limited size that would be representative of the whole disordered material. In particular, it is clear that the introduction of these defects breaks the original cubic symmetry of BaZrO₃.

4.3.2 DFT calculation results

4.3.2.1 Elastic properties of Lanthanum Silicate

Prior to the calculations of the elastic coefficients, we determined the ground state of the La₁₀Si₆O₂₆ composition through DFT calculations. Lattice constants and internal positions in the perfect unit cell were fully optimized until the free energy difference between two optimisation runs was below 10⁻⁶ eV. We verified that the values of the stress components for this configuration were smaller than 0.005 GPa. The refined cell parameters after relaxation were $a = 9.8259 \text{ \AA}$ and $c = 7.2651 \text{ \AA}$, which are in very good agreement (error ~1%) with the cell parameters $a = 9.7248 \text{ \AA}$ and $c = 7.1895 \text{ \AA}$ measured for La_{9.33}Si₆O₂₆ at room temperature [25] and with $a = 9.7393 \text{ \AA}$ and $c = 7.2071 \text{ \AA}$ measured for La₁₀Si₆O₂₇ [26].

The elastic coefficients were then calculated considering 10 configurations for each of the specific stress-strain configurations. The resulting elastic tensor is the following:

$$C_{ij} \text{ (GPa)} = \begin{vmatrix} 177.6(8) & 66.4(4) & 84.6(9) & 0 & 0 & 0 \\ 66.4(4) & 177.6(8) & 84.6(9) & 0 & 0 & 0 \\ 84.6(9) & 84.6(9) & 194.1(7) & 0 & 0 & 0 \\ 0 & 0 & 0 & 49.9(9) & 0 & 0 \\ 0 & 0 & 0 & 0 & 49.9(9) & 0 \\ 0 & 0 & 0 & 0 & 0 & 55.6(6) \end{vmatrix}$$

These calculations reveal a slight anisotropy of the elastic tensor, in particular a ~8% difference for the elastic longitudinal response between a , b axes and c axes. We will see in the following chapter that this anisotropic elastic tensor coupled to the anisotropic thermal expansion is at the origin of the presence of residual stresses in oxy-apatites polycrystalline materials, in particular after sintering. **Table 4.9** shows the elastic properties of lanthanum silicate polycrystals calculated by DFT calculations, which are comparable to the elastic coefficients mentioned above.

Table 4.9. Elastic properties of lanthanum silicate polycrystals deduced from the elastic tensor calculated by DFT calculations.

Averaging scheme	Bulk modulus (GPa)	Young's modulus (GPa)	Shear modulus (GPa)	Poisson's ratio
Voigt	112.8	134.4	51.6	0.301
Reuss	111.7	133.6	51.4	0.300
Hill	112.0	134.0	51.5	0.301

4.3.2.2 Elastic properties of Y-doped Barium Zirconate

Firstly, pure Barium Zirconate has been modelled. The material has cubic symmetry and the cell parameter as refined to be $a = 4.235 \text{ \AA}$. Different Y-doping levels have been then tested, where the compensating charge (usually oxygen vacancy) was in this case defined as a charge spreading over the whole supercell (jellium). Elastic properties were not calculated for dry BZY *i.e.* when the yttrium-dopant is compensated by an oxygen vacancy because it supposes to use a much bigger supercell. And more important, symmetry properties are fully lost in this case making the elastic tensor determination very complex (if not meaningless). BZY properties were nevertheless calculated in its wet state *i.e.* when the dopant is compensated by a proton, the oxygen lattice being in this case fully occupied. For wet BZY, the doping level was 12.5% and the proton was set at its

more stable position, the first neighbour position in reference to the dopant as shown in previous calculations. The resume of these calculations are reported in **Table 4.10**.

Table 4.10. Results of calculated cell parameters and elastic parameters for pure and Y-doped Barium Zirconate (the actual supercell has orthorhombic symmetry with $a = 4.267 \text{ \AA}$, $b = 4.234 \text{ \AA}$, $c = 4.279 \text{ \AA}$; the actual Young's moduli along a , b and c axes are respectively 207, 209, 230 GPa).

Doping level	a cell parameter (\AA)	Young's modulus (GPa)	Poisson's ratio	Bulk modulus (GPa)	Shear Modulus (GPa)
0 %	4.235	259	0.215	150.8	107
3.7 %	4.251	253	0.213	142.9	104
12.5 %	4.284	231	0.207	130.4	96
12.5% + H ⁺	4.260 ^f	215 ^g			

These results clearly show that the doping with Yttrium tends to diminish the elastic coefficients, keeping almost constant the Poisson ratio. Moreover, the presence of protons tends to reduce even more the Young's modulus. Further works are nevertheless needed to determine more efficiently and more precisely the elastic coefficients for large supercells, that would keep the observed cubic symmetry. This goes well beyond the objective of the current work. It seems nevertheless clear from these calculations that dry and wet BZY compounds should present different elastic coefficients.

4.4 REFERENCES

1. Pharr, G.M., Measurement of mechanical properties by ultra-low load indentation. *Materials Science and Engineering: A*, 1998. 253(1–2): p. 151-159.
2. Oliver, W.C. and G.M. Pharr, An improved technique for determining hardness and elastic modulus using load and displacement sensing indentation experiments. *Journal of materials research*, 1992. 7(06): p. 1564-1583.
3. Doerner, M.F. and W.D. Nix, A method for interpreting the data from depth-sensing indentation instruments. *Journal of Materials research*, 1986. 1(04): p. 601-609.
4. Oliver, W.C. and G.M. Pharr, Measurement of hardness and elastic modulus by instrumented indentation: Advances in understanding and refinements to methodology. *Journal of materials research*, 2004. 19(01): p. 3-20.
5. Leisure, R.G. and F. Willis, Resonant ultrasound spectroscopy. *Journal of Physics: Condensed Matter*, 1997. 9(28): p. 6001.

6. Migliori, A., et al., Resonant ultrasound spectroscopic techniques for measurement of the elastic moduli of solids. *Physica B: Condensed Matter*, 1993. 183(1): p. 1-24.
7. Bernard, S., Q. Grimal, and P. Laugier, Resonant ultrasound spectroscopy for viscoelastic characterization of anisotropic attenuative solid materials. *The Journal of the Acoustical Society of America*, 2014. 135(5): p. 2601-2613.
8. Niihara, K., R. Morena, and D. Hasselman, Evaluation of K_{Ic} of brittle solids by the indentation method with low crack-to-indent ratios. *Journal of Materials Science Letters*, 1982. 1(1): p. 13-16.
9. Roa, J.J., et al., Nanohardness and Young's modulus of YBCO samples textured by the Bridgman technique. *Nanotechnology*, 2007. 18(38): p. 385701.
10. Milman, Y.V., A.A. Golubenko, and S.N. Dub, Indentation size effect in nanohardness. *Acta Materialia*, 2011. 59(20): p. 7480-7487.
11. Morales, M., et al., Mechanical properties at the nanometer scale of GDC and YSZ used as electrolytes for solid oxide fuel cells. *Acta Materialia*, 2010. 58(7): p. 2504-2509.
12. McColm, I.J., *Ceramic hardness*. 1990, New York: Plenum Press.
13. Santos, M., et al., Mechanical properties of sintered $\text{La}_{0.93}\text{Si}_2\text{Ge}_4\text{O}_{26}$ oxyapatite materials for SOFC electrolytes. *Ceramics International*, 2012. 38(8): p. 6151-6156.
14. Knott, J.F., *Fundamentals of fracture mechanics*. 1973: Gruppo Italiano Frattura.
15. Suarez, G., et al., Electrophoretic deposition for obtaining dense lanthanum silicate oxyapatite (LSO). *Ceramics International*, 2016. 42(16): p. 19283-19288.
16. Roa, J.J., et al., Determination of hardness, Young's modulus and fracture toughness of lanthanum tungstates as novel proton conductors. *Ceramics International*, 2011. 37(5): p. 1593-1599.
17. Cook, R.F. and G.M. Pharr, Direct Observation and Analysis of Indentation Cracking in Glasses and Ceramics. *Journal of the American Ceramic Society*, 1990. 73(4): p. 787-817.
18. Sazinas, R., M.-A. Einarsrud, and T. Grande, Toughening of Y-doped BaZrO_3 proton conducting electrolytes by hydration. *Journal of Materials Chemistry A*, 2017. 5(12): p. 5846-5857.
19. Vassen, R., et al., Zirconates as New Materials for Thermal Barrier Coatings. *Journal of the American Ceramic Society*, 2000. 83(8): p. 2023-2028.
20. Sholl, D. and J.A. Steckel, *Density functional theory: a practical introduction*. 2011: John Wiley & Sons.
21. Perdew, J.P. and S. Kurth, Density functionals for non-relativistic Coulomb systems in the new century, in *A primer in density functional theory*. 2003, Springer. p. 1-55.
22. Fiolhais, C., F. Nogueira, and M.A. Marques, *A primer in density functional theory*. Vol. 620. 2003: Springer Science & Business Media.

23. Kresse, G. and D. Joubert, From ultrasoft pseudopotentials to the projector augmented-wave method. *Physical Review B*, 1999. 59(3): p. 1758.
24. Nye, J.F., *Physical properties of crystals: their representation by tensors and matrices*. 1985: Oxford university press.
25. Sansom, J., D. Richings, and P. Slater, A powder neutron diffraction study of the oxide-ion-conducting apatite-type phases, $\text{La}_{9.33}\text{Si}_6\text{O}_{26}$ and $\text{La}_8\text{Sr}_2\text{Si}_6\text{O}_{26}$. *Solid State Ionics*, 2001. 139(3): p. 205-210.
26. Chesnaud, A., et al., Influence of synthesis route and composition on electrical properties of $\text{La}_{9.33+x}\text{Si}_6\text{O}_{26} + 3x/2$ oxy-apatite compounds. *Solid State Ionics*, 2008. 179(33–34): p. 1929-1939.

Chapter 5

THERMO-MECHANICAL CHARACTERIZATION

Contents

5.1 Introduction	120
5.2 Experimental characterization of thermo-mechanical properties	120
5.2.1 Experimental procedure	120
5.2.1.1 High-temperature X-Ray diffraction	120
5.2.1.2 Thermo-mechanical analysis	121
5.2.1.3 High-temperature Resonant Ultrasound Spectroscopy	122
5.2.2 Experimental results	123
5.2.2.1 Thermo-mechanical properties of Lanthanum Silicate	123
5.2.2.1.1 Coefficient of thermal expansion	123
5.2.2.1.2 Elastic constants	124
5.2.2.2 Thermo-mechanical properties of Yttrium-doped Barium Zirconate	126
5.2.2.2.1 Coefficient of thermal expansion	126
5.2.2.2.2 Elastic constants	127
5.3 Numerical simulation of residual stresses state in lanthanum silicate	128
5.3.1 Computation procedure	129
5.3.1.1 Description of microstructure	129
5.3.1.2 Numerical simulations	131
5.3.1.2.1 Material properties	131
5.3.1.2.2 Loading and boundary conditions	132
5.3.1.3 Analysis of Stress fields: Localization and prediction of fracture	135
5.3.1.3.1 Maximum principal stress theory	135
5.3.1.3.2 Stress intensity approach	136
5.3.1.4 Strategy of Simulations	137
5.3.1.4.1 Determination of the Mesh Size	137
5.3.1.4.2 Multiple realizations	138
5.3.2 Computation results	139
5.3.2.1 Distribution of stresses	139
5.3.2.2 Prediction of failure	141

5.1 INTRODUCTION

This chapter studies the influence of the temperature on the mechanical properties, including the coefficient of thermal expansion and elastic constants, of Lanthanum Silicates and Yttrium-doped Barium Zirconate. Besides the characterization of the materials as a function of temperature, this information is useful to simulate their behaviour and understand their mechanical response, which is particularly interesting in the case of oxy-apatite because of its anisotropic thermo-elastic properties. The last part of this chapter is therefore focused on studying the residual stress state of this material by finite elements numerical simulations, in order to get a deeper understanding of the potential failure mechanisms and to improve the fabrication processes and applications.

5.2 EXPERIMENTAL CHARACTERIZATION OF THERMO-MECHANICAL PROPERTIES

5.2.1 Experimental procedure

In this study, the coefficient of thermal expansion was experimentally determined at atomic and macroscopic scales by high-temperature XRD and thermo-mechanical analysis, respectively, while the temperature dependence of Young's modulus, Poisson ratio and shear modulus was measured by high-temperature RUS. The macroscopic temperature dependence of the thermal expansion coefficient and elastic constants of samples was determined considering the materials to be isotropic, as the grains are randomly oriented in the samples. However, HT-XRD allows to evaluate the possible anisotropic evolution of the coefficient of thermal expansion at the crystal scale, which is especially interesting in the case of the Lanthanum silicate due to its anisotropic nature. Experiments were carried out in air on specimens of approximately 5 x 3 x 3 mm³ in size which were cut from the sintered pellets with a low-speed diamond saw. After cutting, the samples were rectified to eliminate imperfections and to ensure completely flat-parallel surfaces to avoid wrong estimations of the mechanical parameters.

5.2.1.1 High-temperature X-Ray diffraction

The linear thermal expansion coefficient (α) of the different materials was measured by means of high-temperature X-Ray diffraction. XRD analysis was carried out on a Bruker D8C

diffractometer (X-ray Laboratory, CITIUS, University of Seville, Spain) with Ni-filtered Cu-K α radiation ($\lambda = 1.54060 \text{ \AA}$) in Bragg-Brentano configuration and equipped with an Anton Paar XRK 900 high-temperature chamber. Measurements were carried out on LSO calcined nanopowders and BZY sintered ceramics from room temperature up to 900 °C with heating and cooling ramps of 10 °C/min. Data were collected every 50 °C at constant temperature during the heating/cooling ramps in the 2θ region between 20° and 90° in steps of 0.02° and an acquisition time of 0.2 s/step. Recorded XRD spectra were analyzed by the Le Bail refinement method [1] using the TOPAS 4.2 Bruker AXS software package .

The coefficient of thermal expansion was determined from the relative change in unit cell parameter with temperature:

$$\alpha_{\text{XRD}} = \frac{1}{a_0} \frac{\Delta a}{\Delta T} \quad (5.1)$$

where Δa is the variation of the unit cell parameter corresponding to a temperature change ΔT , and a_0 is the lattice parameter at room temperature. In the case of LSO, both cells parameters a and c can be evaluated with this method in order to study the anisotropic thermal behaviour of a single crystal.

5.2.1.2 Thermo-mechanical analysis

The thermal expansion coefficient was also evaluated by thermo-mechanical analysis, a technique used to measure macroscopic dimensional changes of a material as a function of temperature. Measurements were performed using a TMA Q1000 Thermo-mechanical analyzer (Functional Characterization Laboratory, CITIUS, University of Sevilla, Spain) from room temperature up to 1000 °C with heating/cooling ramps at 5 °C/min. Measurements were carried out at a constant load of 500 mN.

For the macroscopic case, bulk specimen is isotropic, and Equation 5.1 can be rewritten as:

$$\alpha_{\text{TMA}} = \frac{1}{L_0} \frac{\Delta L}{\Delta T} \quad (5.2)$$

where L_0 is the initial sample length and ΔL is the change in specimen length for a given ΔT .

Sample mass and dimensions were measured before and after tests to check the validity of the results.

5.2.1.3 High-temperature Resonant Ultrasound Spectroscopy

The temperature dependence of the elastic constants was determined using a high-temperature RUS setup (Department of Earth Sciences, University of Cambridge, UK) equipped with a controlled-atmosphere system. A prismatic sample was placed between the tips of the alumina rods (Figure 5.1), while transducers were glued to the other ends of the rods and used as emitters and receivers of the ultrasonic excitation; the rods are used as ultrasonic transmission lines to allow the piezoelectric emitter-receiver to be located in the cold zone. Temperature was monitored by a thermocouple placed close to the sample. Spectra were collected every 50 °C at constant temperature; a 20 min-dwell was used at each measurement to achieve thermal equilibrium.



Figure 5.1. High-temperature Resonant Ultrasound Spectroscopy system at the University of Cambridge [2].

Measurements were carried out from room temperature up to 1100 °C at resonant frequencies of vibration between 0.1 and 2 MHz. Fundamentals and procedures of RUS were already addressed in Section 4.2.1.3. Measurements were performed at Professor Michael A. Carpenter's group at Department of Earth Sciences of the University of Cambridge while the analysis of data was realized by X. Bril from SPMS laboratory. It is worth noting here that the dimensions of the sample used in the analysis were those at room temperature and were not corrected for thermal expansion. A more precise analysis would include the sample dimensions variation in the analysis. It is important noting here that sample dimensions vary by ~1% for the explored range of temperature, which is significantly smaller (but not negligible) compared to the elastic constants variation for the same range of temperatures.

5.2.2 Experimental results

5.2.2.1 Thermo-mechanical properties of Lanthanum Silicate

5.2.2.1.1 Coefficient of thermal expansion

As indicated before, the coefficient of thermal expansion was evaluated by two methods. On the one hand, it was calculated from the expansion of the lattice volume with temperature measured by HT-XRD. **Figure 5.2** shows the evolution of cell parameters a and c with temperature for oxy-apatite nanopowders. We deliberately chose a nanopowder and not a bulk ceramic to avoid internal stress effects. As evidenced by **Figure 5.2**, the lattice parameters increase linearly with temperature.

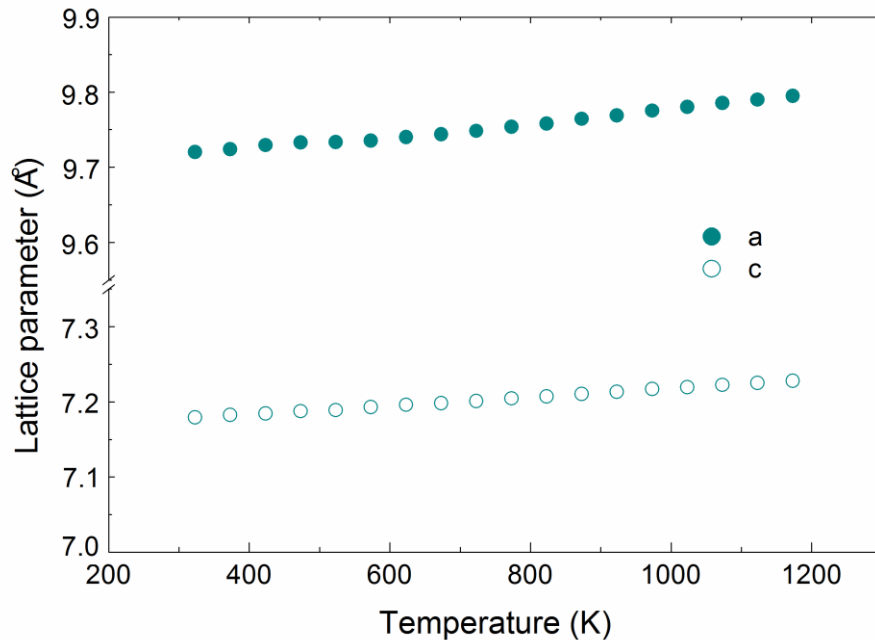


Figure 5.2. Variation in lattice parameters a and c of oxy-apatite calcined nanopowder as a function of temperature.

The thermal expansion coefficient of calcined nanopowders was calculated, following Equation 5.1, as the slope of the plot of expansion ($\Delta a/a_0$) vs temperature. The value of α_{XRD} along the a -axis obtained in the temperature range from 323 to 1173 K was $9.5 \times 10^{-6} \text{ K}^{-1}$, while along the c -axis was $8.2 \times 10^{-6} \text{ K}^{-1}$. These results reveal a slight difference in the oxy-apatite thermal expansion coefficients between a and c axes confirming the anisotropy of its thermal behaviour. Moreover, the isotropic thermal expansion was calculated from the variation of the volume cell with temperature, yielding a value of $9.2 \times 10^{-6} \text{ K}^{-1}$. These values are very different to those obtained by Fokuda *et al.* [3] for $\text{La}_{9.33}\text{Si}_6\text{O}_{26}$ in the temperature range from 298 K to 1473 K. They found a

thermal expansion coefficient of $4.8 \times 10^{-6} \text{ K}^{-1}$ and $1.8 \times 10^{-6} \text{ K}^{-1}$ along the a-axis and c-axis, respectively, with a mean value of $3.8 \times 10^{-6} \text{ K}^{-1}$.

On the other hand, α was also determined from macroscopic changes in sample length with temperature measured by TMA. For the temperature interval of 298 to 1173 K, an identical value of $\alpha_{\text{TMA}} = 9.1 \times 10^{-6} \text{ K}^{-1}$ was estimated for both LSO-CS and LSO-SPS (**Figure 5.3**).

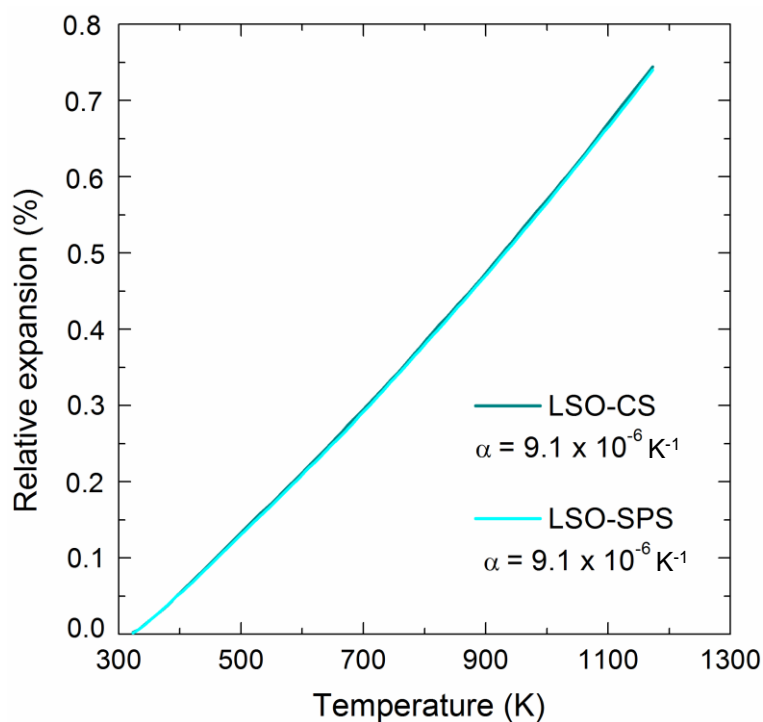


Figure 5.3. Relative thermal expansion of LSO-CS and -SPS as a function of temperature.

The isotropic results obtained by both methods agree very well to each other, and are comparable to the thermal expansion coefficients of LSO reported in the literature. Iwata *et al.* [4] reported a value of $9.4 \times 10^{-6} \text{ K}^{-1}$ for $\text{La}_{9.33}\text{Si}_6\text{O}_{26}$ from 295 to 1073 K. Similarly, in $\text{La}_{10}\text{Si}_6\text{O}_{27}$ compound, Jiang *et al.* [5] found values of α between 9.7×10^{-6} and $10.3 \times 10^{-6} \text{ K}^{-1}$ at temperatures between room temperature and 1173 K. The coefficient of thermal expansion found here is independent of the processing method and material microstructure. It is worth also mentioning that the α values for oxy-apatite are very similar to those found in other electrolyte materials, e.g. $10.0 \times 10^{-6} \text{ K}^{-1}$ for YSZ [6] and $11.8 \times 10^{-6} \text{ K}^{-1}$ for $\text{Ce}_{0.8}\text{Gd}_{0.2}\text{O}_2$ [7].

5.2.2.1.2 Elastic constants

HT-RUS measurements were carried out to determine the elastic constants, Young's modulus E , Poisson ratio ν and shear modulus G , of the materials as a function of temperature. The

shear modulus measured here will be used later to deduce the effective diffusion coefficients of the fine-grained materials from creep data (Chapter 6).

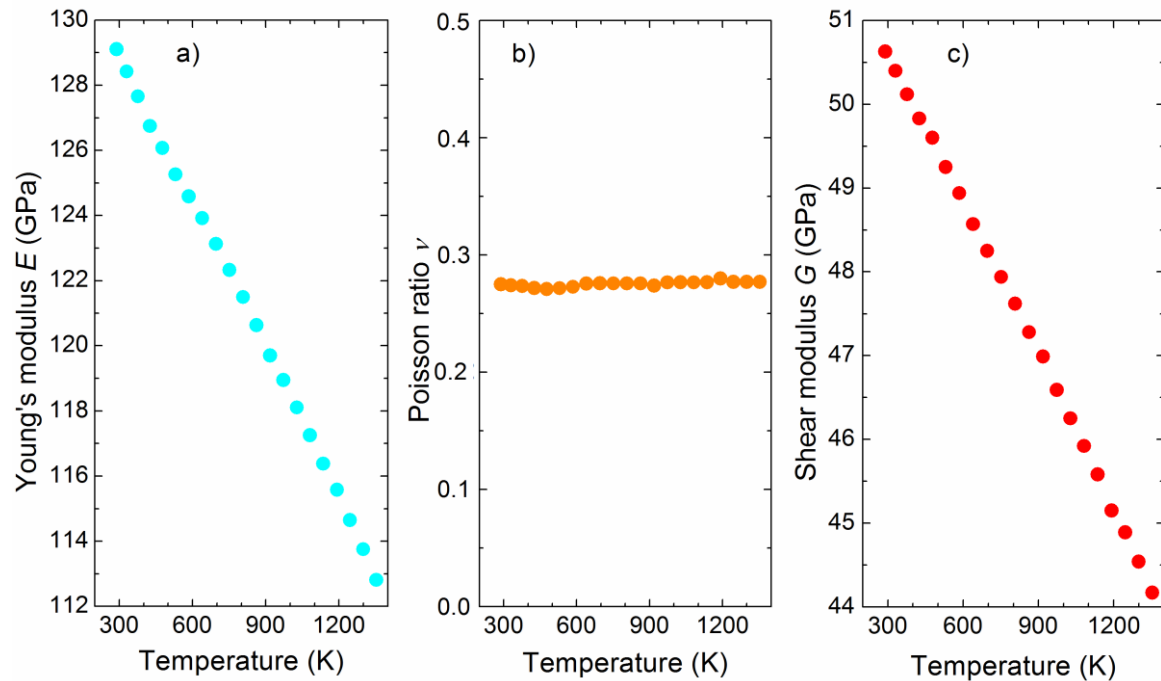


Figure 5.4. Temperature dependence of (a) Young's modulus, (b) Poisson ratio and (c) shear modulus of LSO-SPS. The uncertainty is about 4% in the Young's modulus, 6% in the Poisson ratio and 0.2% in the shear modulus.

Figure 5.4 shows the evolution of Young's modulus, Poisson ratio and shear modulus of LSO-SPS with temperature. As can be observed the Young's modulus decreases linearly from 129 to 113 GPa in the range of temperatures from 298 to 1353 K, which means a drop of about 12% (**Figure 5.4a**). The same tendency is observed (for the shear modulus, which also exhibits a reduction of 12% (from 51 to 45 GPa) in the same range of temperatures (**Figure 5.4c**). These results are in agreement with the rule of thumb for ceramics which predicts a decrease in E and G of about 1% for every 100 K-increase in temperature [8]. On the other hand, the Poisson ratio has been found to be practically constant with temperature, with a value $\nu = 0.275 \pm 0.002$. Temperature-dependent Poisson ratios have been reported in the literature for brittle materials [9, 10]. For example, Fukuhara et al. [11] found an increase in ν from 0.316 to 0.350 with increasing temperature from 295 to 1173 K in Yttria-stabilized Tetragonal Zirconia Polycrystals (YTZP), while a rather constant value of 0.27 was reported in the same study for β' -Sialon. Since the Poisson ratio is defined as:

$$\nu = \frac{(E - 2G)}{2G} \quad (5.3)$$

the temperature dependence of ν is related to the relative change between E and G with temperature. Thus, due to the fact that both moduli exhibit exactly the same reduction, the Poisson ratio remains constant (**Figure 5.4b**).

5.2.2.2 Thermo-mechanical properties of Yttrium-doped Barium Zirconate

5.2.2.2.1 Coefficient of thermal expansion

Figure 5.5 shows the temperature dependence of the unit cell parameter a for BZY and BZY-NiO sintered ceramics measured by HT-XRD. As expected, the lattice parameter increases almost linearly with temperature. The thermal expansion coefficient was calculated by using Equation 5.1, resulting in a value of α_{XRD} obtained in the temperature range from 323 to 1173 K of $8.4 \times 10^{-6} \text{ K}^{-1}$ and $8.1 \times 10^{-6} \text{ K}^{-1}$ for BZY and BZY-NiO respectively.

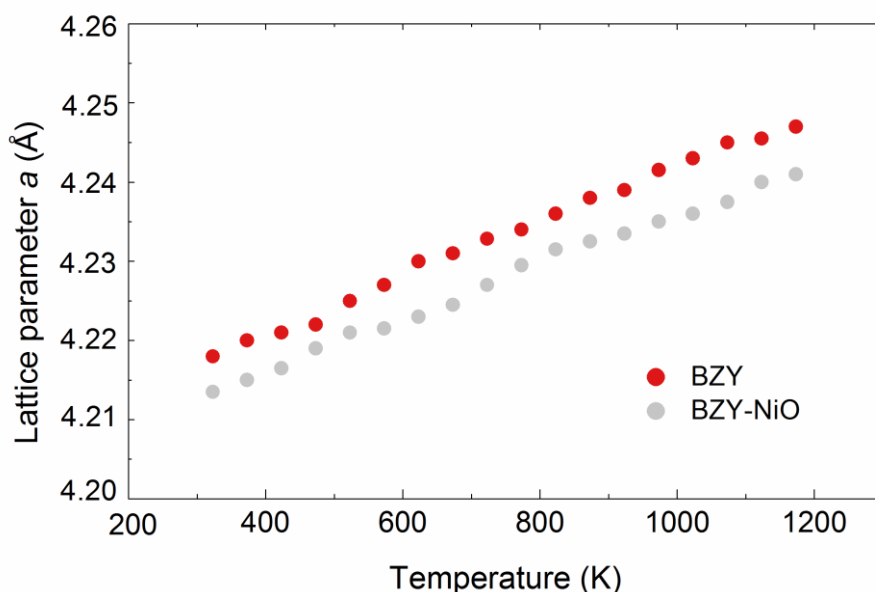


Figure 5.5. Variations in lattice parameter with temperature in dry air of (a) BZY and (b) BZY-NiO, measured by HT-XRD.

On the other hand, α was also determined from changes in sample length with temperature measured by TMA in the same temperature range 298 - 1173 K (**Figure 5.6**). The values of α_{TMA} obtained were $8.5 \times 10^{-6} \text{ K}^{-1}$ and $8.2 \times 10^{-6} \text{ K}^{-1}$ for BZY and BZY-NiO, respectively, in excellent agreement with those measured by at atomic scale by HT-XDR and close to the values reported for

Barium Zirconate ceramics. They are also similar to the values reported in the literature. For undoped BaZrO_3 , α varies between 6.26×10^{-6} and $8.02 \times 10^{-6} \text{ K}^{-1}$ [12-15]. Regarding the Y-doping, Han *et al.* [12] measured the thermal expansion coefficient by HT-XRD on 2 to 30 at% yttrium-doped Barium Zirconate, finding values from $8.47 \times 10^{-6} \text{ K}^{-1}$ to $10.2 \times 10^{-6} \text{ K}^{-1}$ with increasing the doping level; a value of $9.25 \times 10^{-6} \text{ K}^{-1}$ was reported for BZY15, the same nominal composition used in this work, under dry Ar atmosphere. Similarly, Lyagaeva *et al.* [16] reported a mean value of $8.2 \times 10^{-6} \text{ K}^{-1}$ in the temperature range of 50-900 °C, for BZY electrolytes.

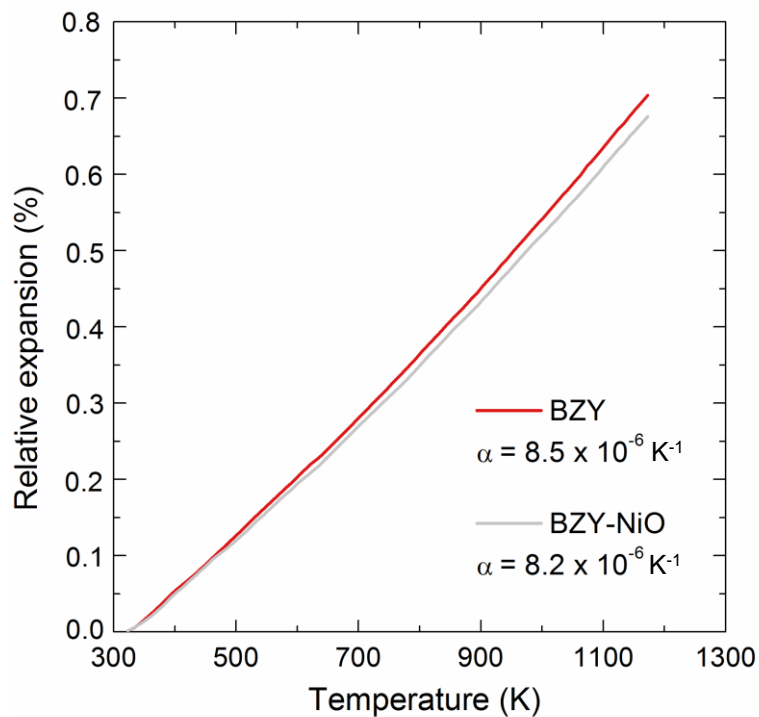


Figure 5.6. Relative thermal expansion of BZY and BZY-NiO as a function of temperature.

5.2.2.2.2 Elastic constants

Figure 5.7 shows the variations of the Young's modulus, Poisson ratio and shear modulus of home-made BZY with temperature. Both elastic moduli decrease with increasing temperature, while the Poisson ratio remains once more practically constant. The same behaviour was found in the oxy-apatite. As can be observed in Figure 5.7a, the Young's modulus decreases from 204 to 176 GPa in the range of temperatures from 288 to 1300 K, which means a drop of about 13%. The shear modulus decreases from 82 to 71 GPa, exhibiting also a reduction of 13% in the same range of temperatures (Figure 5.7c). These results are again in good agreement with the expected reduction of about 1% for each 100 K of temperature increase [8]. As discussed previously for the case of the oxy-apatite, the Poisson ratio follows the relative change between E and G with temperature

(Equation 5.3), thus remaining constant with a value of 0.24 ± 0.01 (Figure 5.7b). This result is identical to that of BZY measured at room temperature in our laboratory (Chapter 4), confirming the excellent reproducibility of the results.

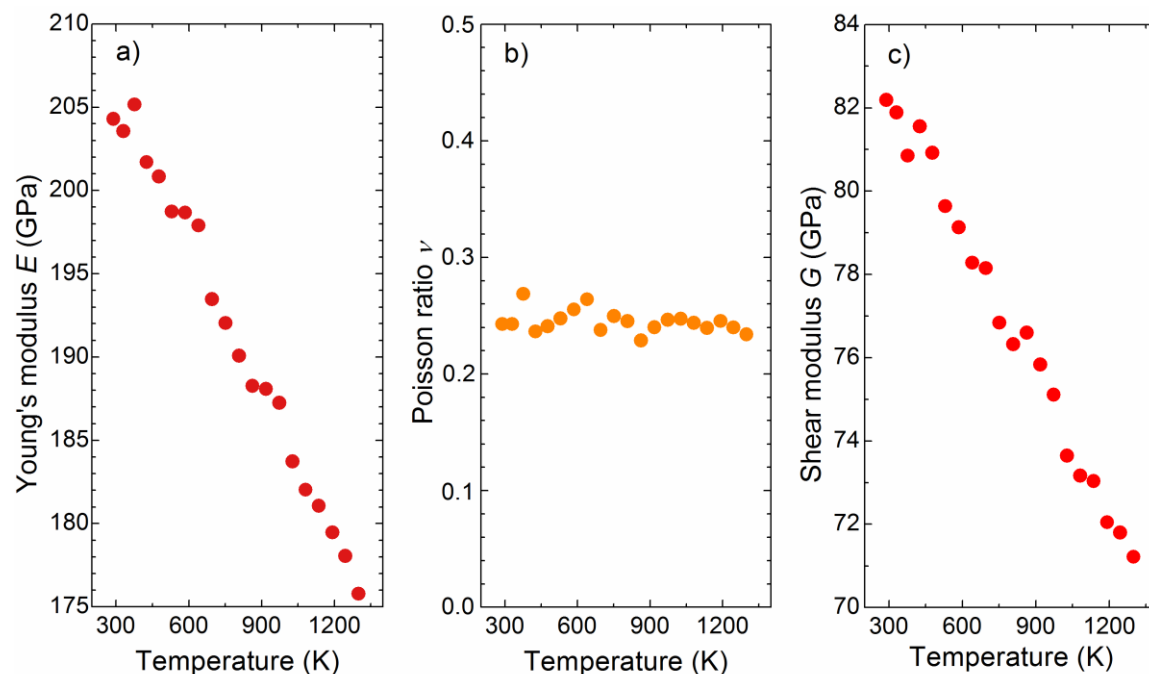


Figure 5.7. Temperature dependence of (a) Young's modulus, (b) Poisson ratio and (c) shear modulus of BZY. The uncertainty is about 7% in Young's modulus, 8% in the Poisson ratio and 0.3% in the shear modulus.

5.3 NUMERICAL SIMULATION OF RESIDUAL STRESSES STATE IN LANTHANUM SILICATE

Many physical phenomena that occur in a polycrystalline material are intimately related with the local mechanical fields developed in its microstructure. It is well-known that the distribution of these mechanical stress fields depend on the polycrystal morphology, orientation grain distribution and crystal behaviour of the material. These microstructural factors mainly control the global behaviours of the material and are generally used to predict local phenomena such as fracture [17].

In brittle materials, fracture is governed by the opening of local cracks which spread through the material causing the macroscopic failure. In some polycrystalline ceramics, such as Lanthanum silicate, crack initiation might be sensitive to the residual stress localization developed along the grains boundaries which come from the crystalline anisotropy of elastic constant and thermal expansion [18]. Therefore, it is of high relevancy to evaluate the stress fields developed between individual crystals in order to be able to predict the mechanical failure of the material. In

this context, finite elements method appears as a very efficient tool to simulate the mechanical behaviour of a polycrystalline aggregate taking into account microstructural and structural details of the material.

The main objective of this section is to characterize the residual stress state and to predict the fracture probability in Lanthanum Silicates for a given thermo-mechanical conditions by using finite elements numerical simulation. This study uses methods proposed in the work of Kanit *et al.* [19], where finite elements numerical simulation was used to determine the effective properties of a specific random microstructure generated by Voronoi tessellations.

5.3.1 Computation procedure

In order to obtain realistic results of the state of stress in oxy-apatite ceramics from simulations which could be used to understand the experimental failure of the material, it was necessary to create a polycrystal as similar as possible to the original compound and to submit it to the “same conditions” of sintering and compression testing that were used experimentally. The model chosen for the description of microstructure, material properties and experimental conditions used in this study are briefly described below.

5.3.1.1 Description of microstructure

For the purpose of simulating microstructure, it may be possible to employ real microstructure obtained directly by experimental three-dimensional reconstructions from samples using Electron Back-Scatter Diffraction measurements [20-22] or Diffraction Contrast Tomography (DCT) [23-26]. However, these methods are lengthy and expensive since a sophisticated experimental facilities are required. As an alternative, computational methods have been developed to create artificial microstructures at a lower time-consuming and cost. It is in this point where finite element method based on the Voronoi cells was developed by Ghosh and Moorthy *et al.* [27].

In this work, the representation of the grains in a polycrystal was performed by a three-dimensional Voronoï mosaic. This choice was motivated by the fact that the oxy-apatite exhibits a simple microstructure with only one phase and a uniform distribution of the grains with defect-free and equiaxial grains as mentioned previously (see Chapter 3).

The principle of construction of the Voronoi tessellations is based on proximity to a given set of points to divide the space into regions. These points, called seeds, are randomly distributed in space. For a finite set of seeds $S_1, S_2, S_3 \dots$ it is possible to make partitions of the space into cells (grains) $C_1, C_2, C_3 \dots$ depending on the distance that every point M in the volume has to the seeds, taking into account that M belongs to C_i if it is closer to S_i than to any S_j ($j \neq i$). The points which are equidistant to the two nearest seeds form a line called half-space (grain boundary). The Voronoi cells C_i are defined by the intersection of several half-spaces as a polyhedron (**Figure 5.8**).

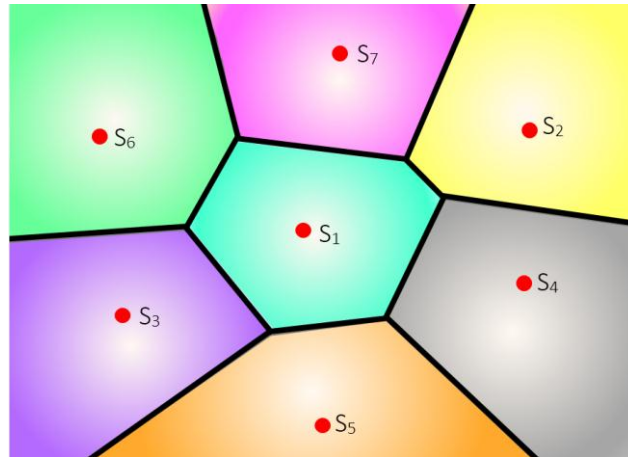


Figure 5.8. 2D Voronoi mosaic of seven random seeds (S) with their corresponding cells.

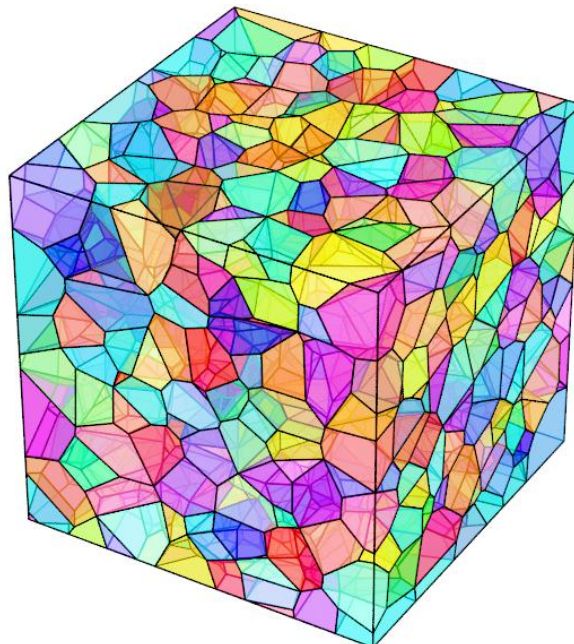


Figure 5.9. 3D Voronoi tessellations of 200 cells [17].

In the generation of a polycrystal as Voronoi tessellation was necessary to define the number of grains, which were created according to a uniform distribution that was similar to the

grain size distribution found for Oxy-apatite (Section 3.3.1.4). Then, the mesh size was imposed and the tessellation was optimized regarding to the element size by removing the smallest edges and faces in order to improve the quality of the mesh. The generation of polycrystals and meshing was conducted with Neper software [17].

5.3.1.2 Numerical simulations

Based on the obtained polycrystal, the numerical simulations were performed using the finite element method. For each grain, was imposed a random orientation defined by Euler angles of a random isotropic crystallographic texture. Euler angles determine the orientation of one grain with respect to the reference system of the aggregate. Moreover, other input parameters were defined such as material properties (taking into account potential anisotropies) and loading and boundary conditions, which are briefly described below. The numerical simulations were conducted with Abaqus.

5.3.1.2.1 Material properties

As indicated in Chapter 4, Lanthanum Silicate can be approximately described as an orthotropic material due to the hexagonal symmetry of the oxy-apatite crystal structure (hexagonal cells can be also expressed in an orthotropic lattice by using $a' = a$, $b' = 2b+a$, $c' = c$). In order to characterize the residual stresses state in LSO, its thermo-elastic properties had to be defined. For this purpose, the full elastic tensor was taken from DFT calculation at 0 K (Section 4.4.1) while the anisotropy thermal expansion coefficients were taken from literature data, where Fukuda *et al.* [3] found that the linear expansion coefficient of the a-axis was $6.8(3) \times 10^{-6} \text{ K}^{-1}$ and that of the c-axis was $2.9(4) \times 10^{-6} \text{ K}^{-1}$ in the temperature range of 298 to 573 K. The choice of these thermal expansion coefficients at low temperature was motivated by the fact that we did not perform yet HT XRD characterization when these computations were realized. The idea was then to make first simulations to evaluate the method and the order of magnitude of the results. Currently, new calculations are being done using our own data of thermal expansion and reasonable evolution of elastic tensor evolution with temperature based on our RUS data. Therefore, based on the results presented in Section 0 about the evolution of E and α of polycrystalline material with temperature, it must be clarified that the numerical simulations presented here were carried out in the extreme case of the highest anisotropy in particular concerning thermal expansion coefficients.

5.3.1.2.2 Loading and boundary conditions

Two different loading conditions were applied to the aggregate in this work: thermal (th) and thermal-mechanical loading (th-m). The interest of choosing these loadings lies in the fact that the material is subjected to these conditions during sintering and during its use as electrolyte for SOFCs. In order to analyze separately the effect of both loading conditions in the state of stress of LSO, two different steps were defined. In the first step, a decrease in temperature from 1500 °C was imposed to simulate the sintering process, while in the second step mechanical loading was applied, which consisted in a compression pressure of 450 MPa (similar to some of the working conditions for the electrolyte part in Solid Oxide Cells devices [28]).

Considering a LSO polycrystal of a given volume element V , two types of boundary conditions, kinematic and uniform boundary conditions, were imposed in order to characterize its overall residual stresses state, since previous works showed that the actual behaviour lies between those induce by these two boundary conditions [29, 30]. The surfaces and the boundary conditions are summarized in **Table 5.1**.

Kinematic boundary conditions (KBC):

1. Thermal loading: The displacement u is imposed on all the surfaces. There is no displacement normal to surfaces S_1 , S_2 and S_3 (see **Table 5.1** for the labels of surfaces).

$$\forall M \in \{S_1, S_2, S_3\} \quad \vec{u}(M) \cdot \vec{n}_i = 0 \quad (5.4)$$

where n_i is the normal to surface S_i .

Besides, in order to keep all the surfaces plane and parallel to themselves during the loading, the following condition is imposed on the three other surfaces:

$$\forall M \in \{S_4, S_5, S_6\} \quad \vec{u}(M) \cdot \vec{n}_i = \vec{u}(A) \cdot \vec{n}_i \quad (5.5)$$

where A is the intersection of surfaces S_4 , S_5 and S_6 .

Under this conditions a thermal loading was imposed:

$$\forall M \in V \quad \Delta T(M) = -1500 \quad (5.6)$$

2. Thermo-mechanical loading: Keeping the boundary conditions of the thermal step still applied, a pressure p of 450 MPa is added on surface S_1 :

$$\underline{\underline{\underline{\sigma}}} \cdot \vec{n}_1 = -p \cdot \vec{n}_1 \quad (5.7)$$

- Static boundary conditions (SBC):

1. Thermal loading: A pressure equal to 0 is imposed on all the surfaces:

$$\forall M \in \{S_i\} \quad \underline{\underline{\underline{\sigma}}} \cdot \vec{n}_i = \vec{0} \quad (5.8)$$

Then, the same thermal loading than in the previous case (Equation 5.6) was applied.

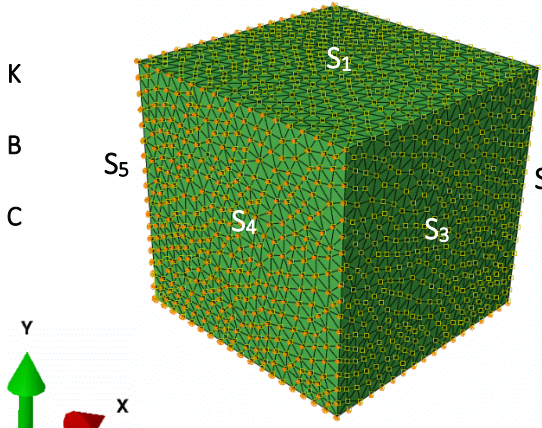
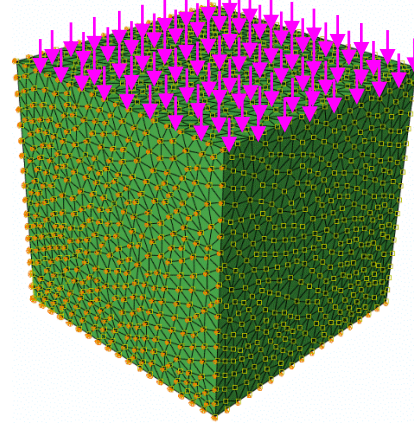
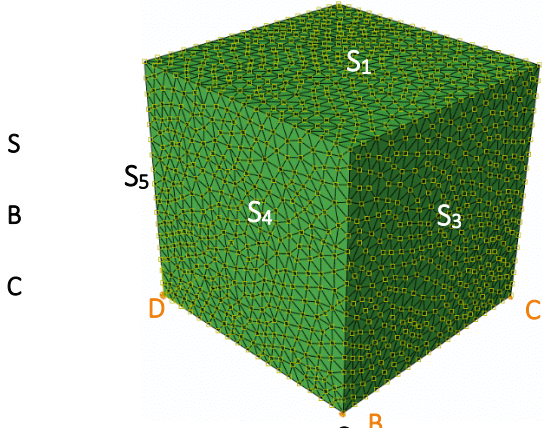
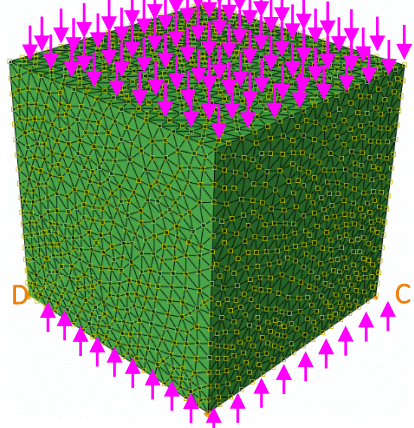
2. Thermo-mechanical loading: A pressure of 450 MPa is added on surfaces S_1 and S_6 (keeping once again the boundary condition of thermal step applied):

$$\forall M \in \{S_1, S_6\} \quad \underline{\underline{\underline{\sigma}}} \cdot \vec{n}_i = -p \cdot \vec{n}_i \quad \vec{n}_i = \vec{n}_1, \vec{n}_6 \quad (5.9)$$

It is necessary to clarify that during these two steps and in order to avoid rigid body motion, on three points, B , C and D which correspond to three corners belonging to S_6 , the following displacements are also imposed:

$$\begin{aligned} \vec{u}(B) &= 0 \\ \vec{u}(C) \cdot \vec{x} &= 0 \quad \vec{u}(C) \cdot \vec{y} = 0 \\ \vec{u}(D) \cdot \vec{y} &= 0 \end{aligned} \quad (5.10)$$

Table 5.1. Boundary conditions applied for the different loading steps. Kinematic (KBC) and Static boundary conditions (SBC).

BC	Thermal step	Mechanical step
	$\forall M \in \{S_1, S_2, S_3\} \quad \vec{u}(M) \cdot \vec{n}_i = 0$ $\forall M \in \{S_4, S_5, S_6\} \quad \vec{u}(M) \cdot \vec{n}_i = \vec{u}(A) \cdot \vec{n}_i$	$\forall M \in \{S_2, S_3\} \quad \vec{u}(M) \cdot \vec{n}_i = 0$ $\forall M \in \{S_4, S_5, S_6\} \quad \vec{u}(M) \cdot \vec{n}_i = \vec{u}(A) \cdot \vec{n}_i$ $\forall M \in S_1 \quad \underline{\underline{\sigma}} \cdot \vec{n}_y = -450 \cdot \vec{n}_y$
K B C	 <p style="text-align: center;">$\forall M \in V \quad \Delta T(M) = -1500$</p>	 <p style="text-align: center;">$\forall M \in V \quad \Delta T(M) = -1500$</p>
	$\forall M \in S_i \quad \underline{\underline{\sigma}} \cdot \vec{n}_i = 0 \cdot \vec{n}_i$	$\forall M \in \{S_2, S_3, S_4, S_5\} \quad \vec{u}(M) \cdot \vec{n}_i = 0$ $\forall M \in \{S_1, S_6\} \quad \underline{\underline{\sigma}} \cdot \vec{n}_y = -450 \cdot \vec{n}_y$
S B C	 <p style="text-align: center;">$\forall M \in V \quad \Delta T(M) = -1500$</p>	 <p style="text-align: center;">$\forall M \in V \quad \Delta T(M) = -1500$</p>
	$\vec{u}(B) = 0$ $\vec{u}(C) \cdot \vec{x} = 0 \quad \vec{u}(C) \cdot \vec{y} = 0$ $\vec{u}(D) \cdot \vec{y} = 0$	$\vec{u}(B) = 0$ $\vec{u}(C) \cdot \vec{x} = 0 \quad \vec{u}(C) \cdot \vec{y} = 0$ $\vec{u}(D) \cdot \vec{y} = 0$

5.3.1.3 Analysis of Stress fields: Localization and prediction of fracture

5.3.1.3.1 Maximum principal stress theory

The interest for studying the state of stress in a material lies in the possibility to determine a failure criterion. The stress state at a point M of a material is given by the stress tensor which is defined by only six independent stress components: three normal components which define the normal component of the stress vector applied to surfaces normal to X , Y or Z and three shear components which characterize the tangential components of the stress vector applied to the same surface (Figure 5.10). Knowing this stress tensor, it is possible to calculate the stress vector applied on every surface passing through point M . Due to the local equilibrium, the stress tensor is symmetrical.

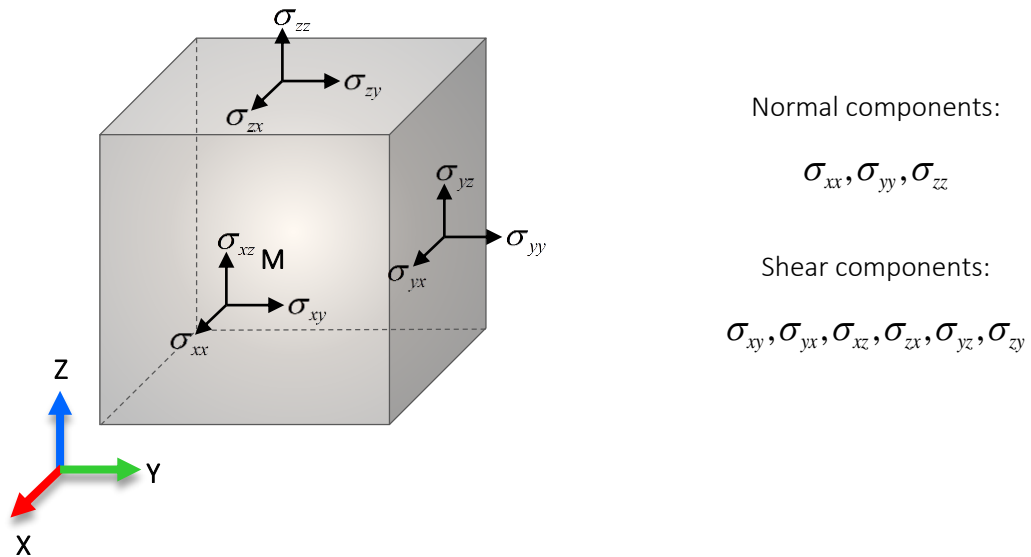


Figure 5.10. Stress components.

The values of these components depend on the coordinate system orientation in which the tensor is written so, for a particular orientation, it is possible to define a coordinate system (oriented to the eigen-vectors of $\underline{\underline{\sigma}}$), in which $\underline{\underline{\sigma}}$ is given by:

$$\underline{\underline{\sigma}} = \begin{bmatrix} \sigma_{xx} & 0 & 0 \\ 0 & \sigma_{yy} & 0 \\ 0 & 0 & \sigma_{zz} \end{bmatrix} \quad (5.11)$$

where the normal components become to the principal stresses.

For brittle materials, failure is governed by opening of cracks, which depends on the stress intensity factor applied to the crack and then, to the normal stress applied on the plane of the crack.

There are numerous proposed theories to predict material failure. However the maximum principal stress is the criterion mostly used to predict the failure of brittle materials, since cracks initiate where the principal stress is maximum and typically propagate perpendicularly to the principal stress direction [31]. The maximum principal stress σ_1 can be defined in 2D as:

$$\sigma_1 = \frac{1}{2}(\sigma_{xx} + \sigma_{yy}) + \frac{1}{2}\sqrt{(\sigma_{xx} - \sigma_{yy})^2 + 4\tau_{xy}^2} \quad (5.12)$$

According to the maximum principal stress theory [32], failure occurs in brittle materials with a certain probability (modelled by Weibull theory) once the maximum principal stress exceeds the value of the maximum strength in simple tension. In this work, all the analyses of the state of stress in finite element numerical simulations were carried out according to this criterion.

5.3.1.3.2 Stress intensity approach

Stress localizations are usually discussed in terms in which a flaw is introduced into a body that was under uniform stress. In this context, the stress intensity factor K is one of the most fundamental parameters used in fracture mechanics [33, 34] to characterize the stress state near the crack-tip caused by an uniform load or residual stresses in a linear elastic material [34].

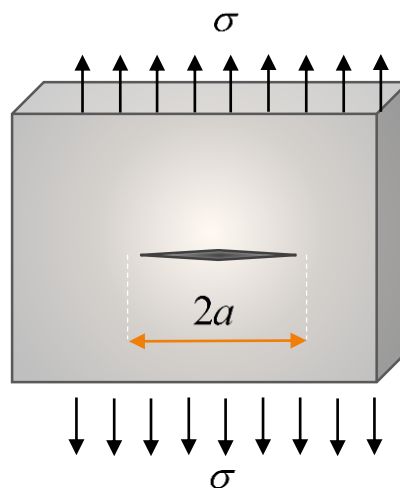


Figure 5.11. Schematic representation of a through crack of length a in an infinite plane subject to a uniform stress σ .

The stress intensity factor for a through crack in an infinite plane subject to a uniform stress field (Figure 5.11) is given by the following equation:

$$K_I = \sigma_1 \sqrt{\pi a} \quad (5.13)$$

where a is the crack length and σ_I is the stress applied. Assuming a local material failure at a critical level of principal maximum stress, then fracture occurs at a critical stress intensity K_{IC} (fracture toughness). Therefore, considering K_I as the driving force for fracture and fracture toughness as the measure of material resistance, crack propagation occurs when $K_I = K_{IC}$ [34]. However, as defects of different lengths exist in the material, the probabilistic failure criterion has to be defined as (Weibull theory):

$$K_I = \sigma_I \sqrt{\pi a} f(a) \quad (5.14)$$

In absence of information about the defect distribution, only the first term of this criterion was studied in this work.

5.3.1.4 Strategy of Simulations

5.3.1.4.1 Determination of the Mesh Size

Numerical simulation requires a proper determination of the average number of finite elements necessary to mesh one Voronoi cell in order to determine properly the overall stress fields. For this purpose, the effect of the mesh size in the stress distribution was studied in a polycrystal of 200 grains for six different mesh sizes, called rcl1, 05, 035, 032, 028, 024. All the computations were performed in the same aggregate and under the same conditions (thermal loading and SBC) having as only variable the mesh size. The number of elements increased from 21305 to 1278303 with mesh size varying from rcl1 to rcl024. The results plotted on **Figure 5.12** show the convergence of the maximum principal stress distribution as function of the increased number of elements. As can also be observed in this figure, the roughest mesh sizes lead to wrong values of stresses, in such a way one must use mesh sizes smaller than rcl0.35 in order that stress values become “independent” of the mesh size (e.i. variations smaller than 10%). The final choice of the mesh size was based on a compromise between getting better precision of values and time of computation, due to this, the mesh size called rcl028, with a number of elements equal to 779.848, was selected taking into account that it led to variations of stress distribution smaller than 2% with respect the values obtained with rcl024.

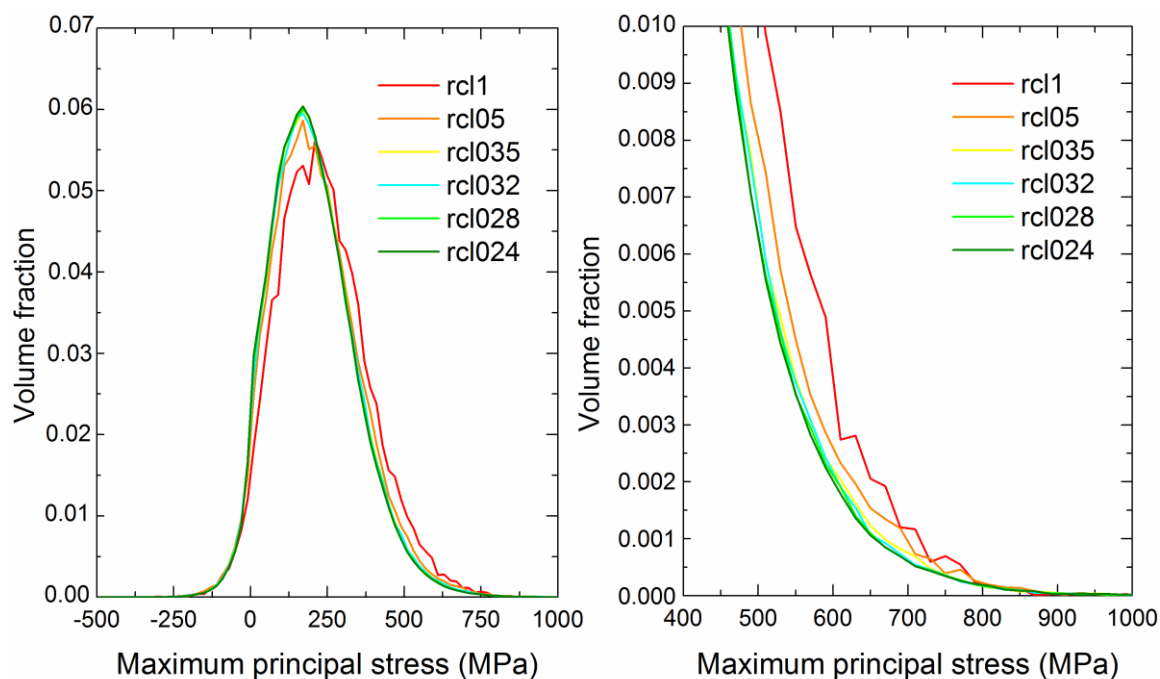


Figure 5.12. Distribution of the maximum principal stress as function of the mesh size.

5.3.1.4.2 Multiple realizations

The effect of the different variables imposed on the simulations (grain orientation and boundary conditions) in the maximum principal stress distribution was studied in aggregates with different number of Voronoi cells, from 12 to 1000 grains. The objective of this section was to study how many realizations are necessary to define the representative volume elements (RVE) in order to obtain results independent of the grain orientation, boundary conditions and volume size. It is clear that only one realization of a small aggregate (one set of grains having each one a given orientation) is not sufficient to be representative for all the configurations encountered in the material. In these conditions, a question arises whether multiplying the realizations of this small aggregate is equivalent or not as to use a larger aggregate. In other words, does an aggregate size exist for which one realization is sufficient to have all the configurations and then predict stress localizations and distributions? These questions were answered in a previous work reported by Kanit *et al.* [19] for some effective properties. In the case of mean elastic properties and thermal conductivity of a biphase material, they found that the size of the RVE depends on the property tested. However, the properties they studied depend on the mean value of the stress distribution, whereas the failure properties depend of the tail of the stress distribution. Therefore, it is necessary to adapt the method used by Kanit *et al.* In this work, twenty numerical simulations of small aggregates with different random orientations were computed in order to properly characterize the stress fields in a polycrystal.

5.3.2 Computation results

5.3.2.1 Distribution of stresses

3D finite element computation for 200 grains are represented in **Figure 5.13** and **Figure 5.14**. These computations show the maps of the maximum principal stress for the different boundary conditions and loadings, indicating that stresses are heterogeneously distributed not only at the macroscopic level but also inside the grains. Under static boundary conditions (**Figure 5.13**), stress localizations were observed after sintering and became stronger after the mechanical loading. As evidence in the images the largest stress gradients are located at grain boundaries and in particular near multiple grain junctions. This is a direct consequence of the anisotropic thermo-elastic behaviour of LSO and of the random crystallographic orientation of each crystal.

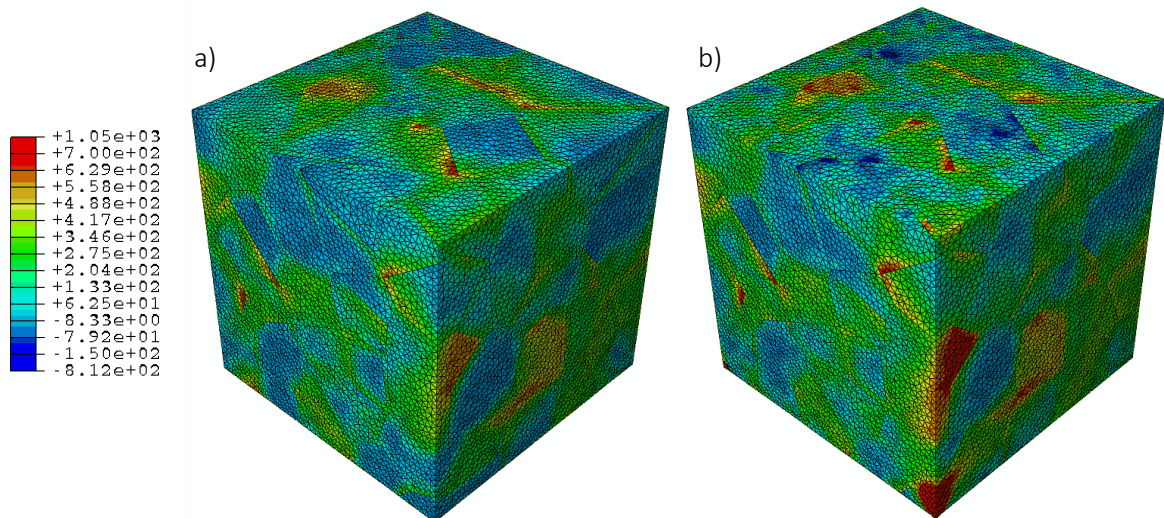


Figure 5.13. Finite element computation for 200 grains of the maximum principal stress distributions for static boundary conditions for an applied (a) thermal loading of $\Delta T = 1500$ °C followed by a (b) mechanical loading of $\sigma = 450$ MPa.

In the case of Kinematic boundary conditions (**Figure 5.14**), the highest values of stress are also located along the grains edges showing the same tendency that for SBC, however the difference of stresses between the two different loadings seems to be lower. **Figure 5.15** shows the maximum stress distribution as function of volume fraction of elements corresponding to the computations displayed in **Figure 5.13** and **Figure 5.14**, confirming slightly smaller changes of the stress distribution with the different loading condition in the case of the KBC compared with those of the SBC.

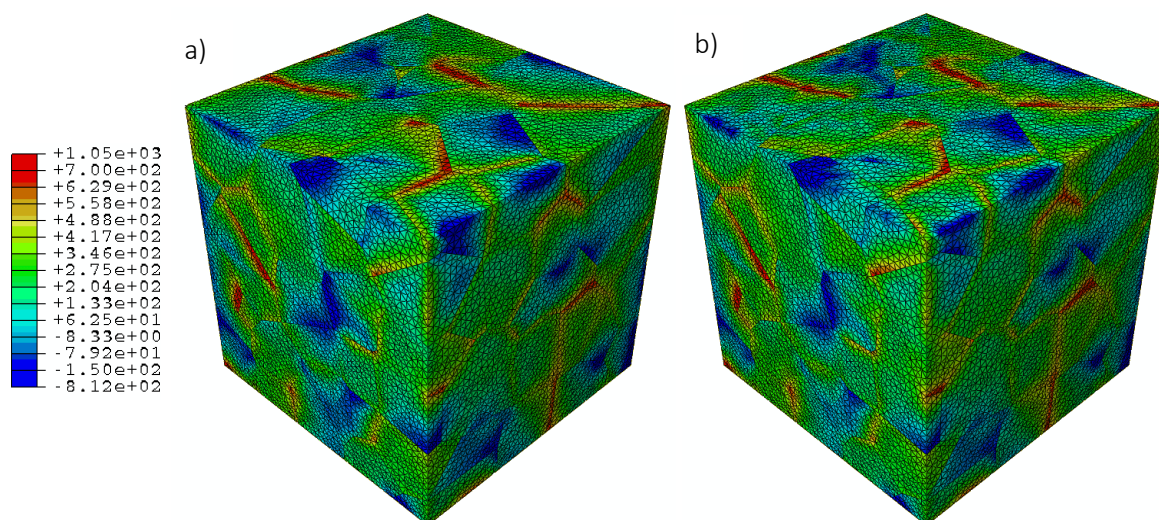


Figure 5.14. Finite element computation for 200 grains of the maximum principal stress distributions for Kinematic boundary conditions for an applied (c) thermal loading of $\Delta T = 1500$ °C followed by a (b) mechanical loading of $\sigma = 450$ MPa.

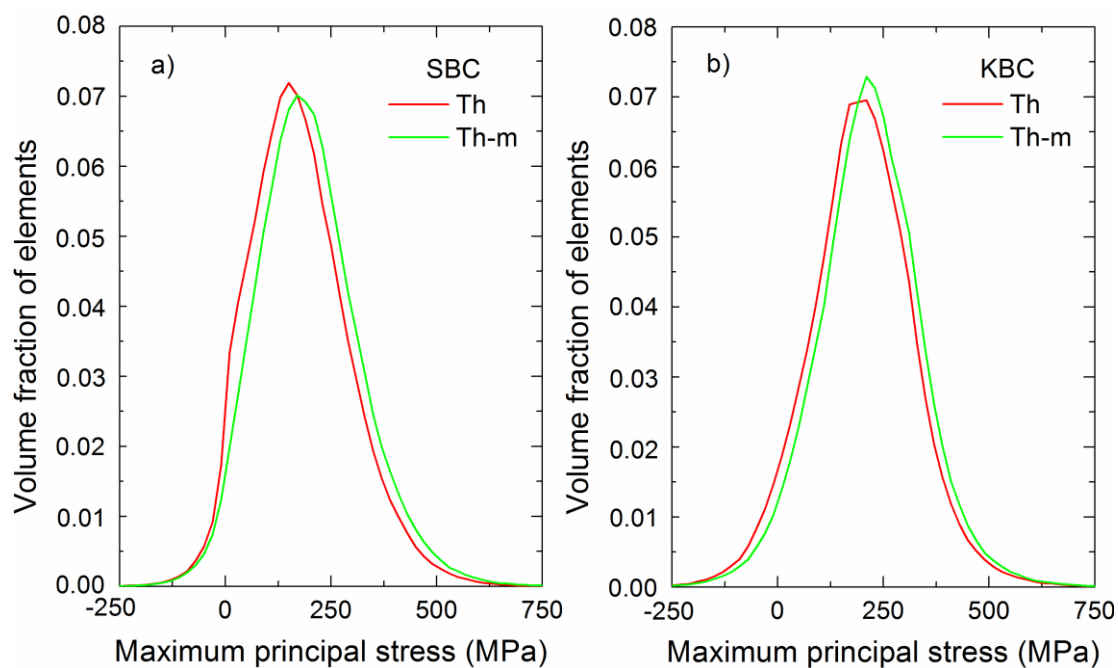


Figure 5.15. Maximum principal stress distribution in 200 grains as function of volume fraction of elements for the different loading (thermal (th) and thermo-mechanical (th-m) and boundary conditions: (a) static boundary conditions and (b) Kinematic boundary conditions.

It is worth mentioning that, independently of the boundary conditions, certain grains seem to be more susceptible to stress localization (Figure 5.13 and Figure 5.14). In order to better understand the origin of these localizations, the normal stress to the grains boundaries were studied as function of the loading direction (Figure 5.16).

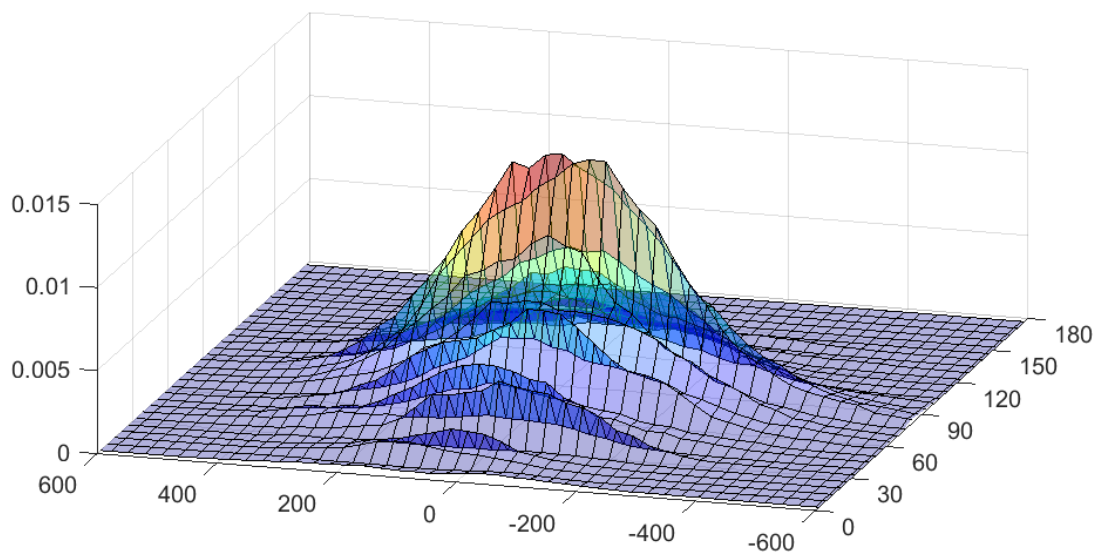


Figure 5.16. Distribution of normal stress to grain boundaries as function of the angle between grain boundary and loading.

As evidence in **Figure 5.16** for both boundary conditions, the maximum values are given by an angle of about 90° between the normal to the grain boundary and the loading direction and correspond to a positive normal stress in the range of 50 - 150 MPa. Due to Poisson ratio, a compression loading will induce a tensile loading along directions normal to the compression direction. This result indicates that a compression pressure will lead to intergranular cracks along the grains boundaries which are parallel to the loading direction.

5.3.2.2 Prediction of failure

Failure criterion are based on stress intensity factor, and indeed on maximum principal stress. Therefore, determining the maximal value of the maximum principal stress distribution could be an objective, however, due to the sharp gradients, stress become locally infinite. Thus, comparing their local values does not have any sense. Due to this, it is necessary to define what is called a “non-local” criterion, which is a stress value averaged over a certain volume. In this work, we considered as criterion the volume of elements in which the maximum principal stress was higher than 600 MPa.

The objective of this study is to establish the size of the representative volume element corresponding to failure criterion, that is, the size of the volume simulated by finite elements representative for a small volume of a real fuel cell component. The RVE has to behave as if it is embedded in the real material, its behaviour should be independent from the boundary conditions.

Figure 5.17 displays for every aggregate size (based on the number of grains) the volume fraction of elements in which the maximal principal stress is over 600 MPa.

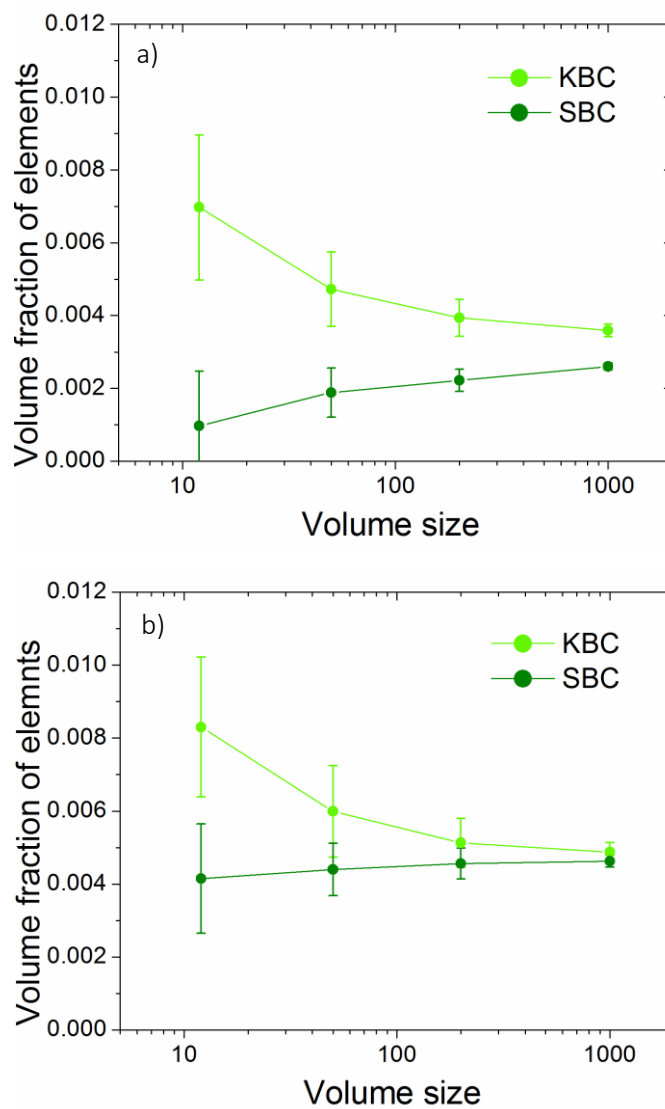


Figure 5.17. Mean volume fraction of elements subjected to stresses higher than 600 MPa and standard deviation of mean values as function of volume size for the different boundary conditions. (a) thermal and (b) thermo-mechanical loading.

For a same aggregate size, the mean value averaged over all the realizations and the standard deviation are plotted. Overall, it can be observed that:

- Standard deviation of the results decreases with the increase of volume size for both boundary conditions.
- Results depend on boundary conditions, it is not equivalent to impose displacements or pressure on the surfaces.

- When the grain size increases, the differences between SBC and KBC calculations tend to vanish. Indeed boundary conditions modify the response of the grains which are near to the boundaries but it has less influence in the grains inside the bulk. This influence is typically of 2-3 grains sizes. When the number of grains increases, the volume fraction of the bulk proportionally increases and the type of boundary conditions imposed is of less importance.
- Results tend to converge towards the same values for large volumes, independently from the boundary conditions.

The probability of failure increase when the mechanical loading is applied, what are in good agreement with the stronger localizations after the mechanical step already analyzed in **Figure 5.13** and **Figure 5.14**.

Prediction of failure was performed from the stress intensity factor taking into account the criterion of 600 MPa and fracture toughness of Lanthanum silicate obtained experimentally in this work (section 4.3.1), where a value of $K_{IC} = 1.2 \pm 0.1 \text{ MPa m}^{1/2}$ were found. From Equation 6.1 a value of $a = 0.98 \text{ }\mu\text{m}$ was determined, what indicates that any crack in the material of $1.96 \text{ }\mu\text{m}$ in length ($2a$) could propagate and lead to material failure if the stress concentration near the crack-tip exceeded the criterion of 600 MPa.

Another way of having a non-local approach to failure is to consider, not only the stress distribution of elements subjected to a high level of stress but also of grains. Stress tensor was averaged in every grain and the maximum principal stress of the mean stress tensor was calculated. **Figure 5.18** shows the volume fraction of grains in which the maximal principal stress is greater than 100 MPa for the different loading and boundary conditions as a function of volume size. Once again the standard deviation of mean value becomes smaller and the results converge towards the same value when the volume size increases. Considering the total volume fraction of 1000 grains as 1, these results indicate that about 79% and 86% of grains were subjected to stresses higher than 100 MPa after the thermal and mechanical loading, respectively. A parallel study in the same conditions indicated that only about 23% and 34% of grains were subjected to stresses higher than 200 MPa while it was not found stressed grains at stress levels higher than 400 MPa, due to this it was not possible to apply the same criterion used above for the volume fraction of elements.

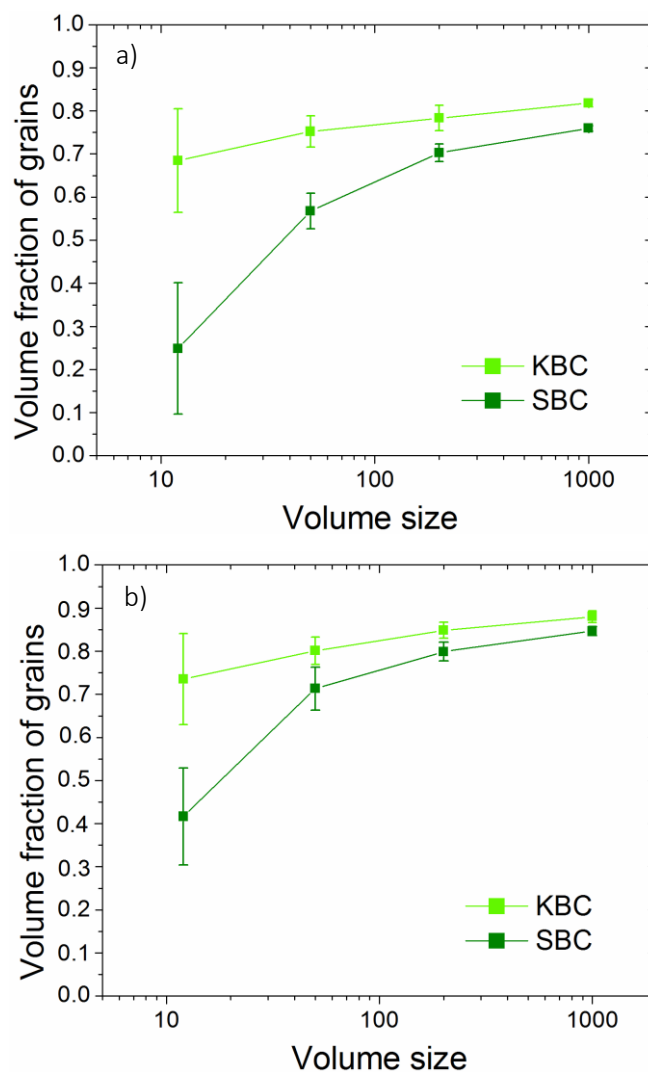


Figure 5.18. Mean values of volume fraction of grains subjected to stresses higher than 100 MPa and standard deviation of mean values as function of volume size for the different boundary conditions. (a) thermal and (b) thermo-mechanical loading.

When considering stresses averaged over grains, the difference between the two loadings applied (thermal and thermo-mechanical loading) is very low. This averaging is probably too rough to be able to distinguish both contributions. Due to this, the first criterion should be kept in the future.

5.4 REFERENCES

1. Le Bail, A., *Whole powder pattern decomposition methods and applications: A retrospection*. Powder Diffraction, 2012. 20(4): p. 316-326.
2. Carpenter, M.A. *High-Temperature Resonant Ultrasound Spectroscopy*. University of Cambridge.

3. Fukuda, K., T. Asaka, and T. Uchida, *Thermal expansion of lanthanum silicate oxyapatite ($La_{9.33+2x}(SiO_4)_6O_{2+3x}$), lanthanum oxyorthosilicate (La_2SiO_5) and lanthanum sorosilicate ($La_2Si_2O_7$)*. Journal of Solid State Chemistry, 2012. 194: p. 157-161.
4. Iwata, T., et al., *Structural change of oxide-ion-conducting lanthanum silicate on heating from 295 to 1073 K*. Solid State Ionics, 2007. 178(27): p. 1523-1529.
5. Jiang, S.P., et al., *Synthesis and characterization of lanthanum silicate apatite by gel-casting route as electrolytes for solid oxide fuel cells*. Journal of Power Sources, 2009. 189(2): p. 972-981.
6. Gauckler, L.J., et al., *Solid oxide fuel cells: systems and materials*. CHIMIA International Journal for Chemistry, 2004. 58(12): p. 837-850.
7. Yokokawa, H., et al., *Electrolytes for solid-oxide fuel cells*. MRS bulletin, 2005. 30(8): p. 591-595.
8. Wachtman, J.B., W.R. Cannon, and M.J. Matthewson, *Mechanical properties of ceramics*. 2009, Hoboken, N.J.: Wiley.
9. Ren, F., et al., *The high-temperature elastic moduli of polycrystalline PbTe measured by resonant ultrasound spectroscopy*. Acta Materialia, 2008. 56(20): p. 5954-5963.
10. Soga, N., E. Schreiber, and O.L. Anderson, *Estimation of bulk modulus and sound velocities of oxides at very high temperatures*. Journal of Geophysical Research, 1966. 71(22): p. 5315-5320.
11. Fukuhara, M. and I. Yamauchi, *Temperature dependence of the elastic moduli, dilational and shear internal frictions and acoustic wave velocity for alumina, (Y)TZP and β' -sialon ceramics*. Journal of Materials Science, 1993. 28(17): p. 4681-4688.
12. Han, D., N. Hatada, and T. Uda, *Chemical Expansion of Yttrium-Doped Barium Zirconate and Correlation with Proton Concentration and Conductivity*. Journal of the American Ceramic Society, 2016. 99(11): p. 3745-3753.
13. Gladysz, G.M. and K.K. Chawla, *Coefficients of thermal expansion of some laminated ceramic composites*. Composites Part A: Applied Science and Manufacturing, 2001. 32(2): p. 173-178.
14. Yamanaka, S., et al., *Thermochemical and thermophysical properties of alkaline-earth perovskites*. Journal of Nuclear Materials, 2005. 344(1): p. 61-66.
15. Yamanaka, S., et al., *Thermophysical properties of $BaZrO_3$ and $BaCeO_3$* . Journal of Alloys and Compounds, 2003. 359(1): p. 109-113.
16. Lyagaeva, J., et al., *A detailed analysis of thermal and chemical compatibility of cathode materials suitable for $BaCe_{0.8}Y_{0.2}O_{3-\delta}$ and $BaZr_{0.8}Y_{0.2}O_{3-\delta}$ proton electrolytes for solid oxide fuel cell application*. International Journal of Hydrogen Energy, 2017. 42(3): p. 1715-1723.
17. Quey, R., P.R. Dawson, and F. Barbe, *Large-scale 3D random polycrystals for the finite element method: Generation, meshing and remeshing*. Computer Methods in Applied Mechanics and Engineering, 2011. 200(17): p. 1729-1745.

18. Yousef, S.G., et al., *Microcrack Evolution in Alumina Ceramics: Experiment and Simulation*. Journal of the American Ceramic Society, 2005. 88(10): p. 2809-2816.
19. Kanit, T., et al., *Determination of the size of the representative volume element for random composites: statistical and numerical approach*. International Journal of Solids and Structures, 2003. 40(13): p. 3647-3679.
20. Brands, D., et al., *On the Reconstruction and Computation of Dual-Phase Steel Microstructures Based on 3D EBSD Data*. PAMM, 2011. 11(1): p. 503-504.
21. Schwartz, J., O. Fandeur, and C. Rey, *Numerical approach of cyclic behaviour of 316LN stainless steel based on a polycrystal modelling including strain gradients*. International Journal of Fatigue, 2013. 55: p. 202-212.
22. Brands, D., et al., *Computational modeling of dual-phase steels based on representative three-dimensional microstructures obtained from EBSD data*. Archive of Applied Mechanics, 2016. 86(3): p. 575-598.
23. Ludwig, W., et al., *New opportunities for 3D materials science of polycrystalline materials at the micrometre lengthscale by combined use of X-ray diffraction and X-ray imaging*. Materials Science and Engineering: A, 2009. 524(1): p. 69-76.
24. Proudhon, H., et al., *Coupling Diffraction Contrast Tomography with the Finite Element Method* Advanced Engineering Materials, 2016. 18(6): p. 903-912.
25. Peetermans, S., et al., *Cold neutron diffraction contrast tomography of polycrystalline material*. Analyst, 2014. 139(22): p. 5765-5771.
26. Thomas J. Marrow, A.K., P. Reischig, S. Rolland du Roscoat, W. Ludwig, *Diffraction contrast tomography of polycrystalline alumina*. 2009.
27. Ghosh, S. and S. Moorthy, *Elastic-plastic analysis of arbitrary heterogeneous materials with the Voronoi Cell finite element method*. Computer Methods in Applied Mechanics and Engineering, 1995. 121(1): p. 373-409.
28. Nakajo, A., et al., *Mechanical reliability and durability of SOFC stacks. Part I : Modelling of the effect of operating conditions and design alternatives on the reliability*. International Journal of Hydrogen Energy, 2012. 37(11): p. 9249-9268.
29. Huet, C., *Application of variational concepts to size effects in elastic heterogeneous bodies*. Journal of the Mechanics and Physics of Solids, 1990. 38(6): p. 813-841.
30. Hazanov, S. and C. Huet, *Order relationships for boundary conditions effect in heterogeneous bodies smaller than the representative volume*. Journal of the Mechanics and Physics of Solids, 1994. 42(12): p. 1995-2011.
31. Wang, J., et al., *Maximum mean principal stress criterion for three-dimensional brittle fracture*. International Journal of Solids and Structures, 2016. 102: p. 142-154.
32. Rankine, W.J.M., *On the Stability of Loose Earth*. Philosophical Transactions of the Royal Society of London, 1857. 147: p. 9-27.

33. Zhu, X.-K. and J.A. Joyce, *Review of fracture toughness (G, K, J, CTOD, CTOA) testing and standardization*. Engineering Fracture Mechanics, 2012. 85: p. 1-46.
34. Anderson, T.L. *Fracture mechanics : fundamentals and applications*. 2005.

Chapter 6

HIGH-TEMPERATURE MECHANICAL CHARACTERIZATION

Contents

6.1 Introduction	150
6.2 Working conditions experiments (T = 700 °C)	150
6.2.1 Experimental procedure	150
6.2.2 Experimental results	151
6.2.2.1 Mechanical response of Lanthanum Silicates in SOFC WCs	151
6.2.2.2 Mechanical response Yttrium-doped Barium Zirconate in PCFC WCs	151
6.3 Creep experiments (T > 1000 °C)	156
6.3.1 Experimental procedure	156
6.3.1.1 Mechanical magnitudes	157
6.3.1.2 High-temperature mechanical tests	159
6.3.1.3 Steady-state deformation	160
6.3.1.4 Determination of creeps parameters	161
6.3.1.4.1 Conventional method	162
6.3.1.4.2 Differential method	162
6.3.2 Experimental results	163
6.3.2.1 High-temperature mechanical behavior of LSO-CS	163
6.3.2.1.1 Fragile-ductile transition	163
6.3.2.1.2 Microstructure after deformation	165
6.3.2.1.3 Creep parameters	170
6.3.2.1.4 High-temperature deformation mechanism	176
6.3.2.2 High-temperature mechanical behavior of LSO-SPS	178
6.3.2.2.1 Fragile-ductile transition	178
6.3.2.2.2 Microstructure after deformation	180
6.3.2.2.3 Creep parameters	182
6.3.2.2.4 High-temperature deformation mechanism	187
6.3.2.3 High-temperature mechanical behavior of BZY	189
6.3.2.3.1 Fragile-ductile transition	189

6.3.2.3.3 Creep parameters	193
6.3.2.3.4 High-temperature deformation mechanism	199
6.4 References	202

6.1 INTRODUCTION

This chapter focuses on the study of the mechanical behaviour of Lanthanum Silicate and Yttrium-doped Barium Zirconate materials at intermediate and high temperatures. On one hand, compressive mechanical tests have been carried out in conditions similar to SOFC/PCFC operating conditions to check the response of the different materials for applications as electrolytes. On the other hand, creep experiments were performed to identify the atomistic mechanisms of plastic deformation and the origin of failure of these materials at high temperatures.

6.2 WORKING CONDITIONS EXPERIMENTS (T = 700 °C)

6.2.1 Experimental procedure

Mechanical essays in working conditions were performed with specimens of approximately 5 x 3 x 3 mm³ in size which were cut from the sintered pellets with a diamond saw. After cutting, the samples were rectified to eliminate imperfections and to ensure that they were completely flat-parallel.

The experiments were carried out in compression on a universal deformation machine (Microtest, University of Seville, Spain) equipped with a controlled-atmosphere system and alumina cylindrical dies of 25 mm in diameter and 300 mm in height. The tests were performed under constant load at 700 °C in different atmospheres i.e. dry air, dry argon and dry 5% hydrogen in Argon (residual water is as much of few ppm). Nominal stresses between 100 and 550 MPa were applied to the samples, according to the stresses estimated for electrolytes in SOFC operating conditions [1, 2] The atmosphere was controlled by monitoring the gas flow in the chamber, which was fixed at 400 ml/min, and the temperature of 700 °C was chosen as a typical operating temperature of PCFCs. The samples were heated in air at a rate of 10 °C/min up to the target temperature of 700 °C, where a 2 h dwell was used to ensure the equilibrium of the machine/sample assembly; a small load of 2 MPa was applied during the heating process to avoid the loss of contact between sample and alumina dies. Then, the samples were loaded at a constant

cross-head speed of 10 $\mu\text{m}/\text{min}$ up to the desired final stress, where the atmosphere was successively changed from air to argon and finally to 5% $\text{H}_2/95\%$ Ar.

6.2.2 Experimental results

6.2.2.1 Mechanical response of Lanthanum Silicates in SOFC working conditions

Both conventionally sintered and SPS oxy-apatites were subjected to this kind of experiments at 150, 300 and 450 MPa, and their stress responses are displayed in **Figure 6.1**. Both materials exhibit the same behaviour, remaining intact throughout the atmosphere changes, indicating that they did not undergo any significant mechanical-chemical degradation during testing.

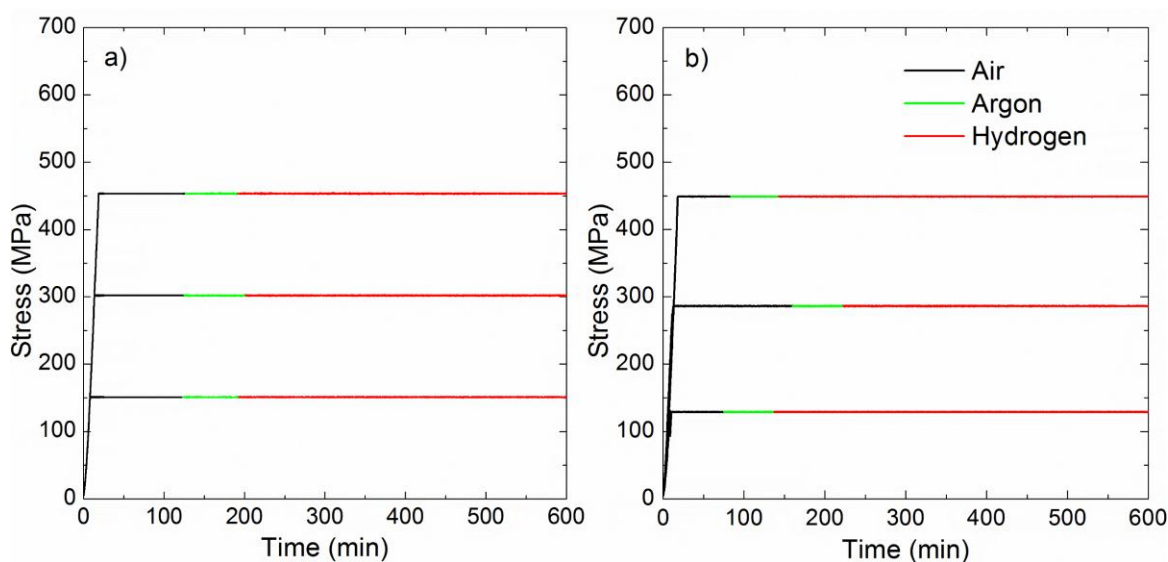


Figure 6.1. Stress response during compression tests at 700 °C under various atmospheres of (a) LSO-CS, and (b) LSO-SPS.

6.2.2.2 Yttrium-doped Barium Zirconate

Figure 6.2 shows the results of the mechanical tests performed on BZY and BZY-NiO. The former material behaves identical to the oxy-apatites, remaining unaffected by the surrounding atmosphere. The same behaviour was also found in BZY-NiO at stresses lower than 300 MPa. However, when the stress level increased up to 350 MPa, the specimens stayed intact under air and argon, but failed catastrophically after about 10 min under H_2 atmosphere. Identical behaviour was found at 560 MPa. The samples literally exploded into many small fragments. These results indicate that the commercial material underwent severe modifications under hydrogen atmosphere at 700 °C, which favours crack formation and propagation and final sample failure. This

point is crucial for fuel cell applications since the observed compressive stress at which failure occurs (350 MPa and above) is within the stress range estimated for the electrolyte part under typical SOFC operating conditions (from 140 [2] to 450 MPa [1]).

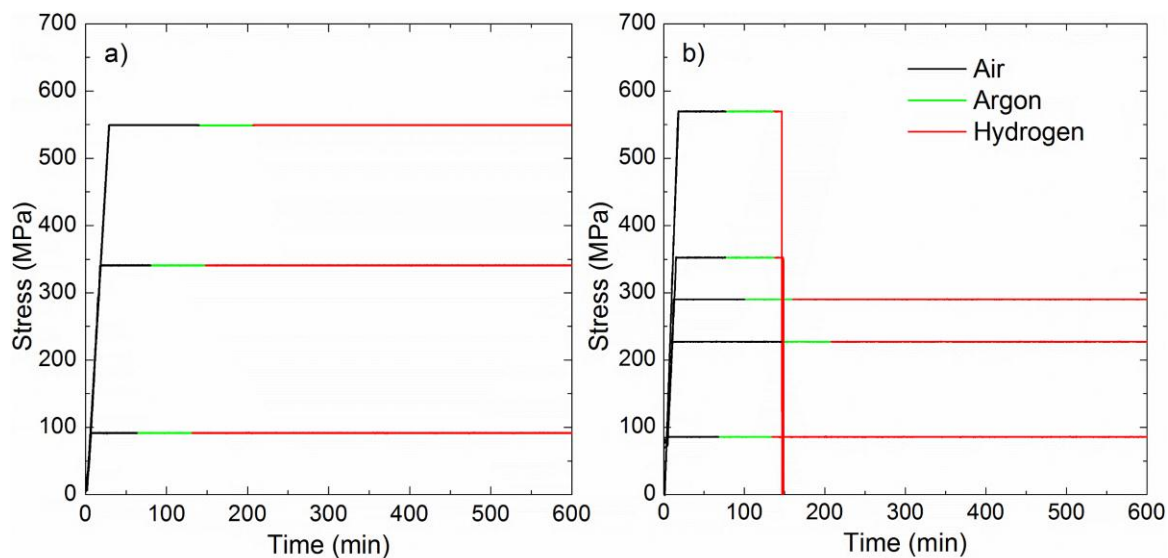


Figure 6.2. Stress response during compression tests at 700 °C under various atmospheres for (a) BZY, and (b) BZY-NiO.

In order to better understand the failure mechanism of these samples prepared with NiO additive, HR-TEM studies were carried out. Because of the lack of information by the supplier, the original BZY-NiO material was firstly investigated.

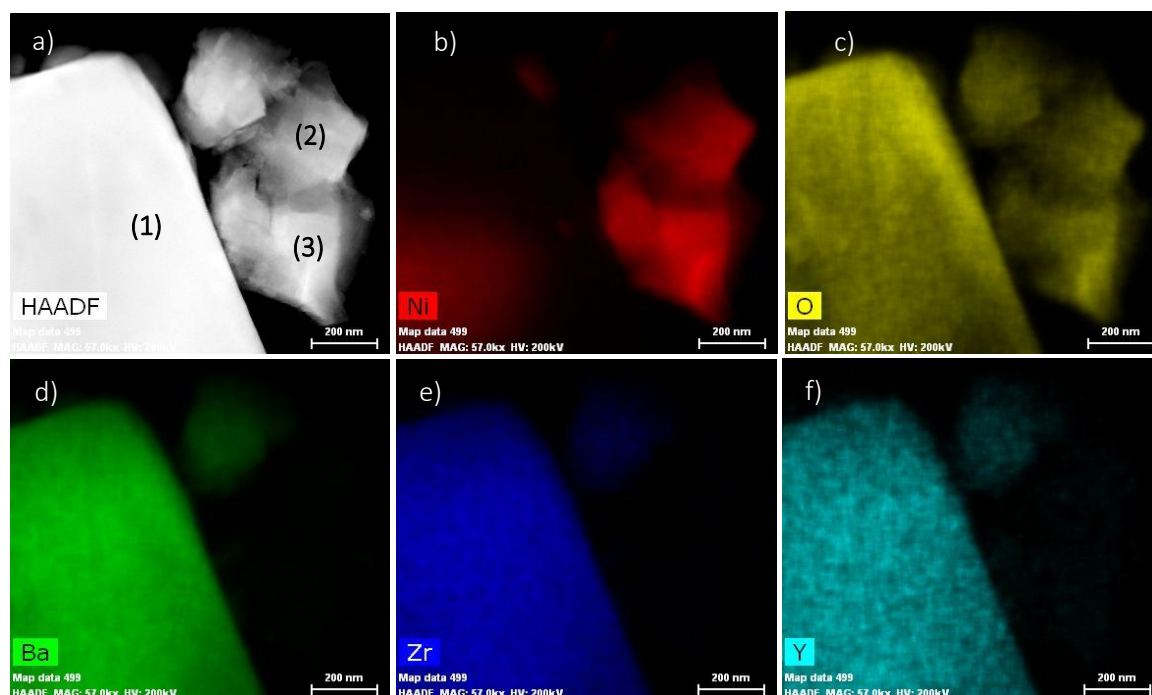


Figure 6.3. EDS mapping of original BZY-NiO particles. (a) HAADF image, and EDS filtered images for elements: (b) Ni, (c) O, (d) Ba, (e) Zr and (f) Y.

Figure 6.3 shows an example of EDS image which helps identifying where the Ni element locates. Particle #1, as identified on the HAADF image, would correspond to $\text{BaZr}_{0.85}\text{Y}_{0.15}\text{O}_{2.925}$ phase, while particles #2 and #3 contains only Ni and O species, and would correspond to NiO. EELS in STEM mode was used to obtain high-resolution information about the material composition.

The fine electronic structure of Ni-rich particles was studied by EELS at Oxygen K edge and Nickel $L_{2,3}$ -edges. **Figure 6.4b** and **c** shows the O-K and Ni- $L_{2,3}$ edge spectra after background subtraction obtained for the Ni-rich particle #3 in the area marked with a circle in **Figure 6.4a**. For an appropriate comparison, similar analyses were also performed on pure NiO (Sigma Aldrich), which has been used as a reference sample (**Figure 6.4b** and **c**). The O-K edge ELNES (electron energy loss near-edge structure) of NiO (**Figure 6.4 b**) consists of five major peaks at 532, 538, 541, 547, and 562 eV. The first peak can be attributed to transitions from O 1s core states to the band mainly consisting of Ni-3d orbitals. The next three peaks at 535 - 550 eV correspond to transitions to the Ni-4sp band, and the last peak results from multiple scattering within oxygen shells [3, 4]. On the other hand, Ni- $L_{2,3}$ edges ELNES (**Figure 6.4c**) consists of two peaks resulting from spin-orbit coupling: L_3 is the main and most intense peak and comes from $2p_{3/2}$ transitions; and L_2 is the peak at higher energy loss and less intense, coming from $2p_{1/2}$ transitions. The position and shape of these contributions are sensitive to the oxidation state of the transition metals involved. As can be seen in **Figure 5.4**, the O-K and Ni- $L_{2,3}$ fine structure (i.e., peak shapes and energy loss positions) of the selected area matches exactly with the NiO reference sample (as well as with literature [3]), confirming that these Ni-rich particles are indeed NiO.

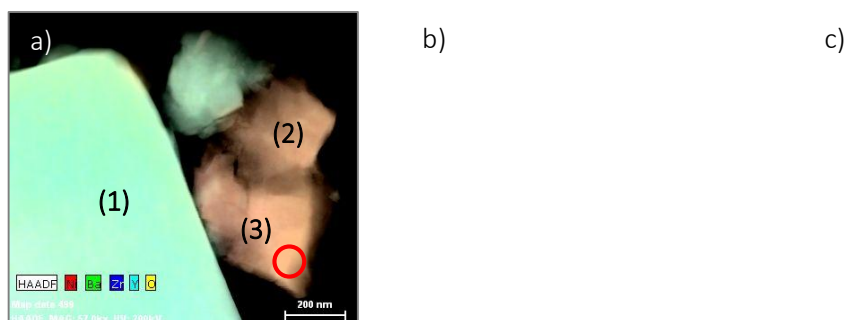


Figure 6.4. TEM characterization of as-received BZY-NiO. (a) HAADF and EDS-filtered image. Selected area for EELS analysis is marked with a red circle, (b) EELS spectra at Oxygen K-edge of BZY-NiO and NiO (reference sample) and (c) Idem at Ni $L_{2,3}$ -edge.

In addition, **Figure 6.5** shows the selected area electron diffraction pattern of particle #3, which was indexed in the $Fm-3m$ space group with a cell parameter $a \approx 4.2 \text{ \AA}$, very close to that of NiO. Similar analyses were performed on other particles, which showed that Ni only appeared at

grain boundaries or in Ni-rich phases with typical sizes of few tens of nanometers. From these analyses, we identified these Ni-rich phases to be NiO.

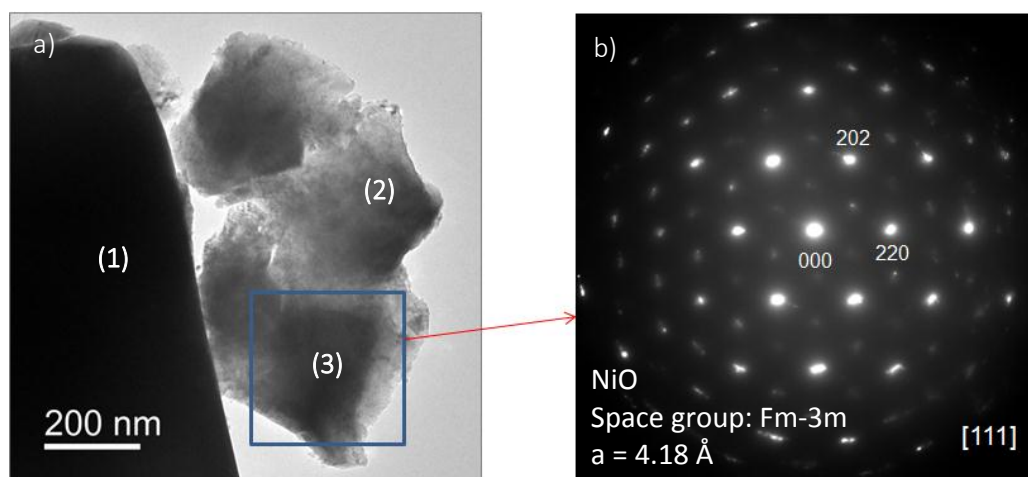


Figure 6.5. (a) HR-TEM image and (b) diffraction pattern of particle #3 which could be identified from indexation as NiO phase.

The same studies were carried out on BZY-NiO after testing at a stress level of 560 MPa at 700 °C under hydrogen atmosphere (**Figure 6.2b**). Ni-rich oxide particles were no longer observed, which were reduced to metallic Ni. **Figure 6.6** shows an example of a metallic Ni particle located close to a BZY particle as evidenced from the EDS map.

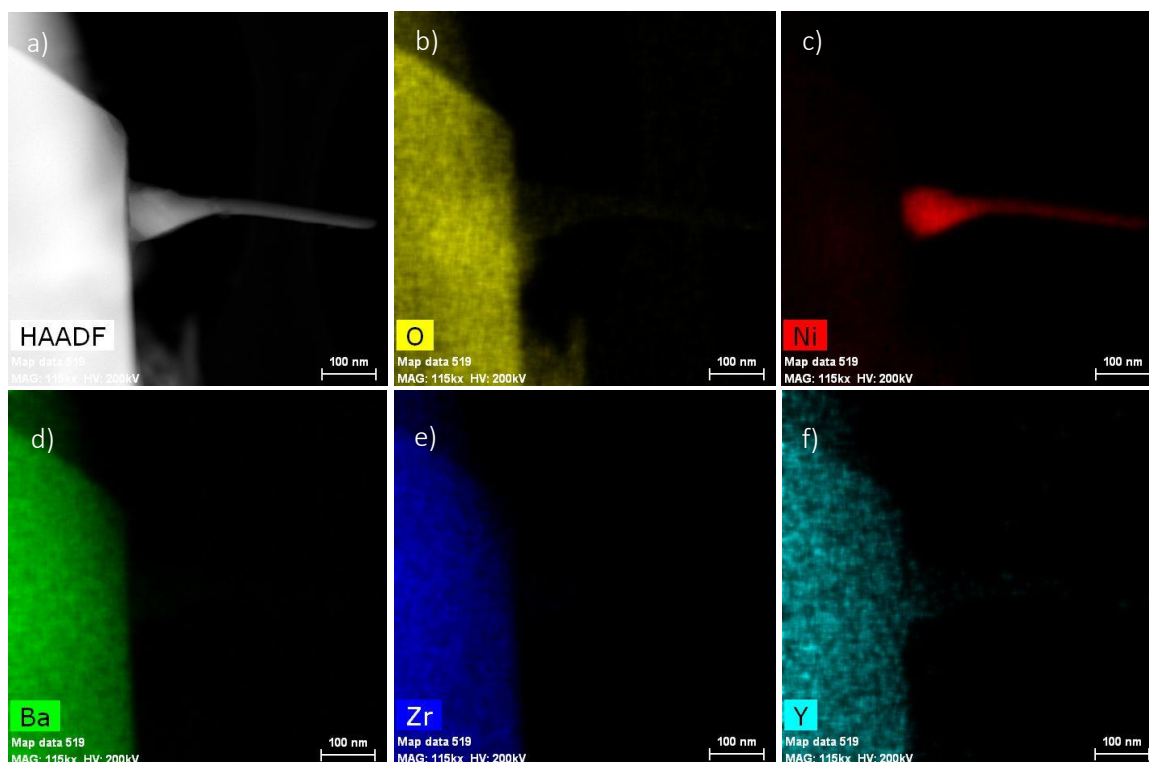


Figure 6.6. EDS mapping of BZY-NiO specimen after mechanical testing at at 700 °C in H₂. (a) HAADF image. EDS-filtered images for elements (b) O, (c) Ni, (d) Ba, (e) Zr and (f) Y.

EELS characterization revealed a loss spectrum analogous to that of pure metallic nickel (Sigma-Aldrich, used as reference) without presence of oxygen (**Figure 6.7**).

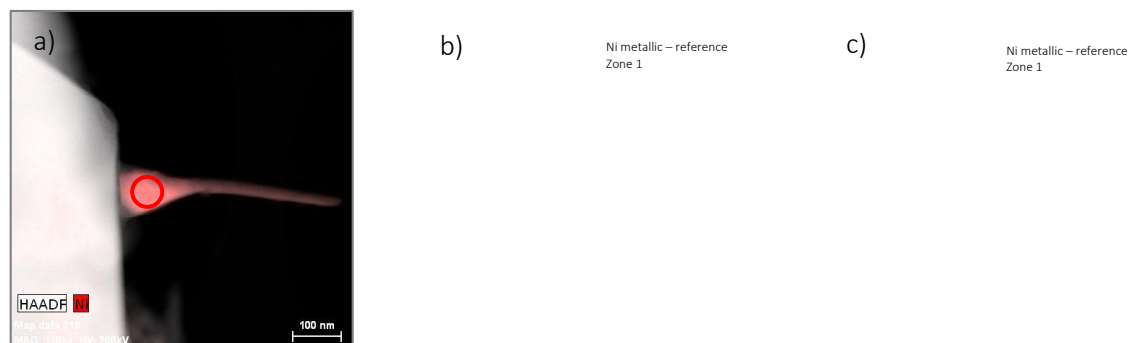


Figure 6.7. TEM characterization of particle in Figure 6.6. (a) HAADF and EDS-filtered image. Selected area for EELS analysis is marked with a red circle. (b) EELS spectra of the selected zone and metallic Ni (reference sample) at Oxygen K-edge. (c) Idem at Ni L_{2,3}-edge.

Figure 6.8 shows that metallic Ni is located mainly along the grain boundaries of BZY. Due to this location, the reduced material is much more prone to fracture under loading. The degradation of properties observed is probably not detrimental for laboratory scale-testing but would potentially become critical for fully-working devices. Indeed, as mentioned in previous articles [1, 2], the electrolyte is submitted during operation and after anode reduction to compressive stresses which can reach several hundreds of MPa. In these conditions, the reduction of Ni on the hydrogen side would lead to an embrittlement of the electrolyte membrane and potentially to an accelerated and premature cell failure.

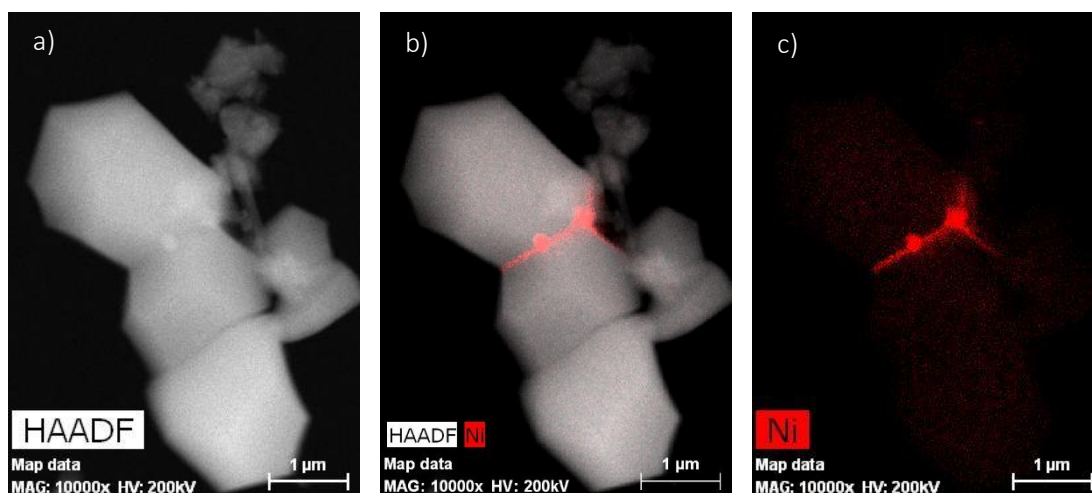


Figure 6.8. EDS mapping of BZY-NiO specimen after testing at 700 °C in H₂. (a) HAADF image, (b) HAADF and EDS-filtered image, (c) EDS-filtered images for Ni.

For these reasons, we also studied the NiO-extraction and the influence of residual nickel in the mechanical properties of BZY compounds. The NiO-extraction procedure and the structural

and microstructural characterization of the material after NiO-extraction have been already addressed in Chapter 2 and Chapter 3.

Samples after NiO-extraction were submitted to the same SOFC operation-condition mechanical tests. As shown in **Figure 6.9**, the specimens remained intact under the different atmospheres at a low stress level. However, the samples failed catastrophically during loading in air at a stress level of about 300 MPa.

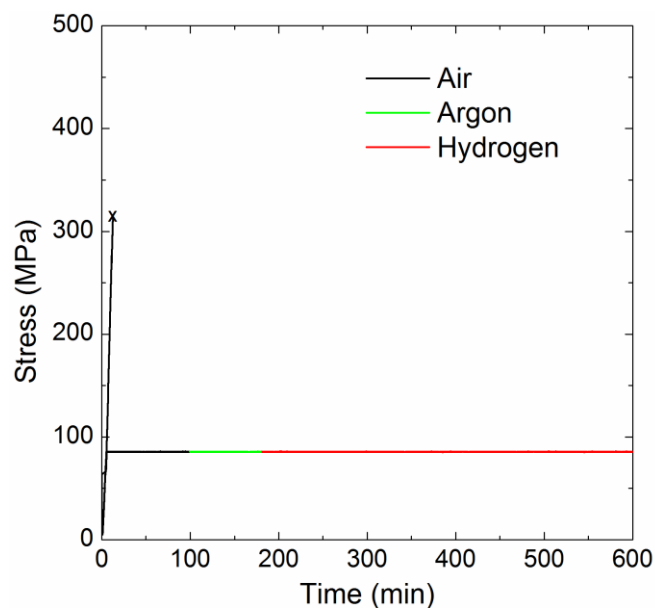


Figure 6.9. Stress response during compression tests at 700 °C under various atmospheres of BZY after NiO-extraction. The “x” mark indicates sample failure.

As shown in Section 3.3.3.3, the NiO-extraction process (120 h at 1600 °C) increased the material porosity and caused an important grain coarsening, along with a change in the chemical nature of the grain boundaries. These factors, which give rise to microcracking, explain the low mechanical resistance after NiO-extraction compared to the as-received material.

6.3 CREEP EXPERIMENTS ($T > 1000\text{ °C}$)

6.3.1 Experimental procedure

This study was carried out by means of compressive mechanical tests to evaluate the influence of strain rate, stress temperature and grain size on the mechanical behaviour of LSO and BZY compounds. The standard high-temperature power law for steady-state deformation is given by [5]:

BZY compounds. The standard high-temperature power law for steady-state deformation is given by [5]:

$$\dot{\varepsilon} = A\sigma^n d^p \exp\left(-\frac{Q}{RT}\right) \quad (6.1)$$

where $\dot{\varepsilon}$ is the steady-state creep rate, A is a parameter depending on the deformation mechanism, d is the grain size, n is the stress exponent, p is the grain size exponent, Q is the activation energy for flow and R is the gas constant. Q , p and n are usually termed creep parameters, and provide essential information about the atomistic mechanisms of plastic deformation.

This section presents firstly the experimental procedure, defining the characteristic mechanical magnitudes and the different types of tests. Then, the experimental results obtained in LSO and BZY are presented, which are correlated with microstructural observations by scanning and transmission electron microscopy. The Chapter ends with the discussion of the probable underlying atomistic mechanisms responsible for plastic deformation and mass transport.

6.3.1.1 Mechanical magnitudes

Consider a specimen of initial height l_0 and initial section S_0 . Under a uniaxial compressive load F , the sample will deform to an instantaneous length $l(t)$ after a time t . The engineering (or nominal) strain ε_e and the engineering (or nominal) stress σ_e are given, respectively, by:

$$\varepsilon_e(t) = -\frac{\Delta l(t)}{l_0} = -\frac{l(t) - l_0}{l_0} \quad (6.2)$$

and:

$$\sigma_e = \frac{F}{S_0} \quad (6.3)$$

The negative sign in Equation 6.2 corresponds to compression tests, in order to obtain positive values of ε_e . The engineering strain is not an additive magnitude, and is thus not useful in the characterization of large strains. The true strain ε is then introduced as:

$$d\varepsilon(t) = -\frac{dl(t)}{l(t)} \quad (6.4)$$

Integrating this Equation, finally results in:

$$\varepsilon(t) = \ln \left[\frac{l_0}{l(t)} \right] \quad (6.5)$$

This magnitude differs significantly from the engineering strain ε_e (Equation 6.2) for strains larger than 10%.

The instantaneous strain rate $\dot{\varepsilon}(t)$ is given by:

$$\dot{\varepsilon}(t) = \frac{d\varepsilon(t)}{dt} = -\frac{1}{l(t)} \frac{dl(t)}{dt} \quad (6.6)$$

which is a state variable in the steady-state deformation regime (secondary creep).

On the other hand, the engineering stress σ_e (Equation 6.2) does not adequately describe the actual stress at which the sample is subjected during test because of the continuous increase in section $S(t)$ as strain proceeds. Therefore, the true stress $\sigma(t)$ is introduced as:

$$\sigma(t) = \frac{F}{S(t)} \quad (6.7)$$

In general, correction of the specimen cross-section is not simple in compression tests owing to the fact that the samples do not usually deform uniformly. On the one hand, cracks or cavities may appear inside the material and, on the other hand, friction between the sample compression faces and the punching rods of the essays machine causes the barrelling of the sample [6]. In this work, pads of SiC were inserted between the specimen and the alumina punching dies to avoid, or at least to reduce, friction at the specimen-die interfaces. This variation in sample shape is not significant for small strains values ($\varepsilon \leq 10\%$), but it can be substantial for large strains such as those achieved in this work ($\varepsilon \geq 40\%$).

The true stress σ can be related to the engineering stress σ_e assuming that the sample deforms at constant volume, *i.e.*, elastic effects and material densification/degradation are not considered. In this case:

$$S_0 l_0 = S(t) \cdot l(t) \quad (6.8)$$

The instantaneous cross-section $S(t)$ is given by:

$$S(t) = \frac{S_0 l_0}{l(t)} = S_0 \cdot e^{-\varepsilon} \quad (6.9)$$

where Equation (6.5) has been used. The true stress is then rewritten as:

$$\sigma(t) = \frac{F}{S_0} e^{-\varepsilon} = \sigma_e \cdot e^{-\varepsilon} \quad (6.10)$$

In this work, the true stress and the true strain have been used to analyse the mechanical data.

6.3.1.2 High-temperature mechanical tests

Compressive deformation tests were performed on specimens of about $5 \times 3 \times 3 \text{ mm}^3$ in size which were cut from sintered pellets with a low-speed diamond saw. The experiments were carried out in air at temperatures between 1000 and 1400 °C. Temperature was monitored by a Pt-Pt/10% Rh thermocouple placed close to the sample. Mechanical tests have been mainly conducted at constant cross-head speed, although some tests at constant load were also performed. Both types of tests are briefly described below.

6.3.1.2.1 Constant cross-head speed tests

These tests were performed in an EM1/FR universal machine (Microtest, University of Seville, Spain) equipped with polycrystalline alumina cylindrical rods of 25 mm in diameter and 300 mm in height. The lower rod moves up at a constant cross-head speed v_T between 5 and 50 $\mu\text{m}/\text{min}$ (corresponding to initial strain rates $\dot{\epsilon}_0$ of 1.7×10^{-5} and $1.7 \times 10^{-4} \text{ s}^{-1}$, respectively). The upper rod is connected to a load cell which instantaneously measures the load $F(t)$ necessary to maintain the compressive speed v_T . The recorded data, load F vs time t , were analysed in σ – ϵ curves. Tests were conducted in air at temperatures between 1000 and 1400 °C, with heating/cooling ramps of 10 °C/min and a 2 h soaking time to achieve the thermal equilibrium of the assembly. A small load of 2 MPa was applied during the heating process to keep the sample in contact with the alumina rods.

During a test at a fixed cross-head speed v_T , the instantaneous sample length $l(t)$ is given by:

$$l(t) = l_0 - v_T t \quad (6.11)$$

Therefore, the instantaneous strain and strain rate (Equations 6.5 and 6.6) are:

$$\epsilon(t) = \ln\left(\frac{l_0}{l_0 - v_T t}\right) = \ln\left(\frac{1}{1 - \dot{\epsilon}_0 t}\right) \quad (6.12)$$

and:

$$\dot{\epsilon}(t) = \frac{1}{l_0 - v_T t} v_T = \frac{\dot{\epsilon}_0}{1 - \dot{\epsilon}_0 t} = \dot{\epsilon}_0 \cdot e^\epsilon \quad (6.13)$$

where $\dot{\epsilon}_0$ is the initial strain rate:

$$\dot{\epsilon}_0 = \frac{1}{l_0} v_T \quad (6.14)$$

The stress-strain curves are obtained from Equations 6.10 and 6.12. It should be pointed out that the strain rate increases as the deformation proceeds (Equation 6.13) because of the continuous decrease in sample height. For example, for a strain of 50%, $\dot{\epsilon} (50\%) = e^{0.50} \cdot \dot{\epsilon}_0 = 1.6 \dot{\epsilon}_0$.

6.3.1.2.2 Constant load tests

These experiments are usually termed creep tests because the material deforms at its own rate under a given load. The tests were carried out in air at temperatures between 1100 and 1350 °C, under constant load at nominal stresses between 50 to 120 MPa. A manual deformation machine (Microtest, University of Sevilla, Spain) has been used, equipped with polycrystalline alumina cylindrical pistons of 25 mm in diameter and 400 mm in height. The load Q is applied by a lever coupled to the upper pull rod, while the lower rod displaces to balance the level arm. The recorded data, instantaneous sample length $l(t)$ vs time t , were plotted as $\dot{\epsilon}$ - ϵ curves on a semi-logarithmic graph. The true strain is given by Equation 6.5, and the strain rate $\dot{\epsilon}(t)$ is calculated by deriving the variation of sample height with time (Equation 6.6):

$$\dot{\epsilon}(t) \approx -\frac{1}{l(t)} \frac{\Delta l(t)}{\Delta t} \quad (6.15)$$

The samples were sandwiched between SiC pads in order to reduce the friction with the alumina punching dies of the deformation machine. A contact load of 20 N was initially applied during the heating process, which was carried out at 10 °C/min followed by a dwell time of 2 h to ensure the thermal equilibrium of the assembly.

6.3.1.3 Steady-state deformation

In a constant load creep experiment, three stages of deformation can generally be distinguished. After the initial load application, the strain rate is relatively high, but slows with increasing time; this regime is called initial stage, primary creep or regime I, and depends on the previous history of the material.

The following stage is characterized by a constant strain rate and is termed steady-state creep, secondary creep or regime II. It is described by the steady-state power-law creep equation (Equation 6.1), and only in this regime the creep parameters n , p and Q have a physical meaning.

In fact, the steady strain rate is independent of time in constant stress tests. In constant load tests, however, the true stress decreases because the sample cross-section increases continuously with time. In this case, it can be easily shown from Equations 6.1 and 6.10 that $\ln \dot{\epsilon}$ decreases linearly with ϵ :

$$\dot{\epsilon} \propto \sigma^n = \sigma_0^n \cdot e^{-n\epsilon} \rightarrow \ln \dot{\epsilon} = A - n\epsilon \quad (6.16)$$

where A is a parameter independent of ϵ and σ_0 is the initial stress (the engineering stress).

Finally, the third stage corresponds to a rapid increase in strain rate as a consequence of the nucleation and coalescence of cavities that eventually may lead to material failure. It is termed tertiary creep or regimen III.

In the case of deformation tests at constant cross-head speed, the σ - ϵ curves exhibit an initial linear stage corresponding to elastic deformation, followed by a transitory regimen (regime I) before reaching the steady state (regime II). In a true constant strain rate test, the steady state is characterized by a constant creep stress (flow stress) with strain. In our tests at constant cross-head speed, however, the instantaneous strain rate increases with increasing strain because of the continuous decrease in specimen height, as noted in the previous Section. Combining Equations 6.1 and 6.13, the flow stress increases with strain in the form:

$$\sigma \propto e^{\epsilon/n} \rightarrow \ln \sigma = B + \frac{1}{n}\epsilon \quad (6.17)$$

where B is a parameter independent of ϵ . In this case, the slope of the $\ln \sigma$ - ϵ curves gives the inverse of the stress exponent n in case of homogeneous deformation. This equation has been widely used in this work in the analysis of the stress-strain curves of LSO and BZY compounds to check the presence/absence of concurrent grain growth.

6.3.1.4 Determination of creep parameters

There are two basic methods for determining the creep parameters from the steady state equation (Equation 6.1): (i) comparing different experiments performed on a set of similar samples in which a single variable has been modified, keeping the others constant (method conventional); and (ii) modifying one variable during the test on the same sample, keeping constant the other conditions (differential method). Briefly, both methods are described below, in particular in relation with constant cross-head speed tests.

6.3.1.4.1 Conventional method

For the determination of the stress exponent n , a set of isothermal tests was performed by varying the initial strain rate in constant compression cross-head speed tests. The slope of the best fit line of the $\log \dot{\epsilon} - \log \sigma$ plot, for a given strain, is the stress exponent. Similarly, to determine the activation energy Q , a series of tests was performed at different temperatures maintaining the same initial strain rate. The slope of the best fit line of the $\log \sigma - 1/T$ plot, for a given strain, is proportional to the parameter Q .

In this work the grain size exponent p was not determined because it requires a set of tests at the same temperature and strain rate on samples with different grain sizes. Although LSO polycrystals with different grain sizes have been obtained, different deformation mechanisms were found for fine- and large-grained materials, preventing a proper determination of p .

The conventional method has two drawbacks: firstly, it requires an large number of reproducible samples, prepared under the same conditions, which is not always possible; and secondly, it does not take into account the possible evolution of the microstructure with experimental conditions, so it is likely that wrong values of the creep parameters can be obtained when the microstructure is unstable.

6.3.1.4.2 Differential method

To determine the stress exponent n , a test is initially performed at a temperature T_1 and at initial strain rate $\dot{\epsilon}_1$. After reaching the steady-state, characterized by a flow stress σ_1 , the strain rate is suddenly changed to $\dot{\epsilon}_2$. After the corresponding transient stage, a new steady-state flow stress σ_2 will be reached. By using the power-law creep equation (Equation 6.1), the stress exponent is given by:

$$n = \left. \frac{\partial \dot{\epsilon}}{\partial \sigma} \right|_{T,d} \simeq \left. \frac{\ln(\dot{\epsilon}_2 / \dot{\epsilon}_1)}{\ln(\sigma_2 / \sigma_1)} \right|_{\epsilon} \quad (6.18)$$

The extrapolation of the flow stresses at the time (strain) of the strain rate change ensures that the exponent n is determined under conditions of constant microstructure.

In the case of constant load tests, the procedure is very similar. Once the steady-state strain rate $\dot{\epsilon}_1$ is reached at T_1 and σ_1 , the load is suddenly changed to σ_2 , resulting in a new steady-state strain rate $\dot{\epsilon}_2$. The stress exponent n can be thus estimated from Equation 6.18.

The determination of the activation energy Q by the differential method requires the change of the testing temperature during the steady-state deformation, keeping constant the other experimental conditions. Once the new steady state has been reached, the comparison of the flow stresses before and after the temperature change in a constant cross-head speed test leads to the activation energy Q :

$$Q = -R \left. \frac{\partial \ln \dot{\epsilon}}{\partial (1/T)} \right|_{\sigma, d} \approx -R \left. \frac{\ln(\dot{\epsilon}_2 / \dot{\epsilon}_1)}{1/T_2 - 1/T_1} \right|_{\epsilon} \quad (6.19)$$

Similarly, in a constant load creep test, Q is given by:

$$Q = nR \left. \frac{\partial \ln \sigma}{\partial (1/T)} \right|_{\dot{\epsilon}, d} \approx nR \left. \frac{\ln(\sigma_2 / \sigma_1)}{1/T_2 - 1/T_1} \right|_{\epsilon} \quad (6.20)$$

Unlike the determination of the stress exponent n , where the strain rate or load changes are instantaneous, the determination of the activation energy Q requires a stabilization time after the temperature change. To this end, the sample was unloaded for the temperature change (a small load of 2 MPa was remained to avoid the loss of contact between sample and alumina dies) and then re-loaded once the new thermal equilibrium was reached. Moreover, the steady-states of deformation are generally linked to the point defect population in the material [5], so it is necessary to wait until the new point defect equilibrium concentrations, corresponding to the new temperature, are reached before proceeding with deformation. This re-equilibration time depends on the chemical diffusion coefficient of the various ionic species in the compound, which are not known. For the temperature range used in the present study, we have verified that re-equilibration times of 2 h are adequate to reach the new equilibrium conditions.

6.3.2 Experimental results

The fragile-ductile transition and the steady-state creep parameters obtained in the high-temperature deformation tests are presented below for each material. The atomistic mechanisms involved in the deformation process are then discussed and compared to literature data.

6.3.2.1 High-temperature mechanical behaviour of LSO-CS

6.3.2.1.1 Fragile-ductile transition

Figure 6.10 shows typical curves of the variation of the true stress σ with true strain ϵ of LSO-CS deformed in air at a given initial strain rate $\dot{\epsilon}_0 = 3.6 \times 10^{-5} \text{ s}^{-1}$ (corresponding to a cross-head

speed of 10 $\mu\text{m}/\text{min}$) and different temperatures between 1020 and 1300 $^{\circ}\text{C}$. The material displays a gradual transition from a brittle-to-ductile regime as the temperature increases. The marks “x” on the curves indicate the macroscopic fracture of specimens. At 1020 $^{\circ}\text{C}$, the lowest temperature studied, the sample failed catastrophically at a stress level of about 730 MPa without undergoing any plastic deformation. At 1090 $^{\circ}\text{C}$, the compound already shows the early onset of plastic deformation, with a slight curvature of the $\sigma - \epsilon$ curve at 450 MPa, but failing finally after a very few percent of plastic strain. A semi-ductile behaviour was observed at 1140 and 1200 $^{\circ}\text{C}$, where the material reached deformations as large as 50% without macroscopic fracture (tests were intentionally stopped at this strain value for subsequent microstructural observations). Stress softening could be observed in this regime, starting at larger strains with increasing temperature: at about 5% and 35% for 1140 and 1200 $^{\circ}\text{C}$, respectively.

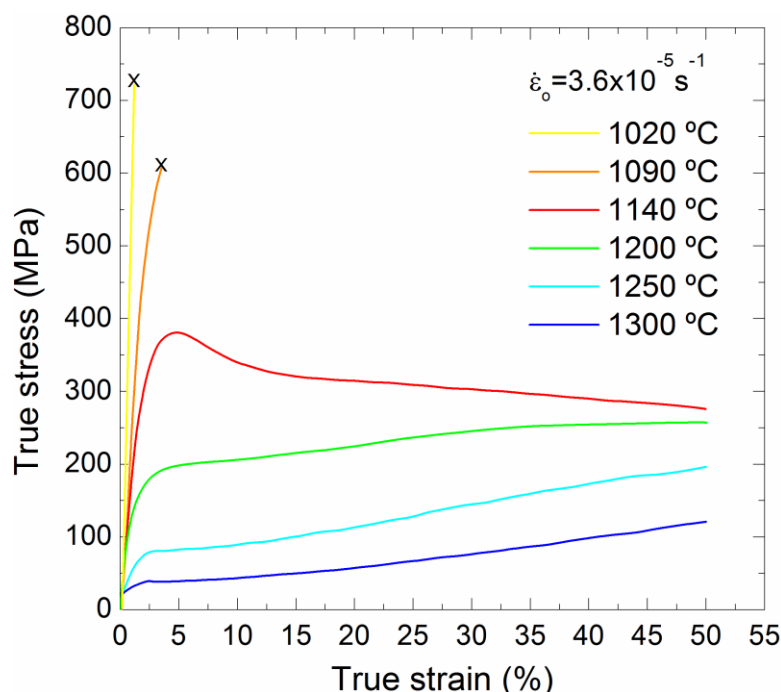


Figure 6.10. True stress σ - true strain ϵ curves for LSO-CS deformed in compression at an initial strain rate of $3.6 \times 10^{-5} \text{ s}^{-1}$ and different temperatures. Marks “x” indicate macroscopic specimen failure.

For higher temperatures, 1250 and 1300 $^{\circ}\text{C}$, extended steady-state regimes of deformation (secondary creep regimes) were attained, characterized by a rather constant positive slope of the stress - strain curves. As shown in Section 6.3.1.1, the slopes gradually increase with increasing strain (Equation (6.17) owing to the shortening of the specimen height in constant cross-head speed tests as used in this study.

In a similar way, a series of tests was performed at a given temperature of 1300 $^{\circ}\text{C}$ and various initial strain rates ranging from 1.9×10^{-5} to $1.9 \times 10^{-4} \text{ s}^{-1}$. **Figure 6.11** shows the corresponding $\sigma - \epsilon$ curves. As expected, proper steady states of deformation are attained at the lower strain rates,

changing gradually towards a brittle behaviour with increasing strain rate: stress softening can be observed at $\dot{\epsilon}_0 = 1.9 \times 10^{-4} \text{ s}^{-1}$ at a stress level of $\epsilon \approx 35\%$. It should be noted again the increase of the σ - ϵ slopes in steady-states conditions when increasing strain rate.

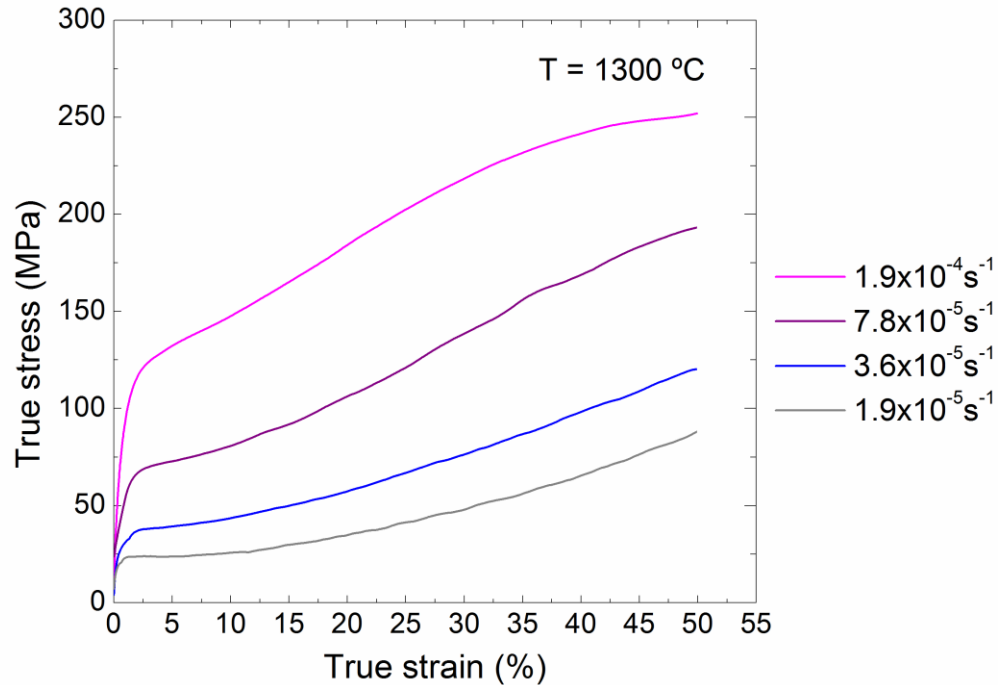


Figure 6.11. True stress σ - true strain ϵ curves for LSO-CS deformed in compression at 1300 °C and different initial strain rates.

6.3.2.1.2 Microstructure after deformation

The macroscopic aspect of the strained samples is shown in **Figure 6.12**, which correlates very well with the shape of the corresponding stress - strain curves. At the lower temperature studied, 1020 °C (curve in yellow, **Figure 6.10**), the specimen completely fractured into multiple small fragments (**Figure 6.12g**), indicating the fast propagation of cracks throughout the overall sample volume of the sample. Similar characteristics were observed in the sample deformed at 1090 °C (curve in orange, **Figure 6.10**), which underwent a very limited plastic deformation before fracture. In this case, the specimen failed by the propagation of several longitudinal cracks along the entire specimen length (**Figure 6.12f**), originated at grain boundary flaws. SEM observations of fracture surfaces indicate a mixed failure mode, changing from predominantly transgranular in the coarser grains to intergranular in the finer ones (**Figure 6.13**). Such a behaviour is consistent with the pore distribution observed in the as-prepared material, preferentially located at grain boundaries in the finer-grained regions (**Figure 3.5**), which facilitates intergranular crack propagation in these areas.

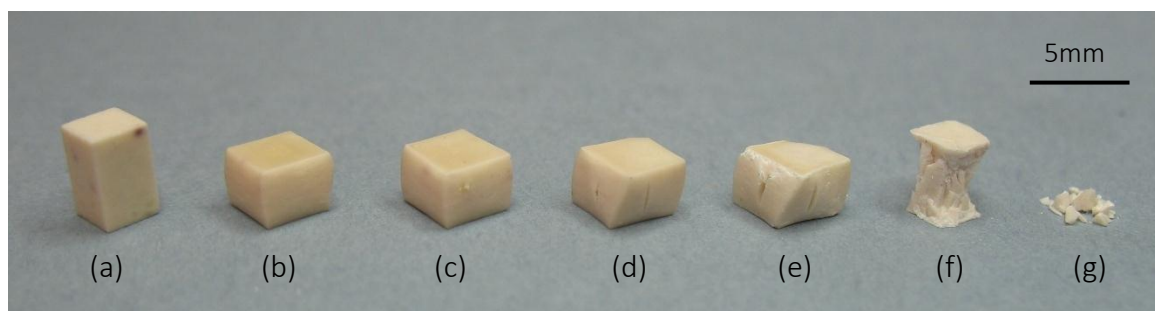


Figure 6.12. Macroscopic aspect of LSO-CS samples deformed in compression at an initial strain rate of $3.6 \times 10^{-5} \text{ s}^{-1}$ and different temperatures (Figure 5.10): (a) as-prepared LSO-CS, (b) 1300 °C, (c) 1250 °C, (d) 1200 °C, (e) 1140 °C, (f) 1090 °C, and (g) 1020 °C.

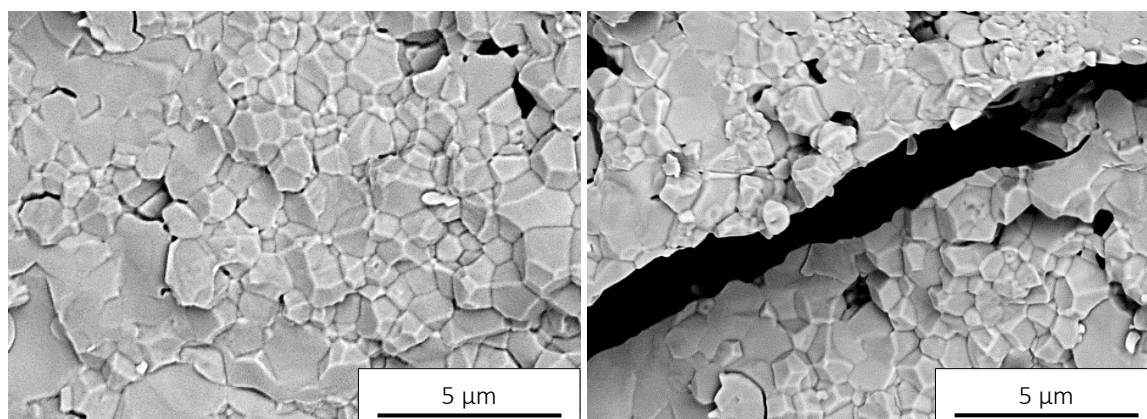


Figure 6.13. SEM micrographs of fracture surfaces of LSO-CS tested at 1090 °C and an initial strain rate of $3.6 \times 10^{-5} \text{ s}^{-1}$.

At the intermediate temperatures of 1140 - 1200 °C and $\dot{\epsilon}_0 = 3.6 \times 10^{-5} \text{ s}^{-1}$ (curves in red and green, **Figure 6.10**), the semi-ductile regime is also characterized by the formation of these large longitudinal cracks, as can be observed in the lateral faces of the specimens (**Figure 6.12d and e**), which are responsible for the flow softening observed in the corresponding $\sigma - \epsilon$ curves. In such conditions, however, the material was able to tolerate the macroscopic flaws without cracking, as can be observed in **Figure 6.14**, where two longitudinal cracks are blocked inside a sample strained up to 50%. In this defect-tolerant regime, extensive grain boundary decohesion takes place around the cracks, whereas nearby regions maintain their original integrity without significant changes in grain morphology and porosity with respect to the as-fabricated material. Similar characteristics were observed in the sample tested at 1200 °C (**Figure 6.15**) where softening appeared at $\epsilon = 35\%$.

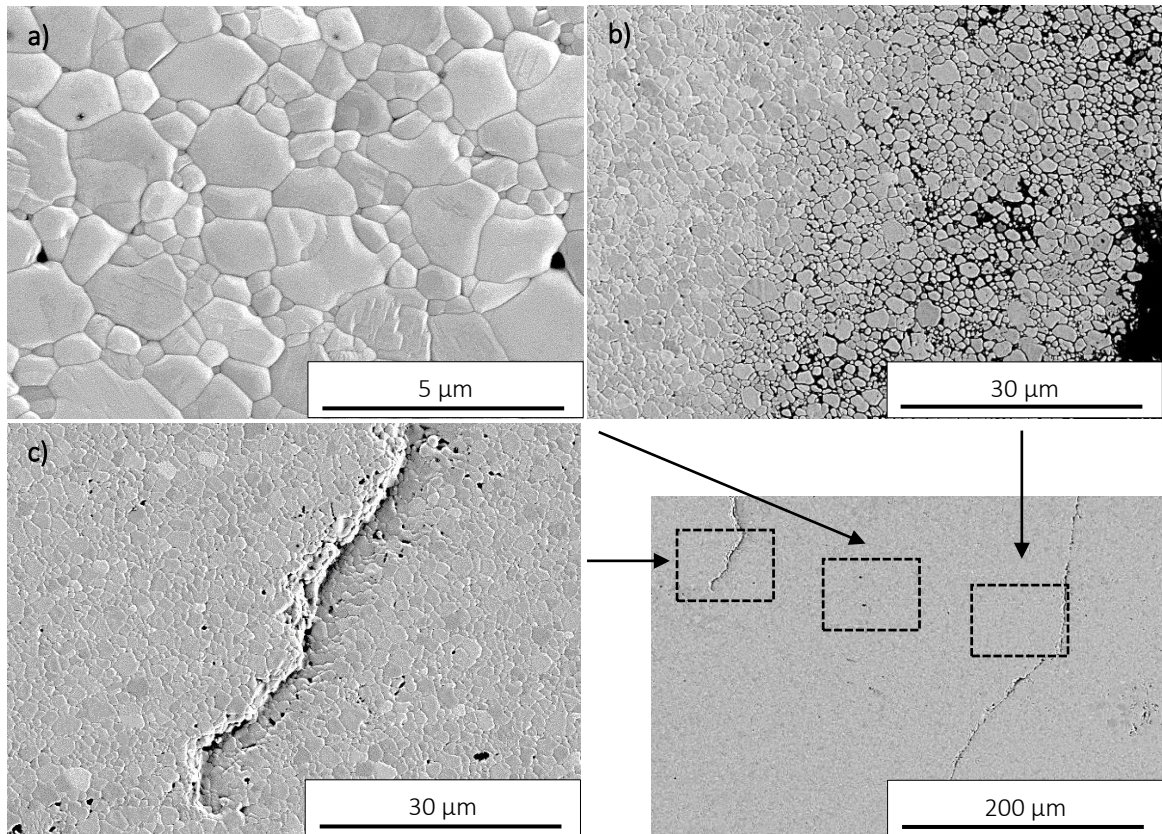


Figure 6.14. SEM micrographs of LSO-CS deformed up to $\varepsilon = 50\%$ in compression at an initial strain rate of $3.6 \times 10^{-5} \text{ s}^{-1}$ and $1140 \text{ }^\circ\text{C}$ (curve in red, Figure 6.10), with flow softening starting at $\varepsilon = 5\%$. Stress axis is vertical. (a) Unmodified regions between cracks; (b) grain boundary decohesion (embrittlement) around the crack surfaces; and (c) longitudinal cracks arrested inside the sample.

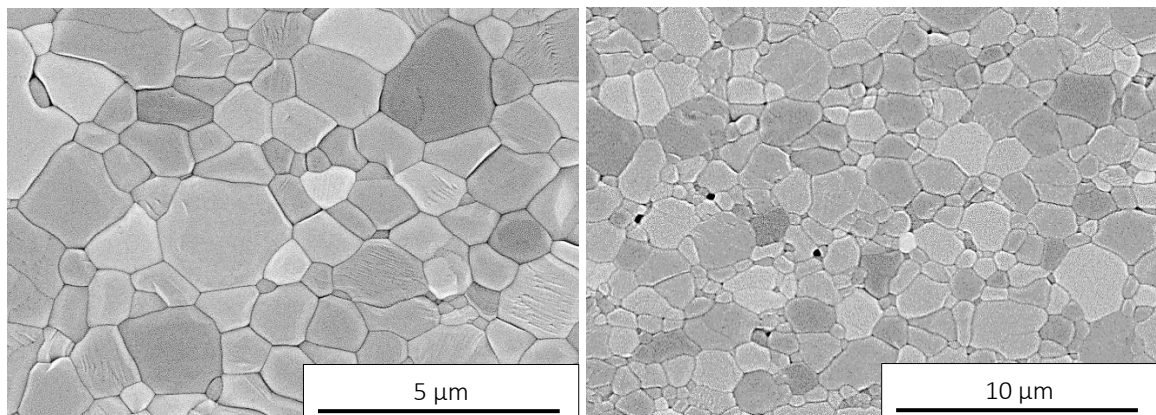


Figure 6.15. SEM micrographs of LSO-CS sample deformed up to $\varepsilon = 50\%$ in compression at an initial strain rate of $3.6 \times 10^{-5} \text{ s}^{-1}$ and $1200 \text{ }^\circ\text{C}$ (curve in green, Figure 5.10), with flow softening at $\varepsilon = 35\%$. Stress axis is vertical.

Further temperature increases give rise to well-deformed samples (**Figure 6.12b and c**), with very little barrelling, corresponding to well-established steady states of deformation (curves in blue and cyan, **Figure 6.10**). SEM observations of these samples reveal that the grains retained their equiaxed shape, although concurrent grain growth took place during testing. **Figure 6.16**

shows SEM micrographs at different magnifications of a specimen strained up to $\varepsilon = 50\%$ at the highest temperature studied $T = 1300\text{ °C}$ and $\dot{\varepsilon}_0 = 3.6 \times 10^{-5}\text{ s}^{-1}$ (curve in blue, **Figure 6.10**). The corresponding grain size d and form factor F distributions led to average values of $d = 1.4 \pm 0.1\text{ }\mu\text{m}$ and $F = 0.8 \pm 0.1$, indicating a final grain size slightly larger than in the as-fabricated material (reminder: $d = 1.1 \pm 0.6\text{ }\mu\text{m}$ and $F = 0.8 \pm 0.1$, Section 3.3.1.4). The grains retain, however, their initial shape despite the large strains attained. Concurrent grain growth was minimal in samples deformed at 1250 °C and below. Static grain growth in conventional pressureless sintered oxyapatites has been recently reported by Suarez *et al.* [7]. They found an increase in grain size from $1.4\text{ }\mu\text{m}$ at 1400 °C and 24 h to $1.9\text{ }\mu\text{m}$ at 1500 °C and 3 h, and up to $2.2\text{ }\mu\text{m}$ at 1500 °C and 10 h. The authors, however, did not attempt to derive a relationship for the grain growth kinetics.

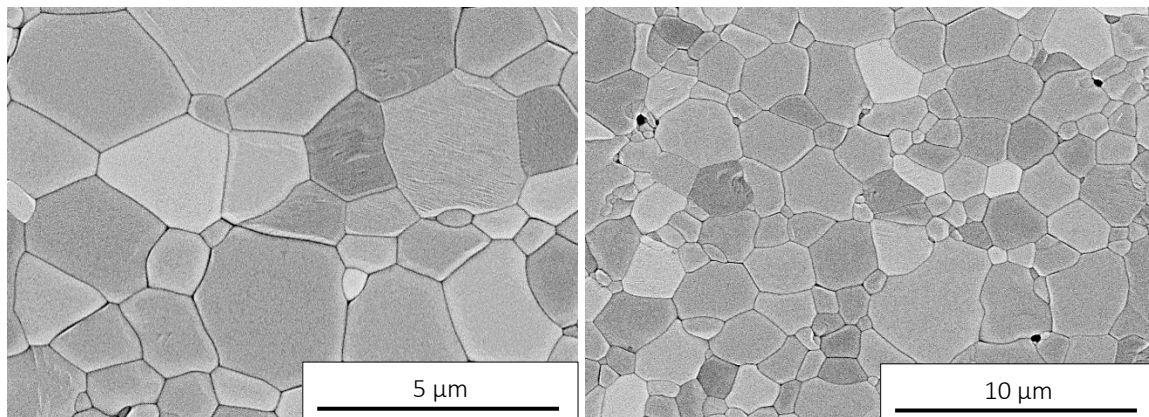


Figure 6.16. SEM micrographs of LSO-CS sample deformed in steady state up to $\varepsilon = 50\%$ in compression at an initial strain rate of $3.6 \times 10^{-5}\text{ s}^{-1}$ and 1300 °C (curve in cyan, Figure 5.10). The final average grain size is $1.4\text{ }\mu\text{m}$. Stress axis is vertical.

TEM observations of thin films cut from specimens deformed in the ductile regime have shown the absence of dislocations and other defects inside the grains, which exhibit straight boundaries and well-defined triple junctions (**Figure 6.17**), as in the as-fabricated material. However, the specimens strained in the semi-ductile regime have shown a relatively high density of dislocations, usually gathered into sub-boundaries, in some of the larger-sized grains, while the finer grains remained clean and free of dislocations (**Figure 6.18**). A closer inspection of the corresponding SEM images shows the presence of small cells limited by sub-boundaries within some of the coarser grains (**Figure 6.19**); they are hardly seen at higher temperatures (**Figure 6.16**). It is therefore assumed that there is a direct correlation between SEM and TEM images. At intermediate temperatures, where the grain growth process still is not finished, the sub-boundaries observed within a given large-sized grain correspond to the original boundaries of small grains that are being consumed by such a grain. At higher temperatures, grain boundary migration is faster, resulting in cleaner grains, as experimentally found.

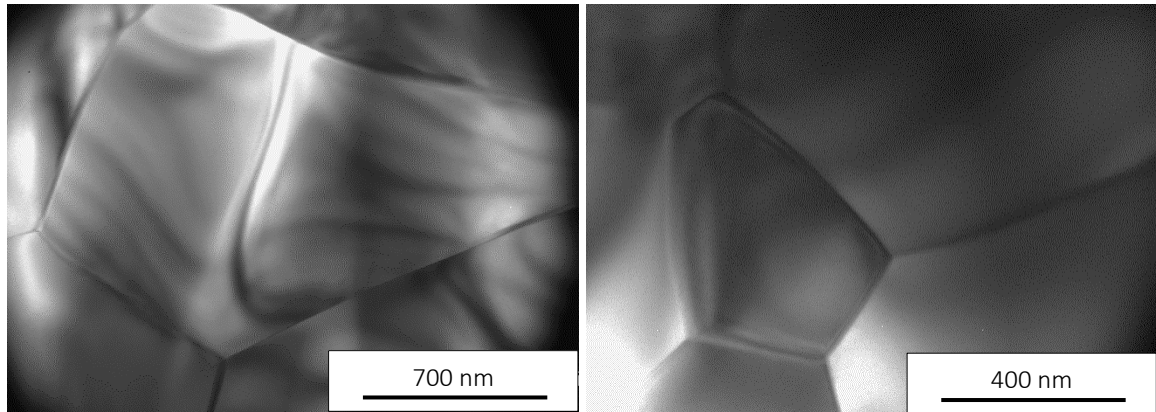


Figure 6.17. TEM images of LSO-CS sample deformed in compression at an initial strain rate of $3.6 \times 10^{-5} \text{ s}^{-1}$ and $1300 \text{ }^\circ\text{C}$ (ductile regime).

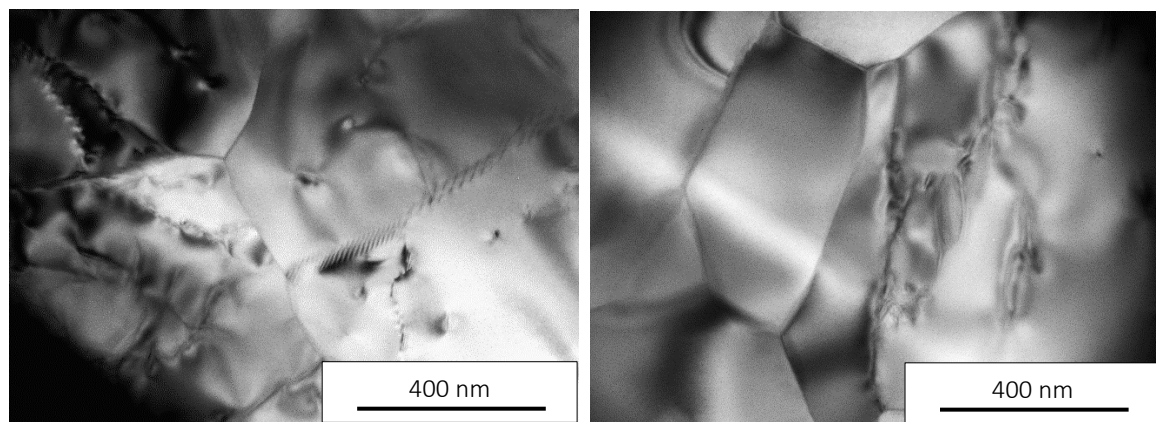


Figure 6.18. TEM images of LSO-CS sample deformed in compression at an initial strain rate of $3.6 \times 10^{-5} \text{ s}^{-1}$ and $1140 \text{ }^\circ\text{C}$ (semi-ductile regime).

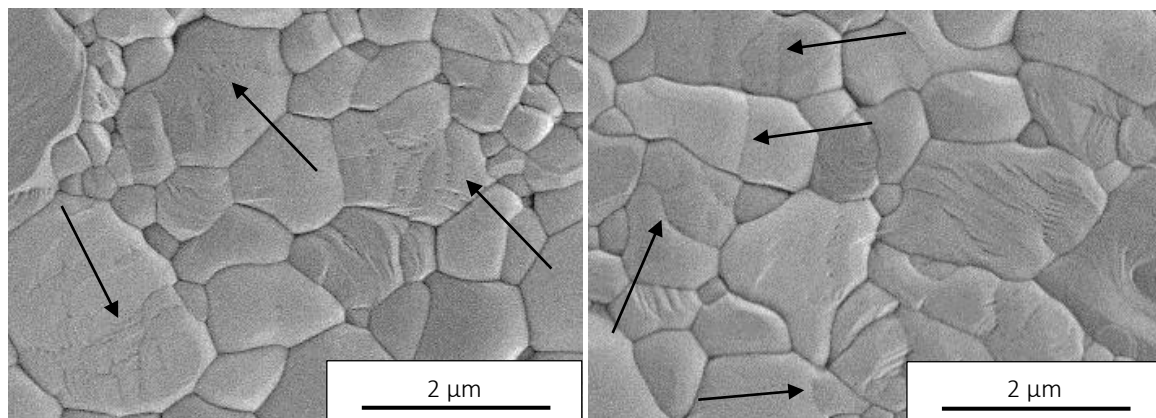


Figure 6.19. SEM images of LSO-CS sample deformed in compression at an initial strain rate of $3.6 \times 10^{-5} \text{ s}^{-1}$ and $1140 \text{ }^\circ\text{C}$ (semi-ductile regime). Black arrows point at sub-boundaries in the larger-sized grains. Stress axis is vertical.

6.3.2.1.3 Creep parameters

As indicated in Section 6.3.1.4, the characteristic parameters of the creep behaviour can be confidentially determined only in steady state; otherwise the values estimated from deformation data using the creep power law are physically meaningless (which indeed are in the root of many controversies that exist in the literature regarding the creep behaviour of ceramic materials).

The stress exponent n can be estimated directly from the isothermal σ - $\dot{\epsilon}$ curves obtained at different strain rates (conventional method, Section 6.3.1.4.1). As already noted, this determination is somewhat complicated in constant cross-head speed tests owing to the variation of the σ - $\dot{\epsilon}$ slope in steady state because of the decrease in sample height as the test proceeds. The flow stresses have been then measured at $\epsilon = 10, 20$ and 30% at $1300\text{ }^\circ\text{C}$ (Figure 6.20), resulting stress exponents of $n = 1.2, 1.2$ and 1.3 , respectively, with an average value $n = 1.2 \pm 0.1$.

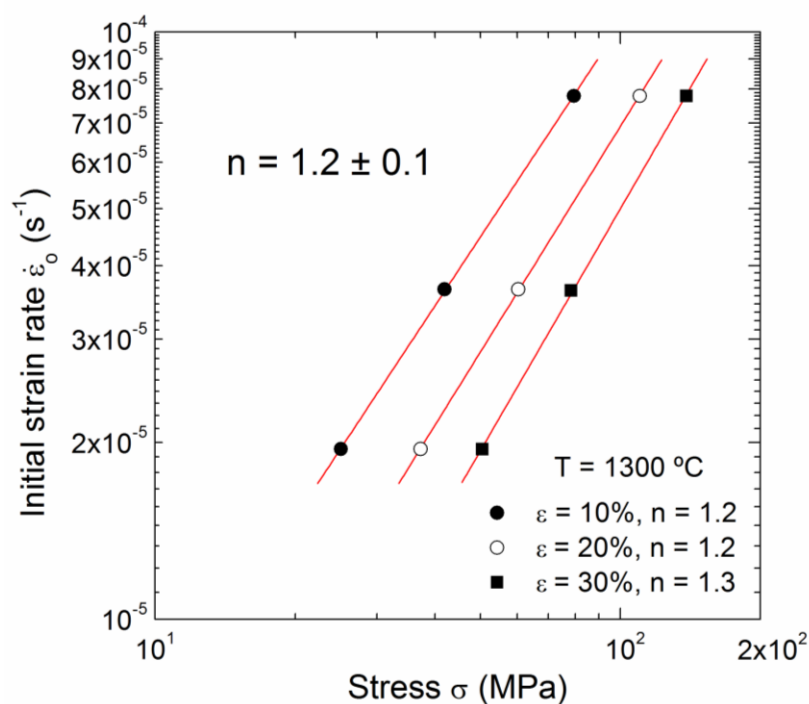


Figure 6.20. Determination of the stress exponent n from isothermal curves in the steady-state creep of LSO-CS for strain levels $\epsilon = 10, 20$ and 30% .

This stress exponent n can be also estimated from fast strain rate changes during a single isothermal test (differential method, Section 6.3.1.4.2). Figure 6.21 shows such a test carried out at $1250\text{ }^\circ\text{C}$ with fast up- and down-strain rate changes between 1.9×10^{-5} and $3.6 \times 10^{-5}\text{ s}^{-1}$ (curve in black). It can be seen that the steady states are rapidly regained after each strain rate jump, with transitory states of about 3%. From the strain rate jumps, an average value of $n = 1.2 \pm 0.1$ was calculated, identical to that obtained by the conventional method. As discussed later, a stress

exponent of 1 is characteristic of a diffusion-controlled grain boundary sliding mechanism, where the grains slide against each other to accommodate the macroscopic deformation of the specimen [5, 8, 9]. This intergranular deformation mechanism has permitted to explain successfully the microstructural and mechanical behaviour observed in different ceramic materials with grain sizes above 1 μm , where a stress exponent close to unity was systematically reported: UO_2 , $n = 1.5$, $d = 2\text{--}10 \mu\text{m}$ [10]; NiO , $n = 1.4$, $d = 9 \mu\text{m}$ [11]; Y_2O_3 -stabilized cubic ZrO_2 , $n = 1.3$, $d = 2\text{--}6 \mu\text{m}$ [12]; $\text{YBa}_2\text{Cu}_3\text{O}_{7-x}$, $n = 1.0$, $d = 10 \mu\text{m}$ [13]; and yttrium aluminium garnet (YAG), $n = 1.0$, $d = 2\text{--}5 \mu\text{m}$ [14].

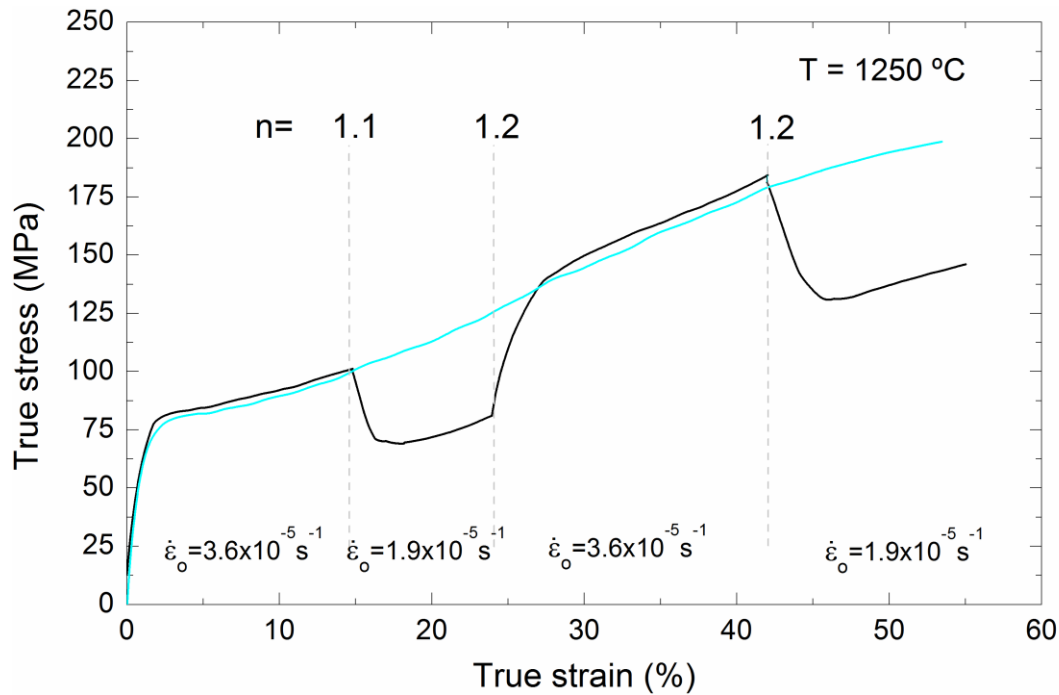


Figure 6.21. True stress σ - true strain ε curve for LSO-CS deformed in compression at 1250 °C with several strain rate jumps to determine the stress exponent (differential method, curve in black). The corresponding curve at 1250 °C and $3.6 \times 10^{-5} \text{ s}^{-1}$ is also shown (curve in cyan).

Figure 6.21 also displays the isothermal test performed at 1250 °C and $3.6 \times 10^{-5} \text{ s}^{-1}$ (curve in cyan) superimposed to the differential test. As can be seen, both curves overlap each other reasonably well at the same experimental conditions, indicating a very good reproducibility of the high-temperature mechanical tests.

Following the same procedures used for the stress exponent, the creep activation energy Q has been estimated from the conventional and differential methods. For the former, **Figure 6.22** shows the variation of flows stress σ (at strain levels of 10, 20 and 30%) against reciprocal temperature $1/T$ for an initial strain rate $\dot{\varepsilon}_0 = 3.6 \times 10^{-5} \text{ s}^{-1}$ at three different temperatures, 1200, 1250 and 1300 °C (curves in green, cyan and blue, **Figure 6.10**). The datum point at $\varepsilon = 30\%$ for $T = 1200 \text{ °C}$ has not been used in the analysis due to the appearance of signals of sample degradation.

Values of $Q = 370$, 330 and 310 kJ/mol were estimated at 10, 20 and 30% of strain, respectively, yielding an average value of $Q = 340 \pm 30$ kJ/mol. The uncertainty assigned to Q is typical for high-temperature measurements, where the accuracies in stress are usually not better than 10%.

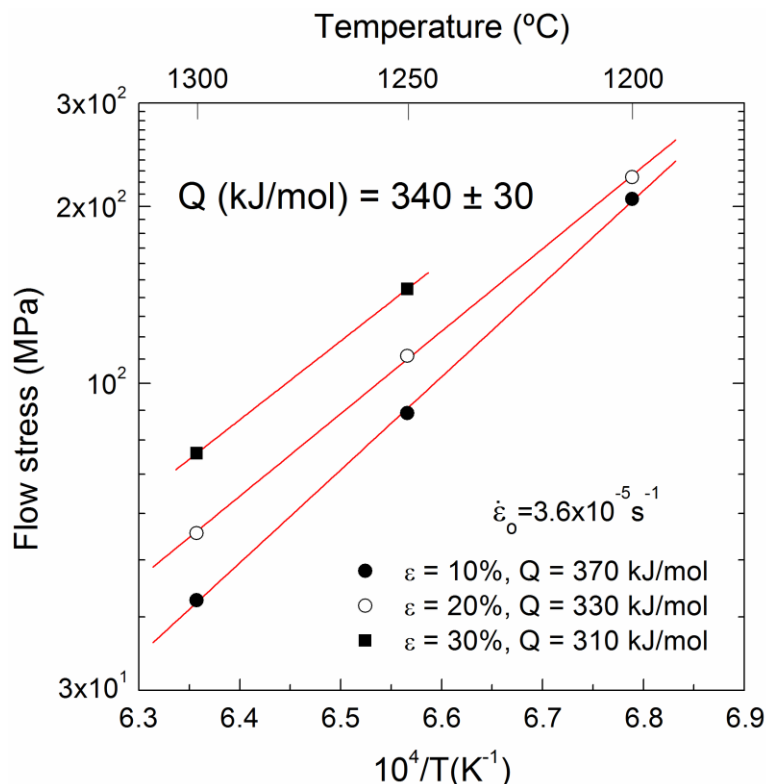


Figure 6.22. Determination of the activation energy Q for LSO-CS at strain levels $\epsilon = 10$, 20 and 30%.

For the differential method, **Figure 6.23** displays a mechanical test performed at a fixed initial strain rate of $\dot{\epsilon}_0 = 3.6 \times 10^{-5} s^{-1}$ with temperature changes between 1250 and 1300 °C (curve in black). Individual Q values of 360, 375 and 300 kJ/mol were obtained, with an average value $Q = 350 \pm 40$ kJ/mol, in good agreement with the value estimated previously from the conventional method $Q = 340 \pm 30$ kJ/mol. At difference with the stress exponent n determination, where the strain rate changes were performed without unloading the sample, the deformation was stopped before each temperature change, and then resumed after establishing the new equilibrium conditions (about 2 h). **Figure 6.23** shows that the steady states of deformation are easily reached after each temperature change, indicating that the establishment or modification of a dislocation substructure is not necessary for attaining the stationary creep regime. This feature attests the idea that diffusion is the rate-controlling mechanism in LSO-CS oxy-apatite with an average grain size of about 1 μm . Within this frame, the activation energy for flow $Q = 350 \pm 40$ kJ/mol can be associated

with the activation energy for diffusion of the slowest moving species along the fastest path, and contains both migration and formation energy terms.

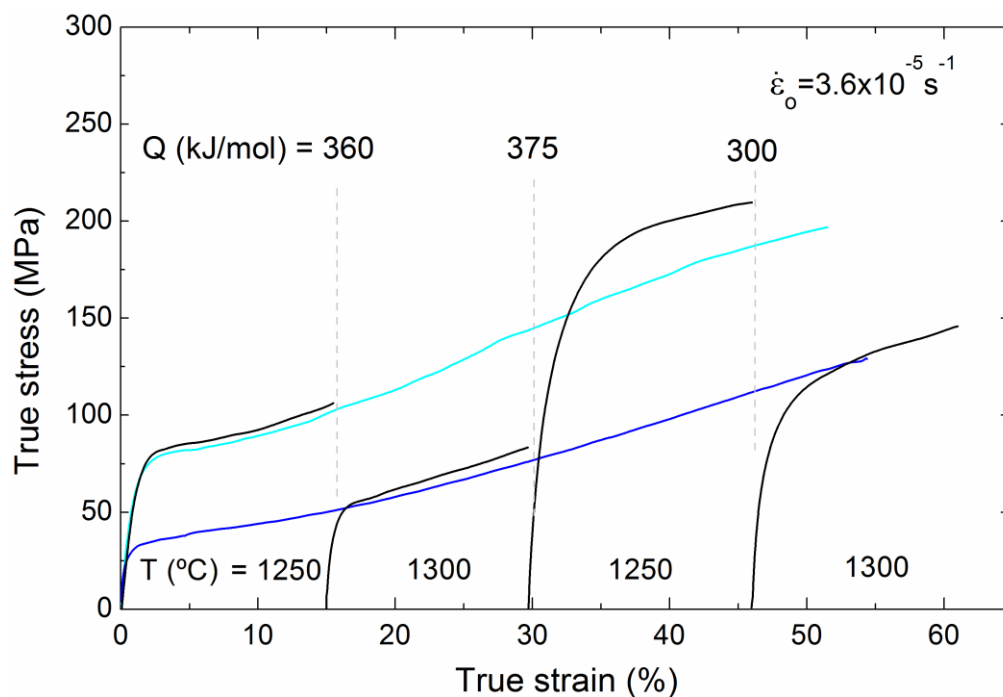


Figure 6.23. True stress σ - true strain ε curve for LSO-CS deformed in compression at an initial strain rate of $3.6 \times 10^{-5} \text{ s}^{-1}$ with temperatures changes between 1250 and 1300 °C (curve in black). The corresponding conventional curves at the same initial strain rate and temperatures are also shown (curves in cyan and blue).

Figure 6.23 also displays the conventional tests performed at 1250 and 1300 °C and at the same initial strain rate (curves in cyan and blue) than the temperature jumping test. It can be seen that the stress levels in the different sections of the curves superimposed reasonably well, except the third section, corresponding to 1250 °C after annealing and deformation at 1300 °C, where the stress is higher than would be expected. The difference can be understood by considering a potential increase in grain size that would take place at 1300 °C, as already noted above, which would hardens the material with respect to the previous section at 1250 °C.

The next paragraphs aims at understanding to which degree the grain growth might explain the deformation curves at high temperature, in particular at and above 1300°C. Concurrent grain growth during the high-temperature deformation of LSO-CS oxy-apatite may affect the slopes of the σ - ε curves. As shown above, in steady-state conditions, the slope α of the σ - ε curve in a log-linear plot yields the reciprocal stress exponent $\alpha = 0.010/n$ assuming homogeneous deformation and the absence of any microstructural change (Equation 6.17, note that in this Equation the strain is given as an absolute quantity, while in the present analysis the strain is expressed as a

percentage). **Figure 6.24** shows such a plot for LSO-CS deformed at the higher temperature $T = 1300\text{ }^{\circ}\text{C}$ and different initial strain rates (**Figure 6.11**). The slopes are similar for the three curves, with values between $\alpha = 0.026$ and 0.029 , much higher than the value of $\alpha = 0.010$ that would be expected for a mechanism with $n = 1$, and consequently leading to erroneous stress exponents n = between 0.35 and 0.38 . For reference, slopes with $n = 1, 2$ and 5 are shown by dashed lines at the bottom of **Figure 6.24**.

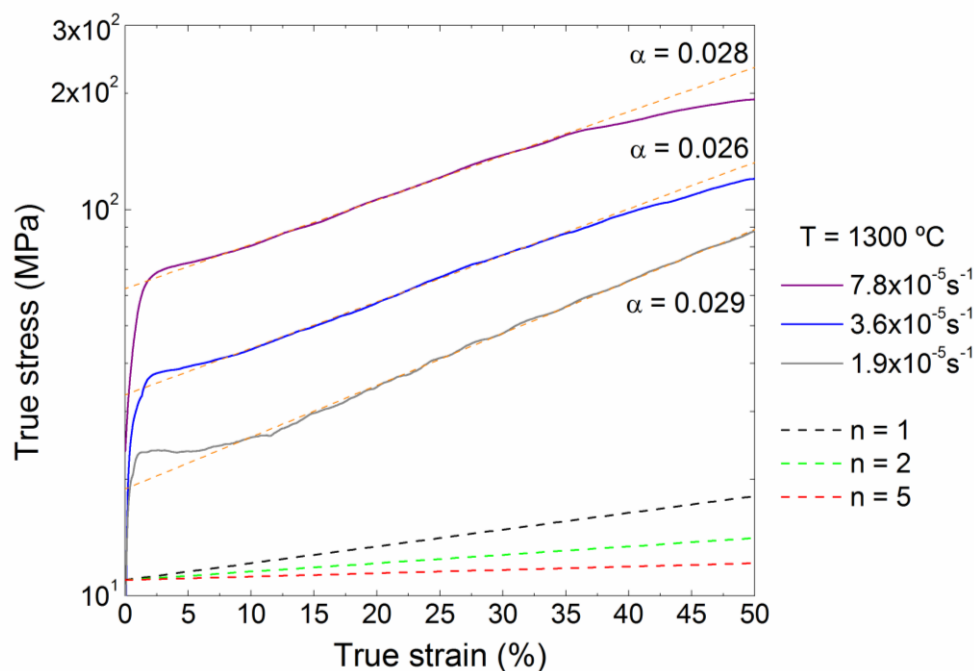


Figure 6.24. Log σ - ε curves for LSO-CS deformed in compression at $1300\text{ }^{\circ}\text{C}$ and different initial strain rates. Predictions for $n = 1, 2$ and 5 are also plotted for the sake of comparison.

According to the creep power law (Equation (6.1)), the flow stress in a constant cross-head speed test changes continuously with strain in the form:

$$\sigma(\varepsilon) = \sigma_0 \cdot e^{\frac{\varepsilon}{n}} \cdot \left(\frac{d_\varepsilon}{d_0} \right)^{\frac{p}{n}} \quad (6.21)$$

where σ_0 is the nominal (engineering) stress, d_0 the initial grain size and p the grain size exponent (usually 2 or 3 depending on the diffusion path [5, 8, 9]). The factor $\exp(\varepsilon/n)$ accounts for the increase in flow stress with increasing strain due to sample shortening (Equation 6.17), whereas the factor $(d_\varepsilon/d_0)^{p/n}$ takes into consideration the possible grain growth during testing (*i.e.*, the material becomes progressively harder).

Table 6.1 shows the initial σ_0 and final $\sigma_{50\%}$ stresses measured in LSO-CS at various conditions of strain rate and temperature (**Figure 6.10** and **Figure 6.11**). In the absence of concurrent grain growth, an increase in flow stress $\sigma_{50\%}/\sigma_0 = 1.6$ would be expected after 50% of

strain (Equation 6.21 with $d_{50\%} = d_o$ and $n = 1$). However, the observed experimental $\sigma_{50\%}/\sigma_o$ ratios are higher, between 2.0 and 4.3 (column 5 in **Table 6.1**), increasing with temperature. This result suggests that significant grain growth occurred during testing, particularly at the higher temperature, in agreement with the microstructural observations reported above (**Figure 6.16**).

Table 6.1. Initial σ_o and final $\sigma_{50\%}$ stresses measured in LSO-CS at various conditions of strain rate and temperature. A $\sigma_{50\%}/\sigma_o$ ratio of 1.6 is expected in the absence of grain growth (Equation 5.21). Grain size $d_{50\%}/d_o$ ratios necessary to explain the observed stress ratios are given in columns 6 and 7 for $p = 2$ and $p = 3$, respectively.

T (°C)	$\dot{\epsilon}_o$ (s ⁻¹)	σ_o (MPa)	$\sigma_{50\%}$ (MPa)	$\sigma_{50\%}/\sigma_o$	$d_{50\%}/d_o$ p = 2	$d_{50\%}/d_o$ p = 3
	1.8×10^{-5}	20	86	4.3	1.6	1.4
1300	3.6×10^{-5}	34	127	3.7	1.5	1.3
	7.8×10^{-5}	60	242	4.0	1.6	1.3
1250	3.6×10^{-5}	75	150	2.0	1.1	1.1

In order to explain the observed stress ratios by concurrent grain growth, the grain size exponent p must be known. Because there is no information available, the usual p values of 2 and 3, corresponding to volume and grain boundary diffusion-controlled creep mechanisms [5, 8, 9], respectively, have been used in Equation 6.21. For $p = 2$ (column 6 in **Table 6.1**), the final grain size $d_{50\%}$ would be close to $1.6d_o = 1.6 \times 1.1 \mu\text{m} = 1.8 \mu\text{m}$ at 1300 °C and $1.1d_o = 1.2 \mu\text{m}$ at 1250 °C. For $p = 3$ (column 7 in **Table 6.1**), $d_{50\%}$ would be about $1.3d_o = 1.4 \mu\text{m}$ at 1300 °C and $1.1d_o = 1.2 \mu\text{m}$ at 1250 °C. For example, **Figure 6.25** shows the necessary increase in grain size (right Y-axis) from $d_o = 1.1 \mu\text{m}$ to explain the slope of the $\log \sigma - \epsilon$ curve obtained at 1300 °C and $3.6 \times 10^{-5} \text{s}^{-1}$. Experimentally, the final grain size at 1300 °C after 50% of strain increased up to 1.4 μm , while a smaller increase of 1.2 μm was found at 1250 °C. The good agreement between the observed and calculated final grain size for $p = 3$ may indicate that the diffusion of the slowest moving species on LSO-CS apatite takes place along the grain boundaries. However, caution must be exercised because of the relatively large standard deviation associated to log-normal grain size distribution and the experimental scatter inherent to high-temperature measurements.

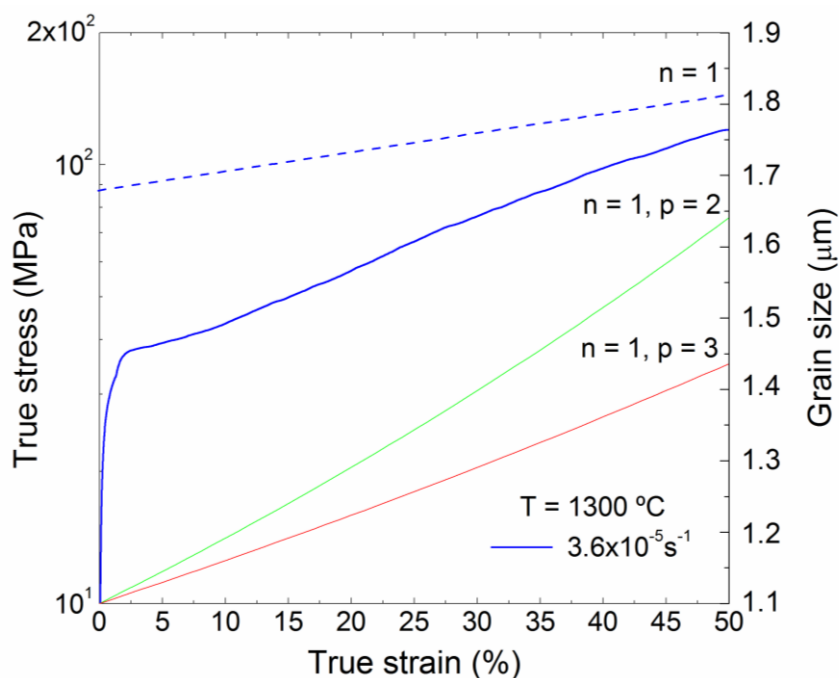


Figure 6.25. True stress vs true strain in logarithmic scale for LSO-CS deformed at 1300 °C and $3.6 \times 10^{-5} \text{ s}^{-1}$. A reference curve with $n = 1$ is also plotted (dashed line). The evolution of the grain size d with strain necessary to explain the observed stress are displayed on the right Y-axis with $p = 2$ and $p = 3$.

There is no information available in the literature concerning concurrent grain growth in oxy-apatites, nor in perovskite-type materials, to quantitatively anticipate the effect of grain growth on the mechanical properties. In 3 mol% yttria-stabilized tetragonal zirconia, Nieh and Wadsworth [15] derived the following equation for both static and dynamic grain growth:

$$d^3 - d_0^3 = K_0 \exp\left(-\frac{Q}{RT}\right)t \quad (6.22)$$

where K_0 is a constant, Q the activation energy for grain growth and t the time; the activation energies were 580 and 520 kJ/mol for static and dynamic grain growth, respectively. It is clear that a law of this type cannot explain even qualitatively the experimental results in the present material because it does not take explicitly into account the stress level during the test, which plays an essential role in dynamic grain growth.

6.3.2.1.4 High-temperature deformation mechanism

As already indicated, a stress exponent of $n = 1$ is characteristic of intergranular mechanisms where the deformation rate is controlled by mass transport without participation of dislocations. The deformation is provided by either the mass transport itself (Nabarro-Herring and Coble models [5, 9]) or by grain boundary sliding (Ashby-Verrall model [8]). This last model has

permitted to explain successfully the mechanical and microstructural features observed in different ceramic materials with grain sizes between 1 and 10 μm , such as UO_2 [10], NiO [11], YSZ [12], YBCO [13] and YAG [14], where a stress exponent close to unity was systematically reported. The Ashby-Verrall model accounts for: the absence of changes in the form factor of the grains which retain their equiaxed shape even after very large strains; the absence of significant creep transients before the establishment of the steady-state regime; and a proper prediction of the magnitude of the strain rates (or flow stresses). It should be noted that this model was proposed before the development of ceramic polycrystals with very fine grain sizes (below about 1 μm), which systematically exhibit a stress exponent $n = 2$. Such a behaviour, usually termed as superplasticity, has been also found in this work in LSO-SPS apatite and BZY polycrystals with $d = 0.2 \mu\text{m}$. The steady-state strain rate in the Ashby-Verrall model is given by [8] (Equation 1.4):

$$\dot{\epsilon} = \frac{98\sigma\Omega}{k_B T d^2} \left(D^{\text{lat}} + \frac{\pi\delta}{d} D^{\text{gb}} \right) \quad (6.23)$$

where σ is the applied stress, Ω is the molecular volume, k_B is the Boltzmann constant, T is the absolute temperature, d is the grain size, δ is the grain boundary thickness and D^{lat} and D^{gb} are the diffusion coefficients for lattice and grain boundary diffusion, respectively. In compounds, D is an effective diffusion coefficient, usually referred as the “molecular” diffusion coefficient, which takes into account the diffusivities of the different species in the crystal along the various diffusion paths. To maintain the electrical neutrality of the crystal, D is controlled by the slower moving species along the fastest path. Because both diffusion processes, lattice and grain boundary, are independent and take place simultaneously, the total strain rate is the sum of the strain rates contributed by each process.

Because there is no information on the diffusion coefficients in oxy-apatites, the validity of the Ashby and Verrall model cannot be checked by itself. An alternative approach has been then used in the present study: the effective diffusion coefficients D^{lat} and D^{gb} has been deduced from individual datum points by using Equation 6.23 assuming that the strain rate is controlled by either lattice or grain-boundary diffusion; a molecular volume $\Omega = 75 \text{ \AA}^3$ and a grain boundary thickness $\delta = 1 \text{ nm}$ were used in the calculations. **Figure 6.26** shows the corresponding diffusivities on an Arrhenius plot. On the other hand, it is observed that the grain boundary diffusivity is only a factor of 500 higher than the volume diffusivity, whereas the difference usually in other ceramic materials is four or five orders of magnitude. The comparison of the present effective diffusion coefficients with those obtained in very fine-grained LSO-SPS with $d = 0.2 \mu\text{m}$ (see next Section), where a different deformation mechanism was found, will shed light on the accommodation mechanism.

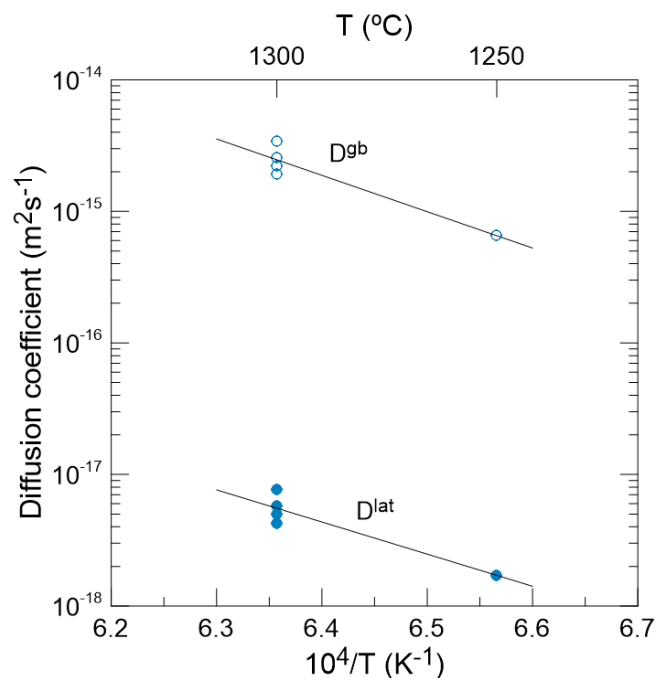


Figure 6.26. Effective diffusion coefficients D^{lat} and D^{gb} for LSO-CS oxy-apatite deduced from deformation data using the Ashby and Verrall model assuming lattice or grain boundary diffusion-controlled strain rate (Equation 6.23).

6.3.2.2 High-temperature mechanical behaviour of LSO-SPS

6.3.2.2.1 Fragile-ductile transition

Figure 6.27 displays the true stress – true strain curves for LSO-SPS deformed at a given initial strain rate $\dot{\epsilon}_0 = 3.4 \times 10^{-5} \text{ s}^{-1}$ (corresponding to a cross-head speed of $10 \mu\text{m}/\text{min}$) between 920 and 1200 °C. A smooth transition from brittle-to-ductile behaviour was observed at this strain rate. It should be noted that the temperature range used for this material is much lower than the one used in conventional sintered LSO materials owing to the large difference in grain size between both materials. At 920 °C, the sample failed catastrophically without any plastic deformation, at a stress level of about 840 MPa. The onset of plastic deformation could be observed at 980 °C with a slight curvature in the $\sigma - \epsilon$ curve at 400 MPa, but the sample finally failed after reaching a very limited strain ($\epsilon \leq 5\%$). A semi-ductile behaviour was observed at 1020 °C, where the material reached deformations as large as 50% without macroscopic fracture, although stress softening was observed in this regime at about 40% . At higher temperatures, the compound exhibits extended steady states of deformation, characterized by a positive slope of the $\sigma - \epsilon$ curves. Compared to LSO-CS strained at the same initial strain rate (Figure 6.10), the temperature needed for steady-state creep is about 200 °C smaller.

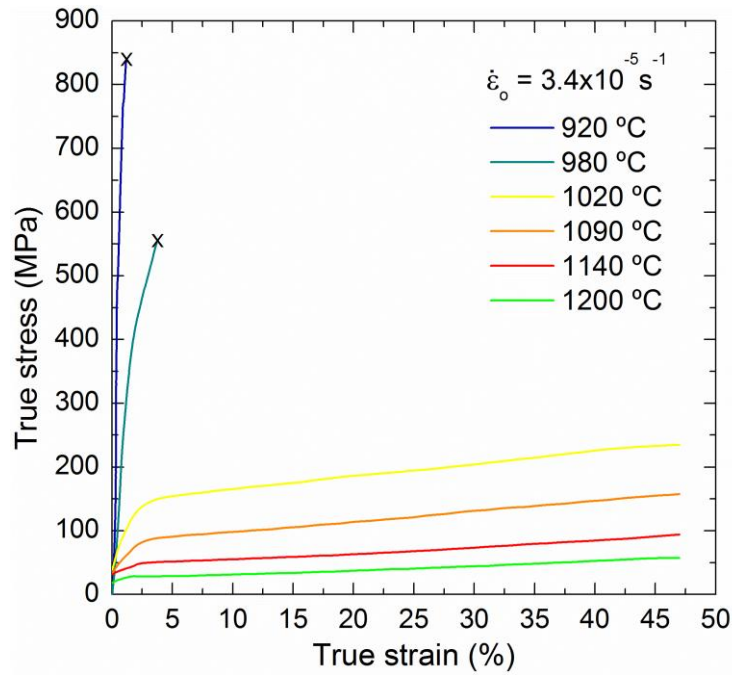


Figure 6.27. True stress σ - true strain ε curves for LSO-SPS deformed in compression at an initial strain rate of $3.4 \times 10^{-5} \text{ s}^{-1}$ and different temperatures. Marks “x” indicate macroscopic specimen failure.

Figure 6.28 shows the $\sigma - \varepsilon$ curves for LSO-SPS obtained at a fixed temperature of $1140 \text{ }^\circ\text{C}$ and different initial strain rates ranging from 1.8×10^{-5} to $1.8 \times 10^{-4} \text{ s}^{-1}$. All the curves display extensive steady states of deformation, though some softening by damage accumulation could be observed at $\varepsilon > 30\%$ in the sample strained at the higher strain rate. The slope of the $\sigma - \varepsilon$ curve increases continuously with increasing $\dot{\varepsilon}_0$, as expected in constant cross-head speed tests.

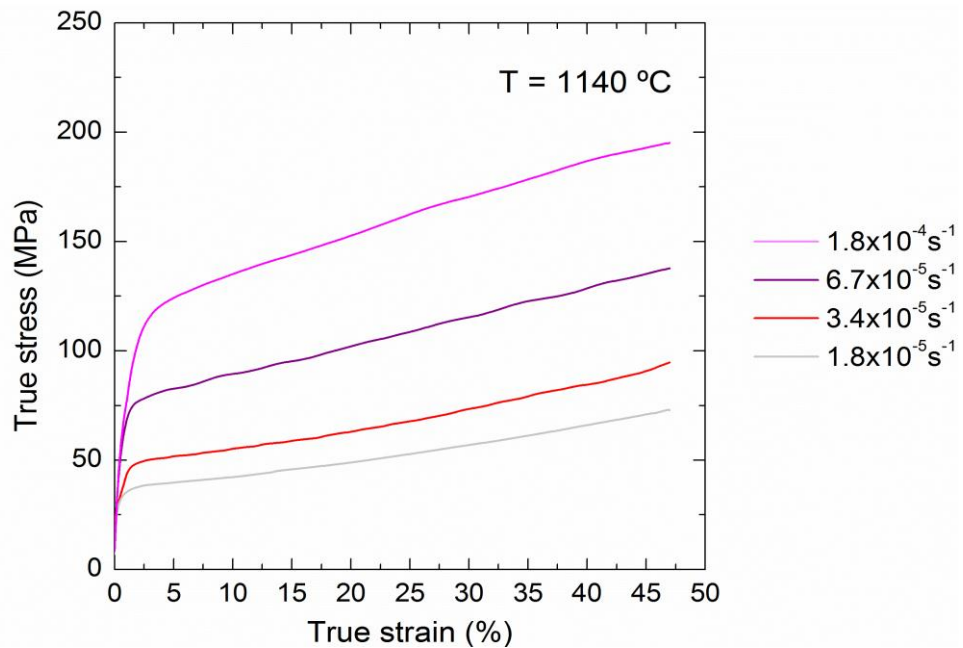


Figure 6.28. True stress σ - true strain ε curves for LSO-SPS deformed in compression at $1140 \text{ }^\circ\text{C}$ and different initial strain rates.

6.3.2.2 Microstructure after deformation

Microstructure after deformation **Figure 6.29** shows the macroscopic aspect of the strained samples, which is consistent with the shape of the corresponding stress – strain curves. The material fractured into multiple pieces at the lowest temperature studied, indicating the fast propagation multiple cracks throughout the entire volume of the sample. SEM observations of the fracture surfaces indicate again a mixed failure mode (**Figure 6.30**), like in LSO-CS, despite the fine-grained microstructure. The porosity remaining inside some of the grains may contribute to the transgranular fracture mode. At 980 °C, the sample underwent a very limited plastic deformation before fracture, corresponding to the development of cracks running longitudinally along the length of the specimen (**Figure 6.29f**). At the intermediate temperature of 1020 °C, the material is damaged (**Figure 6.29e**) but able to tolerate strains up to 50% without macroscopic failure. Finally, at higher temperatures, in the ductile regimen, the specimens deformed very homogeneously, practically without barrelling (**Figure 6.29b, c and d**).

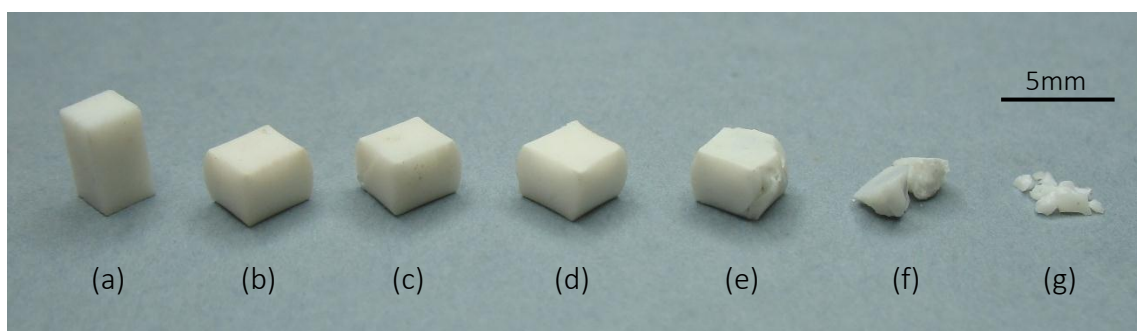


Figure 6.29. Macroscopic aspect of LSO-SPS samples deformed in compression at an initial strain rate of $3.4 \times 10^{-5} \text{ s}^{-1}$ and different temperatures. (a) as-prepared LSO-SPS, (b) 1200 °C, (c) 1140 °C, (d) 1090 °C, (e) 1020 °C, (f) 980 °C and (g) 920 °C.

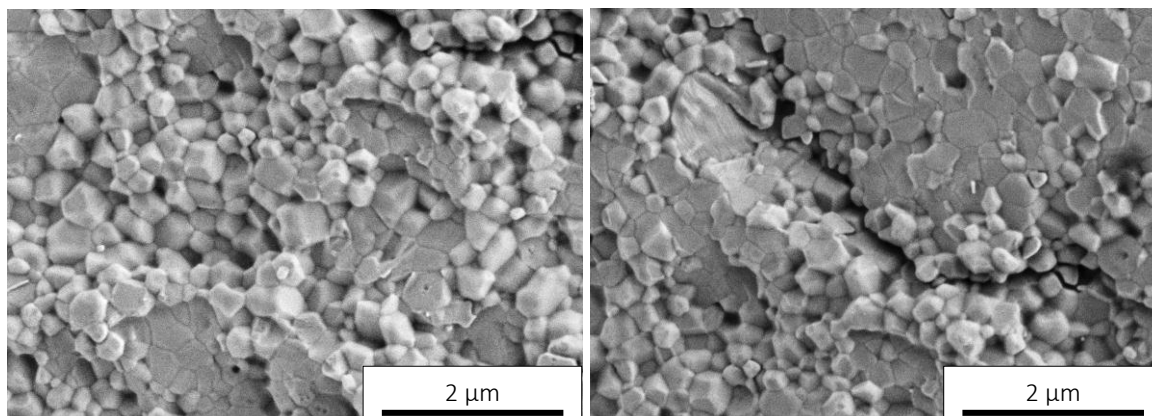


Figure 6.30. SEM micrographs of fracture surfaces of LSO-SPS specimen at 920 °C and an initial strain rate of $3.4 \times 10^{-5} \text{ s}^{-1}$.

SEM observations of the samples deformed in steady state conditions reveal that the grains retain the equiaxed shape, but there is an increase in the final grain size. **Figure 6.31** shows SEM micrographs of a specimen deformed up to $\varepsilon \approx 50\%$ at 1090 °C and $3.4 \times 10^{-5} \text{ s}^{-1}$ (curve in red, **Figure 6.27**). The corresponding grain size d and form factor F distributions led to average values of $d = 0.3 \pm 0.1 \text{ }\mu\text{m}$ and $F = 0.8 \pm 0.1$ after deformation at 1090 °C. Similarly, **Figure 6.32** displays SEM images of a sample strained at 1200 °C (curve in green, **Figure 6.27**), which exhibits average values of $d = 0.5 \pm 0.2 \text{ }\mu\text{m}$ and $F = 0.8 \pm 0.1$. The as-prepared values were $d = 0.2 \pm 0.1 \text{ }\mu\text{m}$ and $F = 0.8 \pm 0.1$, indicating that concurrent grain growth took place during the creep tests. The SEM micrographs additionally show that many of the larger grains, particularly at 1200 °C (**Figure 6.32**), are still in formation, while the small grains are consumed by neighbours.

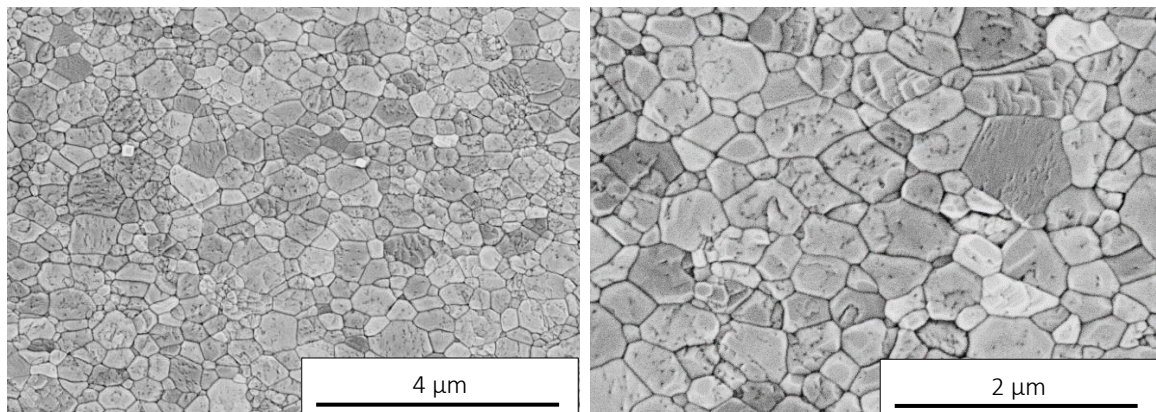


Figure 6.31. SEM micrographs of LSO-SPS sample deformed up to $\varepsilon \approx 50\%$ in compression at an initial strain rate of $3.4 \times 10^{-5} \text{ s}^{-1}$ and 1090 °C.

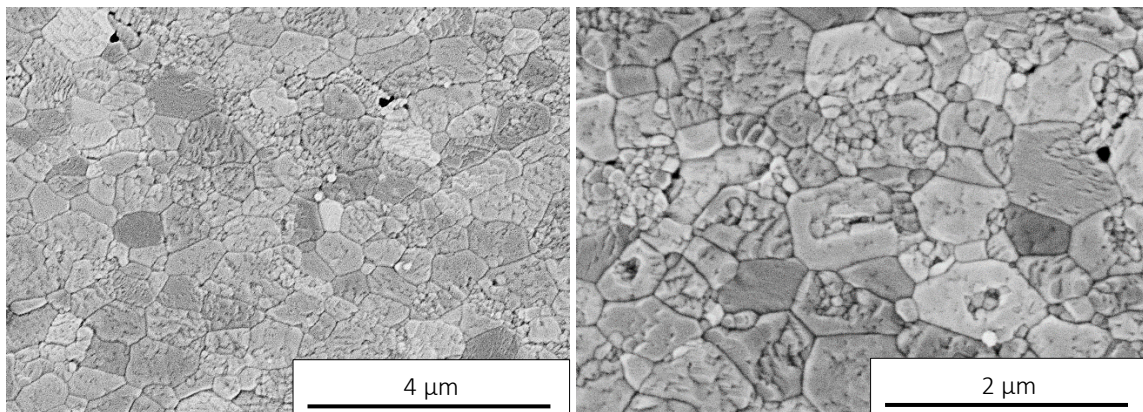


Figure 6.32. SEM micrographs of LSO-SPS sample deformed up to $\varepsilon \approx 50\%$ in compression at an initial strain rate of $3.4 \times 10^{-5} \text{ s}^{-1}$ and 1200 °C.

TEM observations of deformed specimens have shown a grain structure very similar to that found in the as-fabricated material, without relevant differences. The grains remain clean and free of dislocations, and some areas exhibit the original residual porosity inside the grains (**Figure 6.33**).

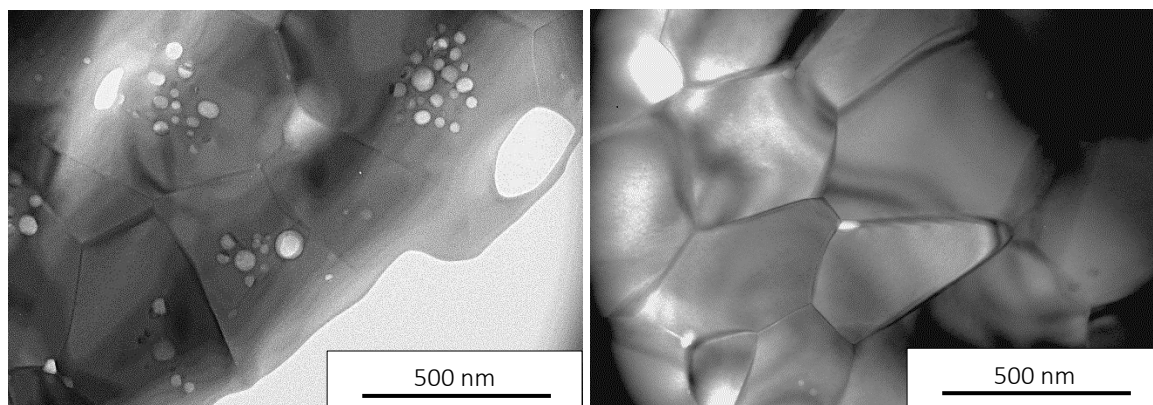


Figure 6.33. TEM images of LSO-SPS sample deformed in compression at an initial strain rate of $3.6 \times 10^{-5} \text{ s}^{-1}$ and $1140 \text{ }^\circ\text{C}$.

6.3.2.2.3 Creep parameters

The stress exponent n and the activation energy for creep Q in LSO-SPS have been determined using the same procedures followed for LSO-CS. Figure 6.34 displays the log – log plot of the initial strain rate vs flow stress obtained at $1140 \text{ }^\circ\text{C}$. Due to the variation of σ with ε , the flow stress was taken at three different strain levels $\varepsilon = 10, 20$ and 30% . An average stress exponent $n = 1.9 \pm 0.1$ was deduced from the best linear fits, which contrasts with the value of $n \approx 1$ found previously in conventionally-sintered LSO-CS polycrystals.

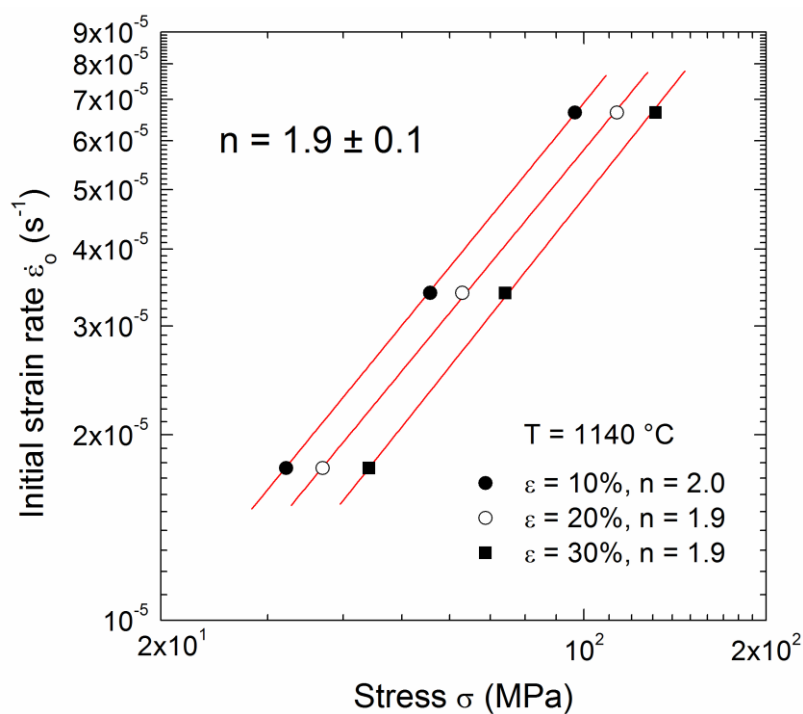


Figure 6.34. Determination of stress exponent n in steady-state creep of LSO-SPS for strain levels ε of 10, 20 and 30%.

A stress exponent n of 2 has been systematically reported in the superplastic behaviour of many metals and metallic alloys with $d < 10 \mu\text{m}$ [9] as well as in submicrometer-grained ceramics ($d < 1 \mu\text{m}$), such as 3 mo% Ytria-Stabilized Tetragonal Zirconia 3YTZP [16], Alumina [17], $\text{Al}_2\text{O}_3/3\text{YTZP}$ composites [18], three-phase Alumina/Zirconia/Mullite [19], and Yttrium- and Ytterbium-doped Barium Cerates [20, 21]. In these materials, it is well documented that grain boundary sliding played the key role in the deformation process, although there are serious discrepancies regarding the nature of the accommodation mechanism.

A similar n value was deduced from fast $\dot{\epsilon}_0$ jumps during an isothermal test at $1090 \text{ }^\circ\text{C}$, as shown in **Figure 6.35**, where the initial strain rate was changed between 3.4×10^{-5} and $1.8 \times 10^{-5} \text{ s}^{-1}$ (corresponding to cross-head speeds of 10 and $5 \mu\text{m}/\text{min}$, respectively). The comparison of the flow stresses before and after the strain rate changes yields an average value of $n = 1.8 \pm 0.1$, in agreement with the value deduced from conventional tests (**Figure 6.34**).

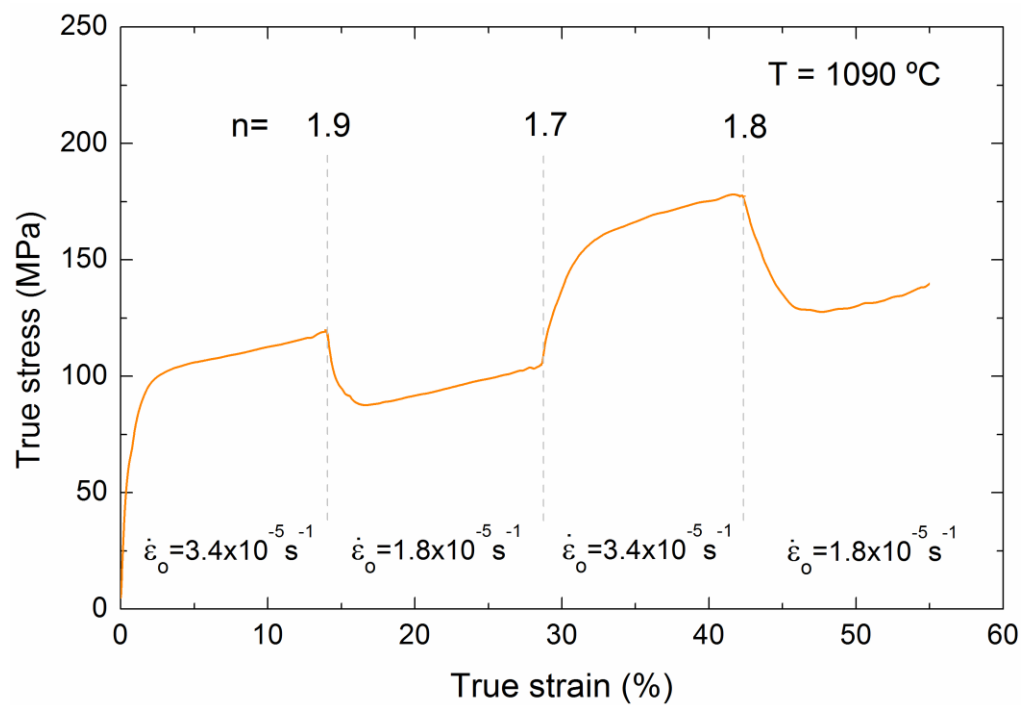


Figure 6.35. True stress σ - true strain ϵ curve for LSO-SPS deformed in compression at $1090 \text{ }^\circ\text{C}$. Several determinations of n by strain rate changes are shown.

Regarding the activation energy Q , **Figure 6.36** shows the $\log \sigma - 1/T$ curve for LSO-SPS obtained at a strain rate of $3.4 \times 10^{-5} \text{ s}^{-1}$ between 1090 and $1200 \text{ }^\circ\text{C}$. A least-squares fit leads to $Q = 340 \pm 20 \text{ kJ/mol}$, identical to the value of $350 \pm 40 \text{ kJ/mol}$ found in LSO-CS apatite with a grain size of $1.1 \mu\text{m}$. This result suggests that the same diffusion mechanism, either into the lattice or along

the grain boundaries, is the rate-controlling step in both large- and fine-grained oxy-apatites, the deformation itself occurring by grain boundary sliding.

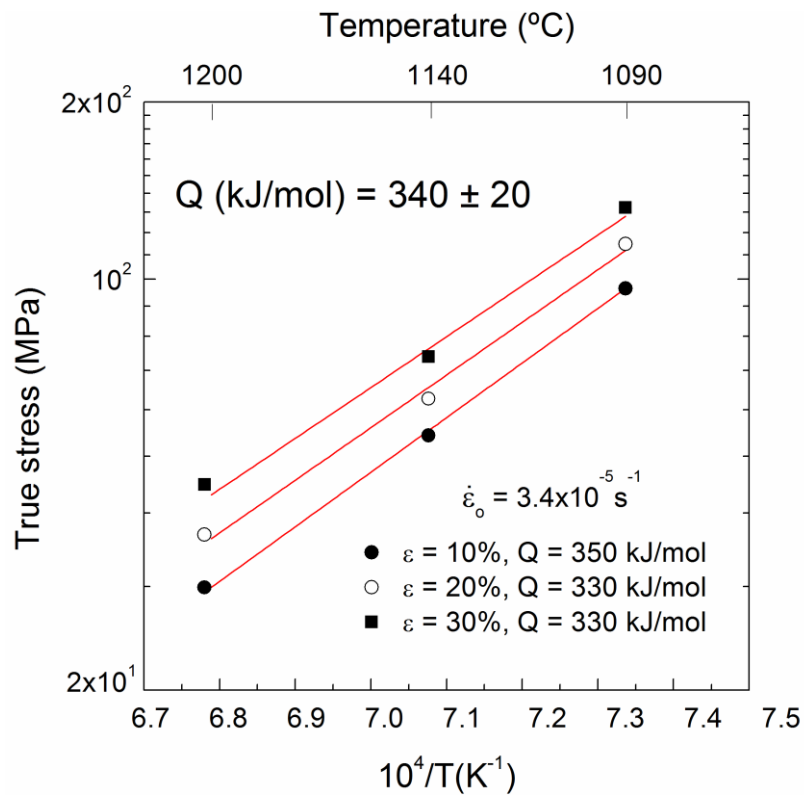


Figure 6.36. Steady-state flow stresses of LSO-SPS as a function of reciprocal temperature for strain levels ϵ of 10, 20 and 30%.

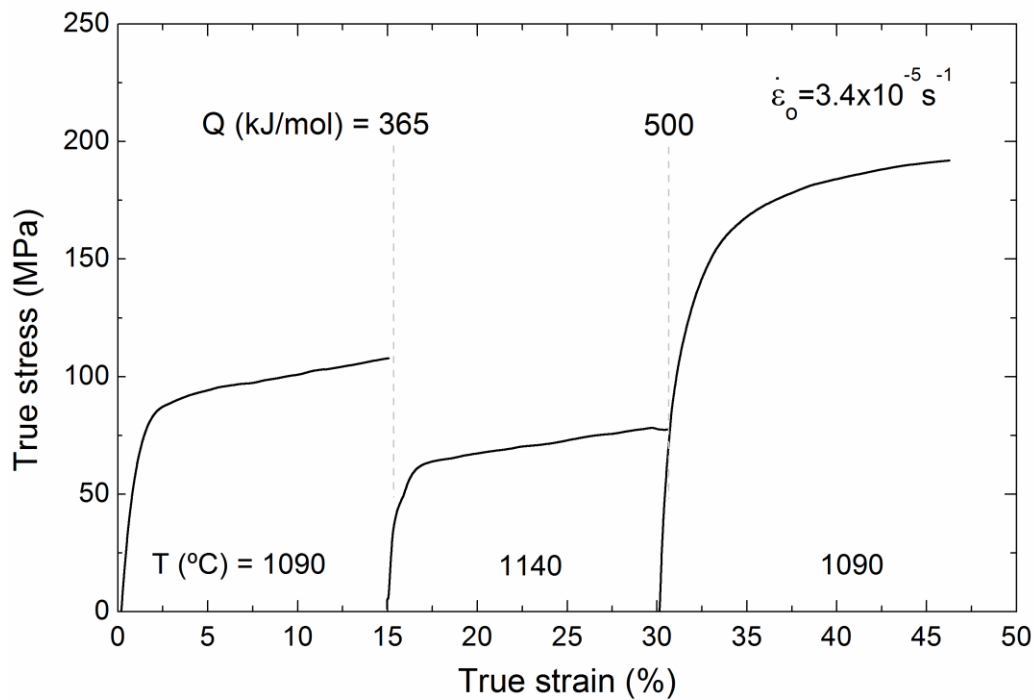


Figure 6.37. True stress σ - true strain ϵ curve for LSO-SPS deformed in compression at an initial strain rate of $3.4 \times 10^{-5} \text{ s}^{-1}$. Two determinations of Q by temperature changes are shown.

The activation energy Q has been also calculated by using the differential method. **Figure 6.37** shows two determinations of Q by temperature changes between 1090 and 1140 °C during a test performed at a fixed initial strain rate of $\dot{\epsilon}_0 = 3.4 \times 10^{-5} \text{ s}^{-1}$. The first jump leads to a value of 365 kJ/mol, in agreement with the average value deduced previously by conventional tests. The second jump, however, yields a value of 500 kJ/mol, indicating that the material became harder than expected because grain coarsening took place particularly during the second section at higher temperature.

The same procedure used for LSO-CS apatite (Section 6.3.2.1) has been used here to analyse the effect of grain growth on the creep of LSO-SPS. **Figure 6.38** displays the $\log \sigma - \epsilon$ plot of LSO - SPS apatite obtained at 1140 °C and different initial strain rates. In this case, the slope α of the steady states decreases from 0.016 to 0.011 when increasing strain rate, in contrast with what was found in LSO - CS oxy-apatite, where the slopes were roughly constant with a larger value $\alpha \approx 0.027$. These results confirm that concurrent grain growth took place during the straining of LSO-SPS, but in a lesser extension than in LSO-CS apatite (nonetheless it should be remember that the testing temperature is very different for both compounds).

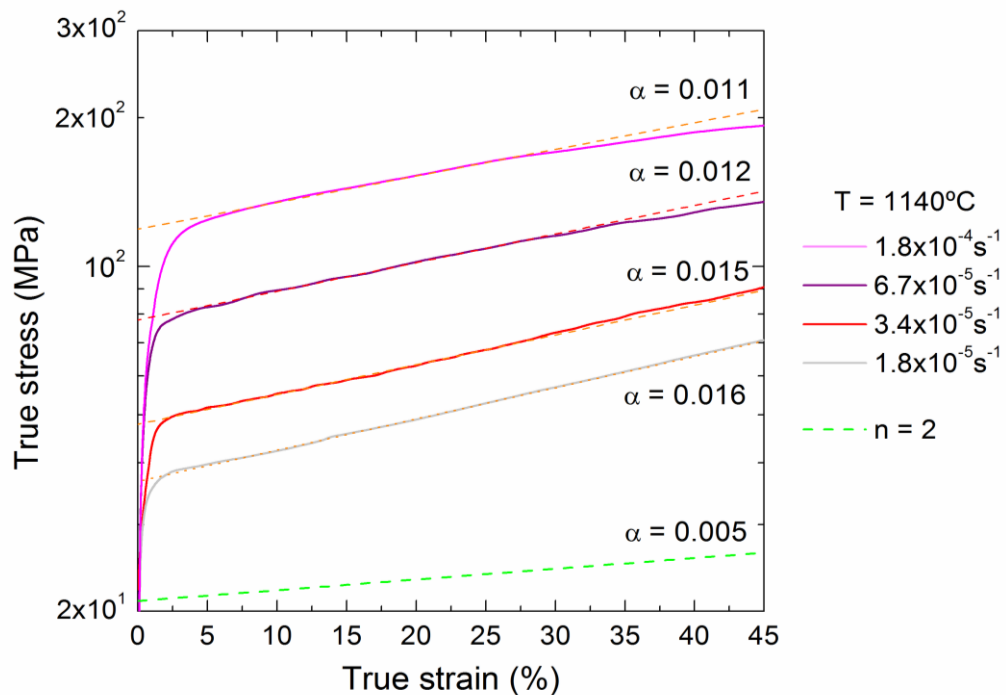


Figure 6.38. Log $\sigma - \epsilon$ curves for LSO-SPS deformed in compression at 1140 °C and different initial strain rates. Prediction for $n = 2$ is also plotted for the sake of comparison.

Table 6.2 shows the initial σ_0 and final $\sigma_{50\%}$ stresses measured in LSO-SPS at various conditions of strain rate and temperature (**Figure 6.27** and **Figure 6.28**). In the absence of grain growth, $\sigma_{50\%} / \sigma_0 = 1.3$ for $n = 2$ (Equation 6.21), however, the experimental ratios are higher than

this value. The $d_{50\%}/d_o$ ratios needed to explain the observed stress ratios (Equation 6.21) are shown in Column 6 for $p=2$ and Column 7 for $p=3$.

Table 6.2. Initial σ_o and final $\sigma_{50\%}$ stresses measured in LSO-SPS at various conditions of strain rate and temperature. A $\sigma_{50\%}/\sigma_o$ ratio of 1.3 would be expected in the absence of grain growth for $n=2$ (Equation (6.21)). Grain size $d_{50\%}/d_o$ ratios necessary to explain the observed stress ratios are given in columns 6 and 7 for $p=2$ and $p=3$, respectively.

T (°C)	$\dot{\epsilon}_o$ (s ⁻¹)	σ_o (MPa)	$\sigma_{50\%}$ (MPa)	$\sigma_{50\%}/\sigma_o$	$d_{50\%}/d_o$	$d_{50\%}/d_o$
					p = 2	p = 3
1020	3.4×10^{-5}	150	245	1.6	1.3	1.2
1090	3.4×10^{-5}	85	164	1.9	1.5	1.3
1140	1.8×10^{-5}	35	75	2.2	1.7	1.4
	3.4×10^{-5}	46	95	2.1	1.6	1.4
	6.8×10^{-5}	79	144	1.8	1.4	1.3
	1.8×10^{-4}	122	211	1.7	1.4	1.2
1200	3.4×10^{-5}	24	60	2.5	1.9	1.6

For instance, **Figure 6.39** shows the increase in grain size (right Y-axis) needed to explain the slope of the log $\sigma - \epsilon$ curve obtained at 1140 °C and $3.4 \times 10^{-5} \text{ s}^{-1}$. The final grain sizes $d_{50\%}$ would be $1.6d_o = 1.6 \times 0.2 \text{ } \mu\text{m} = 0.3 \text{ } \mu\text{m}$ for 1140 °C and $1.9d_o = 0.4 \text{ } \mu\text{m}$ for 1200 °C for $p=2$, while for $p=3$ $d_{50\%}$ would be $1.4d_o = 0.3 \text{ } \mu\text{m}$ for 1140 °C and $1.6d_o = 0.3 \text{ } \mu\text{m}$ for 1200 °C. Experimentally, the measured final grain sizes at 1140 °C and 1200 °C after 50% of strain were 0.4 and 0.5 μm , respectively, with a standard deviation associated to the log-normal grain size distribution of 0.2 μm in both cases. Although the measured d values are higher than those expected from Equation 6.21, it should be noted the difficulty in estimating the final grain size in the samples deformed at the higher temperatures due to the presence of numerous grains in formation (clearly seen in **Figure 6.32**), which leads to an overestimation of d if only the final grains are considered in the analysis.

The experimental $d_{50\%}/d_o$ ratios measured in LSO-CS and LSO-SPS oxy-apatites after testing also support that the stress exponent in both materials is definitively different. If n were 2 in LSO-CS instead of 1, final grain sizes of about 3 μm would be measured after 50% of strain, contrary to the experimental evidence. And vice-versa: if n were 1 in LSO-SPS instead of 2, final grain sizes of about 0.2 μm would be measured after 50% of strain, contrary also to the experimental evidence.

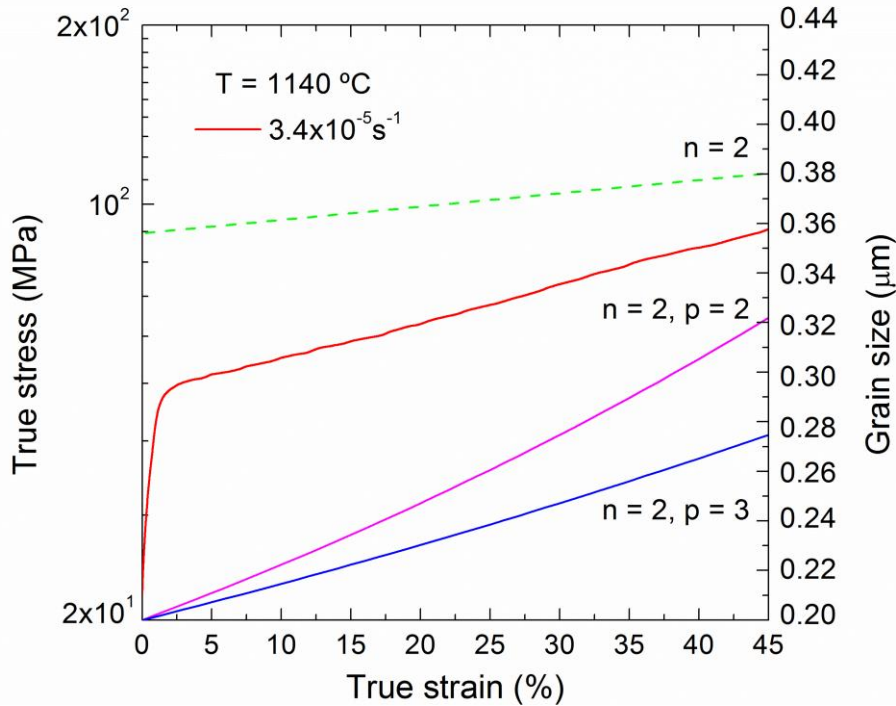


Figure 6.39. True stress vs true strain in logarithmic scale for LSO-SPS deformed at 1140 °C and $3.4 \times 10^{-5} \text{ s}^{-1}$. Reference curve with $n = 2$ is also plotted (dashed line). The evolution of the grain size d with strain necessary to explain the observed flow stress is displayed on the right Y-axis for $p = 2$ and $p = 3$, with $n = 2$.

6.3.2.2.4 High-temperature deformation mechanism

In the previous section it has been shown that LSO-CS and LSO-SPS materials exhibit different stress dependences of the strain rate, with n increasing from 1 in LSO with $d = 1.1 \mu\text{m}$ to 2 in LSO-SPS with $d = 0.2 \mu\text{m}$. The creep activation energy is, however, the same for both compounds with a value $Q = 340 \pm 40 \text{ kJ/mol}$. The increase in stress exponent when decreasing grain size has been reported previously in Yttria-Stabilized Zirconia polycrystals with grain sizes ranging from 0.3 to $2 \mu\text{m}$ [16], where grain boundary sliding was the primary deformation mechanism, as also found in the present study on oxy-apatites.

There is currently no simple explanation for this effect, because the atomistic origin of the value of $n = 2$ itself found in fine-grained materials is not known and is presently a matter of debate [22]. Many different models [9] have been developed to explain superplasticity based in different relaxation processes of the stresses generated by the sliding of the grains on each other: dislocation motion inside the volume of the grains or along the grain boundaries, diffusional flow, interface-reaction-controlled diffusion (i.e. boundaries are not perfect sources and sinks for point defects), grain boundary migration or cavitation. None of them, however, is able to explain successfully the

body of experimental data in superplastic materials. Therefore, it has been used here two phenomenological relationships developed by Sherby *et al.* [9] for superplastic metals corresponding to grain boundary sliding controlled by either lattice diffusion ($n = 2, p = 2$) or grain boundary diffusion ($n = 2, p = 3$) (Equation 1.10 and 1.11):

$$\begin{aligned}\dot{\epsilon} &= 8 \times 10^6 \frac{Gb}{k_B T} \left(\frac{b}{d}\right)^2 \left(\frac{\sigma}{G}\right)^2 D^{\text{lat}} \\ \dot{\epsilon} &= 2 \times 10^5 \frac{Gb}{k_B T} \left(\frac{b}{d}\right)^3 \left(\frac{\sigma}{G}\right)^2 D^{\text{gb}}\end{aligned}\tag{6.24}$$

where b is the Burgers vector, G is the shear modulus and D^{lat} and D^{gb} are, as before, the effective diffusion coefficients for lattice and grain boundary diffusion, respectively. The first equation has been shown to account for the superplastic deformation of fine-grained Yttria-Stabilized tetragonal Zirconia [16] and the second equation for fine-grained YBa₂Cu₃O_{7-x} superconductor [23]. In both cases, the diffusion coefficients were associated with cations, the slower moving species in those materials. Unfortunately, there is no information available about ion diffusivities in oxy-apatites, despite the importance of this magnitude in processes involving mass transport: creep, sintering, grain growth, etc.

Following the same procedure used previously for LSP-CS apatite, the effective diffusivities D^{lat} and D^{gb} have been estimated from individual datum points using Equations 6.24 assuming either lattice diffusion or grain boundary diffusion, respectively. A Burgers vector $b = 5 \text{ \AA}$ and a temperature-dependent shear modulus G measured in this work by Resonant Ultrasound Spectroscopy (see Chapter 5) have been used in the calculations. **Figure 6.40** shows these effective diffusion coefficients for LSO-SPS (cyan points) together with those of LSO-CS for comparison (blue points). There is a factor of about 10^4 between D^{lat} and D^{gb} , as usually found in ceramics. Although there is no way to decide which diffusion path is responsible for the accommodation process by itself, the comparison with the diffusion coefficients derived previously for large-grained LSO oxy-apatite may assist in the identification of the rate-controlling mechanism. It can be seen that there is an excellent agreement between the grain boundary diffusivities deduced from the two independent steady-state creep rate equations, one with $n = 1$ in large-grained LSO (Equation 6.23) and the other with $n = 2$ in fine-grained LSO (Equations 6.24). On the contrary, there is a difference of two orders of magnitude between the lattice diffusivities deduced from the two models. This agreement, with no adjustable parameters, lends credibility to the assumption that superplastic flow is accommodated by grain boundary diffusion in LSO compounds. To the best of our

knowledge, it is the first time where such a comparison has been made in a material using two independent deformation models.

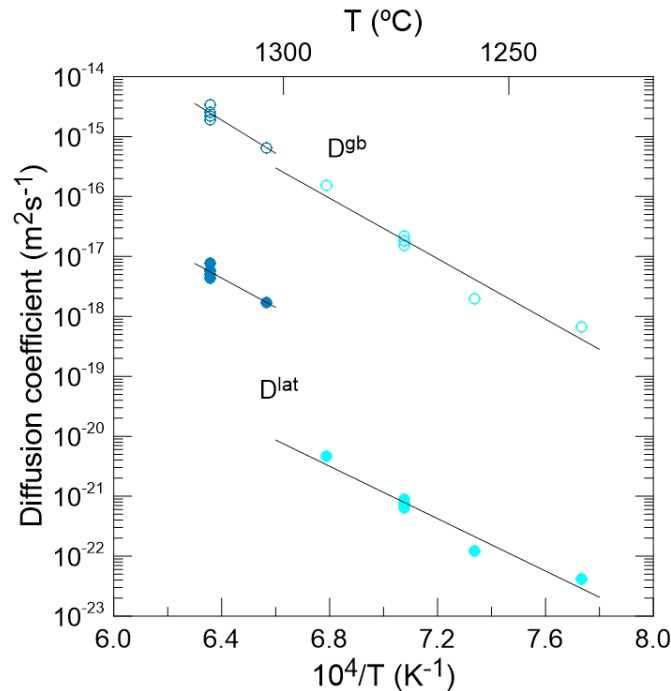


Figure 6.40. Effective diffusion coefficients D^{lat} and D^{gb} for LSO-SPS oxy-apatite (cyan points) deduced from deformation data using the phenomenological equations derived by Sherby et al. [9] for lattice and grain boundary diffusion-controlled strain rate (Equations 6.24). Effective diffusivities derived previously for LSO-CS using the Ashby and Verrall model (blue points, Figure 6.26) are also included. The agreement for grain boundary diffusivities is excellent.

6.3.2.3 High-temperature mechanical behaviour of home-made BZY

6.3.2.3.1 Fragile-ductile transition

Figure 6.41 shows the true stress - true strain curves of BZY deformed between 1100 and 1325 °C at an initial strain rate of $3.6 \times 10^{-5} \text{ s}^{-1}$ (corresponding to 10 $\mu\text{m}/\text{min}$). There is a clear transition from brittle-to-ductile behaviour as the temperature increases. No plastic flow at all was found at 1100 °C, where the material failed catastrophically at a stress level of about 830 MPa. At 1175 °C, however, the sample displayed some plasticity, reaching a total strain of 13% and about 550 MPa before fracture. A similar semi-brittle behaviour was observed at 1210 °C, where the compound underwent a remarkable deformation of 25% before final failure at a stress level of 350 MPa. At temperatures of 1235 °C and above, the material displays extended steady states of deformation, characterized by a rather constant slope of the $\sigma - \epsilon$ curves which increases gradually with decreasing temperature. In these steady state conditions, the tests were intentionally stopped at $\epsilon \approx 40\%$ for further microstructural observations.

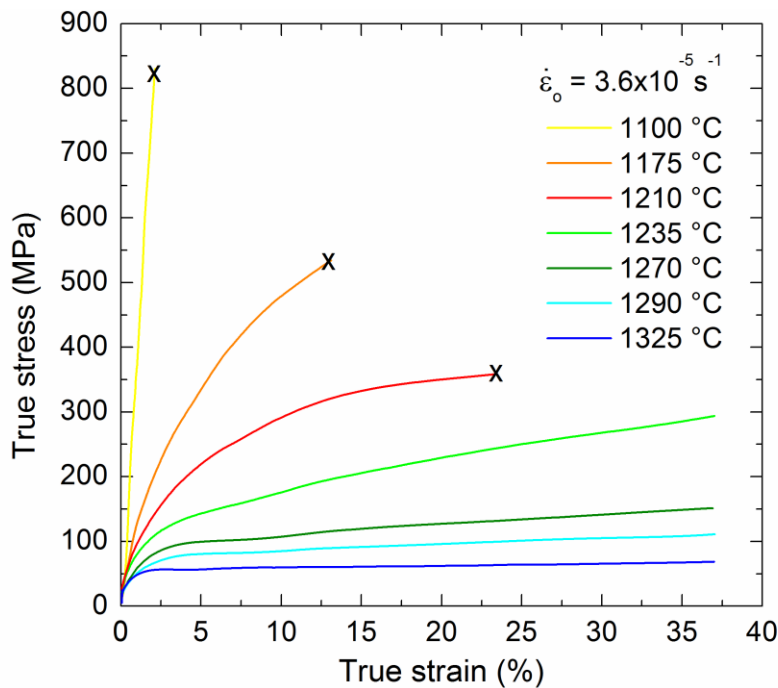


Figure 6.41. True stress σ - true strain ε curves for home-made BZY deformed in compression at an initial strain rate of $3.6 \times 10^{-5} \text{ s}^{-1}$ and different temperatures. Marks “x” indicate macroscopic specimen failure.

In a similar way, several tests were carried out at a given temperature of $1325 \text{ }^\circ\text{C}$ and different initial strain rates ranging from 1.8×10^{-5} to $1.8 \times 10^{-4} \text{ s}^{-1}$ (corresponding to cross-head speeds between 5 and $50 \text{ } \mu\text{m}/\text{min}$). The corresponding $\sigma - \varepsilon$ curves are shown in **Figure 6.42**. As expected at this temperature, the material displays extensive secondary creep regimes.

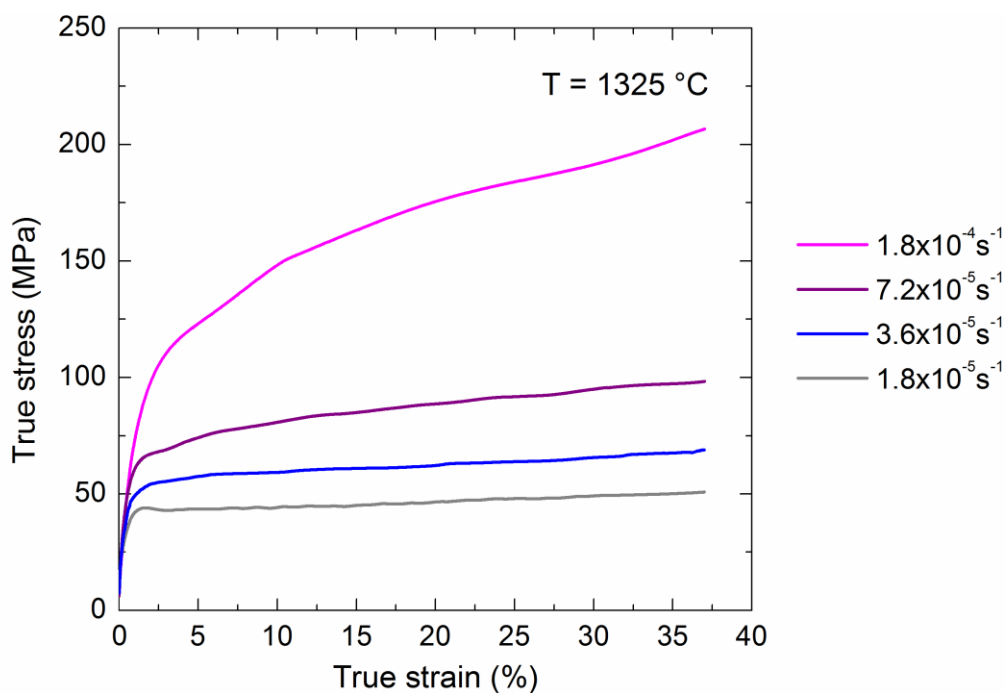


Figure 6.42. True stress σ - true strain ε curves for home-made BZY deformed in compression at $1325 \text{ }^\circ\text{C}$ and different initial strain rates.

6.3.2.3.2 Microstructure after deformation

The macroscopic aspect of the samples after deformation (**Figure 6.43**) agrees well with the shape of the corresponding mechanical $\sigma - \epsilon$ curves. At the lower temperature studied, 1100 °C, the sample completely fractured into multiple small fragments (**Figure 6.43e**), indicating the fast propagation of cracks throughout the entire volume of the sample. SEM observations of fracture surfaces indicate an intergranular failure mode (**Figure 6.44**), as could be expected in a very fine-grained material.

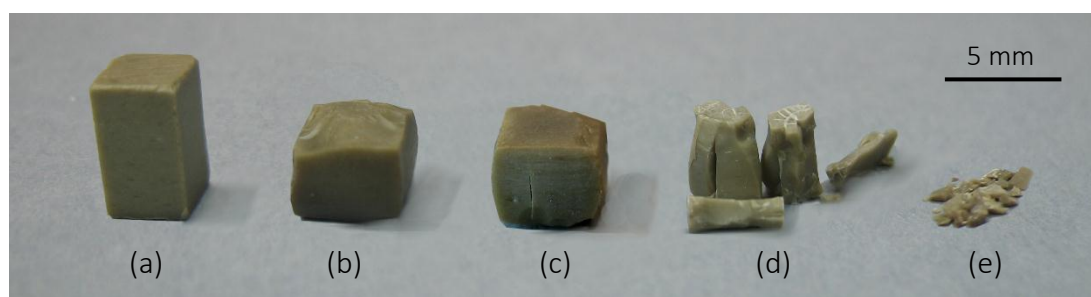


Figure 6.43. Macroscopic aspect of home-made BZY samples deformed in compression at an initial strain rate of $3.6 \times 10^{-5} \text{ s}^{-1}$ and different temperatures. (a) as-prepared, (b) 1290 °C, (c) 1235 °C, (d) 1210 °C and (e) 1100 °C.

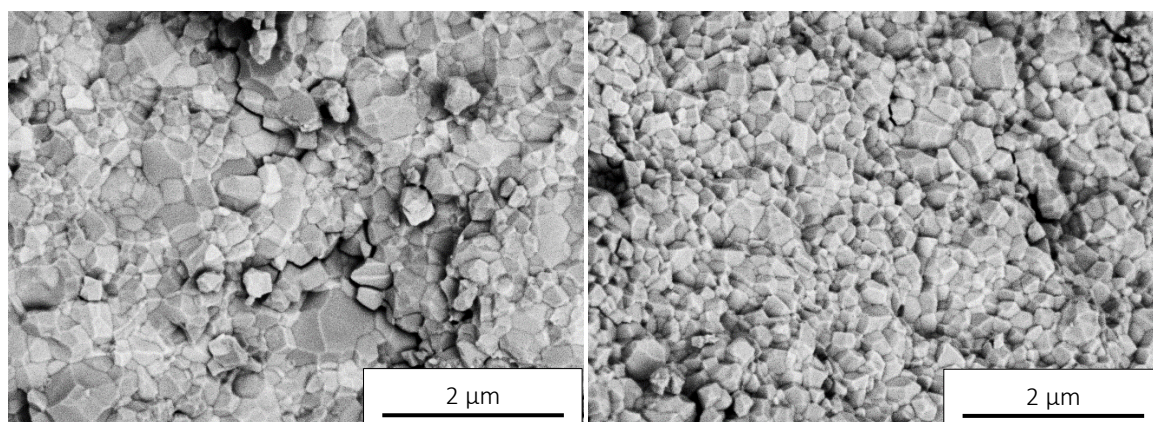


Figure 6.44. SEM micrographs of fracture surfaces of catastrophically failed BZY specimen at 1100 °C and an initial strain rate of $3.6 \times 10^{-5} \text{ s}^{-1}$.

At 1175 and 1210 °C, in the semi-ductile regime, the specimens underwent a strain-controlled delayed fracture, originated by damage accumulation. In order to determine the origin of this damage-tolerant regime, the test performed at 1175 °C (curve in orange, 2) was repeated but voluntarily stopped at a strain of 10% prior to failure. It could be seen a high density of microcavities along the grain boundaries (**Figure 6.45**) distributed throughout the sample but particularly concentrated in the finer-grained areas. As strain proceeds, these stress-assisted microcavities coalesce into cracks leading to final sample failure. These observations are in agreement with the intergranular fracture mode noted above.

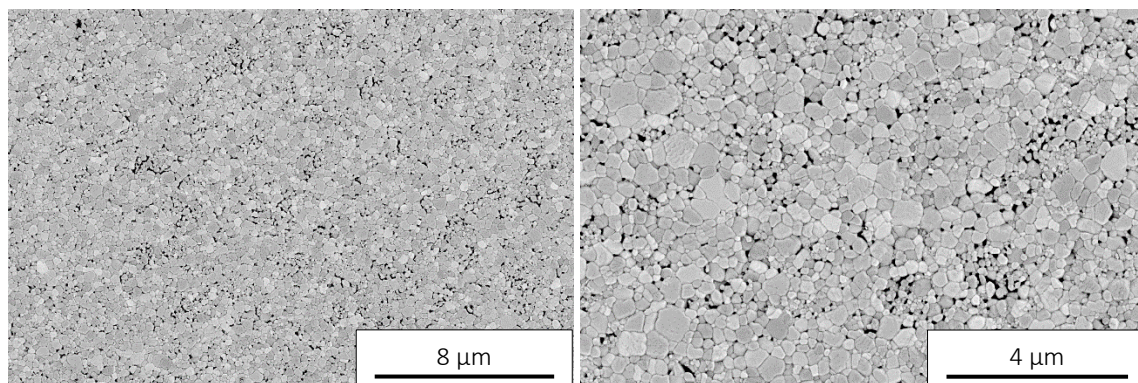


Figure 6.45. SEM micrographs at different magnifications of BZY sample deformed up to $\epsilon \approx 10\%$ in compression at an initial strain rate of $3.6 \times 10^{-5} \text{ s}^{-1}$ and $1175 \text{ }^\circ\text{C}$. Stress axis is vertical.

At temperatures of $1235 \text{ }^\circ\text{C}$ and above, the samples deformed homogeneously, with very little barrelling (**Figure 6.43**), in agreement with the well-established steady-states curves of deformation. SEM observations of the samples deformed in these steady-state conditions show the lack of noticeable changes in grain morphology and porosity with respect to as-fabricated samples. **Figure 6.46** shows SEM micrographs at different magnifications of a specimen deformed up to $\epsilon \approx 40\%$ at the highest temperature and lowest strain rate studied ($1325 \text{ }^\circ\text{C}$ and $1.8 \times 10^{-5} \text{ s}^{-1}$, respectively, curve in grey, **Figure 6.42**). The corresponding grain size d and form factor F distributions led to average values of $d = 0.19 \pm 0.08 \text{ } \mu\text{m}$ and $F = 0.80 \pm 0.09$, identical to those found in unstrained samples ($d = 0.21 \pm 0.10 \text{ } \mu\text{m}$ and $F = 0.79 \pm 0.09$, Section 3.3.2.4). Similar characteristics were found in the other samples deformed in steady-state conditions (**Figure 6.47**). The lack of morphological changes during deformation suggests that grain boundary sliding is the main deformation mechanism in this material, as also found in LSO-SPS with the same small grain size and other fine-grained ceramics [16-21]. Some inter-granular cavitation was found in the samples strained at the lower strain rate, which may help in the accommodation of the grain boundary sliding.

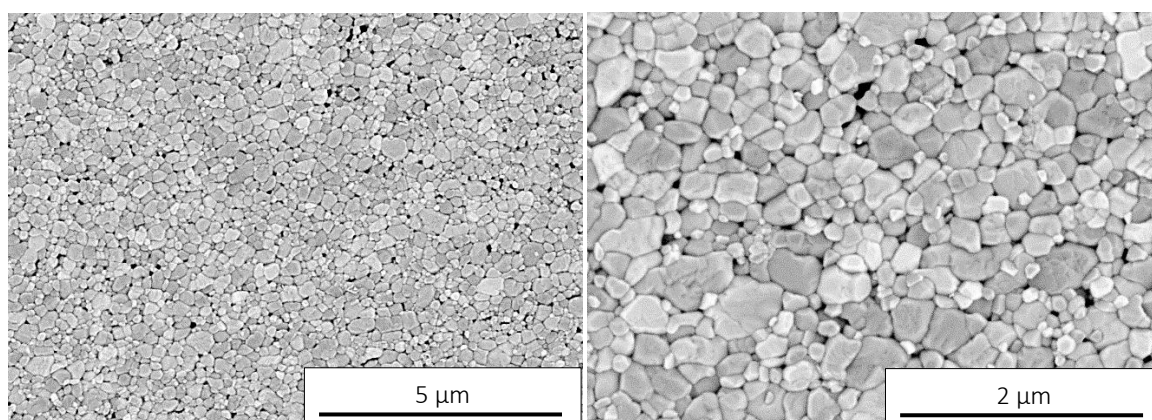


Figure 6.46. SEM micrographs of home-made BZY sample deformed up to $\epsilon \approx 40\%$ in compression at an initial strain rate of $1.8 \times 10^{-5} \text{ s}^{-1}$ and $1325 \text{ }^\circ\text{C}$. Stress axis is vertical.

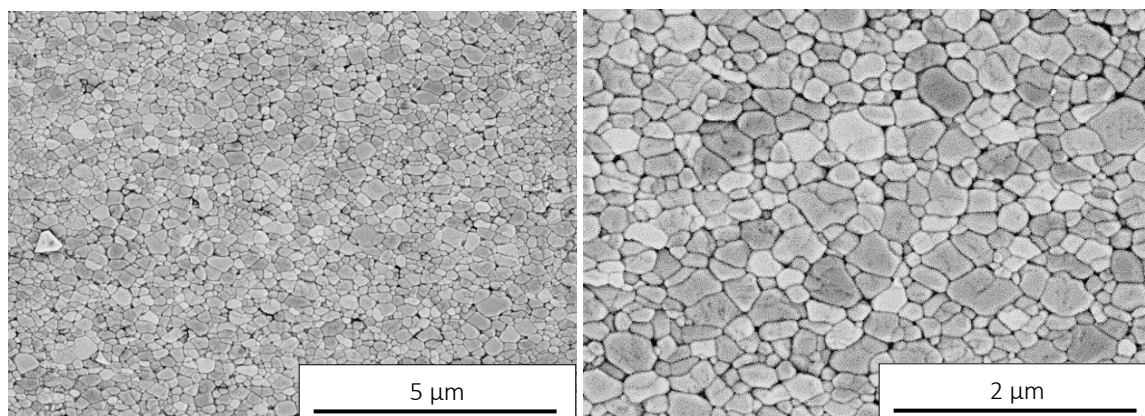


Figure 6.47. SEM micrographs of home-made BZY sample deformed up to $\epsilon \approx 40\%$ in compression at an initial strain rate of $3.6 \times 10^{-5} \text{ s}^{-1}$ and $1325 \text{ }^\circ\text{C}$. Stress axis is vertical.

TEM observations have been also performed on 40%-deformed samples in steady-state conditions (**Figure 6.48**). The grains remained primarily equiaxed, and no signs of cavitation were observed. Rather often, dislocation pile-ups appeared between grain boundaries, indicating that the boundaries are not efficient sites for dislocation absorption. This is probably at the origin of the pretty poor sinterability of this compound. The dislocation activity within the subgrains was practically null. In summary, the overall structure and density of dislocations are similar to those observed in unstrained specimens, suggesting that dislocations do not play an important role in steady-state deformation of BZY.

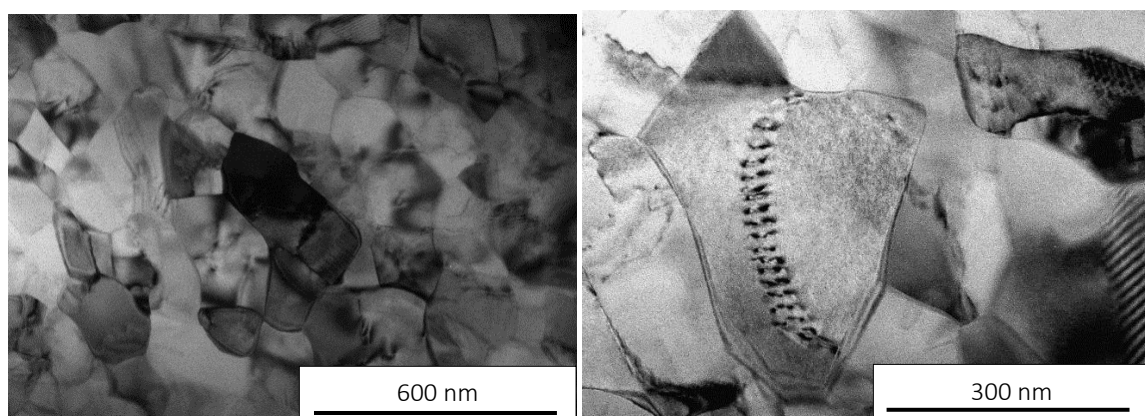


Figure 6.48. TEM images of BZY sample deformed in compression at an initial strain rate of $3.6 \times 10^{-5} \text{ s}^{-1}$ and $1325 \text{ }^\circ\text{C}$.

6.3.2.3.3 Creep parameters

The stress exponent n and the activation energy for flow Q in steady-state conditions (Equation 6.1) have been estimated following the same procedures used previously for apatites. **Figure 6.49** shows the log – log plot of the initial strain rate $\dot{\epsilon}_0$ against steady stress σ obtained at

1325 °C for the lower strain rates (**Figure 6.42**). The stress exponent measured at the strain levels ε of 10, 20 and 30% was $n = 2.2, 2.1$ and 2.1 , respectively. The average value of $n = 2.1 \pm 0.1$ is similar to the value found previously in LSO-SPS and other fine-grained ceramic materials. This result supports the previous idea, based on microstructural observations, that grain boundary sliding is the predominant deformation mechanism in the creep of BZY polycrystals.

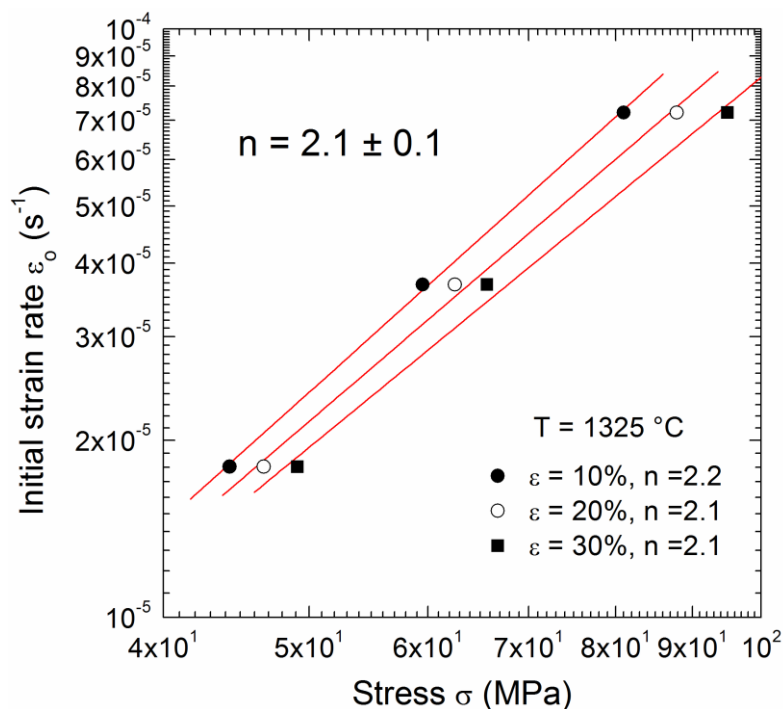


Figure 6.49. Determination of stress exponent n in the steady-state creep of BZY for strain levels ε of 10, 20 and 30%.

At difference of LSO-SPS, however, no concurrent grain growth took place during the straining of BZY samples. This finding is clearly reflected in the slopes of the $\sigma - \varepsilon$ curves. **Figure 6.50** shows again the tests performed at the lower strain rates at 1325 °C but in a log $\sigma - \varepsilon$ representation. The slopes of the curves in steady state are 0.0053, 0.0053 and 0.0057 for $\dot{\varepsilon}_0 = 1.8 \times 10^{-5}, 3.6 \times 10^{-5}$ and $7.2 \times 10^{-5} s^{-1}$, respectively, yielding values of $n = 1.9, 1.9$ and 1.8 , in agreement with the value previously estimated by the conventional method (**Figure 6.49**).

The stress exponent has been also estimated from fast strain rate changes during an isothermal test (differential method, Section 6.3.1.4.2). **Figure 6.51** shows the true stress vs true strain curve obtained at 1290 °C between 3.6×10^{-5} and $1.8 \times 10^{-5} s^{-1}$ (corresponding to cross-head speed jumps between 10 and 5 $\mu m/min$, respectively). The comparison of the steady-state flow stresses before and after the changes yields an average exponent $n = 2.1 \pm 0.1$, again in excellent agreement with previous determinations. It can be thus concluded that BZY polycrystals with $d =$

0.2 μm deform via a grain boundary mechanism characterized by $n = 2$, as found in other ceramic materials with grain sizes below 1 μm .

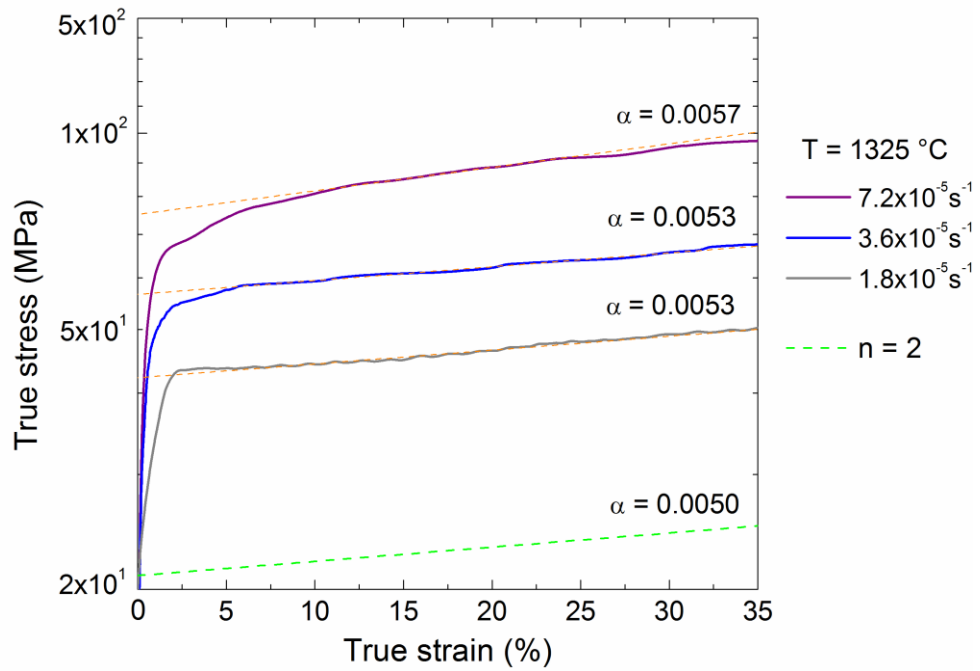


Figure 6.50. Log $\sigma - \epsilon$ curves for BZY deformed in compression at 1325 °C and different initial strain rates. The slopes of the curves yield a value of n close to 2, indicating the absence of concurrent grain growth.

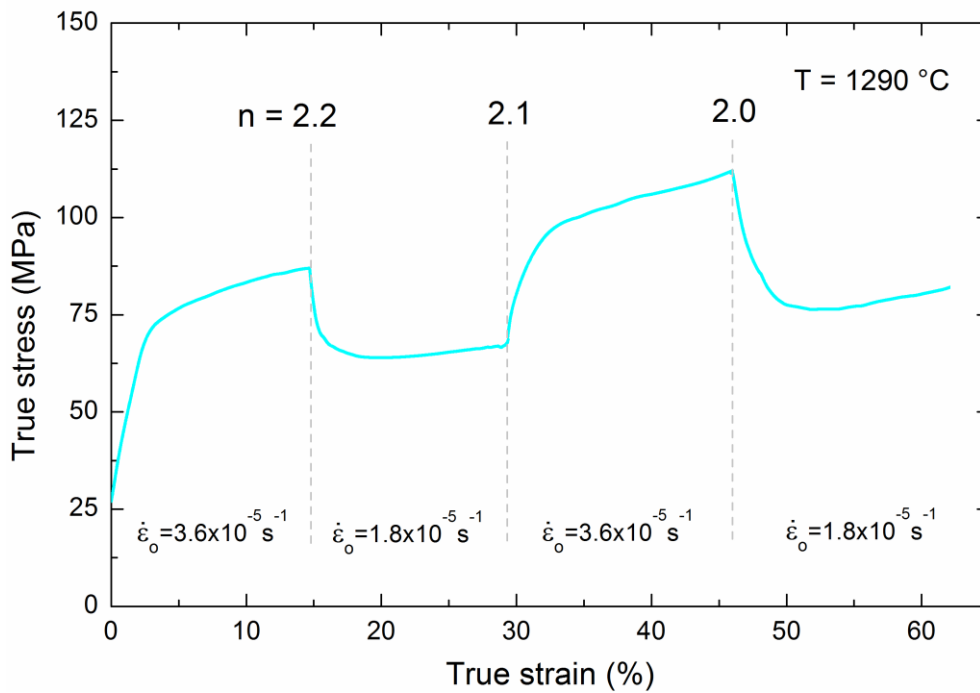


Figure 6.51. True stress $\sigma -$ true strain ϵ curve for BZY deformed in compression at 1290 °C. Several determinations of n by strain rate changes are displayed.

The creep activation energy Q in steady-state has been also measured by both conventional and differential methods. For the former, **Figure 6.52** shows a log - linear plot of the flow stress σ vs reciprocal temperature $1/T$ obtained at an initial strain rate of $3.6 \times 10^{-5} \text{ s}^{-1}$ between 1270 and 1325 °C. As done previously for the stress exponent, the flow stresses was measured at three strain levels $\varepsilon = 10, 20$ and 30%. The least squares fit leads to Q values of 520, 560 and 605 kJ/mol, with an average value $Q = 560 \pm 40 \text{ kJ/mol}$. A stress exponent $n = 2.1$ has been used in the calculations.

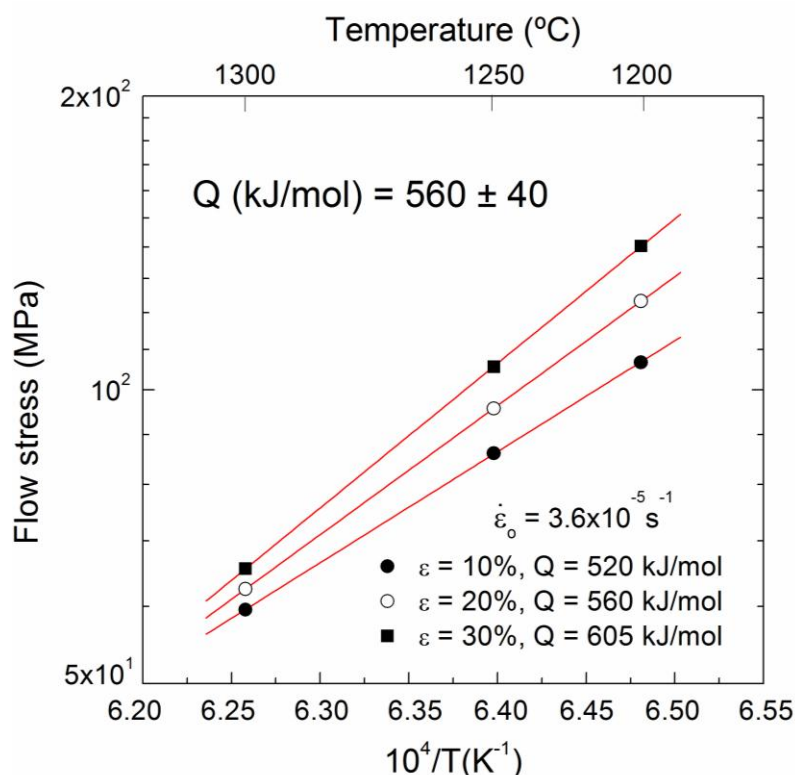


Figure 6.51. Determination of activation energy Q in the steady-state creep of BZY for strain levels ε of 10, 20 and 30%.

The activation energy Q has been also calculated from up- and down-temperature changes during a single iso-strain rate test (differential method, Section 6.3.1.4.2). **Figure 6.53** displays a test performed at $\dot{\varepsilon}_0 = 3.6 \times 10^{-5} \text{ s}^{-1}$ with temperature changes between 1290 and 1270 °C, yielding energies of 530 and 630 kJ/mol, with an average value of $Q = 580 \pm 50 \text{ kJ/mol}$, in agreement with the value estimated previously from conventional tests (**Figure 6.52**). **Figure 6.53** demonstrates the excellent reproducibility of the high-temperature mechanical tests in BZY, with the iso-strain rate curve at 1270 and 1290 °C (curves in green and light blue, respectively) matching adequately the corresponding sections of the differential curve. It also shows the maintenance of the flow stress levels after positive and negative temperature changes, indicating again that no microstructural evolution took place during steady state deformation. These features are related to the great stability of the grain distribution of Barium Zirconate compounds.

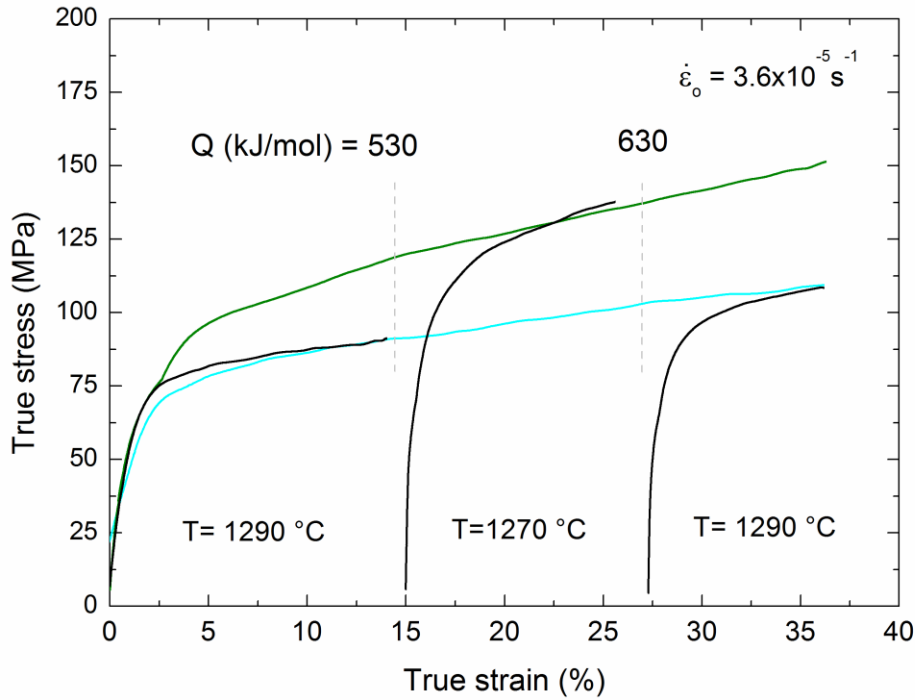


Figure 6.53. True stress σ - true strain ε curve for BZY deformed in compression at an initial strain rate of $3.6 \times 10^{-5} \text{ s}^{-1}$ and different temperatures. Values of Q were determined by temperature changes.

In order to verify the superplastic behaviour of this fine-grained BZY material, a few creep tests at constant load were carried out at high temperatures. **Figure 6.54** displays the $\log \dot{\varepsilon}_0 - \varepsilon$ curve obtained at $1280 \text{ }^\circ\text{C}$, showing several determinations of n by fast load changes. Stress exponents of 1.9, 2.0 and 1.9 were estimated from such load jumps, in excellent agreement with the values measured from conventional and differential constant strain rate tests (**Figure 6.49** and **Figure 6.51**).

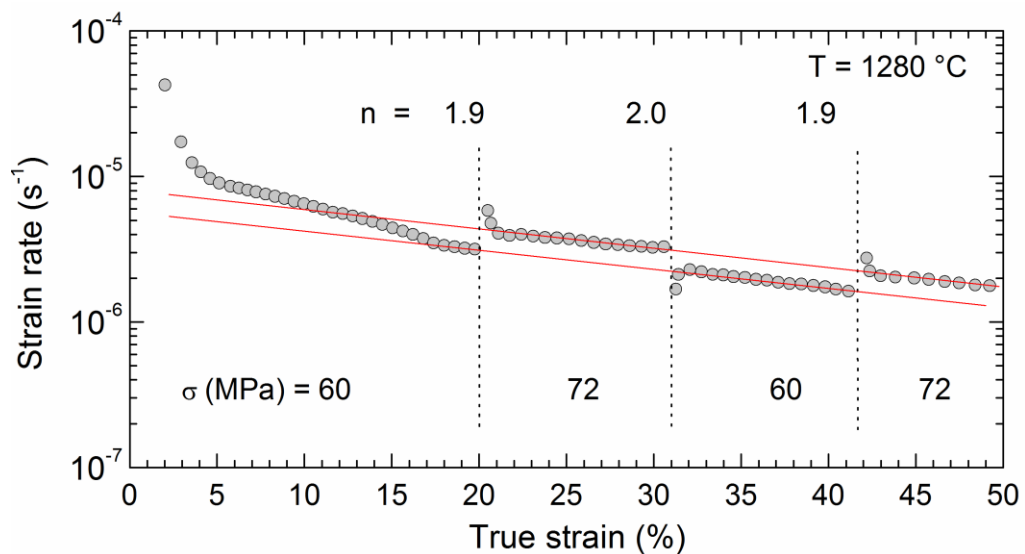


Figure 6.54. Creep curve plotted as $\log \dot{\varepsilon}_0$ against ε for BZY deformed at $1280 \text{ }^\circ\text{C}$. Several determinations of n by load changes are shown. Note the absence of creep transients.

It should be noted that the strain rates after up- and down-load changes remain rather constant, indicating the absence of significant microstructural evolution during creep, in agreement with microstructural observations. The large concurrent grain growth observed in LSO-SPS apatite prevented the use of constant load tests, which usually last several days, for the proper determination of the creep parameters.

In a similar way, the creep activation energy Q has been deduced from temperature changes during creep tests at constant load. **Figure 6.55** displays the $\log \dot{\epsilon}_0 - \epsilon$ curve obtained at $\sigma = 65$ MPa showing two determinations of Q between 1280 and 1250 °C. Energies of 530 and 580 kJ/mol were estimated, again in good agreement with the values deduced from constant cross-head speed tests.

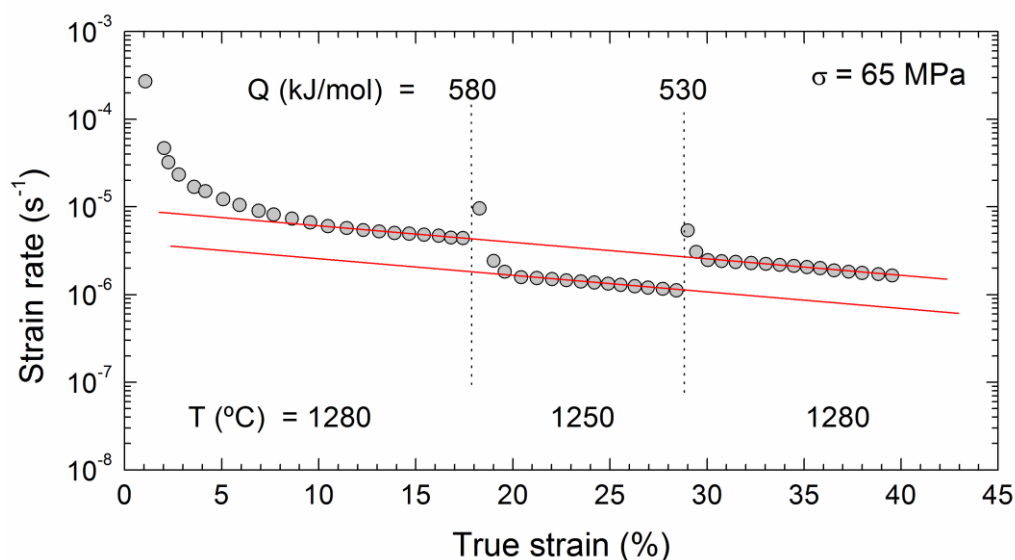


Figure 6.55. Determination of the activation energy Q by temperature changes for BZY at 65 MPa.

As already noted above, diffusion is usually the rate-controlling mechanism when plastic deformation is achieved by grain boundary sliding and thus the creep activation energy Q can be identified with the diffusion energy of the slowest moving species in the compound along the fastest path. In a recent work on $\text{BaZr}_{0.80}\text{Y}_{0.20}\text{O}_{2.9}$ polycrystals by Farlenkov et al. [24], the oxygen tracer diffusion coefficient was measured at 800 - 900 °C using the oxygen isotope exchange method. An activation energy of 115 kJ/mol was reported for bulk oxygen diffusion, which is significantly lower than the activation energy for creep of 580 kJ/mol found in this work. It can be thus concluded that cation diffusion is the rate controlling step. Actually, the presence of oxygen vacancies within the oxygen sublattice and the known oxygen ion conductivity in BZY strongly plays in favour a cation-limited diffusion, independently from the values of activation energies.

6.3.2.3.4 High-temperature deformation mechanism

The steady-state creep of fine-grained BZY with $d = 0.2 \mu\text{m}$ is characterized by $n \approx 2$ and $Q = 570 \text{ kJ/mol}$. The stress exponent n is characteristic of superplastic materials, as also found in the present work in fine-grained LSO-SPS oxy-apatite with $d = 0.2 \mu\text{m}$. The mechanical data have been analyzed by means of the phenomenological Sherby's equations for metals and metallic alloys (Equations 6.24), using the same procedure followed for LSO-SPS. That is, effective diffusion coefficients D^{lat} and D^{gb} have been deduced for each datum point assuming accommodation by lattice or grain boundary diffusion, respectively. The corresponding diffusivities are plotted in **Figure 6.56** (red points), along with the diffusion coefficients found for LSO-SPS apatite (cyan points) using the same phenomenological models with $n = 2$, and for LSO apatite (blue points) using the Ashby-Verrall model with $n = 1$. It can be seen that whatever mass transport is accomplished by volume or grain boundary, the diffusion coefficient is about two orders of magnitude smaller than those found for the oxy-apatites, which is consistent with the poor sinterability of BZY. However, due to the lack of information about the diffusion coefficients in BZY, there is no way to decide which diffusion path is the accommodation process for grain boundary sliding neither the validity itself of the deformation models.

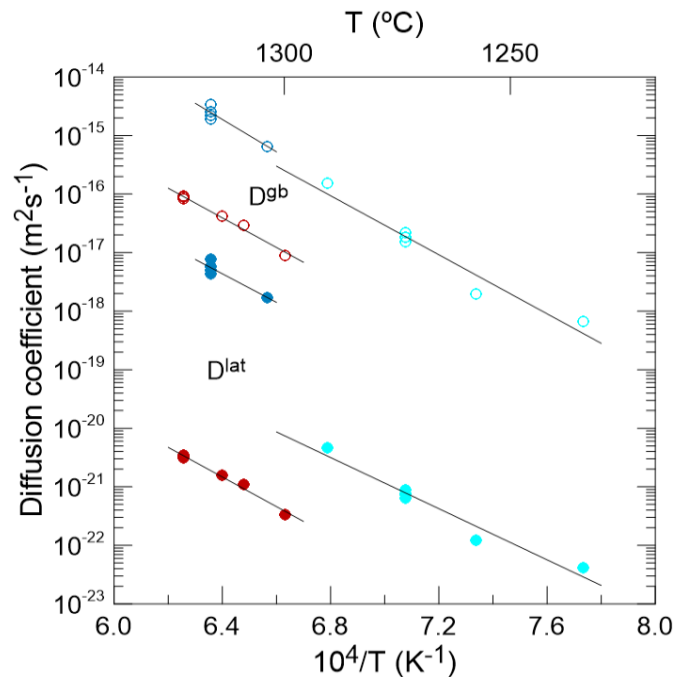


Figure 6.56. Effective diffusion coefficients D^{lat} and D^{gb} for fine-grained BZY (red points) deduced from deformation data using the phenomenological equations derived by Sherby et al. [9] for lattice and grain boundary diffusion-controlled strain rate (Equations 6.24). Effective diffusivities derived for LSO-CS ($n = 1$, blue points, Figure 6.26) and LSO-SPS ($n = 2$, cyan points, Figure 6.40) are also included.

6.3.2.3.5 Creep behaviour of other perovskite-structured oxides

The high-temperature plastic deformation of several ceramic perovskites has been previously reported. Materials, grain sizes and creep parameter are compiled in **Table 6.3**. Except for yttrium- and ytterbium- doped barium cerate, which has a submicrometer grain size of $d = 0.5 \mu\text{m}$ and a stress exponent $n = 2$, the other compounds exhibit grain sizes ranging from 4 to 80 μm and stress exponents close to 1. These results attest again to the systematic variation of n with grain size, increasing from $n = 1$ to 2 when decreasing grain size below about 1 μm . The activation energy for creep ranges from 350 to 750 kJ/mol, and the grain size exponent p is close to 2, although a value of 1 was reported in the deformation of $\text{SrCo}_{0.8}\text{Fe}_{0.2}\text{O}_3$. No information about cation diffusion is available for these perovskite materials, although values below or close to 100 kJ/mol were reported for oxygen diffusion. The creep activation energies are considerably higher than this value for oxygen diffusion, indicating that cations should be most often rate controlling. As noted in the previous section, it seems to be also the case in Yttrium-doped Barium Zirconate.

Table 6.3. Creep parameters n , Q and p , for oxide perovskites reported in the literature.

Material	d (μm)	n	Q (kJ/mol)	p	Reference
$\text{BaZr}_{0.85}\text{Y}_{0.15}\text{O}_{2.925}$	0.2 ± 0.1	2.1 ± 0.1	580 ± 40	-	this work
$\text{BaCe}_{0.95}\text{Y}_{0.05}\text{O}_3$ $\text{BaCe}_{0.95}\text{Yb}_{0.05}\text{O}_3$	≈ 0.5	2.0 ± 0.2	490 ± 40	-	[20, 21]
$\text{BaCe}_{1-x}\text{Y}_x\text{O}_{3-x}$ $x = 0.05 - 0.20$	3 - 7	1.1 ± 0.1	350 ± 50	-	[25, 26]
SrTiO_3	6	≈ 1	630 ± 20	-	[27]
$\text{La}_{0.9}\text{Sr}_{0.1}\text{MnO}_3$	8	1.1 ± 0.2	490 ± 30	-	[28]
$\text{La}_{0.8}\text{Sr}_{0.2}\text{Ga}_{0.85}\text{Mg}_{0.15}\text{O}_3$	15	1.3 ± 0.1	520 ± 20	-	[29, 30]
$\text{SrCo}_{0.8}\text{Fe}_{0.2}\text{O}_3$	4 - 11	≈ 1	470 - 280	≈ 1	[31]
CaTiO_3	5 - 60	1.0 ± 0.1	750	2.1	[32]
BaTiO_3	30 - 80	1.1 ± 0.2	720 ± 70	1.8 ± 0.2	[33]

Regarding the absolute magnitude of the strain rates, **Figure 6.57** shows the variation of strain rate with stress for perovskites deformed at 1300 °C. Data for BZY (dark red line) have been extrapolated from lower temperatures using $Q = 580$ kJ/mol. For the sake of comparison, data for LSO apatite with $d = 1.1 \mu\text{m}$ and $n = 1$ are also included (cyan points), as well as for LSO-SPS (purple points) with $d = 0.2 \mu\text{m}$ and $n = 2$; in this latter case, data have been extrapolated at 1300 °C using the measured value of $Q = 340$ kJ/mol.

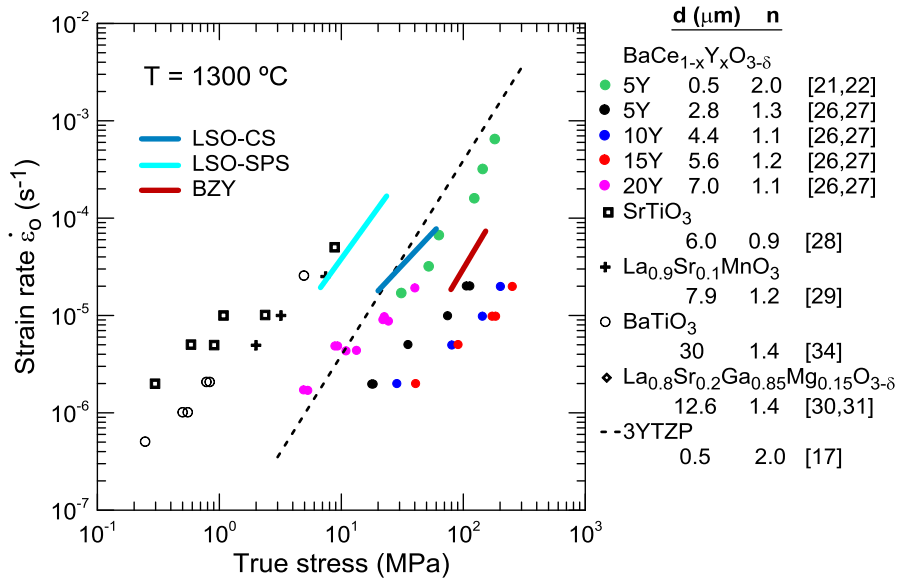


Figure 6.57. Variation of strain rate with stress for perovskite-structure materials deformed at 1300 °C. Data for BZY (dark red line) have extrapolated at 1300 °C with $Q = 580$ kJ/mol. LSO-CS (blue line) and LSO-SPS (cyan line, extrapolated with $Q = 340$ kJ/mol) apatites are also included for the sake of comparison. 3YTZP with $d = 0.5$ μm (dashed line) is shown as reference for superplastic behaviour.

For a proper comparison, raw data have to be compensated with grain size. A value of $p = 3$ have been used for the comparison (**Figure 6.58**), although it has been verified that an analysis with $p = 2$ leads to identical conclusions. As can be seen, BZY is the hardest material, indicating that mass transport is very slow compared to the other ceramic materials. It is followed by LSO-SPS, barium cerate and 3YTZP, all of them with $d < 1$ μm and $n = 2$. LSO apatite is slightly less creep resistant, while the larger-grained perovskites are much softer.

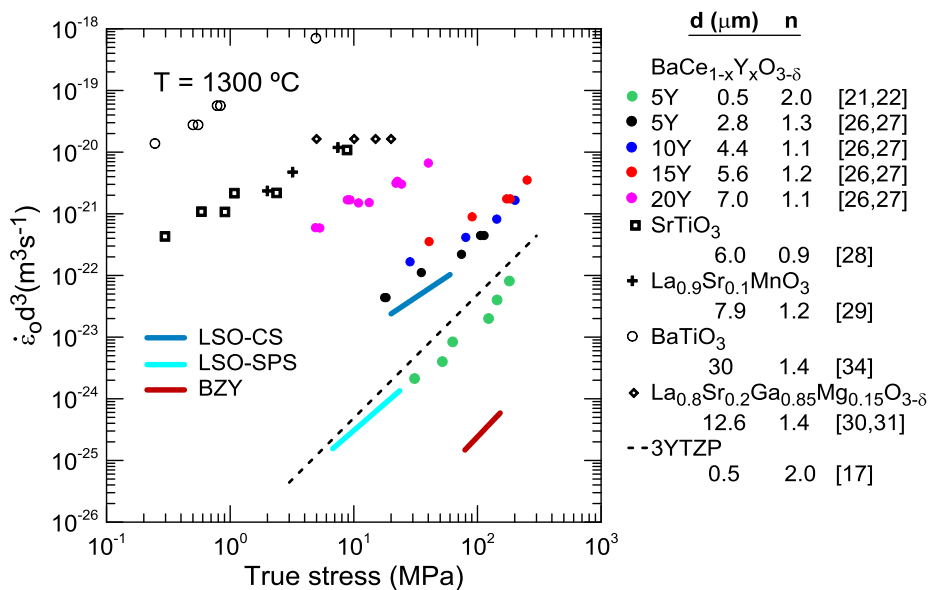


Figure 6.58. Grain-size compensated strain rates with $p = 3$ against stress for perovskite-structure materials.

6.4 REFERENCES

1. Greco, F., et al., *Modelling the impact of creep on the probability of failure of a solid oxide fuel cell stack*. Journal of the European Ceramic Society, 2014. 34(11): p. 2695-2704.
2. Nakajo, A., et al., *Mechanical reliability and durability of SOFC stacks. Part I : Modelling of the effect of operating conditions and design alternatives on the reliability*. International Journal of Hydrogen Energy, 2012. 37(11): p. 9249-9268.
3. Koyama, Y., et al., *Electronic Structure of Lithium Nickel Oxides by Electron Energy Loss Spectroscopy*. The Journal of Physical Chemistry B, 2005. 109(21): p. 10749-10755.
4. Laffont, L. and P. Gibot, *High resolution electron energy loss spectroscopy of manganese oxides: Application to Mn₃O₄ nanoparticles*. Materials Characterization, 2010. 61(11): p. 1268-1273.
5. Paufler, P., J.-P. Poirier. *Creep of crystals. High-temperature deformation processes in metals, ceramics and minerals*. Cambridge University Press. Cambridge – London – New York – New Rochelle – Melbourne – Sydney 1985. 145 figs., XII + 260 p., price £ 10.95 (paperback). ISBN 0-521-27851-1. Crystal Research and Technology, 1986. 21(10): p. 1338-1338.
6. Bretheau, T., et al., *Dislocation motion and high temperature plasticity of binary and ternary oxides*. Advances in Physics, 1979. 28(6): p. 835-1014.
7. Suarez, G., et al., *Electrophoretic deposition for obtaining dense lanthanum silicate oxyapatite (LSO)*. Ceramics International, 2016. 42(16): p. 19283-19288.
8. Ashby, M.F. and R.A. Verrall, *Diffusion-accommodated flow and superplasticity*. Acta Metallurgica, 1973. 21(2): p. 149-163.
9. Nieh, T.G., et al. *Superplasticity in Metals and Ceramics*. 1997.
10. Chung, T.E. and T.J. Davies, *The low-stress creep of fine-grain uranium dioxide*. Acta Metallurgica, 1979. 27(4): p. 627-635.
11. Jiménez-Melendo, M., et al., *Diffusional and dislocation creep of NiO polycrystals*. Philosophical Magazine A, 1987. 56(6): p. 767-781.
12. Bravo-León, A., M. Jiménez-Melendo, and A. Domínguez-Rodríguez, *Mechanical and microstructural aspects of the high temperature plastic deformation of yttria-stabilized zirconia polycrystals*. Acta Metallurgica et Materialia, 1992. 40(10): p. 2717-2726.
13. Jiménez-Melendo, M., et al., *Diffusion-controlled plastic deformation of YBa₂Cu₃O_x*. Acta Metallurgica et Materialia, 1995. 43(6): p. 2429-2434.
14. Jiménez-Melendo, M., H. Haneda, and H. Nozawa, *Ytterbium Cation Diffusion in Yttrium Aluminum Garnet (YAG)—Implications for Creep Mechanisms*. Journal of the American Ceramic Society, 2001. 84(10): p. 2356-2360.

15. Nieh, T.-G. and J. Wadsworth, *Dynamic Grain Growth During Superplastic Deformation of Yttria-Stabilized Tetragonal Zirconia Polycrystals*. Journal of the American Ceramic Society, 1989. 72(8): p. 1469-1472.
16. Jiménez-Melendo, M., A. Domínguez-Rodríguez, and A. Bravo-León, *Superplastic Flow of Fine-Grained Yttria-Stabilized Zirconia Polycrystals: Constitutive Equation and Deformation Mechanisms*. Journal of the American Ceramic Society, 1998. 81(11): p. 2761-2776.
17. Wakai, F., T. Nagano, and T. Iga, *Hardening in Creep of Alumina by Zirconium Segregation at the Grain Boundary*. Journal of the American Ceramic Society, 1997. 80(9): p. 2361-2366.
18. Wakai, F. and H. Kato, *Superplasticity of TZP/Al₂O₃ Composite*. Adv. Ceram. Mat, 1988. 3(1): p. 71-76.
19. Chen, T., F.A. Mohamed, and M.L. Mecartney, *Threshold stress superplastic behavior and dislocation activity in a three-phase alumina–zirconia–mullite composite*. Acta Materialia, 2006. 54(17): p. 4415-4426.
20. Vaquero-Aguilar, C., et al., *High-temperature mechanical behavior of polycrystalline yttrium-doped barium cerate perovskite*. Journal of the European Ceramic Society, 2011. 31(7): p. 1333-1338.
21. Vaquero-Aguilar, C. and M. Jiménez-Melendo, *Characterization and creep properties of proton-conducting Yb-doped barium cerate*. Journal of the European Ceramic Society, 2011. 31(14): p. 2671-2676.
22. Alabort, E., et al., *On the mechanisms of superplasticity in Ti–6Al–4V*. Acta Materialia, 2016. 105: p. 449-463.
23. Jiménez-Melendo, M., A. Domínguez-Rodríguez, and J.L. Routbort, *Deformation maps of YBa₂Cu₃O_{7-x} superconductors*. Scripta Metallurgica et Materialia, 1995. 32(4): p. 621-626.
24. Farlenkov, A.S., et al., *Oxygen isotope exchange in doped calcium and barium zirconates*. Solid State Ionics, 2016. 290: p. 108-115.
25. Goretta, K.C., et al., *Diffusional creep of BaCe_{0.8}Y_{0.2}O_{3-α} mixed conductors*. Solid State Ionics, 1998. 111(3): p. 295-299.
26. Park, E.T., et al., *High-temperature deformation of BaCe_{1-x}Y_xO_{3-y} (0.05 ≤ x ≤ 0.2)*. Solid State Ionics, 1999. 117(3): p. 323-330.
27. Singh, D., et al., *High-temperature deformation behavior in SrTiO₃ ceramics*. Journal of the European Ceramic Society, 2007. 27(11): p. 3377-3384.
28. Wolfenstine, J., et al., *Elevated temperature deformation of fine-grained La_{0.9}Sr_{0.1}MnO₃*. Journal of Materials Research, 1996: p. Medium: X; Size: pp. 657-662.
29. Wolfenstine, J., *Rate-controlling species for creep of the solid state electrolyte: doped lanthanum gallate*. Solid State Ionics, 1999. 126(3): p. 293-298.
30. Wolfenstine, J., P. Huang, and A. Petric, *Creep behavior of doped lanthanum gallate versus cubic zirconia*. Solid State Ionics, 1999. 118(3): p. 257-259.

31. Majkic, G., L. Wheeler, and K. Salama, *Creep of polycrystalline SrCo_{0.8}Fe_{0.2}O_{3-δ}*. Acta Materialia, 2000. 48(8): p. 1907-1917.
32. Li, P., S.-i. Karato, and Z. Wang, *High-temperature creep in fine-grained polycrystalline CaTiO₃, an analogue material of (Mg, Fe)SiO₃ perovskite*. Physics of the Earth and Planetary Interiors, 1996. 95(1): p. 19-36.
33. Park, E.T., et al., *High-temperature creep of polycrystalline BaTiO₃*. Journal of Materials Research, 2011. 14(2): p. 523-528.

Chapter 7

GENERAL CONCLUSIONS

This work is devoted to the fabrication and structural, microstructural and mechanical characterization of Lanthanum Silicate and Yttrium-doped Barium Zirconate, which are potential materials to be used as electrolyte in SOFCs. The main conclusions derived in this work can be summarized as follows:

- Fully dense $\text{La}_{9.33}\text{Si}_6\text{O}_{26}$ and $\text{BaZr}_{0.85}\text{Y}_{0.15}\text{O}_{2.925}$ ceramics have been successfully prepared from nanopowders obtained by different strategies. On the one hand, LSO materials were synthesized by freeze drying and sintered at high-temperature by conventional or spark plasma sintering, resulting oxy-apatite ceramics with relative densities between 97% and 100%. On the other hand, BZY materials were prepared by the modified EDTA-citrate complexing method and sintered at high temperature by conventional sintering, achieving densities higher than 97%.
- A commercial $\text{BaZr}_{0.85}\text{Y}_{0.15}\text{O}_{2.925}$ prepared by SSR with 1 wt% NiO content as sintering-aid provided by NorecsTM has been also investigated. In addition, in order to study the influence of Nickel on the mechanical properties, the mechanical characterization was also carried out in the commercial BZY after NiO-extraction. The extraction process required to pack the commercial ceramic in a bed of BZY nanopowders and a high temperature heat treatment at 1600 °C for 120 h.
- X-ray diffraction of the resulting nanopowders and sintered ceramics indicated the presence of the single $\text{La}_{9.33}\text{Si}_6\text{O}_{26}$ ($P6_3/m$) and $\text{BaZr}_{0.85}\text{Y}_{0.15}\text{O}_{2.925}$ ($Pm\bar{3}m$) phases, respectively. However, commercial BZY-NiO also contained BaY_2NiO_5 ($Immm$), which completely disappeared after NiO-extraction. From XRD diagrams of the LSO calcined nanopowders and sintered ceramics, the refined lattice parameters deduced from Le Bail fitting did not undergo significant changes, with values $a = 9.729(3)$ Å and $c = 7.183(2)$ Å. The crystallite size was estimated to be about 80 - 90 nm that correlates well with TEM observations, where irregular particles of average size of about 100 nm were observed. In

the case of XRD diagrams for BZY, a lattice parameter $a = 4.203(1)$ Å was found for the calcined powder, while the cell parameter increased slightly to $a = 4.223(3)$ Å after sintering. The crystallite size estimated from the peaks width was about 15 - 20 nm, also in agreement with the very small spherical particles, between 10 and 40 nm in diameter, observed by TEM. The cell parameters deduced from the Le Bail method for the commercial materials before and after NiO-extraction were $a = 4.212(3)$ Å and $4.223(3)$ Å, respectively, indicating that NiO addition slightly reduces the cubic unit cell parameter.

- SEM observations reflected that all the sintered compounds exhibited a homogeneous microstructure formed by equiaxed grains, with practically no porosity except in the case of BZY after NiO-extraction, which displayed cavities of about 10 µm in size preferentially located at multiple grain junctions. The average grain sizes varied from 0.2 ± 0.1 µm in BZY and LSO-SPS, to 9 ± 3 µm in the case of the commercial material after NiO-extraction. Intermediate values were found for LSO-CS and BZY-NiO, which exhibited a mean grain size d of 1.1 ± 0.6 and 1.6 ± 0.6 µm, respectively.
- TEM observations showed that the grains of oxy-apatites and BZY-NiO are essentially free of defects, with clean and straight grain boundaries and well-defined triple points. Both BZY and BZY after NiO extraction, however, exhibited a high density of dislocations.
- The room-temperature mechanical characterization of Lanthanum Silicate and Yttrium-doped Barium Zirconate has been carried out by means of different techniques. All the methods showed similar results for the elastic properties, being RUS the most precise technique. However, the values of hardness obtained by microindentation were significantly lower than those determined by nanoindentation, according to the applied load dependence of hardness.
- The values of the Young's modulus obtained at room temperature were in the range of 135 - 141 GPa for LSO-CS and 129 - 136 GPa for LSO-SPS. Higher values were found for BZY compounds, with values in the range of 186 - 200 GPa for BZY, 198 - 207 GPa for BZY-NiO and 191 - 211 for BZY after NiO-extraction.
- Poisson ratios obtained at room temperature for the oxy-apatites were in the range of 0.29 - 0.32, while for BZY ceramics were between 0.24 and 0.32.

- Regarding hardness, values of 9.5 and 9.8 GPa were measured by nanoindentation in LSO-CS and LSO-SPS for an applied load of 500 mN, whereas values of 7.3 and 7.7 GPa were estimated under a 2 N-load by microindentation. For the same loading conditions, values of nanohardness of 10.1, 9.0 and 6.7 GPa were found for BZY, BZY-NiO and BZY after NiO-extraction, respectively, while those calculated by microindentation were 7.7, 7.0 and 4.7 GPa. The softening of BZY after NiO-extraction can be ascribed to its larger grain size in comparison with the other materials, since hardness is inversely proportional to grain size according to the Hall-Petch law.
- Fracture toughness was calculated from cracks propagated from the microindentation corners by using the Niihara equation for oxy-apatites and BZY, obtaining values of 1.2 and 1.6 MPa m^{1/2}, respectively. However, fracture toughness could not be determined in the commercial materials due to the presence of circumferential cracks surrounding the residual imprint which prevent a reliable determination of K_{Ic} .
- The elastic parameters of LSO and BZY compounds were also determined by means of DFT calculations. The results obtained for oxy-apatite showed a slight anisotropy of its elastic longitudinal response between a , b axes and c axes, while those found for BZY revealed that both the increase of Yttrium doping level and the presence of protons tend to reduce the elastic coefficients.
- The temperature dependence of the coefficient of thermal expansion and elastic constants of Lanthanum Silicate and Yttrium-doped Barium Zirconate was studied by means of high-temperature X-ray diffraction, thermo-mechanical analysis and high-temperature resonant ultrasound spectroscopy. On the one hand, in the range of temperature of 298 - 1173 K, the anisotropic thermal expansion coefficient of oxy-apatites was estimated to be $9.5 \times 10^{-6} \text{ K}^{-1}$ along the a -axis and $8.2 \times 10^{-6} \text{ K}^{-1}$ along the c -axis, whereas a value of $9.1 \times 10^{-6} \text{ K}^{-1}$ was found at macroscopic scale. The values of α obtained for BZY and BZY-NiO were $8.5 \times 10^{-6} \text{ K}^{-1}$ and $8.2 \times 10^{-6} \text{ K}^{-1}$, respectively. On the other hand, in all sintered ceramics the elastic constants E and G showed a decrease of about 1% for every 100 K-increase in temperature according with the rule of thumb, while the Poisson ratio remained practically constant.

- Finite elements numerical simulations have been successfully conducted in oxy-apatite polycrystal aggregates created by Voronoi tessellation in order to characterize the residual stresses state and predict fracture in Lanthanum Silicate. The results showed that the stresses were heterogeneously distributed in the aggregate which was completely linked with the thermo-elastic anisotropy of a single crystal. It was observed that stress localized preferably along the grain boundaries of some favorably-oriented grains leading to high levels of residual stresses. However, for the purpose of properly studying failure, it was deduced from the results that it is necessary to consider larger aggregates in order to establish the effective thermo-elastic properties and be more precise concerning the construction of the polycrystal and the material properties.
- The mechanical response of Lanthanum Silicate and Yttrium-doped Barium Zirconate electrolytes has been tested in conditions similar to SOFC operating conditions by means of high-temperature compressive mechanical tests under hydrogen atmosphere. LSO compounds fabricated by either conventional or spark plasma sintering did not show any signal of degradation under hydrogen atmosphere. The same behavior was observed in home-made BZY ceramics fabricated without sintering additives, which did not undergo any significant mechanical degradation during testing even at very high compressive loading. However, commercial NiO-containing BZY failed catastrophically in hydrogen-rich conditions at loads above 350 MPa.
- By using atomic-scale chemical analysis, it has been observed that nickel oxide was mainly located along grain boundaries in commercial NiO-added BZY, which reduced to metallic Ni under hydrogen atmosphere. Such a reduction of NiO at grain boundaries favored sample breaking at lower loading values, limiting thus the material's fracture resistance.
- Although NiO-extraction could be considered as a solution to prevent the premature degradation of commercial BZY-NiO in working conditions, the process led to a porous material with important grain coarsening and low mechanical resistance.
- The high-temperature plastic deformation of oxy-apatites and Y-doped Barium Zirconate has been assessed by compressive mechanical tests. A transition brittle-to-ductile has been observed at a fixed strain rate with increasing temperature. For a typical value of $\dot{\epsilon}_0 = 3.5 \times 10^{-5} \text{ s}^{-1}$, the transition temperature is about 1100 and 1000 °C for LSO-CS ($d = 1.1 \text{ }\mu\text{m}$)

and LSO-SPS ($d = 0.2 \mu\text{m}$), respectively, and 1200 for BZY ($d = 0.2 \mu\text{m}$). In the brittle regime, a mixed fracture mode was observed in both apatites, while it was predominantly intergranular in BZY.

- At higher temperatures, the compounds exhibit extended steady states of deformation. In all cases, grain boundary sliding has been found to be the main deformation mechanism, with the grains retaining their original shape even after strains as large as 50%. Concurrent grain growth took place during deformation in the oxy-apatites, while no change in grain size was found in BZY, according to the poor sinterability reported for this material.
- In the steady-state regime, the creep parameters were derived from conventional and differential mechanical tests. The stress exponent n was found to be close to 2 in LSO-SPS and undoped BZY, i.e., in materials with very fine-grained microstructures. This value is characteristic of superplasticity in metals and ceramics. In LSO-CS with $d > 1 \mu\text{m}$, the stress exponent is close to unity, as reported in various ceramic materials with grain sizes $d > 1 \mu\text{m}$. The atomistic origin of the transition in n from 2 to 1 when increasing grain size is presently unknown.
- Regardless the exact value of the stress exponent, the activation energy for creep Q is usually associated with the diffusion energy of the slowest moving ionic species in the compound when grain boundary sliding is the main deformation mechanism. A value of $Q = 340 \text{ kJ/mol}$ has been measured for both LSO-CS and LSO-SPS oxy-apatites, indicating that the same diffusion mechanism is rate controlling, despite the difference in stress exponent. In BZY, the creep activation energy was 570 kJ/mol . No data concerning diffusion energies have been reported in the literature for a proper comparison.
- Effective diffusivities for lattice and grain boundary diffusion were derived from mechanical data by using the Ashby-Verrall model for LSO-CS ($n = 1$) and the Sherby's phenomenological equations for LSO-SPS and BZY ($n = 2$). There is an excellent agreement between the grain boundary diffusivities estimated for both oxy-apatites, giving confidence to the present analysis. On the other hand, the diffusivities derived for BZY are two orders of magnitude smaller than for apatites, which may justify the low sinterability of this material. In this regard, it should be noted the importance in determining the diffusion coefficient of the slowest moving species in compounds because it plays an essential role

not only in creep, but in all mass transport-related processes, such as sintering and grain growth. Such an information can be thus used to devise optimum processing schedules.

Chapter 7

CONCLUSIONS GENERALES

Ce travail avait pour objectif la fabrication et l'étude des propriétés structurales, microstructurales et mécaniques de Silicate de Lanthane et Zirconate de Baryum dopé à l'Yttrium, qui sont considérés comme matériaux d'électrolytes potentiels au sein de piles à combustible. Les principales conclusions de ce travail sont les suivantes:

- Des céramiques denses des matériaux $\text{La}_{9.33}\text{Si}_6\text{O}_{26}$ et $\text{BaZr}_{0.85}\text{Y}_{0.15}\text{O}_{2.925}$ ont été préparées à partir de nanopoudres, elles-mêmes synthétisées par différentes méthodes. D'un côté, les silicates de lanthane de type apatite (LSO) ont été préparés sous forme de nanopoudres par lyophilisation puis frittage conventionnel ou spark plasma. Les céramiques obtenues présentent des densités relatives de 97 et 100%. D'un autre côté, le matériau BZY a été préparé par une méthode de type « complexe de citrate » puis fritté par frittage conventionnel permettant d'obtenir des céramiques de densité supérieures à 97%.
- Un échantillon commercial de formule $\text{BaZr}_{0.85}\text{Y}_{0.15}\text{O}_{2.925}$, préparé par la méthode de frittage réactif avec 1% d'additif sous forme d'oxyde de nickel, a également été étudié. Le but était de déterminer l'influence de la présence du nickel sur les propriétés mécaniques des échantillons. Nous avons également évalué l'influence d'un traitement de 1600 °C pendant 120 h sur l'extraction du nickel et sur l'évolution des propriétés mécaniques.
- L'étude par diffraction des rayons X des nanopoudres et céramiques frittées montrent que les échantillons préparés au laboratoire présentent respectivement les seules phases $\text{La}_{9.33}\text{Si}_6\text{O}_{26}$ ($P6_3/m$) et $\text{BaZr}_{0.85}\text{Y}_{0.15}\text{O}_{2.925}$ ($Pm\bar{3}m$). Cependant, nous avons montré que l'échantillon commercial montre également la phase BaY_2NiO_5 ($Immm$) qui disparaît complètement après le procédé d'extraction du nickel. Les paramètres de maille déduits pour la phase apatite sous forme poudre, $a = 9.729(3)$ Å et $c = 7.183(2)$ Å sont en accord avec des résultats des échantillons frittés. On a estimé que la taille des cristallites était d'environ 80 à 90 nm qui correspond bien aux observations TEM, où des particules irrégulières de taille moyenne d'environ 100 nm ont été observées. Pour BZY, le paramètre

de maille $a = 4.203(1)$ Å obtenu pour la poudre est légèrement inférieur à celui obtenu pour l'échantillon fritté avec $a = 4.223(3)$ Å. La taille des cristallites estimée à partir de la largeur des pics était d'environ 15 à 20 nm, également en accord avec les très petites particules sphériques, entre 10 et 40 nm de diamètre, observées par TEM. Les paramètres de maille déduits pour les matériaux commerciaux avant et après le procédé d'extraction du nickel étaient respectivement $a = 4.212(3)$ Å et $4.223(3)$ Å, indiquant que l'addition du nickel réduit légèrement le paramètre de maille.

- Les observations par microscopie électronique à balayage (SEM) montrent que les échantillons ont une microstructure régulière et homogène formée de grains équi-axes, avec une porosité pratiquement nulle, excepté dans le cas de l'échantillon de BZY après extraction du nickel qui montrent des porosités d'environ 10 µm en taille située aux joints triples. La taille des grains au sein de la céramique évolue de quelques centaines de nanomètres à quelques microns en fonction du matériau, du mode de frittage et du traitement post-frittage (0.2 ± 0.1 µm pour le BZY et le LSO-SPS, 1.1 ± 0.6 pour le LSO-CS, 1.6 ± 0.6 pour le BZY-NiO et 9 ± 3 µm pour le BZY après extraction du nickel).
- Les caractérisations par microscopie électronique à transmission (TEM) montrent que les grains d'oxy-apatites et de BZY-NiO sont libres de défauts étendus avec des joints de grains et des joints triples bien définis. Les échantillons de BZY et de BZY après l'extraction de NiO montrent par contre une haute densité de dislocations.
- Les propriétés mécaniques de Silicate de Lanthane et Zirconate de Baryum dopé à l'Yttrium ont été évaluées à température ambiante par différentes méthodes. Toutes ces méthodes montrent des résultats sensiblement identiques. Les propriétés élastiques, la méthode la plus précise semblant être celle de résonance ultrasonore. Les résultats de dureté varient cependant entre les essais de micro-dureté et ceux de nano-indentation ce qui peut s'expliquer en partie par l'influence de la charge sur les valeurs de dureté.
- Les valeurs de module d'Young sont dans la gamme 135 - 141 GPa pour les apatites préparées par frittage conventionnel et 129 - 136 GPa pour celles préparées par frittage spark plasma. Des valeurs plus élevées ont été trouvées pour les échantillons de BZYs, les valeurs du module d'Young sont dans la gamme approximative de 186 et 200 GPa pour le BZY, 198 - 207 GPa pour le BZY-NiO et 191 - 211 pour le BZY après l'extraction de NiO.

- Les coefficients de Poisson obtenus à température ambiante pour les apatites sont dans la gamme 0.29 - 0.32 alors qu'il semble varier plus pour les échantillons de BZY entre 0.24 et 0.32.
- En ce qui concerne la dureté, des valeurs de 9.5 et 9.8 GPa ont ainsi été mesurées par nanoindentation sous une charge de 500 mN pour les échantillons d'apatites fabriquées par frittage conventionnel et spark plasma respectivement alors que les mesures de de micro-indentation sous une charge de 2N donnent des valeurs de 7.3 and 7.7 GPa. De la même manière, pour le zirconate de baryum, des valeurs de 10.1, 9.0 et 6.7 GPa ont été mesurées par nanoindentation pour les échantillons BZY, BZY-NiO et BZY-NiO après extraction, alors que les mesures de micro-dureté donnent les valeurs 7.7, 7.0 et 4.7 GPa respectivement. La diminution de la dureté pour les échantillons après extraction est en grande partie due à l'évolution de la taille de grains suite au traitement thermique imposé.
- La ténacité de la fracture calculée à partir de la propagation des cracks lors des essais de micro-dureté est de 1.2 et 1.6 MPa m^{1/2}, respectivement pour l'oxyapatite et BZY.
- Les coefficients élastiques de LSO et BZY ont également été déterminés par calculs DFT. Les résultats montrant que l'oxyapatite présente une légère anisotropie du tenseur élastique alors que pour BZY, le dopage à l'yttrium et la présence des protons tend à diminuer la valeur du coefficient élastique.
- La variation en température du coefficient d'expansion thermique et des coefficients élastiques a été évaluée expérimentalement par diffraction des rayons X, dilatométrie et résonance ultrasonore. Dans la gamme 298 - 1173 K, le coefficient d'expansion thermique a été mesuré à $9.5 \times 10^{-6} \text{ K}^{-1}$ suivant la direction *a* et $8.2 \times 10^{-6} \text{ K}^{-1}$ suivant la direction *c*. Pour BZY, les valeurs mesurées de coefficient d'expansion thermique sont $8.5 \times 10^{-6} \text{ K}^{-1}$ et $8.2 \times 10^{-6} \text{ K}^{-1}$, pour BZY et BZY-NiO respectivement. Dans toutes ces céramiques, les coefficients élastiques *E* et *G* montrent une baisse d'environ 1% pour chaque augmentation de 100 K, le coefficient de Poisson demeurant pratiquement constant sur toute la gamme de températures explorées.

- Des simulations par la méthode des éléments-finis ont été menées pour évaluer la présence de contraintes résiduelles au sein des composés apatite. Les résultats montrent ces contraintes sont distribuées de manière hétérogène en fonction de l'orientation des différents grains, du fait de la différence de coefficient d'expansion thermique et d'élasticité suivant les directions a ou c .
- La réponse mécanique de Silicate de Lanthane et Zirconate de Baryum dopé à l'Yttrium a été testée à haute température dans les conditions proches de celles de fonctionnement d'une pile, en particulier sous hydrogène. Dans tous les cas, les échantillons de type oxyapatite montrent une réponse identique entre les atmosphères oxydantes et les atmosphères réductrices. C'est également le cas pour l'échantillon de BZY préparé au laboratoire. L'échantillon commercial de BZY-NiO montre par contre une forte dégradation de ses propriétés mécaniques sous hydrogène menant à la rupture de l'échantillon sous forte charge en compression (>350 MPa).
- Cette dégradation a été expliquée par la réduction des ions Nickel en Nickel métallique sous atmosphère hydrogénée, menant à la fragilisation du matériau, d'autant plus que le nickel a montré (TEM) être localisé essentiellement aux joints de grains.
- L'hypothèse que l'extraction du nickel permettrait d'améliorer les propriétés mécaniques n'a pas pu être démontrée car les échantillons après extraction présentent une porosité importante.
- L'évaluation de la déformation plastique à haute température des échantillons d'oxyapatite et de Zirconate de Baryum a été réalisée par des essais mécaniques en compression. La transition fragile-ductile a été identifiée à vitesse constante de déformation avec une température croissante. Pour une vitesse de déformation typique de $\dot{\epsilon}_0 = 3.5 \times 10^{-5} \text{ s}^{-1}$, cette transition a lieu aux environs de 1100 et 1000 °C pour les échantillons LSO-CS ($d = 1.1 \text{ }\mu\text{m}$) et LSO-SPS ($d = 0.2 \text{ }\mu\text{m}$), respectivement. Dans le cas de BZY préparé au laboratoire, cette transition a lieu aux environs de 1200 °C ($d = 0.2 \text{ }\mu\text{m}$). Dans le régime fragile, un mode de fracture mixte a été observé dans les deux apatites, alors qu'il était principalement intergranulaire dans BZY.

- Aux plus hautes températures, les échantillons montrent un comportement plastique. Dans tous les cas, la déformation observée a été associée au glissement des joints de grains conservant la forme des grains après déformation. Dans plusieurs des échantillons d'oxyapatite, nous avons observé le phénomène parasite de croissance de grains en parallèle de la déformation plastique, alors qu'aucun changement de la taille des grains n'a été observé dans le BZY, conformément à la mauvaise sinistérabilité signalée pour ce matériau.
- Dans le régime stationnaire, les paramètres de fluage ont été déterminés à partir des essais mécaniques classiques et différentiels. L'exposant de stress n a été évalué pour être égale à 2 dans l'oxyapatite préparée par SPS et dans BZY i.e. dans les matériaux présentant une très faible taille de grains. Cette valeur est caractéristique d'une superplasticité comme observée dans d'autres céramiques nanostructurées. Dans l'apatite préparée par frittage conventionnel avec une taille de grains micronique, l'exposant de stress est proche de 1 comme reporté dans plusieurs matériaux oxydes avec des grains $d > 1 \mu\text{m}$. L'origine atomistique de cette transition est actuellement inconnue.
- Indépendamment des valeurs d'exposant de stress, l'énergie d'activation du mécanisme de fluage a été calculée pour tous les échantillons. Une valeur de $Q = 340 \text{ kJ/mol}$ a été mesurée pour les échantillons d'oxyapatite préparés par frittage conventionnel et spark plasma, indiquant que le mécanisme de diffusion contrôlant le fluage a probablement la même origine dans les deux cas. Dans BZY, la valeur de l'énergie d'activation a été mesurée à 570 kJ/mol .
- Les diffusivités effectives du matériau massif et des joints de grains ont été déterminées par un modèle de type Ashby-Verrall dans le cas de l'oxyapatite préparée par frittage conventionnel ($n = 1$) et par un modèle de type Sherby pour l'oxyapatite fabriquée par SPS ($n = 2$). Malgré l'utilisation de modèles différents (dû à la présence de microstructures très différentes), on observe un excellent accord entre les diffusivités de joints de grains obtenues pour les deux types d'échantillons. Notre approche a également permis de montrer que la diffusivité du bulk pour BZY est de 2 ordres de grandeur inférieure à celle de l'oxyapatite permettant d'expliquer en partie les problèmes de frittage rencontrés pour ce matériau. Il est important de souligner ici que la détermination de la diffusivité du matériau est de première importance pour comprendre la plasticité à haute température

mais également dans tous les process impliquant des transferts de masse tels que la croissance des grains, le frittage ou la relaxation des contraintes. Une telle information peut donc être utilisée pour optimiser le procédé d'élaboration ou de mise en forme de ces céramiques.

Chapter 7

CONCLUSIONES GENERALES

Este trabajo se ha dirigido a la fabricación y caracterización estructural, microestructural y mecánica de Silicato de Lantano y Circonato de Bario dopado con Itrio, que son considerados materiales muy prometedores para ser utilizados como electrolito en las SOFCs. A continuación se presentan las principales conclusiones derivadas de este trabajo:

- Se han obtenido con éxito cerámicos de $\text{La}_{9.33}\text{Si}_6\text{O}_{26}$ y $\text{BaZr}_{0.85}\text{Y}_{0.15}\text{O}_{2.925}$ totalmente densos a partir de nanopulvos obtenidos mediante diferentes estrategias. Por una parte, los materiales de LSO se sintetizaron mediante liofilización y se sinterizaron a alta temperatura por sinterización convencional o asistida por descarga eléctrica pulsada, dando como resultado oxi-apatitas con densidades relativas entre 97% y 100%. Por otra parte, los materiales de BZY se prepararon mediante el método de agentes complejantes EDTA- ácido cítrico y se sinterizaron a alta temperatura por sinterización convencional, lográndose densidades superiores al 97%.
- Se ha estudiado también un material comercial de $\text{BaZr}_{0.85}\text{Y}_{0.15}\text{O}_{2.925}$ fabricado mediante reacción en estado sólido con 1% en peso de NiO como aditivo y proporcionado por NorecsTM. Además, con el fin de evaluar la influencia del níquel en las propiedades mecánicas, la caracterización mecánica también se llevó a cabo en el material comercial de BZY después de la extracción del NiO. Para realizar el proceso de extracción fue necesario poner el material comercial en una cama de polvos de BZY y someterlo a un tratamiento térmico a alta temperatura a 1600 °C durante 120 h.
- Los análisis de difracción de rayos X, tanto de los polvos calcinados como de los materiales sinterizados, muestran la presencia de las fases puras de $\text{La}_{9.33}\text{Si}_6\text{O}_{26}$ (*P63/m*) y $\text{BaZr}_{0.85}\text{Y}_{0.15}\text{O}_{2.925}$ (*Pm3m*), respectivamente. Sin embargo, el material comercial de BZY-NiO contiene también BaY_2NiO_5 (*Immm*), que desaparece completamente después del proceso de extracción del NiO. Los parámetros reticulares deducidos de los diagramas de XRD de los nanopulvos y de los masivos de LSO mediante el método de Le Bail, no revelaron

cambios significativos, encontrando valores de $a = 9.729$ (3) Å y $c = 7.183$ (2) Å. Se estimó que el tamaño de cristalitas era aproximadamente 80-90 nm, lo que se correlacionaba bien con las observaciones de TEM, donde se observaron partículas irregulares de un tamaño medio aproximado de 100 nm. En el caso del BZY, se encontró un parámetro de red $a = 4.203$ (1) Å para el polvo calcinado, que aumentó ligeramente hasta $a = 4.223$ (3) Å después de la sinterización. El tamaño de cristallito estimado fue de aproximadamente 15-20 nm, también en concordancia con el tamaño de las pequeñas partículas esféricas de entre 10 y 40 nm de diámetro observadas por TEM. Los parámetros reticulares deducidos por Le Bail para los materiales comerciales antes y después de la extracción del NiO fueron $a = 4.212$ (3) Å y 4.223 (3) Å, respectivamente, lo que indica que la adición de NiO reduce ligeramente el parámetro de red de la celda de unidad cúbica.

- Las observaciones de SEM reflejaron que todos los compuestos exhibían una microestructura homogénea formada por granos equiaxiados y prácticamente sin porosidad, excepto en el caso de BZY después de la extracción del NiO, que presentaba cavidades de aproximadamente 10 µm de tamaño ubicadas preferentemente en los puntos triples de unión de los granos. Los tamaños medios de grano variaron de 0.2 ± 0.1 µm en BZY y LSO-SPS, a 9 ± 3 µm en el caso del material comercial después de la extracción del NiO. Se encontraron valores intermedios para LSO-CS y BZY-NiO, que mostraron un tamaño de grano medio d de 1.1 ± 0.6 y 1.6 ± 0.6 , respectivamente.
- Las observaciones de TEM de las oxi-apatitas y del BZY-NiO mostraron que los granos estaban mayoritariamente libres de defectos, con bordes limpios y rectos y puntos triples bien definidos. Sin embargo, tanto el BZY como el BZY después de la extracción del NiO presentaban una alta densidad de dislocaciones.
- La caracterización mecánica a temperatura ambiente del Silicato de Lantano y del Circonato de Bario dopado con Itrio se realizó mediante diferentes técnicas. Todos los métodos mostraron resultados similares de las propiedades elásticas, siendo RUS la técnica más precisa. Sin embargo, los valores de dureza obtenidos por microindentación fueron significativamente más bajos que aquellos determinados por nanoindentación, lo que puede ser justificado en base a la dependencia de la dureza con la carga aplicada.

- Los valores del módulo elástico obtenidos a temperatura ambiente fueron entre 135 - 141 GPa para LSO-CS y 129 - 136 GPa para LSO-SPS. Mientras que valores más altos se determinaron para los compuestos de BZY, con valores de E en el intervalo de 186 - 200 GPa para el BZY, 198 - 207 GPa para el BZY - NiO y 191 - 211 para el BZY después de la extracción del NiO.
- Los valores de coeficientes de Poisson obtenidos a temperatura ambiente se encontraron en el intervalo de 0.29 - 0.32 para las oxi-apatitas, mientras que para las cerámicas BZY estaban entre 0.24 y 0.32.
- En cuanto a la dureza, mediante nanoindentación se obtuvieron resultados de 9.5 y 9.8 GPa en LSO-CS y LSO-SPS para una carga aplicada de 500 mN, mientras que se determinaron valores de 7.3 y 7.7 GPa para una carga de 2 N por microindentación. Para las mismas condiciones de carga, se encontraron valores de nanodureza de 10.1, 9.0 y 6.7 GPa para el BZY, BZY-NiO y BZY después de la extracción del NiO, respectivamente, mientras que los obtenidos por microindentación fueron 7.7, 7.0 y 4.7 GPa. La abrupta disminución de la dureza del BZY después de la extracción del NiO se puede atribuir al mayor tamaño de grano que presenta este material en comparación con los otros compuestos, ya que la dureza es inversamente proporcional al tamaño de grano de acuerdo con la ley de Hall-Petch.
- La tenacidad de fractura se calculó a partir de las grietas propagadas desde las esquinas de las microindentaciones utilizando la ecuación de Niihara para las oxi-apatitas y el BZY, obteniéndose valores de 1.2 y 1.6 MPa m^{1/2}, respectivamente. Sin embargo, la tenacidad de fractura no se pudo determinar en los materiales comerciales debido a la presencia de grietas circunferenciales que rodeaban las huellas residuales, lo que impidió una determinación fiable de K_{Ic} .
- Las constantes elásticas de los compuestos LSO y BZY también se determinaron mediante cálculos DFT. En el caso de la oxi-apatita, los resultados revelaron una ligera anisotropía en su respuesta longitudinal elástica entre ejes a , b y c , mientras que en el caso del BZY, se observó que tanto el aumento del nivel de dopaje de Itrio como la presencia de protones tienden a reducir los coeficientes elásticos.

- La evolución del coeficiente de expansión térmica y de las constantes elásticas del Silicato de Lantano y del Circonato de Bario dopado con Itrio se estudió mediante difracción de rayos X a alta temperatura, análisis termomecánico y espectroscopía de resonancia ultrasónica a alta temperatura. Por una parte, en el intervalo de temperatura de 298 - 1173 K, se estimó que para las oxi-apatitas el coeficiente de expansión térmica anisotrópico era $9.5 \times 10^{-6} \text{ K}^{-1}$ en el eje a y $8.2 \times 10^{-6} \text{ K}^{-1}$ en el eje c , mientras que un valor de $9.1 \times 10^{-6} \text{ K}^{-1}$ se determinó a escala macroscópica. Los valores obtenidos para el BZY y BZY-NiO fueron $8.5 \times 10^{-6} \text{ K}^{-1}$ y $8.2 \times 10^{-6} \text{ K}^{-1}$, respectivamente. Por otra parte, todos los cerámicos muestran la misma evolución de sus constantes elásticas, con E y G disminuyendo aproximadamente un 1% por cada incremento de 100 K de acuerdo con la regla general, mientras que el coeficiente de Poisson permaneció prácticamente constante.
- Se han llevado a cabo con éxito simulaciones numéricas por elementos finitos en un agregado policristalino de oxi-apatita creado mediante una teselación de Voronoi para caracterizar el estado de tensiones residuales y predecir su fractura. Los resultados mostraron que las tensiones residuales se distribuían heterogéneamente en el agregado lo cual estaba completamente ligado con la anisotropía termoelástica de los cristales. Se observó que las tensiones se localizaba preferiblemente a lo largo de los bordes de algunos granos orientados favorablemente generando a altos niveles de tensiones residuales. Sin embargo, con el fin de estudiar adecuadamente el fallo de este material, se observó que es necesario considerar los agregados más grandes con el objetivo de establecer adecuadamente las propiedades termoelásticas y ser más precisos con la construcción del policristal y con las propiedades del material.
- La respuesta mecánica de los electrolitos de Silicato de Lantano y Circonato de Bario dopado con Itrio se ha estudiado en condiciones similares a las condiciones de operación de las SOFCs, mediante ensayos mecánicos de compresión a alta temperatura y en atmósfera de hidrógeno. Los compuestos de LSO no mostraron ninguna señal de degradación en atmósfera de hidrógeno. El mismo comportamiento fue observado en los materiales cerámicos de BZY fabricados sin aditivos, los cuales no sufrieron ninguna degradación mecánica significativa durante los experimentos, incluso bajo una tensión de compresión muy elevada. Sin embargo, el material comercial de BZY que contiene NiO falló catastróficamente en atmósfera de hidrógeno a tensiones superiores a 350 MPa.

- Mediante un análisis químico a escala atómica, se ha observado que en el material comercial de BZY fabricado con NiO, el óxido de níquel se localizaba principalmente a lo largo de los bordes de grano y que éste se reducía a Ni metálico en atmósfera de hidrógeno. Esta reducción de NiO en los bordes de grano favorece la ruptura de la muestra incluso a tensiones muy bajas, limitando así la resistencia a la fractura del material.
- Aunque la extracción con NiO puede considerarse como una solución para prevenir la degradación prematura del BZY-NiO en las condiciones de trabajo, el proceso de extracción da lugar a un material poroso con un importante crecimiento de grano y una baja resistencia mecánica.
- La deformación plástica a alta temperatura de oxi-apatitas y Circonato de Bario dopado con Itrio se ha evaluado mediante ensayos mecánicos de compresión. Se ha observado una transición de frágil a dúctil a medida que aumenta la temperatura para una velocidad de deformación dada. Para un valor típico de $\dot{\epsilon}_0 = 3.5 \times 10^{-5} \text{ s}^{-1}$, la temperatura de transición es de aproximadamente 1100 y 1000 °C para LSO-CS ($d = 1.1 \text{ }\mu\text{m}$) y LSO-SPS ($d = 0.2 \text{ }\mu\text{m}$), respectivamente, y 1200 °C para BZY ($d = 0,2 \text{ }\mu\text{m}$). En el régimen frágil, ambas apatitas presentaron una fractura mixta, mientras que el modo de fractura del BZY era predominantemente intrergranular.
- A temperaturas superiores, los compuestos alcanzaron estados de deformación estacionaria prolongados. En todos los casos, se ha encontrado que el deslizamiento de fronteras de grano es el principal mecanismo de deformación, con los granos conservando su forma original incluso después de deformaciones tan grandes como el 50%. Se observó un significativo crecimiento grano durante la deformación de las oxi-apatitas, mientras que no se encontró ningún cambio en el tamaño de grano en el BZY, de acuerdo con la pobre sinterabilidad reportada para este material.
- En el régimen de estado estacionario, los parámetros de fluencia se obtuvieron a partir de ensayos mecánicos convencionales y diferenciales. Se obtuvo un exponente de tensión n cercano a 2 en LSO-SPS y BZY, es decir, en materiales con microestructuras de grano fino. Este valor es característico de la superplasticidad en metales y cerámicas. En LSO-CS con $d > 1 \text{ }\mu\text{m}$, el exponente de tensión es cercano a la unidad, tal como se ha encontrado también en diversos materiales cerámicos con tamaños de grano $d > 1 \text{ }\mu\text{m}$. El origen

atómico de la transición en n de 2 a 1 cuando se incrementa el tamaño de grano es actualmente desconocido.

- Independientemente del valor exacto del exponente de tensión, la energía de activación de fluencia Q se asocia generalmente con la energía de difusión de la especie iónica más lenta del compuesto cuando el deslizamiento de fronteras de grano es el principal mecanismo de deformación. Se ha medido un valor de $Q = 340$ kJ/mol para las oxi-apatitas LSO-CS y LSO-SPS, lo que indica que el mismo mecanismo de difusión controla la velocidad de deformación, a pesar de la diferencia en el exponente de la tensión. En el BZY, la energía de activación de fluencia fue de 570 kJ/mol. No se han reportado en la literatura valores para la energía de difusión en estos materiales, para poder realizar una comparación adecuada.
- Las difusividades efectivas para la difusión a través del volumen y a lo largo de las fronteras de grano se obtuvieron a partir de datos mecánicos utilizando el modelo de Ashby-Verrall para LSO-CS ($n = 1$) y las ecuaciones fenomenológicas de Sherby para LSO-SPS y BZY ($n = 2$). Existe una excelente concordancia entre los coeficientes de difusión por bordes de grano estimados para las oxi-apatitas, dando confianza al presente análisis. Por otra parte, las difusividades derivadas para BZY son dos órdenes de magnitud más pequeñas que para las apatitas, lo que puede justificar la baja sinterabilidad de este material. En este sentido, debe tenerse en cuenta la importancia de determinar el coeficiente de difusión de las especies que se mueven más lentamente en los compuestos, ya que desempeña un papel esencial no sólo en la fluencia, sino en todos los procesos relacionados con el transporte de masa, como la sinterización y el crecimiento de grano. Dicha información se puede utilizar para diseñar programas de procesamiento óptimos.

Titre : Propriétés thermo-mécaniques des matériaux pour les piles à combustible.

Mots clés : Piles à combustible à oxyde solide, matériaux d'électrolyte, propriétés mécaniques, fluage.

Résumé : Les piles à combustible à oxyde solide (SOFC) offrent une alternative réelle aux technologies classiques de génération d'électricité en étant à la fois propre, efficace et respectueuse de l'environnement. Toutefois, leur principale limitation réside en leur durée de vie et fiabilité limitées dues à leur haute température de fonctionnement. Des recherches intenses de matériaux pour SOFC sont actuellement poursuivies pour essayer d'abaisser la température de fonctionnement de ces dispositifs afin de dépasser ces limitations. Parmi les différents candidats qui ont émergé, le Silicate de Lanthane (LSO) et le Zirconate de Baryum dopé à l'Yttrium (BZY) ont été identifiés comme des alternatives potentielles à utiliser comme matériaux d'électrolyte pour SOFC à température intermédiaire. De manière surprenante, alors que de nombreuses études concernent l'optimisation microstructurale et électrochimiques des composants de la pile, très peu d'études concernant l'évaluation de leurs propriétés mécaniques et de leur influence sur la durée de vie du dispositif.

La fiabilité et durée de ces dispositifs dépend non seulement de leur stabilité électrochimique, mais aussi de la capacité de leur structure à supporter les contraintes résiduelles issues du procédé de fabrication et de contraintes mécaniques de fonctionnement. En raison du fait que les SOFC sont composés d'empilement de plusieurs cellules individuelles qui, à leur tour, sont constituées de couches fragiles individuelles en contact étroit, ces contraintes proviennent principalement de la différence entre le coefficient de dilatation thermique et les propriétés élastiques des couches adjacentes et la déformation du fluage. Des contraintes non coordonnées peuvent entraîner une défaillance mécanique d'une seule cellule et avoir des conséquences dramatiques sur l'ensemble de la pile. De ce fait, la connaissance des propriétés mécaniques des composants de la cellule est une étape importante pour préserver l'intégrité et le développement des SOFC. Le but de cette thèse est la fabrication et l'étude des propriétés structurales, microstructurales et mécaniques de matériaux de type LSO et BZY.

Title : Thermo-mechanical properties of materials for fuel cells.

Keywords : Solid oxide fuel cells, electrolyte materials, mechanical properties, creep.

Abstract : Solid oxide fuel cells (SOFCs) offer a real alternative to classical technologies for the generation of electricity by clean, efficient and environmental-friendly means. Nevertheless, the main limitation of SOFCs lies in their unsatisfactory durability and reliability due to the high operating temperatures and thermal cycling characteristic of these devices. An intense search is currently underway for materials for SOFCs with the objective of lowering the working temperature and then overcoming these limitations. Among the different candidates which have emerged, Lanthanum Silicate (LSO) and Yttrium-doped Barium Zirconate (BZY) were considered as potential alternatives to be used as electrolyte materials for SOFC at intermediate-temperature. While numerous studies have been devoted to characterizing and optimizing the microstructural and electro-chemical properties of SOFC components, as yet there is little research available on mechanical properties and the influence they have on SOFC lifespan.

The reliability and durability of these devices depends not only on their electro-chemical stability, but also on the ability of their structure to withstand residual stresses arising from the cell manufacturing process and mechanical stresses from operation. Owing to the fact that SOFCs are composed by stacking of several single cells which in turn are made up of individual brittle layers in close contact, these stresses mainly originate from the difference between the coefficient of thermal expansion and elastic properties of adjacent layers and creep deformation. Mismatched stresses can result in the mechanical failure of a single cell and have dramatic consequences on the whole stack. Therefore, knowledge of mechanical properties of the cell components becomes an important issue for the mechanical integrity and development of SOFCs. The aim of this PhD thesis is the fabrication and structural, microstructural and mechanical characterization of LSO and BZY.

